PAVEMENTS AND MATERIALS

Characterization, Modeling, and Simulation

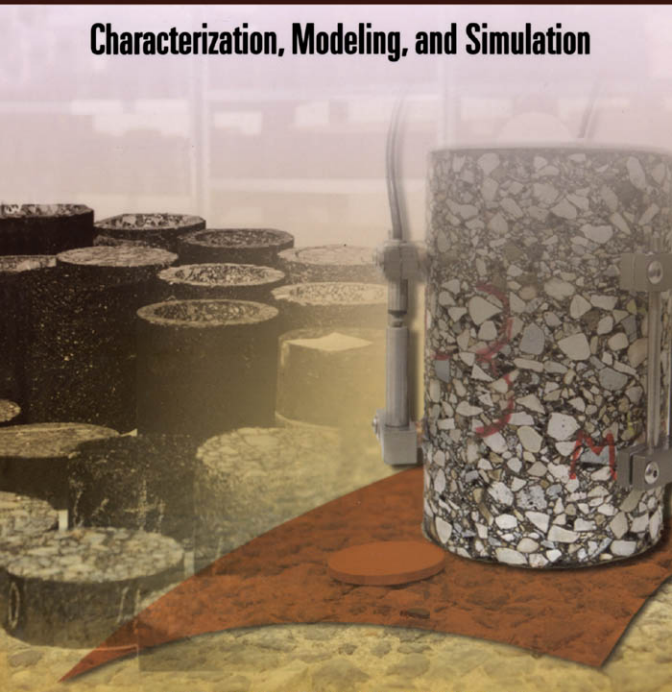

GEOTECHNICAL SPECIAL PUBLICATION NO. 182

Edited by
Zhanping You
Ala R. Abbas
Linbing Wang

ASCE

GEO INSTITUTE

GEOTECHNICAL SPECIAL PUBLICATION NO. 182

PAVEMENTS AND MATERIALS

CHARACTERIZATION, MODELING, AND SIMULATION

PROCEEDINGS OF SYMPOSIUM ON PAVEMENT MECHANICS AND MATERIALS AT THE 18TH ASCE ENGINEERING MECHANICS DIVISION (EMD) CONFERENCE

June 3-6, 2007
Blacksburg, Virginia

SPONSORED BY
Pavements Committee of The Geo-Institute
American Society of Civil Engineers

Task Committee on Mechanics of Pavements, Inelastic Committee, and Granular Materials Committee of The Engineering Mechanics Institute, American Society of Civil Engineers

EDITED BY
Zhanping You
Ala R. Abbas
Linbing Wang

Published by the American Society of Civil Engineers

Library of Congress Cataloging-in-Publication Data

Symposium on Pavement Mechanics and Materials (2007 : Blacksburg, Va.)
Pavements and materials : characterization, modeling, and simulation : proceedings of Symposium on Pavement Mechanics and Materials at the 18th ASCE Engineering Mechanics Division (EMD) Conference : June 3-6, 2007, Blacksburg, Virginia / sponsored by Pavements Committee of the Geo-Institute, American Society of Civil Engineers ... [et al.] ; edited by Zhanping You, Ala R. Abbas, Linbing Wang.
p. cm. -- (Geotechnical special publication ; no. 182)
Includes bibliographical references and indexes.
ISBN 978-0-7844-0986-2
1. Pavements--Congresses. 2. Road materials--Congresses. 3. Pavement--Performance--Congresses. 4. Pavements, Asphalt--Congresses. I. You, Zhanping. II. Abbas, Ala R. III. Wang, Linbing, 1963- IV. American Society of Civil Engineers. Geo-Institute. Pavements Committee. V. ASCE Engineering Mechanics Conference (18th : 2007 : Blacksburg, Va.) VI. Title.

TE250.S924 2007 2008027069
625.8'5--dc22

American Society of Civil Engineers
1801 Alexander Bell Drive
Reston, Virginia, 20191-4400

www.pubs.asce.org

ISBN 13: 978-0-7844-0986-2
Manufactured in the United States of America.

Geotechnical Special Publications

1 *Terzaghi Lectures*
2 *Geotechnical Aspects of Stiff and Hard Clays*
3 *Landslide Dams: Processes, Risk, and Mitigation*
7 *Timber Bulkheads*
9 *Foundations & Excavations in Decomposed Rock of the Piedmont Province*
11 *Dynamic Response of Pile Foundations¥ Experiment, Analysis and Observation*
14 *Geotechnical Aspects of Karst Terrains*
15 *Measured Performance Shallow Foundations*
16 *Special Topics in Foundations*
17 *Soil Properties Evaluation from Centrifugal Models*
18 *Geosynthetics for Soil Improvement*
19 *Mine Induced Subsidence: Effects on Engineered Structures*
21 *Hydraulic Fill Structures*
22 *Foundation Engineering*
23 *Predicted and Observed Axial Behavior of Piles*
24 *Resilient Moduli of Soils: Laboratory Conditions*
25 *Design and Performance of Earth Retaining Structures*
27 *Geotechnical Engineering Congress*
28 *Detection of and Construction at the Soil/Rock Interface*
29 *Recent Advances in Instrumentation, Data Acquisition and Testing in Soil Dynamics*
32 *Embankment of Dams¥James L. Sherard Contributions*
33 *Excavation and Support for the Urban Infrastructure*
34 *Piles Under Dynamic Loads*
35 *Geotechnical Practice in Dam Rehabilitation*
37 *Advances in Site Characterization: Data Acquisition, Data Management and Data Interpretation*
39 *Unsaturated Soils*
40 *Vertical and Horizontal Deformations of Foundations and Embankments*
41 *Predicted and Measured Behavior of Five Spread Footings on Sand*
42 *Serviceability of Earth Retaining Structures*
43 *Fracture Mechanics Applied to Geotechnical Engineering*
44 *Ground Failures Under Seismic Conditions*
45 *In Situ Deep Soil Improvement*
46 *Geoenvironment 2000*
47 *Geo-Environmental Issues Facing the Americas*
48 *Soil Suction Applications in Geotechnical Engineering*
49 *Soil Improvement for Earthquake Hazard Mitigation*
50 *Foundation Upgrading and Repair for Infrastructure Improvement*
51 *Performance of Deep Foundations Under Seismic Loading*
52 *Landslides Under Static and Dynamic Conditions¥Analysis, Monitoring, and Mitigation*
53 *Landfill Closures¥Environmental Protection and Land Recovery*
54 *Earthquake Design and Performance of Solid Waste Landfills*
55 *Earthquake-Induced Movements and Seismic Remediation of Existing Foundations and Abutments*
56 *Static and Dynamic Properties of Gravelly Soils*
57 *Verification of Geotechnical Grouting*
58 *Uncertainty in the Geologic Environment*
59 *Engineered Contaminated Soils and Interaction of Soil Geomembranes*
60 *Analysis and Design of Retaining Structures Against Earthquakes*
61 *Measuring and Modeling Time Dependent Soil Behavior*
62 *Case Histories of Geophysics Applied to Civil Engineering and Public Policy*
63 *Design with Residual Materials: Geotechnical and Construction Considerations*
64 *Observation and Modeling in Numerical Analysis and Model Tests in Dynamic Soil-Structure Interaction Problems*
65 *Dredging and Management of Dredged Material*
66 *Grouting: Compaction, Remediation and Testing*
67 *Spatial Analysis in Soil Dynamics and Earthquake Engineering*
68 *Unsaturated Soil Engineering Practice*
69 *Ground Improvement, Ground Reinforcement, Ground Treatment: Developments 1987-1997*
70 *Seismic Analysis and Design for Soil-Pile-Structure Interactions*
71 *In Situ Remediation of the Geoenvironment*
72 *Degradation of Natural Building Stone*
73 *Innovative Design and Construction for Foundations and Substructures Subject to Freezing and Frost*

74 *Guidelines of Engineering Practice for Braced and Tied-Back Excavations*
75 *Geotechnical Earthquake Engineering and Soil Dynamics III*
76 *Geosynthetics in Foundation Reinforcement and Erosion Control Systems*
77 *Stability of Natural Slopes in the Coastal Plain*
78 *Filtration and Drainage in Geotechnical/Geoenvironmental Engineering*
79 *Recycled Materials in Geotechnical Applications*
80 *Grouts and Grouting: A Potpourri of Projects*
81 *Soil Improvement for Big Digs*
82 *Risk-Based Corrective Action and Brownfields Restorations*
83 *Design and Construction of Earth Retaining Systems*
84 *Effects of Construction on Structures*
85 *Application of Geotechnical Principles in Pavement Engineering*
86 *Big Digs Around the World*
87 *Jacked Tunnel Design and Construction*
88 *Analysis, Design, Construction, and Testing of Deep Foundations*
89 *Recent Advances in the Characterization of Transportation Geo-Materials*
90 *Geo-Engineering for Underground Facilities*
91 *Special Geotechnical Testing: Central Artery/Tunnel Project in Boston, Massachusetts*
94 *Performance Confirmation of Constructed Geotechnical Facilities*
95 *Soil-Cement and Other Construction Practices in Geotechnical Engineering*
96 *Numerical Methods in Geotechnical Engineering: Recent Developments*
97 *Innovations and Applications in Geotechnical Site Characterization*
98 *Pavement Subgrade, Unbound Materials, and Nondestructive Testing*
99 *Advances in Unsaturated Geotechnics*
100 *New Technological and Design Developments in Deep Foundations*
101 *Slope Stability 2000*
102 *Trends in Rock Mechanics*
103 *Advances in Transportation and Geoenvironmental Systems Using Geosynthetics*
104 *Advances in Grouting and Ground Modification*
105 *Environmental Geotechnics*
106 *Geotechnical Measurements: Lab & Field*
107 *Soil Dynamics and Liquefaction 2000*
108 *Use of Geophysical Methods in Construction*
109 *Educational Issues in Geotechnical Engineering*
110 *Computer Simulation of Earthquake Effects*
111 *Judgment and Innovation: The Heritage and Future of the Geotechnical Engineering Profession*
112 *Soft Ground Technology*
114 *Soils Magic*
115 *Expansive Clay Soils and Vegetative Influence on Shallow Foundations*
116 *Deep Foundations 2002: An International Perspective on Theory, Design, Construction, and Performance*
117 *Discrete Element Methods: Numerical Modeling of Discontinua*
118 *A History of Progress: Selected U.S. Papers in Geotechnical Engineering*
119 *Soil Behavior and Soft Ground Construction*
120 *Grouting and Ground Treatment*
121 *Probabilistic Site Characterization at the National Geotechnical Experimentation Sites*
122 *Sinkholes and the Engineering and Environmental Impacts of Karst*
123 *Recent Advances in Materials Characterization and Modeling of Pavement Systems*
124 *GeoSupport 2004: Drilled Shafts, Micropiling, Deep Mixing, Remedial and Specialty Foundation Systems*
125 *Current Practices and Future Trends in Deep Foundations*
126 *Geotechnical Engineering for Transportation Projects*
127 *Recycled Materials in Geotechnics*
128 *Soil Constitutive Models: Evaluation, Selection, and Calibration*
129 *Advances in Designing and Testing Deep Foundations*
130 *Advances in Pavement Engineering*
131 *Contemporary Issues in Foundation Engineering*
132 *Advances in Deep Foundations: In Memory of Michael W. O'Neill*
133 *Earthquake Engineering and Soil Dynamics*
134 *Soil Dynamics Symposium in Honor of Professor Richard D. Woods*
135 *Erosion of Soils and Scour of Foundations*
136 *Innovations in Grouting and Soil Improvement*

137 *Legal and Liability Issues in Geotechnical Engineering*
138 *Site Characterization and Modeling*
139 *Calibration of Constitutive Models*
140 *Slopes and Retaining Structures under Seismic and Static Conditions*
141 *International Perspectives on Soil Reinforcement Applications*
142 *Waste Containment and Remediation*
143 *Geomechanics: Testing, Modeling, and Simulation*
144 *Sinkholes and the Engineering and Environmental Impacts of Karst*
145 *Seismic Performance and Simulation of Pile Foundations in Liquefied and Laterally Spreading Ground*
146 *Asphalt Concrete: Simulation, Modeling and Experimental Characterization*
147 *Unsaturated Soils 2006*
148 *Advances in Unsaturated Soil, Seepage, and Environmental Geotechnics*
149 *Site and Geomaterial Characterization*
150 *Soil and Rock Behavior and Modeling*
151 *Advances in Earth Structures: Research to Practice*
152 *Ground Modification and Seismic Mitigation*
153 *Foundation Analysis and Design: Innovative Methods*
154 *Pavement Mechanics and Performance*
155 *Underground Construction and Ground Movement*
156 *Geomechanics II: Testing, Modeling, and Simulation*
157 *Computer Applications in Geotechnical Engineering*
158 *Contemporary Issues in Deep Foundations*
159 *Case Studies in Earth Retaining Structures*
160 *Dynamic Response and Soil Properties*
161 *Embankments, Dams, and Slopes: Lessons from the New Orleans Levee Failures and Other Issues*
162 *Problematic Soils and Rocks and In Situ Characterization*
163 *Geoenvironmental Engineering*
164 *Innovative Applications of Geophysics in Civil Engineering*
165 *Geosynthetics in Reinforcement and Hydraulic Applications*
166 *Educational Activities in Geotechnical Engineering*
167 *Geotechnics of Soil Erosion*
168 *Grouting for Ground Improvement: Innovative Concepts and Applications*
169 *Soil and Material Inputs for Mechanistic-Empirical Pavement Design*
170 *Probabilistic Applications in Geotechnical Engineering*
171 *Advances in Shallow Foundations*
172 *Soil Improvement*
173 *Advances in Measurement and Modeling of Soil Behavior*
174 *Designing Our Underground Space*
175 *Field Measurements in Geomechanics 2007*
176 *Analysis of Asphalt Pavement Materials and Systems: Emerging Methods*
177 *GeoCongress 2008: Geotechnics of Waste Management and Remediation*
178 *GeoCongress 2008: Geosustainability and Geohazard Mitigation*
179 *GeoCongress 2008: Characterization, Monitoring, and Modeling of GeoSystems*
180 *From Research to Practice in Geotechnical Engineering*
181 *Geotechnical Earthquake Engineering and Soil Dynamics IV*

This page intentionally left blank

Preface

This special publication includes 16 papers on characterization, modeling and simulation of asphalt mixtures, asphalt pavements, and concrete mixtures, addressing a variety of timely issues in pavement mechanics. They include five papers on modeling and simulations of asphalt concrete by incorporating the microscopic structures of the material, the interactions between aggregates, mastics and voids, and the use of Finite Element Method (FEM) and Discrete Element Method (DEM); two papers on the continuum approaches including nonlinear viscoelastic analysis and temperature dependency; four papers on pavement stress and strain analysis; two papers on laboratory characterization of modified asphalt concrete; one paper on pavement fatigue analysis, one paper on tire-pavement interaction, and; one paper on coefficient of thermal expansion of concrete for rigid pavement design.

Each paper published in this GSP was rigorously evaluated by peer reviewers and the editors. The review comments were sent to the authors and they have been addressed to the reviewers and the editors' satisfaction. The editors sincerely acknowledge reviewers' time and efforts. The editors also acknowledge Graduate student Shu Wei Goh at Michigan Technological University in the assistance of the cover design.

The papers in this GSP include eight papers that were presented in the symposium on Pavement Mechanics and Materials at the 18th ASCE Engineering Mechanics Division (EMD) Conference, held at Blacksburg, Virginia, June 3-6 2007 and eight papers submitted for publication only. The symposium was supported by the Geo-Institute Pavements Committee, the Task Committee on Mechanics of Pavements, the Inelastic Committee and the Granular Materials Committee of the ASCE Engineering Mechanics Institute.

The editors of this GSP would like to thank the Board of Governors of the Geo-Institute for their approving the symposium and the special publication.

Zhanping You, Ph.D., P.E., Michigan Technological University
Ala R. Abbas, Ph.D., University of Akron
Linbing Wang, Ph.D., P.E., Virginia Tech

December 30, 2007

This page intentionally left blank

Contents

Indexes

Theoretical Aspects in Modeling Asphalt Concrete and Pavements

Vassilis P. Panoskaltsis[1] and Dinesh Panneerselvam[2]

[1]Associate Professor, Department of Civil Engineering, Case Western Reserve University, Cleveland, Ohio, 44106-7201, U.S.A., (corresponding author); vpp@nestor.cwru.edu
[2]Advanced Application Engineer, Dassault Systemes Simulia Corp., Northville, Michigan 48167

ABSTRACT: A new nonlinear second order hyperelastic-viscoplastic-damage constitutive model in multi dimensions is developed and its theoretical foundations are presented. The model is used to analyze experiments for asphalt concrete both in the elastic as well as in the irreversible domain of the material. Model's comparisons to experiments are very favorable. The experiments are analyzed both as homogeneous and as boundary-value problems.

INTRODUCTION

Rutting defined in ASTM Standard E 867 as "a contiguous longitudinal depression deviating from a surface plane defined by transverse cross slope and longitudinal profile" is rated as the most significant distress type regarding damage in pavements. The longitudinal depressions (sometimes referred to as "ruts") are accompanied by upheavals to the side. In the asphalt – concrete layer, the rutting is caused by a combination of densification (compaction) and shear flow. The initial rut is caused by densification of the pavement under the path of the wheel. However, the subsequent rut is a result of shear flow of the mix. In properly compacted pavements, it has been found that shear flow in asphalt – concrete layer is the primary rutting mechanism, see e.g. Eisenmann and Hilmer (1987). Also, the mix exhibits volumetric/deviatoric coupling behavior; this manifests as the mix dilates under shear loading. A multi-dimensional hyperelastic-viscoplastic-damage model is developed to describe and predict the permanent deformations and coupling behavior of asphalt concrete. The elastic behavior of asphalt concrete is modeled by a second order hyperelastic model, since the volumetric/deviatoric coupling behavior of the mix is observed even at very small strain values and at lower temperatures. The rate-dependent behavior of asphalt concrete, as well as its permanent deformations are described by a constitutive model based on viscoplasticity and damage theories.

CONSTITUTIVE MODEL

In this section we present the aforementioned constitutive model. The model is developed in series and consists of a hyperelastic part and a viscoplastic-damage part.

Hyperelastic Model

Asphalt concrete exhibits volumetric/deviatoric coupling within its elastic region as is clearly evident in a repeated simple shear test at constant height (RSST-CH) experiment, developed at the University of California, Berkeley (Sousa et al. 1993). In this test, cylindrical specimens of 0.15 m (6 in.) in diameter by 0.05 m (2 in.) high are used. The height of the specimen is kept constant (by applying a vertical load provided by a vertical hydraulic actuator), while horizontal loads are applied by a horizontal actuator. The horizontal load is described by a haversine function with 0.05 s loading and 0.05 s unloading time followed by rest time of 0.6 s and is applied on a 0.2 in thick steel plate, which is glued to the cylindrical specimen. As is observed in these experiments, in which the evolution of the normal force was recorded, the normal force starts evolving from the very first cycles of the experiment during which no permanent shear strain has occurred. In order to describe this coupling behavior in the elastic regime we propose a second order hyperelastic model, that is, the stress is a second-order polynomial of the strain. A third-order hyperelastic model has been earlier proposed by Bahuguna et al. (2006). Clearly, a linear elastic model, which can be considered as a first order elastic model, cannot describe this behavior.

The strain energy function $W(\boldsymbol{\varepsilon}): R^6 \rightarrow R$ (where R^6 is the six dimensional Euclidean space of strains) that we propose here for the second order hyperelastic isotropic model is given by

$$W(\varepsilon) = b_1 I_1^2 + b_2 I_2 + b_3 I_1^3 + b_4 I_1 I_2 + b_5 I_3, \tag{1}$$

where $\boldsymbol{\varepsilon}$ is the strain tensor and b_1, b_2, b_3, b_4, and b_5 are material parameters. This form satisfies the condition that at zero strain state (material's natural state) the value of the strain energy function and the stress tensor be zero. I_1, I_2, I_3 are the invariants of the strain tensor defined as $I_1 = tr\boldsymbol{\varepsilon}$, $I_2 = tr\boldsymbol{\varepsilon}^2$, $I_3 = tr\boldsymbol{\varepsilon}^3$.

The stress tensor is given by

$$\sigma_{ij} = \frac{\partial W(\boldsymbol{\varepsilon})}{\partial \varepsilon_{ij}} = \left(2b_1 I_1 + 3b_3 I_1^2 + b_4 I_2\right)\delta_{ij} + \left(b_2 + b_4 I_1\right)\varepsilon_{ij} + b_5 \varepsilon_{im}\varepsilon_{mj}, \tag{2}$$

where δ_{ij} is Kronecker delta and repeated index implies summation convention.

To determine the five material parameters in the second order hyperelastic model, the tests conducted by Sousa et al. (1993) are used. The following three experiments, simple shear test, volumetric compression test and uniaxial strain compression test

were conducted in the elastic range. In other words, the experiments were conducted at low strain levels to minimize the irreversible effects and at low temperature (4°C) to minimize viscous effects. It is therefore assumed that the strains measured are elastic strains, since in the experiments no unloading has been reported. The simple shear test is the same as the repetitive simple shear test (RSST-CH), except only the loading part of one cycle is considered. In this test evolution of normal stress is also observed. In the uniaxial strain compression test the axial stress is applied while the lateral expansion of the specimen is prohibited. In the volumetric compression test the strain is the same in the three principal directions. All three tests are fitted simultaneously by using a nonlinear optimization scheme and a unique set of parameters is obtained. The objective function for the optimization procedure is a least square function given by

$$f = \left(\sum_{i=1}^{N_1} \left(\sigma_{11,i} - \sigma_{\exp,i} \right)^2 \right)_{Uniaxial} + \left(\sum_{i=1}^{N_2} \left(\sigma_{11,i} - \sigma_{\exp,i} \right)^2 \right)_{Volumetric} + \left(\sum_{i=1}^{N_3} \left(\sigma_{12,i} - \sigma_{\exp,i} \right)^2 \right)_{Shear} \quad (3)$$

where N_1, N_2, and N_3 are the number of data points taken from the uniaxial, volumetric and shear experiments, respectively; $\sigma_{11,i}$ is the normal stress predicted by the hyperelastic model for the i^{th} data point, $\sigma_{12,i}$ is the shear stress predicted by the model for the i^{th} data point and $\sigma_{\exp,i}$ is the stress value at i^{th} experimental point. The minimization of the objective function was performed using the optimization toolbox of MATLAB. The values obtained for the parameters are tabulated in Table 1.

Table 1. List of parameters

Parameter	b_1	b_2	b_3	b_4	b_5
Value	0.0004×10^8	0.4175×10^8	-5.53×10^8	0.005×10^8	-5.85×10^8

Fig. 1, Fig. 2 and Fig. 3 show the model simulations for shear, volumetric and uniaxial tests respectively. In Fig. 2 confining stress is the σ_{11} stress and radial strain is the principal strain. All figures show very good fit between the model results and experimental data. With the values of the parameters obtained from the parameter estimation procedure, the model's prediction of dilatancy behavior is compared to experimental results. Fig. 4 shows model prediction of the normal force developed during the simple shear test and the experimental data for the same. As is seen from the figure the model's prediction is very good.

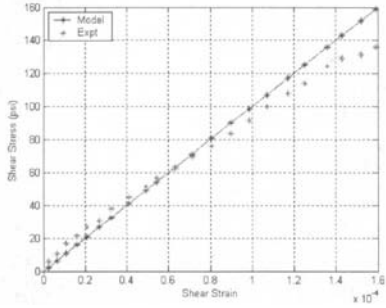

Fig. 1. Shear stress vs. shear strain.

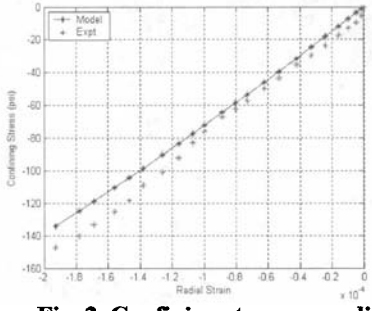

Fig. 2. Confining stress vs. radial strain.

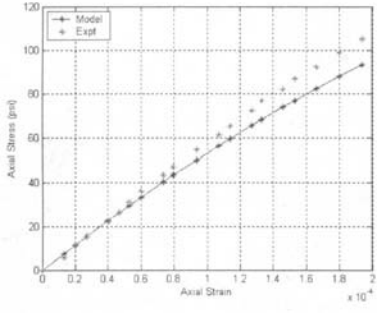

Fig. 3. Axial stress vs. axial strain.

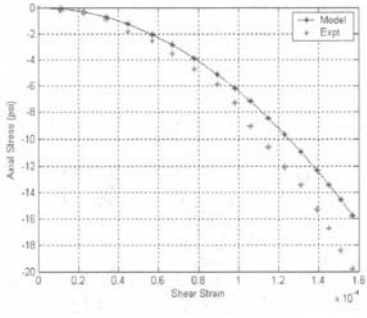

Fig. 4. Axial stress vs. shear strain.

Stability Analysis: Positive Definiteness of Tangent Stiffness

It is well known that the work done on an elastic body by any external agency on the changes in displacements it produces is positive. This is manifest in terms of stresses and elastic strains as follows:

$$\dot{\sigma}_{ij}\dot{\varepsilon}_{ij} > 0, \tag{4}$$

where a superimposed dot indicates time derivative. Materials which satisfy the above condition are called stable. It is necessary that constitutive laws proposed to characterize elastic material behavior satisfy the stability criterion given by Eq. 4. This stability criterion when applied to the hyperelastic model developed here requires that the Hessian matrix of the strain energy function be positive definite. This can be shown as follows: By differentiating the stress tensor with respect to time and using the first part of Eq. 2 we have that

$$\dot{\sigma}_{ij} = \frac{\partial \sigma_{ij}}{\partial \varepsilon_{kl}} \dot{\varepsilon}_{kl} = \frac{\partial^2 W}{\partial \varepsilon_{ij} \partial \varepsilon_{kl}} \dot{\varepsilon}_{kl} . \tag{5}$$

Substituting Eq. 5 into the stability condition Eq. 4 we obtain the following inequality

$$\frac{\partial^2 W}{\partial \varepsilon_{ij} \partial \varepsilon_{kl}} \dot{\varepsilon}_{ij} \dot{\varepsilon}_{kl} > 0 , \tag{6}$$

that is, the quadratic form given in Eq. 6 must be positive for arbitrary values of the components of strain rate. The inequality may be rewritten as

$$H_{ijkl} \dot{\varepsilon}_{ij} \dot{\varepsilon}_{kl} > 0 , \tag{7}$$

where H_{ijkl} is the tangent material stiffness and is a fourth order symmetric tensor given by

$$H_{ijkl} = \frac{\partial^2 W}{\partial \varepsilon_{ij} \partial \varepsilon_{kl}} . \tag{8}$$

Rewriting Eq. 7 in matrix form we obtain,

$$\dot{\boldsymbol{\varepsilon}}^T \boldsymbol{H} \dot{\boldsymbol{\varepsilon}} > 0 , \tag{9}$$

where $\dot{\boldsymbol{\varepsilon}}$ is the [6x1] vector containing the elastic strain rates and $\boldsymbol{H}$ is the [6x6] symmetric tangent stiffness matrix, also known as the Hessian matrix of the function W. The Hessian matrix $\boldsymbol{H}$ must be positive definite since Eq. 9 must hold for all

$$\dot{\boldsymbol{\varepsilon}} \neq \boldsymbol{0} .$$

When strain is expressed in a vector form, the elements of the Hessian matrix of W are written as

$$[H]=\begin{bmatrix} \frac{\partial^2 W}{\partial \varepsilon_1^2} & \frac{\partial^2 W}{\partial \varepsilon_1 \partial \varepsilon_2} & \frac{\partial^2 W}{\partial \varepsilon_1 \partial \varepsilon_3} & \frac{\partial^2 W}{\partial \varepsilon_1 \partial \varepsilon_4} & \frac{\partial^2 W}{\partial \varepsilon_1 \partial \varepsilon_5} & \frac{\partial^2 W}{\partial \varepsilon_1 \partial \varepsilon_6} \\ & \frac{\partial^2 W}{\partial \varepsilon_2^2} & \frac{\partial^2 W}{\partial \varepsilon_2 \partial \varepsilon_3} & \frac{\partial^2 W}{\partial \varepsilon_2 \partial \varepsilon_4} & \frac{\partial^2 W}{\partial \varepsilon_2 \partial \varepsilon_5} & \frac{\partial^2 W}{\partial \varepsilon_2 \partial \varepsilon_6} \\ & & \frac{\partial^2 W}{\partial \varepsilon_3^2} & \frac{\partial^2 W}{\partial \varepsilon_3 \partial \varepsilon_4} & \frac{\partial^2 W}{\partial \varepsilon_3 \partial \varepsilon_5} & \frac{\partial^2 W}{\partial \varepsilon_3 \partial \varepsilon_6} \\ & & & \frac{\partial^2 W}{\partial \varepsilon_4^2} & \frac{\partial^2 W}{\partial \varepsilon_4 \partial \varepsilon_5} & \frac{\partial^2 W}{\partial \varepsilon_4 \partial \varepsilon_5} \\ & & & & \frac{\partial^2 W}{\partial \varepsilon_5^2} & \frac{\partial^2 W}{\partial \varepsilon_5 \partial \varepsilon_6} \\ & & & & & \frac{\partial^2 W}{\partial \varepsilon_6^2} \end{bmatrix}. \tag{10}$$

Positive definiteness of the Hessian matrix ensures that the surfaces corresponding to constant W in strain space are convex. We will now perform the stability check on our hyperelastic model for the three different experiments described above and we will establish the strain ranges within which the model satisfies the stability criterion.

Stability Analysis for a Uniaxial Strain Compression Test

In this case the strain tensor is given by

$$\varepsilon=\begin{bmatrix} \varepsilon_0 & 0 & 0 \\ 0 & 0 & 0 \\ 0 & 0 & 0 \end{bmatrix}.$$

By using Eq. 1 we obtain the strain energy function for this case and from this the only non zero component of the Hessian matrix as

$$H_{1111}=\frac{\partial^2 W}{\partial \varepsilon_0^2}=\left(6b_3+3b_4+2b_6\right)\varepsilon_0+\left(2b_2+b_5\right). \tag{11}$$

Substituting the values of the parameters from Table 1 we have that

$$H_{1111}=\left(-2.785x10^9\right)\varepsilon_0+5.8x10^5 \tag{12}$$

$$H_{1111}>0 \Rightarrow \varepsilon_0<2.08x10^{-4}. \tag{13}$$

The above condition in Eq. 13 requires that for Hessian to be positive definite, the magnitudes of compressive strains have to be less than 2.08 x 10^{-4}. This condition is satisfied as is seen in Fig. 3 and hence the Hessian is positive definite and the strain energy function is convex.

Stability Analysis for a Volumetric Compression Test

The strain state is given by

$$\varepsilon = \begin{bmatrix} \varepsilon_0 & 0 & 0 \\ 0 & \varepsilon_0 & 0 \\ 0 & 0 & \varepsilon_0 \end{bmatrix}.$$

For a volumetric compression test, the Hessian matrix has all elements equal to zero except the first three main diagonal elements,

$$H_{1111} = H_{2222} = H_{3333} = 2\left(27b_3 + \frac{9}{2}b_4 + b_6\right)\varepsilon_0 + 2b_2 + b_5. \tag{14}$$

Substituting the values of the parameters from the Table 1 we obtain

$$H_{1111} = H_{2222} = H_{3333} = \left(-38.92x10^8\right)\varepsilon_0 + 5.8x10^5 \tag{15}$$

$$H_{1111} > 0 \text{ for } \varepsilon_0 < 1.49x10^{-4}. \tag{16}$$

The Hessian matrix is positive definite for $\varepsilon_0 < 1.49x10^{-4}$ and the strain energy function is convex. This condition is satisfied for almost the whole range of strains as is seen in Fig. 2.

Stability Analysis for a Simple Shear Test

The strain state is given by

$$\varepsilon = \begin{bmatrix} 0 & \varepsilon_0 & 0 \\ \varepsilon_0 & 0 & 0 \\ 0 & 0 & 0 \end{bmatrix}.$$

The Hessian matrix has only one non zero element which is $H_{4444} = 2b_5 = 0.01x10^8 > 0$ and the eigenvalues of the Hessian matrix are positive. Hence, the Hessian matrix is always positive definite and the strain energy function is always convex.

In Fig. 5, the strain energy function corresponding to a uniaxial compression test is plotted against axial strain. From the graph it can be seen that

$$W(\varepsilon) \text{ is } \begin{cases} \text{Convex for } \varepsilon_0 < 2.0x10^{-4} \\ \text{Concave for } \varepsilon_0 > 2.0x10^{-4} \end{cases}.$$

This is in complete agreement with the limiting value found earlier for the uniaxial case. Similar plots could also be shown for shear and volumetric tests.

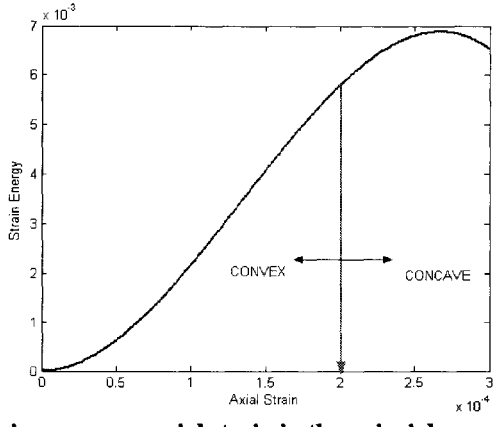

Fig. 5. Strain energy vs. axial strain in the uniaxial compression test.

Viscoplastic Model

To model the rate effects, as well as the irreversible deformations in asphalt concrete, we develop a constitutive model based on viscoplasticity theory. Viscoplasticity is a local internal variable theory. We will follow the theory which was proposed by Perzyna (Perzyna, 1963). This theory is based on the existence of a yield surface in stress space that separates the states in its interior (elastic domain) from states outside it. The stress states outside the yield surface lead to the evolution of inelastic deformations. The theory is a generalization of the classical theory of plasticity, and classical plasticity is included in as a special case. If the function $f: R^6 \rightarrow R$, where R^6 denotes the six-dimensional Euclidean stress space, denotes the yield function, then the viscoplastic strain rate is zero when $f \leq 0$ and is finite when $f > 0$. The surface corresponding to $f = 0$ is the yield surface and in the subset of the stress space which is within this surface the viscoplastic strain rate is zero. At stress points outside the yield surface the viscoplastic strain rate is different than zero and is normal to the surface $f = c$, where c is the value of f corresponding to the stress coordinates outside the yield surface (associative viscoplasticity). The surface

corresponding to $f = c$ belongs to the same family of surfaces as the yield surface and is called the dynamic loading surface. The surface $f = 0$ is sometimes called the quasistatic yield surface.

Based on the above discussion, the viscoplastic strain rate is given by

$$\dot{\varepsilon}_{ij}^{vp} = \gamma^o h(\langle f \rangle) \frac{\partial f}{\partial \sigma_{ij}}, \tag{17}$$

where γ^o is a material constant, h is a scalar function of f and the Macauley bracket operator $\langle . \rangle$ is defined as

$$\langle f \rangle = \begin{cases} 0 \text{ for } f \le 0 \\ f \text{ for } f > 0 \end{cases}. \tag{18}$$

The function $\langle h(f) \rangle$ is chosen differently to describe different experimental results. For other approaches to modeling viscoplasticity and rate effects in materials one can refer to Panoskaltsis et al. (1998) and Panneerselvam (2005).

One important characteristic of asphalt concrete's behavior is that the accumulation of permanent deformation with an increasing number of loading cycles under repetitive shear loading is almost linear on a log-log scale (Sousa et al. 1993). This means that the accumulation of permanent deformation has a polynomial relation with decreasing rate to the number of cycles on a linear scale. Similar results have been reported by Witczak et al. (2002). This behavior also characterizes granular materials as well as metals and sometimes is called ratcheting. Bahuguna et al. (2006) were the first to model this behavior of asphalt concrete by using generalized plasticity theory. In our work we will model this behavior by using the theory of viscoplasticity. Clearly, this behavior cannot be captured by classical plasticity theories.

Damage is also included in the model to characterize the softening behavior of asphalt concrete. Apart from the loading surface, other ingredients of a viscoplasticity theory are the flow rule for the evolution of viscoplastic strain and the hardening rule for the evolution of hardening parameter. A nonassociative flow rule is adopted in order to prevent excessive dilation predicted by an associative one. The proposed loading surface, flow rule and hardening law will be described next.

Loading Surface

The concept of loading surface plays an important role in viscoplasticity theory and the ability of the theory to model real material behavior depends crucially on the choice of the loading surface. The form of the loading surface proposed here is based on the following observations. Asphalt concrete consists of aggregates bound together by the viscous bituminous material. Due to the presence of these aggregates the behavior of asphalt concrete is similar to the behavior of granular materials like sands in many respects, one of them being that both materials exhibit dilation under

shear loading. Therefore, the loading surface proposed here is similar to the yield surface proposed by Vermeer (1982) for sands. The form of the loading surface is

$$f = I_1^c I_2^c + \alpha I_3^c - H\kappa, \tag{19}$$

where I_1^c, I_2^c and I_3^c are the modified first, second and third invariants of stress tensor, κ is the hardening variable, H is the hardening parameter and α is a material parameter. The invariants are properly modified, in order to account for the damage, as follows: The damage variable ω is defined as

$$\omega = \frac{A}{A_0};\ 0 \le \omega \le 1, \tag{20}$$

where A_0 is the initial area of the undamaged section and A is the area lost due to damage. It is a positive, monotonically increasing function, i.e. $\dot{\omega} > 0$; in other words, damage is irreversible. The effective stress σ_a is

$$\sigma_a = \frac{\sigma}{1-\omega}, \tag{21}$$

where σ is the nominal stress. The damage is incorporated in the model and stress invariants are modified accordingly:

$$I_1^c = \frac{I_1}{1-\omega},\ I_2^c = \frac{I_2}{(1-\omega)^2},\ I_3^c = \frac{I_3}{(1-\omega)^3}, \tag{22}$$

where I_1, I_2 and I_3 are the stress invariants defined as

$$I_1 = \sigma_{ii},\ I_2 = \frac{1}{2}(\sigma_{ij}\sigma_{ij} - I_1^2),\ I_3 = \det(\boldsymbol{\sigma}). \tag{23}$$

The damage variable is assumed to be a function of the total viscoplastic strain, i.e.

$$\omega = a_1(\varepsilon^{vp})^{a_2}, \tag{24}$$

where a_1 and a_2 are parameters (for more details see, Panneerselvam, 2005).

Flow Rule (Evolution Equation for Viscoplastic Strain Tensor)

Following the general form given in Eq. 17 the flow rule proposed here is given by Eq. 25

$$\dot{\boldsymbol{\varepsilon}}^{vp} = h(f,\kappa)\boldsymbol{\nu}, \tag{25}$$

where $\boldsymbol{\nu}$ represents the direction of the plastic flow and h is a scalar function of loading surface and hardening variable. The following form of h is proposed here on the basis of the observed evolution of permanent shear strains in RSST-CH experiments,

$$h = \left(\frac{\langle f \rangle}{\eta} \right)^m \frac{1}{x + \kappa^l}, \tag{26}$$

where η is the viscosity parameter and x, m and l are material parameters. This is a modified version of the form proposed by Bahuguna et al. (2006) in the context of generalized plasticity. Eq. 25 because of Eq. 26 becomes

$$\dot{\boldsymbol{\varepsilon}}^{vp} = \left(\frac{\langle f \rangle}{\eta} \right)^m \frac{1}{\left(x + \kappa^l \right)} \boldsymbol{\nu}. \tag{27}$$

Because an associative flow rule predicts excessive plastic dilatancy, a non-associative rule will be adopted here, i.e. $\boldsymbol{\nu}$ will be normal to a viscoplastic potential surface Ω and not to the loading surface f. The viscoplastic potential chosen is of Drucker-Prager form and it is given by

$$\Omega = \sqrt{J_2^c} + \gamma I_1^c, \tag{28}$$

where J_2^c is the modified, because of damage, second invariant of the deviatoric stress tensor $\boldsymbol{s}$ given by $J_2^c = J_2/(1-\omega)^2$, where J_2 is the second invariant of the stress deviator and γ is a material parameter. The normal to the viscoplastic potential is therefore given by

$$\boldsymbol{\nu} = \frac{\partial \Omega}{\partial \boldsymbol{\sigma}} = \frac{\boldsymbol{s}}{2\sqrt{J_2^c}} + \frac{\gamma}{1-\omega} \boldsymbol{I}, \tag{29}$$

where $\boldsymbol{I}$ is the unit tensor.

Hardening Rule (Evolution Equation for Hardening Variable)

The evolution equation of the hardening variable, which we propose here, is given by

$$\dot{\kappa} = \left(\frac{\langle f \rangle}{\eta} \right)^m \frac{1}{\left(x + \kappa^l \right)}. \tag{30}$$

For the complete hyperelastic-viscoplastic-damage model in series, the above equations are supplemented by the additive decomposition of the strain tensor into elastic and viscoplastic components and the hyperelastic stress-strain relations, i.e.

$$\boldsymbol{\varepsilon} = \boldsymbol{\varepsilon}^{el} + \boldsymbol{\varepsilon}^{vp} \tag{31}$$

$$\boldsymbol{\sigma} = \frac{\partial W(\boldsymbol{\varepsilon}^{el})}{\partial \boldsymbol{\varepsilon}^{el}}, \tag{32}$$

where $\boldsymbol{\varepsilon}^{el}$ is the elastic component of the total strain.

MODEL SIMULATIONS AND PREDICTIONS

The hyperelastic model and the complete hyperelastic-viscoplastic-damage model are implemented within the finite element program ABAQUS. The implementation is done through user subroutine modules UHYPER and UMAT respectively. For the implementation of the model see Panneerselvam and Panoskaltsis (2005). First, the three experiments, whose simulation we showed in a previous section describing the hyperelastic model, are analyzed again. In the previous analysis the experiments were considered as homogeneous and the results were interpreted as providing stress and strain at a point of the specimen, i.e. the stresses and strains are assumed to be uniform within the specimen; we can call them local fitting results. Now the experiments are analyzed as boundary-value problems so that the reality is better represented. For the finite element model we used 1560 fully integrated 8-noded linear brick elements. With parameter values *already determined* (Table 1) the obtained results are shown in Figs. 6, 7 and 8. The agreement is remarkable. (In all figures the legends 'model' refer to local fitting results also shown in a previous section.) Figures 6, 7 and 8 represent the finite element analysis *predictions*.

Next, the repeated simple shear test at constant height is also modeled as a boundary-value problem and the results obtained from finite element analysis are compared to experimental results. The experiments are from Sousa et al. (1993). The same number and type of elements as before are used. In this case, the complete hyperelastic-viscoplastic-damage model is employed. First, the model is fitted to experimental results with amplitude of shear stress equal to 8 psi. For the parameters of the hyperelastic model b_1 to b_5 the values already obtained in Table 1 are used, since the material used in the RSST-CH experiments is the same as the material used in the experiments described in a previous section. The parameters of the viscoplastic-damage model are obtained by a nonlinear optimization procedure similar to the one described in a previous section. The values of the parameters are given below:

$b_1 = 4e4,\ b_2 = 4.175e7,\ b_3 = -5.53e8,\ b_4 = 5e5,\ b_5 = -5.85e8$

$\alpha = 12,\ \eta = 2.82e6,\ H = 5,\ m = 1,\ x = 1.3e-3,\ l = 2.1,\ \gamma = -2.3,\ a_1 = 3.7,\ a_2 = 2$

With these values of the parameters the model's prediction for the RSST-CH experiment with amplitude of shear stress equal to 10 psi is found. The results are shown in Fig. 9, where the evolution of permanent shear strain with number of cycles is depicted in log-log scale. As shown in the figure the model's prediction is very good. It is important that the constitutive model match experimental results at different stress levels with the same parameter set, because in a boundary-value problem such as the pavement structure, different points of the pavement are under different stress states.

It should be mentioned here that the RSST-CH experiment has been criticized as not representing true simple shear results. With our approach (i.e. to treat the experiment as a boundary-value problem) we completely bypass this controversy and we show the validity of this test as a tool to determine asphalt's behavior.

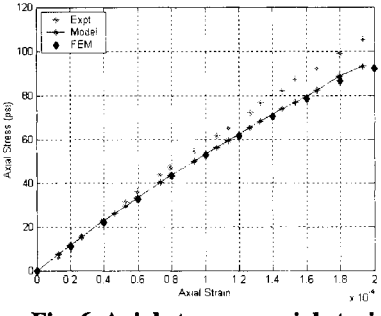

Fig. 6. Axial stress vs. axial strain. Comparison of finite element results to experimental data.

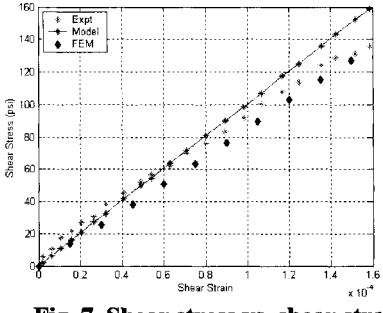

Fig. 7. Shear stress vs. shear strain. Comparison of finite element results to experimental data.

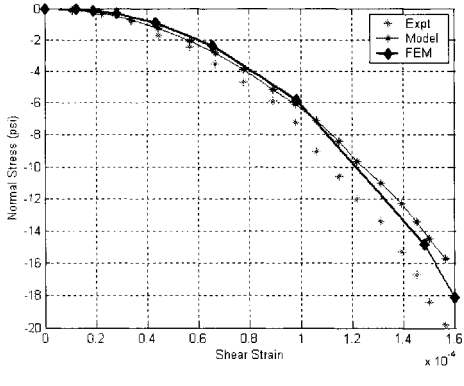

Fig. 8. Evolution of normal stress with shear strain. Comparison of finite element results to experimental data.

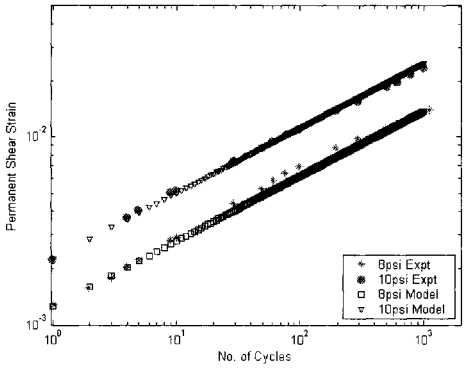

Fig. 9. Evolution of permanent shear strain with number of cycles.

CONCLUSIONS

In this paper a new nonlinear hyperelastic-viscoplastic-damage constitutive model in series for asphalt concrete is developed. The model is developed in multi dimensions. The second order hyperelastic model is analyzed with respect to stability requirements and it is shown that the model is stable for the range of strains studied. The hyperelastic model is used to analyze the uniaxial strain compression test, the volumetric compression test and the simple shear test, considered as homogeneous. The model's comparisons to experimental results are very favorable. The model is also able to predict the evolution of the normal stress during the simple shear test. Next, the same experiments are modeled as boundary-value problems and they are analyzed by the finite element method. In this case, the model's predictions, with the same set of parameters obtained from the tests considered as homogeneous, are remarkably good.

The complete model is used for the analysis of the RSST-CH experiment, which is modeled as a boundary-value problem. The model parameters are obtained from the test for a given stress amplitude and the model's prediction for the test for a different stress amplitude is very good. With our approach we completely bypass the controversy regarding the validity of the RSST-CH.

REFERENCES

Bahuguna, S., Panoskaltsis, V. P., and Papoulia, K. D. (2006). "Identification and modeling of permanent deformations of asphalt concrete." *Journal of Engineering Mechanics, ASCE,* 132, (3): 231-239.

Eisenmann, J., and Hilmer, A. (1987). "Influence of wheel load and inflation pressure on the rutting effect at asphalt pavements – Experiments and theoretical investigations." *Proceedings of the Sixth International Conference on Structural Design of Asphalt Pavements*: 392-403.

Panneerselvam, D. (2005). "Mechanics of asphalt concrete: Analytical and computational aspects", Ph.D. Dissertation, Department of Civil Engineering, Case Western Reserve University, Cleveland, Ohio.

Panneerselvam, D. and Panoskaltsis, V. P. (2005). "Numerical implementation of a hyperelastic-viscoplastic damage model for asphalt concrete materials and pavements." *ASCE Geotechnical Special Publication,* No. 146, ASCE, Reston/VA: 61-72.

Panoskaltsis, V. P., Bahuguna, S., and Soldatos, D. (1998). "On the description of mechanisms with different characteristic times in solid materials: A non-conventional approach." *Mechanics Research Communications,* 25, (2): 155-164.

Perzyna, P. (1963). "The constitutive equations for rate sensitive plastic materials." *Quarterly of Applied Mathematics*, 20: 321-332.

Sousa, J.B., Weissman, S.L., Sackman, J.L., and Monismith, C.L. (1993). "A nonlinear elastic viscous with damage model to predict permanent deformation of asphalt concrete mixes." *Transportation Research Record,* 1384: 80- 93.

Vermeer, P.A. (1982). "A five constant model unifying well established concepts." *International Workshop on Constitutive Relations for Soils,* Grenoble, France: 175 – 197.

Witczak, M.W., Kaloush, K., Pellinen, T., El-Basyouny, M., and Von Quintus, H. (2002). "Simple performance test for superpave mix design." *NCHRP Report* No. 465, Transportation Research Board, National Research Council, Washington, D.C.

Simulating the Deformation Behavior of Hot Mix Asphalt in the Indirect Tension Test

Ala R. Abbas[1], A.M. ASCE

[1]Assitant Professor, Department of Civil Engineering, University of Akron, Akron, OH 44325-3905; abbas@uakron.edu

ABSTRACT: The deformation behavior of hot mix asphalt (HMA) in the indirect tension test (IDT) is simulated using the discrete element method (DEM). The internal structure of the HMA is described using two sets of discrete particles representing the aggregates and the binder. The constitutive behavior of these materials is defined using linear elastic properties along with a damage model to capture debonding. Different adhesion and cohesion strength ratios are included in the analysis along with varying binder film thicknesses. The analysis revealed that cracking has the tendency to occur at the interface between the aggregate and the binder due to the high concentration of stresses in that region. Furthermore, it is noticed that models containing thin films of binder are more sensitive to the adhesive bond strength than those containing thick films of binder. The latter suggests that adhesive failure is more critical in thin film specimens, whereas cohesive failure is more critical in thick film specimens.

INTRODUCTION

Low temperature cracking in asphalt pavements is a non-load associated phenomenon that is attributed to the shrinkage in the hot mix asphalt (HMA) layer upon reduction in ambient temperature (Roberts et al. 1996). As the temperature drops, tensile stresses develop within the HMA layer. Once these stresses exceed the tensile strength of the HMA, failure takes place. This could be the result of one extreme temperature cycle or a series of smaller repetitive cycles.

The propensity of HMA to low temperature cracking is commonly characterized using the indirect tension test (IDT) by determining its tensile strength at temperatures below 0°C as documented in AASHTO T 322-03. In this test, a cylindrical specimen measuring 150 mm (6 inches) in diameter and about 50 mm (2 inches) in height is loaded along its diametral axis using a constant rate of deformation of 12.5 mm/min. The vertical load is measured using a load cell and the horizontal and axial deformations are measured using two linear variable differential transformers (LVDTs) attached to the middle of the specimen, with an initial gauge length of 38 mm. The tensile strength, S_t, is taken as the maximum tensile stress; and

is related to the vertical load at failure, P_f, according to the following relationship:

$$S_t = \frac{2P_f}{\pi t D} \quad (1)$$

where t is the specimen thickness and D is the specimen diameter. Due to the brittle nature of HMA at such low temperatures, failure occurs within a very short period of time (fraction of a second), and hence no distinction can be made between failure and specimen breakage.

This paper describes a novel approach for modeling the fracture mechanism in the IDT test using the discrete element method (DEM). It follows by describing the HMA internal structure using a set of discrete particles interacting through contact points that incorporate the inter-particle material behavior, and analyzing the material response upon loading. A commercial DEM code called Particle Flow Code in 2-Dimensions (PFC2D) is used in the analysis. Two models consisting of the same volumetric concentration of aggregates, but varying binder film thicknesses, are artificially generated. Both aggregate and binder particles are defined using linear elastic particles connected with contact bonds of varying strengths. Three types of bonds are included in these simulations in order to account for the cohesion within the asphalt binder, the cohesion within each aggregate particle, and the adhesion between the aggregate and the binder. Conclusions are driven based on the effect of the asphalt binder film thickness and the relative magnitudes of adhesion and cohesion strengths specified.

DISCRETE ELEMENT MODELING OF HMA

The approach towards modeling the HMA micromechanical behavior using the DEM is based on defining three aspects, namely model geometry, material properties, and boundary/loading conditions. Each aspect is covered separately in the following subsections.

Model Geometry

The effect of the asphalt binder film thickness was investigated through the generation of two models containing consisting of the same amount of aggregates, but varying aggregate sizes (Figure 1). It can be seen that the use of large aggregates resulted in thick films of binder, and that smaller aggregates resulted in thin films of binder. Each model consisted of a total of 36,267 discrete cylindrical particles, out of which about 21,000 are aggregate particles and the remaining are binder particles. Each particle has a diameter of 0.5 mm and a thickness of 50 mm. The discrete particles within these models are arranged using a hexagonal packing, whereby each particle is in contact with six neighboring particles in advance to loading.

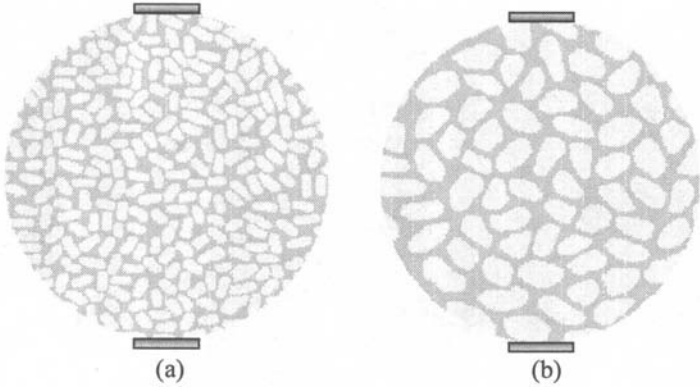

FIG. 1. Discrete Element IDT Models Containing (a) Thin Films of Binder (b) Thick Films of Binder.

Material Properties

The stiffness of the asphalt binder significantly increases at low temperatures and exhibits signs of less time-dependency, as can be measured in a creep test such as the bending beam rheometer (BBR), whereby smaller strain accumulation is noticed as compared to that at high temperatures. Therefore, it was decided to model the interaction among the mix constituents using the linear elastic model. An elastic modulus of 35 GPa was assumed for the aggregate and an elastic modulus of 3 GPa was assumed for the asphalt mastic. The later is a value that was experimentally established for most asphalt binders at extremely low temperatures (Christensen and Anderson 1992).

The Interaction among the particles was modeled using the linear contact model. This model is defined using two parameters, namely the normal and shear stiffness parameter. For each contact, an effective normal and shear contact stiffness is calculated from the particles' stiffnesses assuming that they act in series,

$$K^n = \frac{K_n^{[1]} K_n^{[2]}}{K_n^{[1]} + K_n^{[2]}} \tag{2}$$

$$K^s = \frac{K_s^{[1]} K_s^{[2]}}{K_s^{[1]} + K_s^{[2]}} \tag{3}$$

where,

K^n and K^s = effective normal and shear contact stiffnesses, respectively,

$K_n^{[1]}$ and $K_n^{[2]}$ = normal stiffnesses of particles 1 and 2, respectively, and

$K_s^{[1]}$ and $K_s^{[2]}$ = shear stiffnesses of particles 1 and 2, respectively.

Bonding between the mix constituents was accounted for through the use of the contact bond model. Two strength parameters along the normal and the tangential

directions define this model, whereby the bond in either direction breaks once its strength value is exceeded. In this work, the bond strength was assumed to be equal in both directions.

Upon cracking, three failure mechanisms are identified within the asphalt mixture, namely cohesive failure within the binder phase, cohesive failure within the aggregate particle, and adhesive failure at the interface between the binder and the aggregate. Due to the difference in stiffness between the aggregate and the binder, high stress concentrations are expected at the interface. However, due to the physiochemical interaction between the binder and the aggregate, the adhesive bond strength is expected to be higher than that of the cohesive bonds within the binder, and thus depending on the amount of interaction and the binder film thickness, failure might take either form. For modeling purposes, a strength value of 2.8 MPa that is quite common for the asphalt binder was used in the simulation to describe the cohesive failure within that phase. Adhesive failure, on the other hand, was defined using two strength values of 2.8 MPa and 8.4 MPa in order to simulate weak and strong systems, respectively. A rather high strength value of 24 MPa was used for the fracture within the aggregate particles. Lytton (2004) shows that the adhesive and cohesive tensile strengths are related to film thickness as well as the cohesive and adhesive bond energies, which are functions of material surface energies. The ratio of adhesive to cohesive tensile strength used here is motivated by the bond energy ratios reported by Lytton (2004) and Cheng et al. (2003).

Boundary and Loading Conditions

The upper and lower loading platens in the IDT were represented using two boundary walls, each of which is 19 mm wide. The boundary walls were generated so that they barely touch the top and the bottom sets of particles as can be seen in Figure 1. Due to the dynamic nature of the analysis method utilized, the deformation rate was gradually increased from zero at the beginning of the simulation to 50 mm per second using an analysis time step of 10^{-7} seconds. Higher deformation rate was applied in the simulation than what is used in the actual test in order to reduce the computation time. The simulation lasted for about 8 hours using 200,000 time steps. The deformation rate was selected small enough to ensure that the model remains in quasi-static equilibrium. The adequacy of the deformation rate was verified by stopping the analysis within the linear region (i.e., before cracking), and monitoring the load level at the platens. A constant load was attained, which indicates that the deformation rate was low enough not to produce large acceleration and thus, high inertia forces that might result in premature damage to the specimen.

SIMULATION RESULTS

The stress-strain behavior for the two cases of weak and strong adhesive bonding is presented in Figure 2. The vertical load was calculated as the average reaction forces on the upper and lower loading platens and the vertical displacement was taken as the change in the model height along the loading axis. It can be seen in this figure that the model containing thin films of binder is more sensitive to the adhesive bond strength

than that containing the thick films of binder. This implies that fracture is mainly dominated by the adhesive failure in the case of the thin films, while it is controlled by the cohesive failure in the case of the thick films. As expected, a sharp drop in load level is noticed after failure in the case of the thin film model, which is an indication of a brittle material, while the load level gradually decreased after failure in the case of the thick film model, which is an indication of a ductile material.

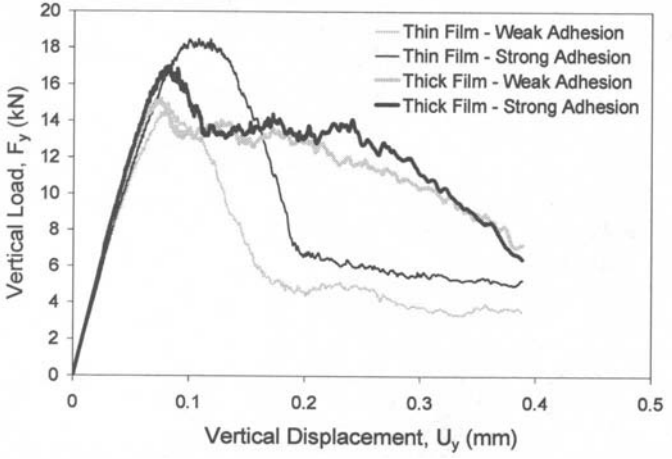

FIG. 2. Resulting Response of Two Models Containing Thin and Thick Films of Asphalt Binder Using Strong and Weak Adhesion Bonds.

The fracture patterns are presented in Figures 3 and 4 for thin and thick films of binder, respectively. It can be noticed that cracking was concentrated within the middle portion of the specimen along the loading direction. It can also be observed that the cracks are not exactly perpendicular to the loading direction but inclined with an angle of about 60°. The reason for this is that the particles within these models are arranged using a hexagonal, in which each particle is surrounded by six neighboring particles at 60° increments. It can be also seen that cracking has the tendency to occur at the interface between the aggregate and the binder (i.e., adhesive failure) due to the high stress concentration. The increase in the adhesive bond strength with regard to the cohesive bond strength resulted in cracks within the weaker region, and this fracture was dominated by the cohesive failure mode. Therefore, it is concluded that if the asphalt binder is present in the asphalt mixture in the form of thin films, the fracture behavior of asphalt mixture is dictated by the adhesion between the asphalt binder and the aggregate particles, and if it is present in the form of thick films, fracture might be dominated by failure within the binder phase should the adhesion between the aggregate and the binder be higher than the attractions between the binder particles themselves. This behavior is consistent with what was found by Lytton (2004), who compared analytical solutions of the tensile strength of asphalt cement as a function of the binder film thickness to experimental data obtained by Marek and Herrin (1968).

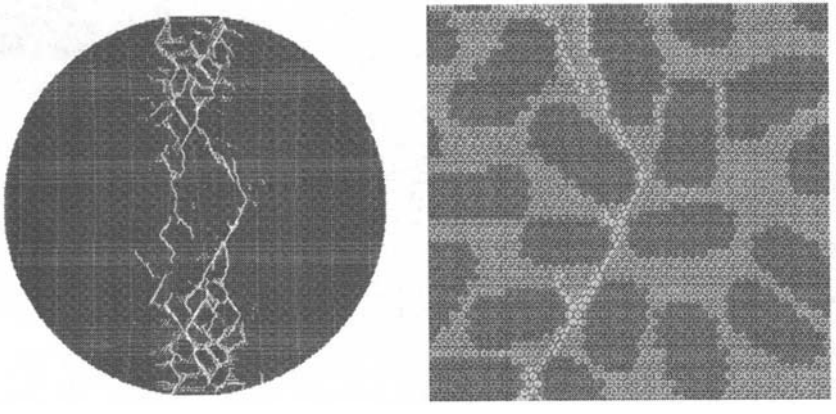

(a) Thin Films – Weak Adhesive Bonds

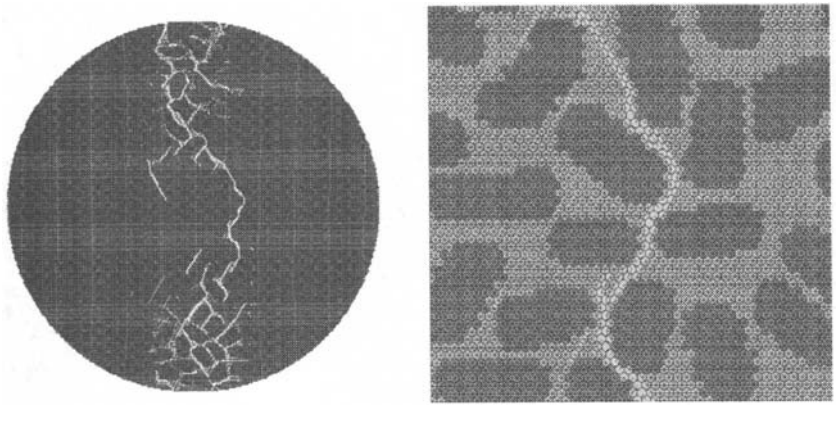

(b) Thin Films – Strong Adhesive Bonds

FIG. 3. Fracture Patterns within the Thin Film Models Presented in Figure 1 Using (a) Weak and (b) Strong Adhesive Bond Strengths.

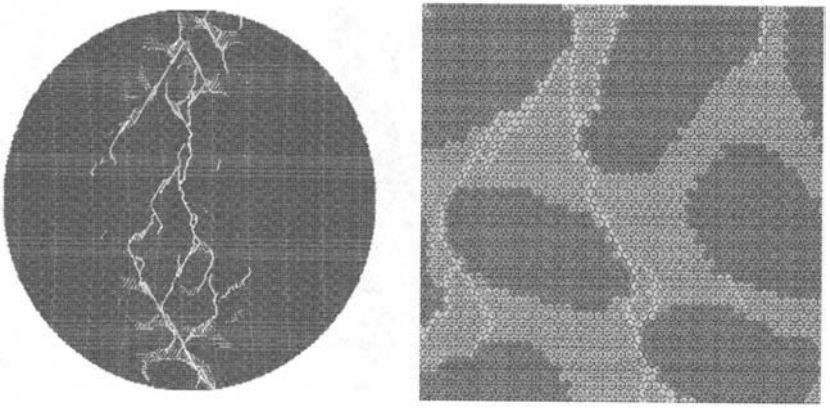

(a) Thick Films – Weak Adhesive Bonds

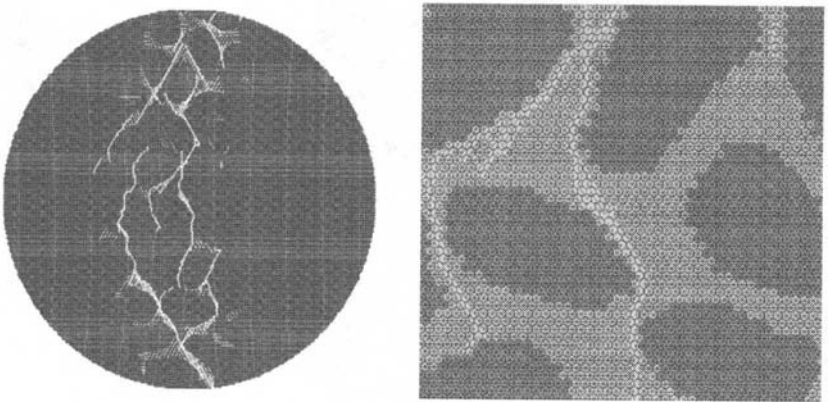

(b) Thick Films – Strong Adhesive Bonds

FIG. 4. Fracture Patterns within the Thick Film Models Presented in Figure 1 Using (a) Weak and (b) Strong Adhesive Bond Strengths.

SUMMARY AND CONCLUSIONS

The HMA deformation behavior in the IDT test was simulated using the discrete element method. Two models were generated using large and small aggregates. The same amount of aggregates was used in both models. The use of large aggregate particles resulted in thick films of asphalt binder and the use of small aggregate particles resulted in thin films of asphalt binder. Three types of bonds were included in the simulations in order to account for the cohesion within the asphalt binder, the cohesion within each aggregate particle, and the adhesion between the aggregate and the binder. Low and high strength values were used to describe the cohesion within the asphalt binder and the aggregate, respectively. Meanwhile, two systems of weak and strong adhesive bonds were included. It was noticed that the model containing thin films of binder was more sensitive to the adhesive bond strength than that containing thick films of binder. Furthermore, it was observed that cracking has the tendency to occur at the interface between the aggregate and the binder due to the high concentration of stresses. Therefore, it was concluded that if the asphalt binder is present in the asphalt mixture in the form of thin films, the fracture behavior of asphalt mixture is dictated by the adhesion between the asphalt binder and the aggregate particles, and if it is present in the form of thick films, fracture is dominated by failure within the binder phase.

REFERENCES

Christensen, D.W. and Anderson, D.A. (1992). Interpretation of Dynamic Mechanical Test Data for Paving Grade Asphalt Cements. Journal of the Association of Asphalt Paving Technologists, Vol. 61: 67-116.

Cheng, D.X., Little, D.N., Lytton, R.L., and Holste, J.C. (2003). Microstructure Damage Evaluation of Asphalt Mixtures by Considering Both Moisture Diffusion and Repeated Load Conditions. Transportation Research Record 1832, TRB, National Research Council, Washington, D. C.: 42-49.

Lytton, R.L (2004). Adhesive Fracture in Asphalt Concrete Mixtures. Course Notes.

Marek, C.R. and Herrin, M. (1968). Tensile Behavior and Failure Characteristics of Asphalt Cements in Thin Films. Journal of the Association of Asphalt Paving Technologists, AAPT, Vol. 37: 386-421.

PFC2D (2003). Particle Flow Code in 2-Dimensions. Version 3-163. Itasca Consulting Group.

Roberts, F.L., Kandhal, P.S., Brown, E.R., Lee, D.Y., and Kennedy, T.W. (1996). Hot Mix Asphalt Materials, Mixture Design and Construction. National Asphalt Paving Association Education Foundation, Lanham, MD, 2nd Edition.

A Three-Dimensional Micro-Frame Element Network Model for Damage Behavior of Asphalt Mixtures

Qingli Dai[1] and Zhanping You[2]

[1]Research Assistant Professor, Dept. of Mechanical Engineering-Engineering Mechanics and Dept. of Civil and Environmental Engineering, Michigan Technological University, Houghton, MI 49931, qingdai@mtu.edu.

[2]Donald and Ruth Ann Tomasini Assistant Professor, Dept. of Civil and Environmental Engineering, Michigan Technological University, Houghton, MI 49931, zyou@mtu.edu.

ABSTRACT: This paper presents a numerical study of damage behavior of asphalt mixtures by using a three-dimensional (3D) micro-frame element network (MFEN) model and damage mechanics principles. Asphalt mixtures are composed of aggregates, mastic cement and air voids. The load carrying behavior is strongly related to the local microstructural load transfer between neighboring aggregate particles. The 3D finite element scheme used a network of special frame elements. Each element stiffness matrix was developed based on an approximate elasticity solution of the stress-strain field in a cementation layer between neighboring particle pairs. Numerical simulation of this micro-mechanical behavior was accomplished by using *ABAQUS UEL* subroutine that incorporated the mechanical load-carrying response between aggregates. Continuum damage mechanics was then incorporated within each mastic micro-frame element, leading to the construction of a micro-damage model capable of predicting typical global inelastic behavior found in asphalt materials. The Damage behavior simulation was conducted by using the Riks method (Crisfield 1980; 1986). Model simulation results indicate that the MFEN model is capable of predicting the damage behavior under the mechanical loading.

INTRODUCTION

Asphalt mixtures are complex heterogeneous materials composed of graded aggregates, asphalt binder, additives and void space. Recycling of the materials obtained from the milling of asphalt pavement, known as RAP (Reclaimed Asphalt Pavement), involves mixing RAP with asphalt cement/emulsion and aggregates in definite proportions to produce a new asphalt concrete mix or cold-in place recycled mixture. Due to limited resources, most of the asphalt mixtures are recycled and used in new pavement construction. A fundamental knowledge of the material behavior is needed to understand and explain recycling issues, and a micromechanical model would be an excellent tool to establish such basic mechanisms.

Asphalt concrete pavements must withstand a wide variety of loading and temperature conditions. For example, traffic loadings can vary from quasi-static to dynamic impact, and pavement breakdown commonly occurs as a result of fracture and/or fatigue failure, time-dependent permanent deformation (creep-rutting) and low temperature (thermal) cracking. Studies on the failure and fracture behaviors of asphalt materials include the work of (Dai 2004; Dai and Sadd 2004; Dai et al. 2005; Dai et al. 2006; Luther et al. 1976; Roque et al. 2004; Song et al. 2006a; b; Sousa et al. 1998; Wen and Kim 2002; You 2003; You and Buttlar 2004).

Many researches have been conducted on the micromechanical behaviors of particulate, porous and heterogeneous materials. For example, studies on cemented particulate materials by (Dvorkin et al. 1994; Zhu et al. 1996a) presented the load transfer between particles which are cemented through an elastic binder, and studies on inter-particle behavior for two elastic particles bonded through a viscoelastic binder can be found in the work by (Chang and Meegoda 1997; Zhu et al. 1996b; Zhu et al. 2001). Such elastic and viscoelastic analyses provide the details in normal and tangential inter-particle load transfer, and would be the fundamental mechanics in developing a micromechanical theory for load distribution and failure of such materials.

The damage behavior of asphalt materials is extremely complex due to its microstructure. The interior binder is composed of microcracks, microvoids and defects that result in strength loss. As the load is increased, local cracks would start to form near the existing-cracks and thus would lead to the interior failure and interfacial debonding. Continuum damage mechanics is based on the thermodynamics of irreversible processes to characterize elastic damage behaviors, (Chaboche 1988). A scalar damage variable is suitable for characterizing isotropic damage behavior, whereas a tensor-valued variable is necessary in order to account for anisotropic damage effects, (Simo and Ju 1987).

Damage mechanics was applied to study asphalt mixtures in the past several decades (Park et al. 1999; Park et al. 1996; Park and Schapery 1997; Schapery 1989; 1990a; b; 1999). This study incorporated the damage mechanics principles into the finite element approaches. The scope of this work is as follows:

- To develop a micro-frame element network model for simulating the micromechanical behavior of asphalt mixture
- To present a bilinear damage model based on fracture release energy for crack propagation
- To show the microstructure effects on damage behavior of asphalt mixtures.

In our previous work, the 2D equivalent MFEN approaches were applied to asphalt mixtures, where the local interaction between neighboring particles was modeled with a special frame-type finite element (Dai and Sadd 2004; Dai et al. 2005; Sadd et al. 2004a; Sadd et al. 2004b). The stiffness matrix of these elements was developed to predict the load transfer between cemented particles through an effective cement zone. MFEN model incorporated damage mechanics principles to simulate the two-dimensional damage behavior. Following these approaches, the 3D MFEN model was developed for 3D behavior simulation of asphalt mixture. The continuum damage mechanics principles were also incorporated into 3D MFEN model to simulate the microstructure-based damage behavior.

3D MICRO-FRAME FINITE ELEMENT MODEL

Bituminous asphalt concrete can be described as a multi-phase material containing aggregates, mastic cement (including asphalt binder and fine aggregates) and air voids. The load transfer between the aggregates plays a primary role in determining the load carrying capacity and failure of such complex materials. The aggregate material is normally much stiffer than the mastic, and thus aggregates are taken as rigid particles. On the other hand, the mastic cement is a compliant material with inelastic, softening and time-dependent behaviors. In order to properly account for the load transfer between aggregates, it is assumed that there is an effective mastic zone between neighboring particles. The micro-mechanical load transfer occurs through the effective mastic zone. The 3D load transfer between each aggregate pair includes resultant normal and tangential forces and moments.

For the 3D model, the aggregates were modeled as idealized ellipsoids with different sizes and shape ratios. The effective mastic zones were simplified as cylinders with different average thickness $\overline{h}$ and width w as shown in Fig. 1.

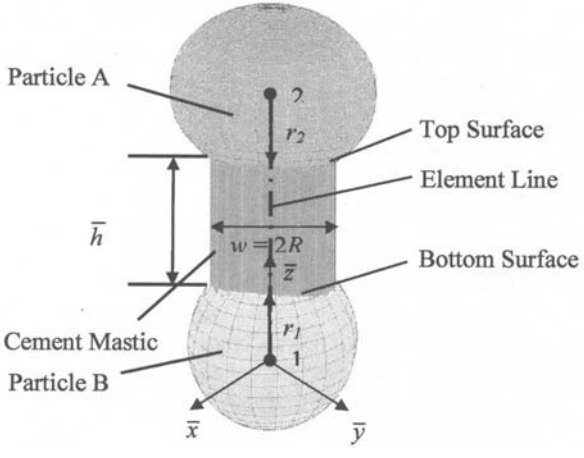

FIG.1. Two cemented particles in a local coordinate system.

These two-node micro-frame elements have the usual six degree-of-freedom, three displacements and three rotations at each node, and thus require a 12x12 stiffness matrix to relate nodal (aggregate) motions to the applied forces and moments. The element displacement-rotation and force-moment vectors (U and F) have 12 components.

$$\begin{aligned} U &= \{U_{x1}\ U_{y1}\ U_{z1}\ \theta_{x1}\ \theta_{y1}\ \theta_{z1}\ U_{x2}\ U_{y2}\ U_{z2}\ \theta_{x2}\ \theta_{y2}\ \theta_{z2}\} \\ F &= \{F_{x1}\ F_{y1}\ F_{z1}\ M_{x1}\ M_{y1}\ M_{z1}\ F_{x2}\ F_{y2}\ F_{z2}\ M_{x2}\ M_{y2}\ M_{z2}\} \end{aligned} \tag{1}$$

where $U_{..}$ and $\theta_{..}$ are the nodal displacements and rotations, and $F_{..}$ and $M_{..}$ are the nodal forces and moments. The finite element model then uses an *equivalent lattice network approach*, whereby the inter-particle load transfer is simulated by a network

of specially created frame-type finite elements connected at particle centers. The current network model uses a specially developed, three-dimensional frame-type element to simulate the inter-particle load transfer. This element elastic equation can be written with the displacement-rotation and force-moment vectors in the local coordinate system.

$$F_{ij} = K_{ijkl} U_{kl} \tag{2}$$

The stresses σ_x, σ_z and τ_{xz} within the cementation layer can be calculated for the cases of unit normal, tangential and rotational particle motions. Due to the limited pages, the details of these stress formulation cannot be presented in this paper and will be found in a prepared publication by authors. These stresses can then be integrated to determine the various stiffness terms needed in the element equation. The final 3D micro-frame element matrix is given by

$$[K] = \begin{bmatrix}
K_n & 0 & 0 & 0 & -K_n r_1 & 0 & -K_n & 0 & 0 & 0 & -K_n r_2 & 0 \\
\cdot & K_t & 0 & K_t r_1 & 0 & 0 & 0 & -K_t & 0 & K_t r_2 & 0 & 0 \\
\cdot & \cdot & K_m & 0 & 0 & 0 & 0 & 0 & -K_m & 0 & 0 & 0 \\
\cdot & \cdot & \cdot & K_t r_1^2 + K_m & 0 & 0 & 0 & -K_t r_1 & 0 & K_t r_1 r_2 - K_m & 0 & 0 \\
\cdot & \cdot & \cdot & \cdot & K_n r_1^2 + K_m & 0 & K_n r_1 & 0 & 0 & 0 & K_n r_1 r_2 - K_m & 0 \\
\cdot & \cdot & \cdot & \cdot & \cdot & K_r & 0 & 0 & 0 & 0 & 0 & -K_r \\
\cdot & \cdot & \cdot & \cdot & \cdot & \cdot & K_n & 0 & 0 & 0 & K_n r_2 & 0 \\
\cdot & \cdot & \cdot & \cdot & \cdot & \cdot & \cdot & K_t & 0 & -K_t r_2 & 0 & 0 \\
\cdot & \cdot & \cdot & \cdot & \cdot & \cdot & \cdot & \cdot & K_m & 0 & 0 & 0 \\
\cdot & \cdot & \cdot & \cdot & \cdot & \cdot & \cdot & \cdot & \cdot & K_t r_2^2 + K_m & 0 & 0 \\
\cdot & \cdot & \cdot & \cdot & \cdot & \cdot & \cdot & \cdot & \cdot & \cdot & K_n r_2^2 + K_m & 0 \\
\cdot & \cdot & \cdot & \cdot & \cdot & \cdot & \cdot & \cdot & \cdot & \cdot & \cdot & K_r
\end{bmatrix} \tag{3}$$

where normal force stiffness $K_{nn} = \frac{(\lambda+2\mu)}{h}\pi R^2$ and tangential force stiffness $K_{tt} = \frac{\mu}{h}\pi R^2$ are generated from the unit normal and tangential displacement loading behavior, normal moment stiffness $K_m = \frac{(\lambda+2\mu)}{4h}\pi R^4 = \frac{1}{4}K_{nn}R^2$ and tangential moment stiffness $K_{rt} = K_{tt} r_i r_j$ are obtained from the unit bending rotation loading, torsion stiffness $K_{rr} = \frac{\mu}{2h}\pi R^4 = \frac{1}{2}K_{tt}R^2$ is from the unit torsion rotation loading, λ and μ are the usual elastic moduli, the others are mastic and aggregate geometry sizes as mentioned before. This elastic stiffness matrix only depends on the normal and tangential force stiffness K_{nn} and K_{tt}, and the element and particle geometry sizes. And the element stiffness matrix varies with different particle pair. With this procedure, the generated elastic stiffness matrix is a function of mastic material variables and mixture microstructure.

BILINEAR DAMAGE MODEL

Bilinear cohesive zone model was adopted and tailored to simulate the mixed-mode crack propagation in asphalt concrete by (Song et al. 2005; 2006a; b). Bilinear cohesive zone model has the improved feature to reduce the artificial compliance by providing an adjustable initial slope in the cohesive law.

To simulate the damage behavior within the asphalt mixture, a bilinear damage model based on the fracture release energy was developed to combine with the micro-frame element network. This theory was originally developed for concrete materials whereby the internal micro-cracks within the matrix cement and around the aggregates are modeled as a continuous defect field. Inelastic behavior is thus developed by the growth of damage within the material with increasing loading.

For the multi-axial micro-frame element, the normal and tangential damage behavior was defined with the separated uniaxial tension/compression and shear behavior. Fig. 2 shows the stress-strain relations of compression, tension and shear damage behavior for a micro-frame element between two rigid aggregates. The pre-peak region represents the elastic part of the bilinear damage model, while the post failure portion after the peak load accounts for the damage occurring in the fracture processes. The elastic normal and tangential force stiffness K_{nn} and K_{tt} defined in Eq. 3 was still used for elastic region in the bilinear damage model, to account for the initial material stiffness. The stresses σ_{nt}, σ_{nc} and σ_{tt} indicate the average critical strength for tension, compression and shear behavior, and $\varepsilon_{nt}, \varepsilon_{nc}$ and ε_{tt} represent the corresponding softening strains. From the fracture release energy G_{nt}, G_{nc} and G_{tt} of individual behavior, the post-failure tension, compression and shear stiffness: $\left(K_{nn}^{t}\right)_D$, $\left(K_{nn}^{c}\right)_D$ and $\left(K_{tt}\right)_D$ are determined to simulate the multi-axial damage behavior.

This damage behavior could lead to a separation or debonding between aggregate pairs. In order to simulate such total failure, elements were given a mastic failure criterion for tension, compression or shear based on the average failure strength

$$\begin{aligned} \sigma_{nt}^{f} &= c_f \sigma_{nt} \\ \sigma_{nc}^{f} &= c_f \sigma_{nc} \\ \sigma_{tt}^{f} &= c_f \sigma_{tt} \end{aligned} \tag{4}$$

where c_f is a failure factor related to the average failure strength in each behavior. For this case, the failed elements still remain in the computation model, but their stiffness are very small and they carry very little load.

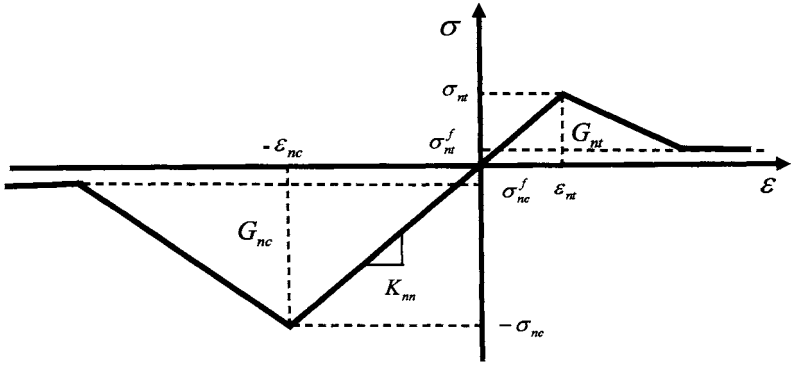

(a)

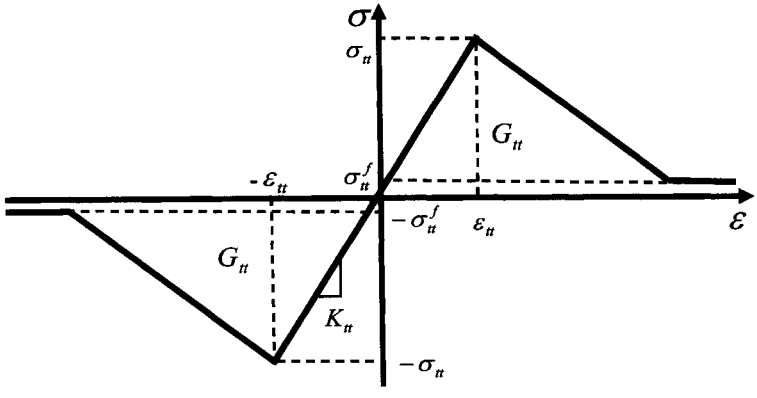

(b)

FIG. 2. Stress-strain relationships for compression, tension and shear damage behavior for a micro-frame element between two rigid aggregates, a) separate normal behavior, b) separate tangential behavior. (Note that normal compression/tension behavior is coupled with tangential shear behavior).

The incorporation of bilinear damage and MFEN models were defined in a nonlinear user defined element (UEL) subroutine of the ABAQUS finite element code (ABAQUS 2004). UEL subroutine determines the compression and tension force in each element and performs the required damage calculations in the normal and tangential directions based on the prescribed softening and failure criteria. Displacement controlled boundary conditions were employed, and the Modified Riks method (Crisfield 1980) was used in order to provide a more stable solution scheme. Also, because aggregate (nodal) displacements became sizeable, the mesh geometry was updated during each load increment.

DAMAGE SIMULATION ON NUMERICAL SAMPLES OF ASPHALT MIXTURE

After developing damage-coupled micro-frame element network model, the preliminary simulation was conducted on numerical samples of asphalt mixture. Numerical samples were generated with computer program MATLAB. Fig. 3 shows the damage simulation results including the damage distribution and behavior of numerical samples A and B.

Sample A has very uniform particle structure with slightly different ellipsoidal particle sizes: (5.2, 4.5, 5.0), (5.5, 5.0, 5.2), (5.5, 5.5, 5.0), (5.5, 5.5, 5.5). 260 particles were distributed in the four layers with different orientation. The particle percentage is about 60.8%, calculated with the volume ratio of the total aggregate and cylinder sample. This mixture sample has about 1849 mastic elements to connect the neighboring particles in the sample. The geometry of the sample includes the diameter D = 107 mm and thickness h= 48 mm.

Sample B was generated from 352 ellipsoidal particles with a graded particle size and distribution percentage: (2, 2, 2) – 20.4%, (3.5, 3.5, 3.5) – 37.5%, (5.5, 5.5, 5.5) – 30.7%, and (7, 7, 7) – 11.4%. To simulate the laboratory specimen, the large size particles distribute in the outer domain and small particles lie in the inner region. The microstructure of the sample B varies along the thickness. The particle percentage is calculated about 57.3%. This mixture sample has about 2260 generated mastic elements. The geometry sizes of this sample are the diameter D = 102 mm and thickness h= 48 mm.

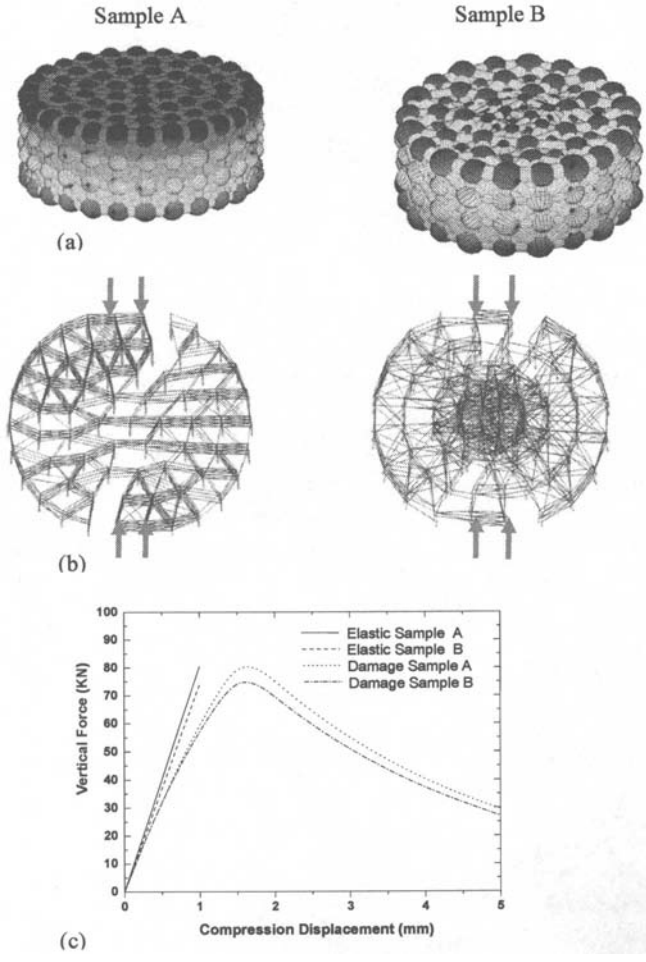

FIG. 3. Damage simulation on numerical samples A and B: a) computer generated 3D samples A and B, including ellipsoids connected by mastic cylinders, b) deformed element structure with removed failed elements, c) elastic and damage simulation results on numerical samples.

The indirect tension damage simulation was conducted on these numerical samples. For the indirect tension loading, the x- and y-displacements of bottom particles and x-displacement of top particles along the thickness were fixed. Sample loading was achieved by incrementing the y-displacement of the top particles. The model material parameters were chosen as E = 1.0 GPa, υ = 0.3, softening strains of ε_{nc} = 0.3, ε_{nt} = 0.1, ε_{tt} = 0.1, and the failure criterion with $c_f = 0.05$. The simulation results show that the sample A generated slightly stiffer behavior than sample B with a little higher aggregate percentage. The comparison between damage and elastic behavior indicate that bilinear damage model is capable to predict the damage behavior generated inside the asphalt mixture.

CONCLUSIONS

A three-dimensional MFEN model was developed to study the damage behavior of asphalt mixtures. This model comprises a network of frame-type element, which stiffness matrix was derived from the approximate elasticity solution of the stress-strain field in a cementation layer between particle pairs. Bilinear damage model was incorporated to the micro-frame element to simulate the damage behavior within the materials under the mechanical loading. The proposed model was employed to conduct simulation on the numerical sample of asphalt mixture. The comparisons between elastic and damage simulation results indicate this damage model is capable of predict the micro-damage within the specimen. In the future work, this modeling scheme will be applied to study the damage behavior of asphalt mixture test specimen with laboratory calibrated model parameters.

REFERENCES

ABAQUS. (2004). In: *Hibitt, Karlsson and Sorenson*, Version 6.5, Pawtucket, R.I.

Chaboche, J. L. (1988). "Continuum damage mechanics: part I - general concepts." *Journal of Applied Mechanics, Transactions ASME*, 55(1), 59-64.

Chang, G. K., and Meegoda, J. N. (1997). "Micromechanical Simulation of Hot Mixture Asphalt." *ASCE J. Engng. Mech.*, 123(5), 495-503.

Crisfield, M. A. (1980). "Fast incremental/iterative solution procedure that handles left double quote snap-through right double quote." *Computers and Structures*, 13(1-3), 55-62.

Crisfield, M. A. (1986). "Snap-through and snap-back response in concrete structures and the dangers of under-integration." *International Journal for Numerical Methods in Engineering*, 22(3), 751-767.

Dai, Q. (2004). "Micromechanical Modeling of Constitutive and Damage Behavior of Heterogeneous Asphalt Materials," University of Rhode Island.

Dai, Q., and Sadd, M. H. (2004). "Parametric model study of microstructure effects on damage behavior of asphalt samples." *International Journal of Pavement Engineering*, 5(1), 19-30.

Dai, Q., Sadd, M. H., Parameswaran, V., and Shukla, A. (2005). "Prediction of damage behaviors in asphalt materials using a micromechanical finite-element model and image analysis." *Journal of Engineering Mechanics*, 131(7), 668-677.

Dai, Q., Sadd, M. H., and You, Z. (2006). "A micromechanical finite element model for linear and damage-coupled viscoelastic behaviour of asphalt mixture." *International Journal for Numerical and Analytical Methods in Geomechanics*, 30(11), 1135-1158.

Dvorkin, J., Nur, A., and Yin, H. (1994). "Effective Properties of Cemented Granular Materials." *Mech.of Materials*, 18, 351-366.

Luther, M. S., Majidzadeh, K., and Chang, C.-W. (1976). "Mechanistic Investigation of Reflection Cracking of Asphalt Overlays." *Transportation Research Record*, 572, 111-122.

Park, S. W., Kim, Y. R., and Lee, H. J. (1999). "Fracture toughness for microcracking in a viscoelastic particulate composite." *Journal of Engineering Mechanics*, 125(6), 722-725.

Park, S. W., Kim, Y. R., and Schapery, R. A. (1996). "Viscoelastic continuum damage model and its application to uniaxial behavior of asphalt concrete." *Mechanics of Materials*, 24(4), 241-255.

Park, S. W., and Schapery, R. A. (1997). "Viscoelastic constitutive model for particulate composites with growing damage." *International Journal of Solids and Structures*, 34(8), 931-947.

Roque, R., Birgisson, B., Drakos, C., and Dietrich, B. (2004). *Development and field evaluation of energy-based criteria for top-down cracking performance of hot mix asphalt (with discussion)*, Association of Asphalt Paving Technologists.

Sadd, M. H., Dai, Q., and Parameswaran, V. (2004a). "Microstructural simulation of asphalt materials: Modeling and experimental studies." *Journal of Materials in Civil Engineering*, 16(2), 107-115.

Sadd, M. H., Dai, Q., Parameswaran, V., and Shukla, A. (2004b). "Simulation of Asphalt Materials Using Finite Element Micromechanical Model with Damage Mechanics." *Transportation Research Record*(1832), 86-95.

Schapery, R. A. (Year). "Mechanical characterization and analysis of inelastic composite laminates with growing damage." Publ by American Soc of Mechanical Engineers (ASME), New York, NY, USA, La Jolla, CA, USA, 1-9.

Schapery, R. A. (Year). "Analysis of damage growth in particulate composites using a work potential." Publ by ASME, New York, NY, USA, Dallas, TX, USA, 55-64.

Schapery, R. A. (1990b). "Theory of mechanical behavior of elastic media with growing damage and other changes in structure." *Journal of the Mechanics and Physics of Solids*, 38(2), 215.

Schapery, R. A. (1999). "Nonlinear viscoelastic and viscoplastic constitutive equations with growing damage." *International Journal of Fracture*, 97(1-4), 33-66.

Simo, J. C., and Ju, J. W. (1987). "Strain- and Stress-Based Continuum Damage Models - I. Formulation." *International Journal of Solids and Structures*, 23(7), 821-840.

Song, S. H., Paulino, G. H., and Buttlar, W. G. (Year). "Cohesive zone simulation of mode i and mixed-mode crack propagation in asphalt concrete." American Society of Civil Engineers, Reston, VA 20191-4400, United States, Austin, TX, United States, 189-198.

Song, S. H., Paulino, G. H., and Buttlar, W. G. (2006a). "A bilinear cohesive zone model tailored for fracture of asphalt concrete considering viscoelastic bulk material." *Engineering Fracture Mechanics*, 73(18), 2829-2848.

Song, S. H., Paulino, G. H., and Buttlar, W. G. (2006b). "Simulation of crack propagation in asphalt concrete using an intrinsic cohesive zone model." *Journal of Engineering Mechanics*, 132(11), 1215-1223.

Sousa, J. B., Pais, J. C., Prates, M., Barros, R., Langlois, P., and Leclerc, A. M. (1998). "Effect of Aggregate Gradation on Fatigue Life of Asphalt Concrete Mixes." *Jounal of Transportation Research Board*, 62-68.

Wen, H., and Kim, Y. R. (2002). "Simple performance test for fatigue cracking and validation with WesTrack mixtures." *Journal of Transportation Research Record*(1789), 66-72.

You, Z. (2003). "Development of a Micromechanical Modeling Approach to Predict Asphalt Mixture Stiffness Using Discrete Element Method," University of Illinois at Urbana-Champaign, published by UMI, a Bell & Howell Information Company, Ann Arbor, MI.

You, Z., and Buttlar, W. G. (2004). "Discrete Element Modeling to Predict the Modulus of Asphalt Concrete Mixtures." *Journal of Materials in Civil Engineering, ASCE*, 16(2), 140-146.

Zhu, H., Chang, C. S., and Rish, J. W., III. (1996a). "Normal and tangential compliance for conforming binder contact. I. Elastic binder." *International Journal of Solids and Structures*, 33(29), 4337-4349.

Zhu, H., Chang, C. S., and Rish, J. W., III. (1996b). "Normal and tangential compliance for conforming binder contact. II. Visco-elastic binder." *International Journal of Solids and Structures*, 33(29), 4351-4363.

Zhu, H., Rish Iii, J. W., and Batra, S. (2001). "A constitutive study of two-phase materials part II. Maxwell binder." *Computers and Geotechnics*, 28(5), 309-323.

The Effect of Water on Pavement Response Based on 3D FEM Simulation and Experiment Evaluation

Zejiao Dong[1], Yiqiu Tan[2] and Liping Cao[3]

[1]Doctor, School of Transportation Science & Engineering, Harbin Institute of Technology, No.202 Haihe Road, Nangang District, Harbin 150090, China; dongzejiao79@163.com
[2]Doctor, School of Transportation Science & Engineering, Harbin Institute of Technology, No.202 Haihe Road, Nangang District, Harbin 150090, China; yiqiutan@163.com
[3]Doctor, School of Transportation Science & Engineering, Harbin Institute of Technology, No.202 Haihe Road, Nangang District, Harbin 150090, China; caoliping79@163.com

ABSTRACT: It has been recognized that asphalt pavement performance will decrease with the presence of water within the pavement structure, while current pavement mechanics analysis has not taken into account the effect of moisture on dynamic response of pavement appropriately. Consequently, a 3D finite element simulation model was performed to study the mechanical response of saturated asphalt pavement based on Biot consolidation theory. Then, a laboratory test procedure was developed to analyze the attenuation of mixture performance induced by the coupled water/loading action. The result indicates that the presence of water changes stress distribution within pavement structure. What's more, it is interesting to find that the adverse position is in the middle and bottom HMA layer according to the distribution of pore pressure, which tallies with the raveling phenomenon of asphalt pavement caused by water. Another finding from the research is that the fatigue life of specimen subject to the coupled water/loading action decreases obviously. It is recommended to consider the effect of water when analyzing and designing flexible pavements.

INTRODUCTION

It is accepted that newly placed HMA pavements are placed at a higher than designed air void content (generally 6-7%) with the assumption that traffic loadings will decrease the air void content over time. This air void level can allow water to move through the pavement (Kanitpong et al. 2001). However, the infiltration of water into the pavement can develop pore pressure leading to excessive deflection, cracking and reduction in load carrying capacity of pavement (Choubane et al. 1998).

It is common that some degree of saturation is possible in all pavements, which indicates that water should not be ignored in mechanics analysis of asphalt pavement. As a result, some relative researches have been done. Masad et al. (2003) used two dimensional SEEP/W finite element to study the relationship between the water flow

patterns and the gradients in percent air voids in HMA. Novak et al. (2002) used theory of mixture to describe the saturated asphalt pavement and studied the effects of vehicle speed and permeability on pore pressure with a two dimensional finite element program-PlasFEM. Kringos et al. (2005) is developing a finite element tool-RoAM (Raveling of Asphalt Mixes) to describe the raveling of asphalt Mixes due to water damage from the point of microcosmic view. Yang et al. (2006) discussed the use of Stiffness Matrix Method to calculate pore pressure within a saturated pavement. Zejiao et al. (2006) finished theoretical derivation and FEM simulation for the saturated pavement subject to transient vehicle loading.

As a result, in order to account for the water effect on pavement response under dynamic loading action, layered porous medium system was employed based on Biot consolidation theory. The pavement response was calculated using a 3D finite element model in transient dynamic analysis mode. At the same time, a laboratory test was designed to describe the effect of the coupled water/loading action on the performance of asphalt mixture. This material performance variation was evaluated with the fatigue life comparison between the conditioned and unconditioned specimens.

FINITE ELEMENT MODELING

In the saturated pavement analysis, the asphalt layers, base, and subgrade are composed of two phases, the solid phase or skeleton (road construction material) and the fluid phase occupying the void volume (water in voids). Biot Consolidation theory is used to describe the saturated pavement, which consists of balance equations for both the solid and the fluid phase and conservation of mass of the total system (Biot 1941, 1956, 1962). The governing equations can be expressed as follows:

Balance equations for solid phase:

$$\frac{\partial \sigma_x}{\partial x}+\frac{\partial \tau_{yx}}{\partial y}+\frac{\partial \tau_{zx}}{\partial z}-\frac{\partial p}{\partial x}=\rho \ddot{u}_s \tag{1}$$

$$\frac{\partial \sigma_y}{\partial y}+\frac{\partial \tau_{zy}}{\partial z}+\frac{\partial \tau_{xy}}{\partial x}-\frac{\partial p}{\partial y}=\rho \ddot{v}_s \tag{2}$$

$$\frac{\partial \sigma_z}{\partial z}+\frac{\partial \tau_{xz}}{\partial x}+\frac{\partial \tau_{yz}}{\partial y}-\frac{\partial p}{\partial z}=\rho \ddot{w}_s \tag{3}$$

Balance equations for fluid phase:

$$-\frac{\partial p}{\partial x}=\frac{\rho_f g}{k_x}\dot{u}_f+\rho_f \ddot{u}_s \tag{4}$$

$$-\frac{\partial p}{\partial y}=\frac{\rho_f g}{k_y}\dot{v}_f+\rho_f \ddot{v}_s \tag{5}$$

$$-\frac{\partial p}{\partial z}=\frac{\rho_f g}{k_z}\dot{w}_f+\rho_f \ddot{w}_s \tag{6}$$

Conservation of mass of the total system:

$$\frac{\partial \dot{u}_s}{\partial x}+\frac{\partial \dot{v}_s}{\partial y}+\frac{\partial \dot{w}_s}{\partial z}=-(\frac{\partial \dot{u}_f}{\partial x}+\frac{\partial \dot{v}_f}{\partial y}+\frac{\partial \dot{w}_f}{\partial z}) \tag{7}$$

In the above equations, u_s, v_s and w_s are the displacements of the solid skeleton in x, y and z directions respectively; u_f, v_f and w_f are the fluid displacements relative to the solid skeleton in x, y and z directions, respectively; k_x, k_y and k_z are the permeabilities in x, y and z directions, respectively; σ_x, σ_y and σ_z are the effective stresses in x, y and z directions, respectively; p is the pore pressure; ρ is the mass density; ρ_f is the pore fluid density; $\cdot$ and $\cdot\cdot$ denote the first order and second order differential of displacement variables, respectively.

The theoretical derivation and numerical simulation for the saturated asphalt pavement in axisymmetric case is performed in Zejiao et al. (2006). Here, we use ADINA finite element program to carry out the simulation. General information is listed followed by a brief description of dynamic loading and material properties.

Basic Parameters of Finite Element Modeling

Three dimensional finite element mesh is shown in Figure 1. Eight-node brick element is used, which gives a comparative accuracy and is not memory consuming at the same time. The nodes, when analyzed in a transient dynamic saturated state, have seven degrees of freedom corresponding to the fluid and solid displacements in X, Y and Z direction as well as pore pressure. The total vertical, longitudinal and transverse dimensions of the mesh are 3.0 m by 3.0 m by 3.0 m. Elements are finer near the top and middle (where the wheel load will be applied) of the mesh and gradually grow coarser toward the sides and bottom of the pavement structure.

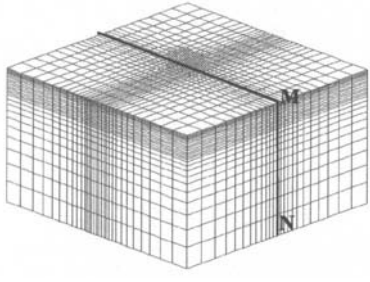

FIG. 1. 3D finite element mesh.

For the solid phase, the left and right boundaries were free to move vertically and longitudinally but not transversely, the front and back boundaries were free to move vertically and transversely but not longitudinally, the bottom boundary was fixed in all directions, and the top boundary was free to move in all directions. For the fluid phase,

the surrounding boundaries and top boundary, except for the loading area, were pervious while the bottom boundary and loading area were impervious.

Transient Dynamic Loading

The wheel load as proposed in Xiaodi et al. (2005) was assumed to be 0.24 m long and 0.16 m wide with a contact pressure of 651 kPa for a single rectangle loading area, and the center distance between two loading areas is 0.24 m. A time dependent haversine function is used to simulate an assumed smoothly varying tire loading, followed from the definition of Novak et al. (2002). The applied loading at any time t is presented by:

$$p = P_{max} \sin(\frac{\pi t}{T}) \quad 0 \le t \le T \tag{8}$$

Where P_{max} is the loading peak. T is the total duration of the loading, which is based upon the vehicle speed and the assumption that the tire has no effect at the distance of its sextuple length. This paper looked at a wheel load traveling at 60 km/h, 90 km/h, and 120 km/h, or a haversine load duration of 0.0864, 0.0576 and 0.0432 seconds, respectively.

Material Properties

The material parameters used in the simulation are shown in Table 1, which are common for many dense graded HMA in China.

Table 1. Material properties used in three dimensional finite element simulation

Properties	Upper asphalt layer	Middle asphalt layer	Lower asphalt layer	Upper base layer	Lower base layer	Subgrade
Thickness(m)	0.05	0.06	0.08	0.20	0.20	2.41
Elastic modulus(MPa)	1400	1400	1400	1600	600	50
Poisson's ratio	0.30	0.35	0.35	0.20	0.30	0.40
Solid bulk density (kg/m^3)	2400	2400	2400	2100	1900	1900
Fluid bulk modulus (MPa)	1.0E+11	1.0E+11	1.0E+11	1.0E+11	1.0E+11	1.0E+11
Fluid density(kg/m^3)	1000	1000	1000	1000	1000	1000
Permeability(cm/s)	1.0E-04	1.0E-04	1.0E-04	1.0E-04	1.0E-05	1.0E-06

Figure 2 shows the pore pressure history for the center of one tire area at different depths. In this case, the vehicle speed is 60 km/h. For each depth level, the pore pressure increases very rapidly with the increase of loading at the initial stage, as the applied

loading is transferred to the fluid in the voids mostly. Subsequently, as the fluid starts to escape the voids, the pore pressure decreases. Then the positive pore pressure changes to the negative suction pressure and the surrounding solid skeleton recovers from the loading and sucks fluid back into the voids gradually. The maximum negative pore pressure reaches when the loading is almost gone. Finally, as the loading has already gone, the negative pore pressure starts to dissipate.

It is interesting to find that the peak time of pore pressure is earlier than that of the applied loading. The possible reason is that, there has already certain time for the fluid to escape through the surrounding interconnected voids after the initial stage of the loading, although the applied loading increases to its peak value subsequently, the transferred pressure to the fluid could not continue to go up.

The similar reversals from positive pore pressures to sizable suctions, as the wheel loading is applied, are found at all the depth, while the different point is their peak value.

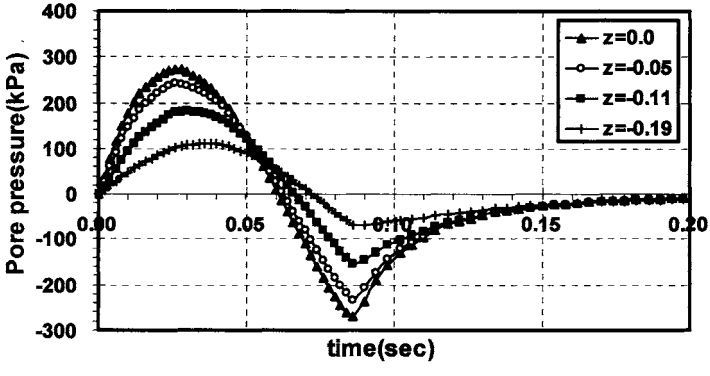

FIG. 2. Pore pressure histories at different depths.

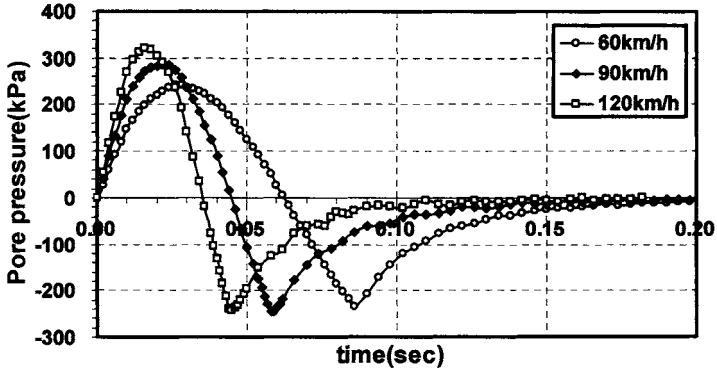

FIG. 3. Pore pressure histories for different speeds.

Figure 3 shows the pore pressure history for the center of one tire area at the interface between the upper and middle asphalt layer (at the depth of 0.05 m) for different speeds. In this case, the vehicle speed varied from 60 km/h to 120 km/h. As the vehicle speed increases, the positive pore pressure increases slightly, from 242 kPa at 60 km/h to 321 kPa at 120 km/h, which is caused by the less escaping time for the fluid at higher vehicle speed. The results here are similar with the work done by Novak et al. (2002) with PlasFEM, which indicates the validity of the simulation presented here.

As it can be seen from Figure 4 which illustrates the pore pressure distribution of M-N section at different time, pore pressure mainly concentrates in asphalt layers, both the arising and dissipating phase. What's more, the transverse influencing scope is the widest at the depth from 0.05 m to 0.2 m, which are just right the middle and bottom asphalt layer. This means that the adverse position is the middle and bottom HMA layer once water enters the pavement structure, which tallies with the raveling phenomenon of asphalt pavement due to water action. As a result, the concentration in certain area for pore pressure, combining with its reversal from positive to negative during the vehicle loading, may be thought as one of the reasons for the stripping failure caused by water, which is similar with Figure 5, from the results presented here.

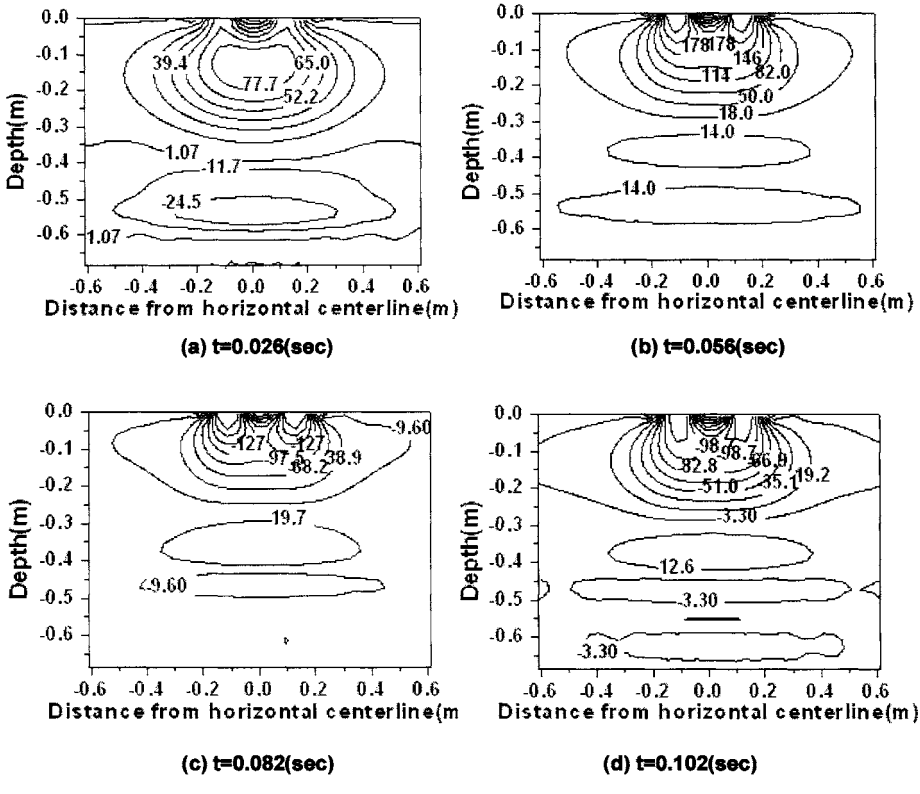

FIG. 4. Pore pressure distribution for different time.

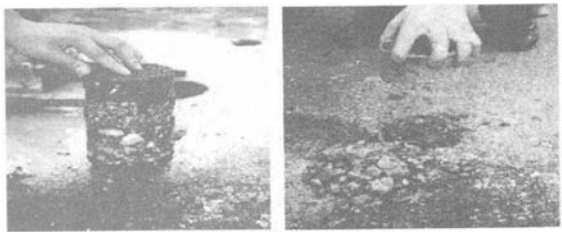

FIG. 5. Coring of asphalt pavement with initial failure.

Figure 6 presents the comparison result of vertical stress distribution between the saturated and dry condition, at the loading peak time (vehicle speed is 60 km/h), assuming that all the parameters used in FEM simulation are the same except for the moisture condition. Larger vertical tensile stress occurs outside the two wheels in the saturated case comparing with the dry case, although vertical compressive stress under the applied area is smaller in the former. The fluid under the tire is forced to flow to the surrounding area when loading, which results in the increase of pressure transferred to the ambient solid skeleton. This means water existing within pavement structure is more likely to induce the lifting outside the two wheels, comparing with the dry case. This further demonstrates that moisture makes asphalt pavement weak.

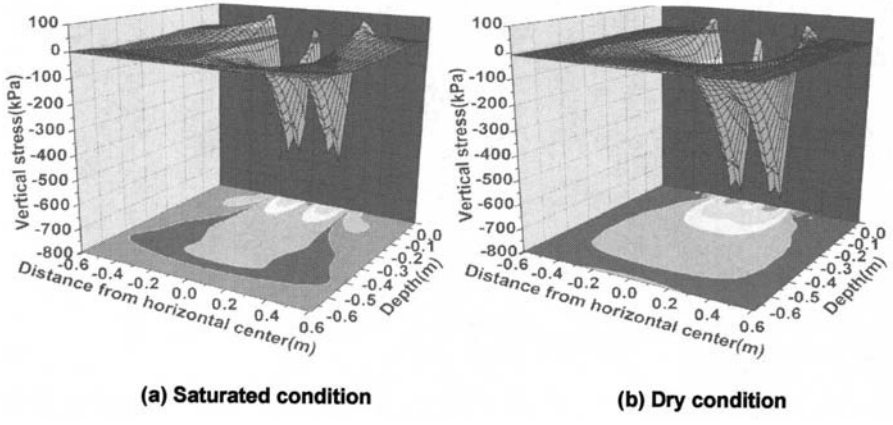

FIG. 6. Comparison of vertical stress distribution between dry and saturated case.

LABORATORY TEST DESIGN

To identify the effect of pore pressure, a laboratory test procedure was developed. Differing from the procedure developed by Jimenez et al. (1974) and Mallick et al. (2003), which separated the pore pressure action from vehicle loading, a procedure of laboratory test with a repeated loading directly on specimens in a conditioned chamber is carried out. Then, the fatigue life of conditioned specimen is used to present the influence of the coupled water/loading action. The sketch map of the test is shown in

Figure 7. Indirect tension and uniaxial compression modes are used to simulate the repeated tension and compression stress state in real pavement structure, in which pore pressure arises spontaneously. Authors believe that this is an easier and simpler method to simulate the coupled water/loading action comparing with other researches.

The specimens are compacted to 6 % to 8 % voids firstly, and subjected to a water preconditioning which includes vacuum saturation of specimens for 15 minutes with a saturation level between 55 % and 80 %, then cured in the water for 48 hours at 25 °C. After these treatments, the specimens can be used for the proposed test. Here, traditional dense grading mixture AC-16 is used. The penetration of asphalt is 90, while aggregate is basalt in Heilongjiang Province. Further information is listed in Zejiao et al. (2006).

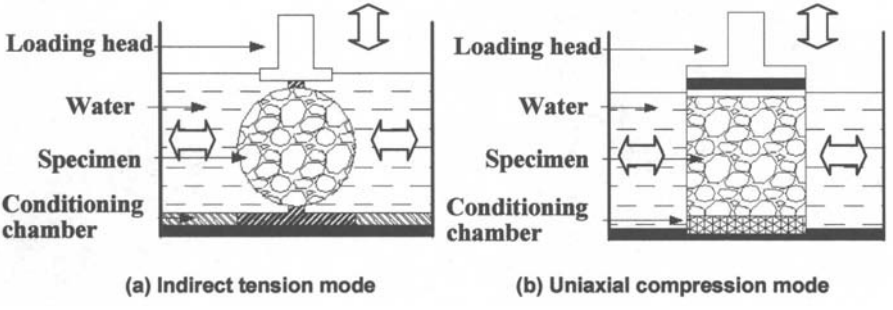

FIG. 7. Sketch map of specimens subject to the coupled water/loading action.

ANALYSIS OF THE LABORATORY TEST RESULT

The repeated haversine pulse load of 10 Hz, approximately simulating vehicle traveling at the speed of 60 km/h (its loading frequency is 11.6 Hz), is used in both loading modes. The magnitude of loading is determined by the corresponding strength test after the specimens are preconditioned. Figure 8 shows the result of the repeated indirect tension test. Retained life varies from 67 % to 84 %, and increases slightly as the stress level increases. That means fatigue life decreases 20-30 % due to the coupled water/loading action.

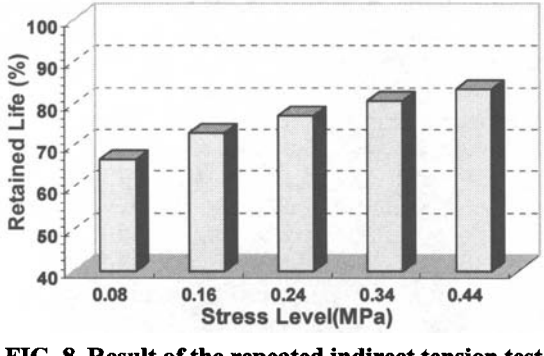

FIG. 8. Result of the repeated indirect tension test.

Figure 9 presents the result of the repeated uniaxial compression test. Retained life varies from 1 % at 0.7 MPa to 45 % at 1.1 MPa, and decreases obviously with the increase of the compression stress. This rule is different from that shown in the repeated indirect tension test. In the compression mode, the pore fluid was compressed to scour asphalt film wrapping on aggregate surface. The larger the compression stress, the larger the positive pore pressure occurs, resulting in a relatively smaller retained life. In contrast, the larger the tension stress, the larger pore size becomes between aggregates, and the less scouring action on the film, which leads to a relatively higher retained life. In any case, it shows that the coupled water/loading action has a visible adverse influence on the performance of asphalt mixture, which requests that the adverse effect caused by water should be considered in asphalt pavement analysis.

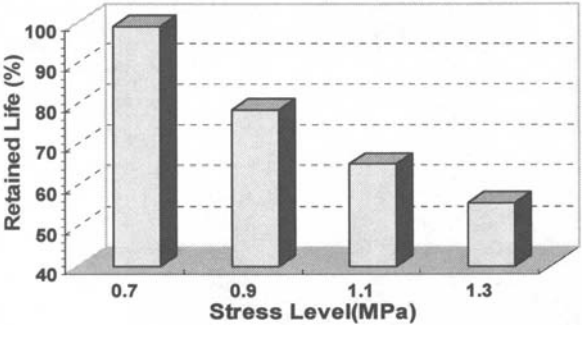

FIG. 9. Result of the repeated uniaxial compression test.

CONCLUSIONS

This paper presents a three dimensional finite element simulation of a saturated asphalt pavement system subject to a dynamic vehicle load, and develops a laboratory test procedure to quantitate the adverse effect caused by the coupled water/loading action. Some key observations from this analysis were:

1. A reversal of pore pressures occurs in the saturated asphalt pavement due to the dynamic vehicle loading, which may induce the stripping and scouring phenomenon.
2. Pore pressure arising in the saturated pavement is relevant to the vehicle speed. Higher vehicle speed will result in a higher pore pressure, due to the shorter time for the fluid under the tire to flow.
3. It shows that the adverse position is in the middle and bottom asphalt layer as the arising and dissipating of pore pressure concentrates here, which tallies with the raveling phenomenon of asphalt pavement caused by water.
4. Larger vertical tensile stress occurs outside the two wheels of vehicle in the saturated pavement comparing with the dry case, which is more likely to cause the lifting outside the two wheels.
5. A simple laboratory procedure is developed to simulate the coupled water/loading action, which indicates that the presence of water weakens the mixture performance, and higher compression stress makes asphalt mixture have more stripping potential.

It is recommended that the relationship between permeability and pore pressure should be analyzed, as the former highly influences the latter. Further improvement and refinement of the test procedure should be carried out so that it can be used widely. Recommendation is also made for further research work with different types of mixes.

ACKNOWLEDGEMENTS

The authors appreciate "Chinese Specialized Research Fund for the Doctoral Program of Higher Education" for the funding support (Research item: Research on rutting mechanism of asphalt pavement, Serial number: 20060213002). The help of Master Hu bin in preparing mixes is greatly appreciated. The authors are grateful to Prof. Guo Dazhi for providing valuable suggestions and to Prof. Ren Ruibo in supporting valuable information.

REFERENCES

Kanitpong, K., Benson, C.H. and Bahia, H.U. (2001). "Hydraulic conductivity (permeability) of laboratory compacted asphalt mixtures." *Transportation Research Record*, TRB, Washington D.C.: 1-12.

Choubane, B., Page, G.C. and Musselman, J.A. (1998). "Investigation of water permeability of coarse graded superpave pavements." *Proceedings of Association of Asphalt Paving Technologists*, Vol. 67: 1-13.

Masad, E., Birgisson, B., Al-Omari, A. and Cooley, A. (2003). "Analysis of permeability and fluid flow in asphalt mixes." *the 82nd Annual Meeting of the Transportation Research Board*, TRB, Washington D.C.: 1-33.

Novak, M., Birgisson, B. and McVay, M. (2002). "Effects of permeability and vehicle speed on pore pressure in hot mix asphalt pavements." *the 81th Annual Meeting of the Transportation Research Board*, TRB, Washington D.C.: 1-19.

Kringos, N. and Scarpas, A. (2005). "Raveling of asphaltic mixes due to water damage: computational identification of controlling parameters." *the 84th Annual Meeting of the Transportation Research Board*, TRB, Washington D.C.: 1-19.

Yang, Z., Litao, G., Linzhou, F. (2006). "Computing the express pore fluid stress of flexible pavement by stiffness matrix method." *Journal of ShenyangJianzhu University*, 22(1): 25-29.

Zejiao, D. (2006). "Dynamic response analysis of saturated asphalt pavement based on porous medium theory." *Ph.D. Dissertation*, Harbin Institute of Technology, Harbin: 120-158.

Biot, M.A. (1941). "General theory of three-dimensional consolidation." *J Appl Phys*, 12: 155–164.

Biot, M.A. (1956). "Theory of propagation of elastic waves in a fluid-saturated porous solid Low-frequency range." *J Acoust Soc Am*, 28(2): 168–178.

Biot, M.A. (1962). "Mechanics of deformation and acoustic propagation in porous media." *J Appl Phys*, 33(4): 1482–1498.

Xiaodi, H. (2003). "Measurement of tire pressure distribution and mechanical response analysis of asphalt pavement." *Ph.D. Dissertation*, Tongji University, Shanghai: 29-50.

Jimenez, R.A. (1974). "Testing for debonding of asphalts from aggregates." *Transportation Research Record 515*, TRB, Washington DC.: 1-3.

Lijun, S. (2005). "The action of dynamic water pressure." *Structural behavior theory of asphalt pavement*, the people communication press, Beijing: 219-223.

Mallick, G., Bhattacharjee, R., James and Brown (2003). "Development of a rational procedure for evaluation of moisture susceptibility of asphalt paving mixes." *the 82th Annual Meeting of the Transportation Research Board*, TRB, Washington D.C.: 1-23.

Bathe, K.J. (2005). "Formulation of fluid flows through porous media." *Theory and modeling guide-Volume III: ADINA-F*, ADINA R& D Inc., Watertown: 145-151.

Pinto, P. (1998). "Coupled finite element formulations for dynamic soil-structure interaction." *Ph.D. Dissertation*, University of Florida, Gainesville: 3-10.

Study on the Influence of the Fiber and Modified Asphalt upon the Performance of Asphalt Mixture

Tianqing Ling[1], Wei Xia[2], Qiang Dong[2], and Deyun He[2]

[1]PhD, School of Civil and Architecture, Chongqing Jiaotong University, Chongqing, China, 400074; lingtq@163.com

[2]M.S, School of Civil and Architecture, Chongqing Jiaotong University, Chongqing, China, 400074; sabranna@163.com

ABSTRACT: The effect of fiber on the asphalt mixtures has been concerned at all times. Bearing this problem in mind, four kinds of polyester fiber, one kind of methyl cellulose, one kind of mineral fiber, AC-16 and SMA-16 asphalt mixtures, AH-70 and the SBS (I-D) modified asphalt were chosen and used in the present study. Practical performances such as Marshall Test indexes, low-temperature split strength, residual stability, freezing and thawing splitting strength ratio and dynamic stability of the mixtures made of the above mentioned materials were studied. Though there is optimal asphalt content contained in the mixture, the improving effect of fiber on the asphalt mixtures (AC-16 and SMA-16) performance is not apparent. Therefore from a general view of economy and technology, it seems unnecessary to put fiber into AC asphalt mixtures with high-quality modified asphalts. However, the effect of fiber as a stabilizing agent is bigger than that of as the agent strengthening the wheel tracking resistance capacity in the SMA mixtures.

INTRODUCTION

Asphalt pavement is the main form of Pavement Structure of the freeway. The chief forms of the destructions of freeway are wheel tracking, split and fatigue destructions. Since 1960s, most of the research about asphalt pavement has focused on these destructions. However, in the past 10 years of China, in most cases, the life of asphalt pavement of freeway are shorter than the design life, therefore, the other two destructions – water damage and reflection cracks, have gradually caught the attention of engineers and become a world-wide problem. In addition, China's Asphalt Pavement Design (e.g., Ministry of communications of PRC 2004a) notes that adding fiber to asphalt concrete can improve its performance when it is allowed.

In china, the asphalt pavement under heavy carry and the gradient is very steep, which result in the wheel tracking of asphalt pavement is serious. Bearing this problem in mind, the study attempts to improve the wheel tracking resistance capability of asphalt mixture by asphalt modified and adding fiber in the asphalt mixture, then to make a contrast analysis of its results.

What role can fiber play in AC and SMA asphalt concrete? Are they effective? Bearing this problem in mind, Four kinds of polyester fiber, one kind of methyl cellulose, one kind of mineral fiber, AC-16 and SMA-16 asphalt mixture, AH-70 and the SBS(I-D) modified asphalt were chosen and used in this study. Practical performances such as Marshall Test index, low-temperature split strength, residual stability, freezing and thawing splitting strength ratio and dynamic stability of the mixtures made of the above mentioned materials were studied.

RAW MATERIALS AND THE TYPES OF MIXTURE

Asphalt

Ordinary asphalt in test is Zhonghai 36-1AH-70. Zhonghai AH-70 was chosen as raw asphalt of modified asphalt, and modified agent was Shenzhen Luante SBS (I-D), with a content of 3.8%. Asphalt content used in the Marshall Test is the optimal asphalt content

Aggregate

Aggregate adopted basalt detritus, which was produced by stone factory of Lantian Kewangda in Shanxi. The mineral powder, which was produced by cement factory of Pingliangxiazhong in Shanxi, was used as filler.

Fiber

Many fiber such as Dolanit® AS polyacrylonitrile fiber, ARBOCEL methyl cellulose, BoniFbers® polyester fiber, FORTA® AR fiber which was composed of polypropylene and Aramid Fiber, DCPET polyester fiber which was made in China, and FIBROX mineral fiber which was made in Canada were chosen and used in this study.

Asphalt Mixture

The middle value gradation of AC-16 and SMA-16 asphalt mixture were chosen and used in this study (e.g., Ministry of communications of PRC. 2004b).

THE INFLUENCE OF FIBER ON THE MARSHALL TEST INDEX OF ASPHALT MIXTURE

The Influence of the Fiber Content on the Marshall Test

The study using Dolanit® AS polyacrylonitrile fiber and ordinary asphalt to analyze the influence of the fiber content on Marshall Test, AC-16 middle value gradation was used in all of the gradation of mineral aggregate. The ratios of fiber, which were chosen in the study, were 0%, 0.25%, 0.30%, 0.35% and 0.50%. Marshall Test in laboratory determined the optimal bitumie-aggregate ratios under different

fiber content, and then the study tested every Marshall Test index under the optimal bitumie-aggregate ratio. From the results of the test, there is an optimal fiber content for the fiber asphalt concrete. Under present study conditions, the optimal Dolanit® AS polyacrylonitrile fiber content is 0.3%, and 4.7% for the corresponding quantity of asphalt.

The Influence of the Fiber Type on the Marshall Test Index

Ordinary asphalt, modified asphalt and optimal fiber content were chosen in this study. The effects of six kinds of fiber on the Marshall Test of the AC-16 middle value gradation can be seen from Table 1 and Table 2.

It is shown from Table 1 and Table 2 that there is no notable difference among the effects of six kinds of fiber on the Marshall Test index of the AC-16 middle value gradation, but polyester fiber of BoniFbers® is the one upon others.

In order to study the effect of fiber on the SMA-16, the tests of adding fiber and no fiber were made separately for contrast, Dolanit® fiber was chosen for the study, ordinary asphalt and modified asphalt were chosen for contrast. The result of the tests can be seen from Table 3, for the Marshall Test index of SMA-16 mixture, the function of fiber is quite apparent while the performance of the modified asphalt is not.

Table 1. The Effect of Ordinary Asphalt Concrete AC-16 with Different Kinds of Additional Fiber on the Marshall Test Index

Fiber type	Amount of asphalt (%)	Stability (KN)	Flour value (mm)	Density (g/cm^3)	VV (%)	VA (%)	VMA (%)	VFA (%)
Without fiber	4.6	9.96	3.68	2.454	3.548	10.508	14.056	74.760
Dolanit® AS	4.7	11.22	3.83	2.444	3.805	10.683	14.488	73.735
BoniFbers®	4.7	11.47	3.91	2.446	3.727	10.691	14.418	74.153
FORTA® AR	4.7	11.16	3.74	2.441	3.923	10.670	14.593	73.115
DCPET	4.7	11.09	3.79	2.439	4.002	10.661	14.663	72.706
Methyl cellulose	4.7	10.64	3.77	2.435	4.160	11.462	15.622	73.374
Mineral fiber	4.7	10.85	3.85	2.437	4.056	11.155	15.211	73.335

The Influence of the Asphalt Type on the Marshall Test Index

From Table 1 and Table 2, it is easy to find that the application of the modified asphalt AC-16 can have the same effect as the ordinary asphalt with additional fiber; Of course, the performance of the modified asphalt concrete with additional fiber can be further enhanced. From Table 3, for the SMA-16 mixture under the Marshall Test index, the performance of the modified asphalt is insignificant.

THE INFLUENCE OF FIBER ON THE CRACK-RESISTANCE CAPACITY IN THE LOW TEMPERATURE OF ASPHALT MIXTURE

Indirect tensile test (Splitting test) under different temperatures was chosen for this study, the asphalt mixture of six kinds of fiber and two kinds of asphalt were chosen for splitting test. The results are shown in Table 4.

From Table 4, in the AC-16 ordinary asphalt concrete, fiber almost has no contributions to enhance the crack-resistance capacity in the low temperature, and there is no difference among various kinds of fiber. In the AC-16 modified asphalt concrete, although fiber has certain contributions to enhance the crack-resistance capacity in the low temperature, it does not meet expectations, and there is no obvious difference among various kinds of fiber too. It is also found that the contributions of the modified asphalt are bigger than that of fiber, which is worth considering.

For SMA-16 mixture, the contributions of fiber to improve the splitting strength are increased compared with the fiber in AC-16 asphalt mixture, but with only 10-15% of increase which is not sharp while there is 15-40% of increase in the modified asphalt mixture.

Table 2. The Effect of Modified Asphalt Concrete AC-16 with Different Kinds of Additional Fiber on the Marshall Test Index

Fiber type	Amount of asphalt (%)	Stability (KN)	Flour value (mm)	Density (g/cm^3)	VV (%)	VA (%)	VMA (%)	VFA (%)
Without fiber	4.7	13.25	3.72	2.458	4.131	11.205	15.336	73.063
Dolanit® AS	4.8	14.56	3.89	2.450	4.224	11.236	15.460	72.678
BoniFbers®	4.8	14.830	3.96	2.451	4.147	11.244	15.391	73.056
FORTA® AR	4.8	14.52	3.78	2.444	4.283	11.229	15.512	72.389
DCPET	4.8	14.36	3.81	2.432	4.356	11.211	15.567	72.018
Methyl cellulose	4.8	13.78	3.83	2.439	4.475	12.188	16.663	73.144
Mineral fiber	4.8	13.91	3.88	2.440	4.394	11.834	16.228	72.923

Table 3. The Influence of Dolanit® AS Polyacrylonitrile Fiber on the Marshall Test Index of SMA-16

Type of mixture	Amount of asphalt (%)	Stability (KN)	Flour value (mm)	Density (g/cm^3)	VV (%)	VA (%)	VMA (%)	VFA (%)
AH-70 SAM-16 without adding fiber	5.80	6.03	4.28	2.433	4.257	14.108	18.365	76.820
AH-70 SMA-16 with additional fiber	5.90	7.44	3.47	2.428	3.832	13.651	17.483	78.082
Modified asphalt SAM-16 without adding fiber	6.00	7.68	3.82	2.439	4.133	14.003	18.136	77.215
Modified asphalt SMA-16 with additional fiber	6.10	8.95	3.01	2.436	3.746	13.512	17.258	78.294

Table 4. The Influence of Fiber upon the Splitting Strength under Different Temperature of Asphalt Mixture

Type of mixture	Type of fiber	15℃ (MPa)	10℃(MPa)	0℃(MPa)	-10℃(MPa)	-20℃ (MPa)
Ordinary asphalt	Without fiber	1.523	2.424	3.501	4.192	3.236
	Dolanit® AS	1.648	2.565	3.577	4.272	3.366
	BoniFbers®	1.614	2.587	3.550	4.256	3.331
	FORTA® AR	1.585	2.502	3.592	4.245	3.309
	DCPET	1.576	2.533	3.535	4.232	3.287
	Methyl cellulose	1.553	2.465	3.514	4.211	3.268
	Mineral fiber	1.568	2.479	3.527	4.226	3.251
Modified asphalt	Without fiber	1.855	2.782	3.577	4.318	3.523
	Dolanit® AS	1.962	2.873	3.815	4.642	3.847
	BoniFbers®	1.986	2.849	3.772	4.600	3.888
	FORTA® AR	1.950	2.895	3.839	4.566	3.804
	DCPET	1.916	2.864	3.795	4.518	3.726
	Methyl cellulose	1.875	2.806	3.623	4.379	3.597
	Mineral fiber	1.892	2.819	3.686	4.445	3.653
AH-70 SMA-16 with additional fiber		0.885	1.428	2.058	2.637	3.124
SBS modified asphalt SMA-16 without adding fiber		0.903	1.520	2.164	℃℃2.745	3.282
SBS modified asphalt SMA-16 with additional fiber		1.020	1.729	2.491	3.008	3.643

Notes: a. The fiber type which was added in SMA is Dolanit® AS polyacrylonitrile fiber

Table 5. The Influence of Fiber on Marshall Residual Stability (%) of Asphalt Concrete AC-16

Asphalt type	Without fiber	Dolanit® AS	BoniFbers®	FORTA® AR	DCPET	Methyl cellulose	Mineral fiber
Ordinary asphalt	85	92	90	88	89	85	87
Modified asphalt	87	93	92	92	90	87	89

Table 6. The Influence of Fiber on Marshall Residual Stability of Asphalt Concrete SMA-16

Type of gradation	AH-70 SMA-16 without adding fiber	AH-70 SMA-16 with additional fiber	SBS modified asphalt SMA-16 Without adding fiber	SBS modified asphalt SMA-16 with additional fiber
Residual stability MS_0 (%)	72	84	89	93

Notes: a. The fiber type which was added in SMA is Dolanit® AS polyacrylonitrile fiber.

THE INFLUENCE OF FIBER ON THE WATER STABILITY OF ASPHALT MIXTURE

The Test Results and Analysis of Soaking Marshall Test

The test results of AC-16 are shown in Table 5, the test results of SMA-16 are shown in Table 6.

Conclusions can be drawn from Table 5: there are certain contributions of fiber to enhance the residual stability of asphalt concrete either in ordinary asphalt AC-16 or in modified asphalt AC-16, and the polyester fiber has more contributions than other types of fiber, but it still does not meet the expectations.

From Table 6, it is found that the contributions of fiber to enhance the residual stability of SMA are greater than that of AC-16 (17% of increase for ordinary asphalt, 4.5% of increase for modified asphalt); but it is also found that in the standard SMA mixture, the contributions of modified asphalt to improve residual stability are 11% higher than fiber. These two findings indicate that the binding power between asphalt and aggregate is a critical factor.

The Results and Analysis of Freezing and Thawing Splitting Test

Samples were divided into two groups: Six kinds of fiber and two kinds of asphalt were chosen for contrast in the experiment, the results are shown in Table 7.

From Table 7, it can be seen that fiber has a certain effect to TSR of AC-16 but not notable, its conclusion is almost the same as the other experiment's conclusion –

the influence of fiber on the splitting strength under different temperature of asphalt mixture. The effect of fiber on the TSR of SMA-16 mixture is more noticeable than that of AC-16 mixture. In the standard SMA mixture, the mixture with additional fiber can improve the freezing and thawing splitting strength by 13.6% while the modified asphalt only enhances the strength by 8.2%.

Table 7. The Influence of Fiber on TSR (%) of Asphalt Mixture

Asphalt type	Without fiber	Dolanit® AS	BoniFbers®	FORTA® AR	DCPET	Methyl cellulose	Mineral fiber
Ordinary asphalt AC-16	82	85	89	86	88	85	86
Modified asphalt AC-16	85	89	91	90	91	90	88
AH-70 SMA-16 without adding fiber	73						
AH-70 SMA-16 With additional fiber		85				83	87
SBS modified asphalt SMA-16 without adding fiber	81						
SBSmodified asphalt SMA-16 With additional fiber		92				88	90

Table 8.The Influence of Fiber Dose on the Residual Stability of Asphalt Concrete

Fiber content (%)	0.00	0.20	0.30	0.35	0.50
Residual stability (%)	84	87	92	90	88

Table 9. The Influence of Fiber Dose on the TSR (%) of Asphalt Concrete

Fiber content (%)	0.00	0.20	0.30	0.35	0.50
TSR (%)	82	83	85	84	82

The Influence of Fiber Dose on the Water Stability of Asphalt Concrete

In order to analyze the influence of fiber content on the resistance to water damage capability of asphalt concrete with additional fiber, Dolanit® AS polyacrylonitrile fiber and ordinary asphalt were adopted in the study. The radios of fiber chosen in the study were 0%, 0.25%, 0.30%, 0.35% and 0.50%. The optimal bitumie-aggregate ratios under different fiber content had been determined by Marshall Test in the laboratory, so that the influence of different fiber content on the index of resistance to water damage capability could be discussed in the later. The results are shown in Table 8 and Table 9.

The results in Tables 8 and 9 indicate that for the fiber asphalt concrete, there is an optimal fiber content. Under present study conditions, the optimal amount of Dolanit® AS polyacrylonitrile fiber is 0.3%, nevertheless, with only not more than 9.5% of increase to the residual stability and 3.6% of increase to the freezing and

thawing splitting strength ratio, so the further conclusion can be made that the effect of fiber on enhancing the water stability of asphalt concrete is not significant.

THE INFLUENCE OF FIBER ON THE HIGH TEMPERATURE STABILITY OF ASPHALT CONCRETE

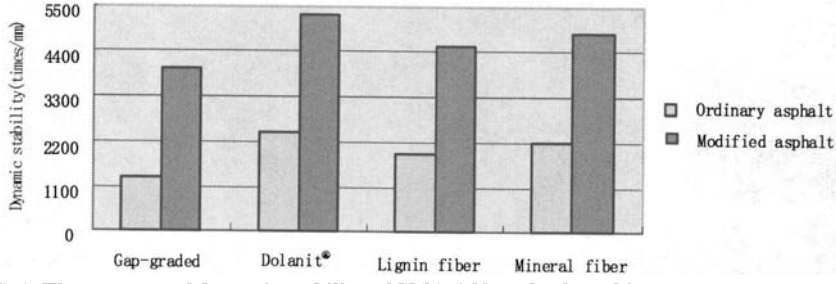

FIG. 1. The contrast of dynamic stability of SMA-16 by wheel tracking test.

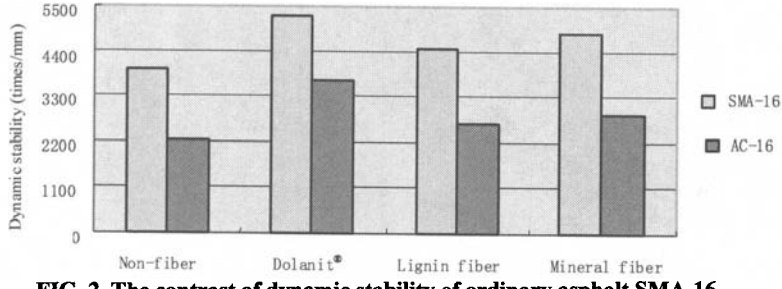

FIG. 2. The contrast of dynamic stability of ordinary asphalt SMA-16.

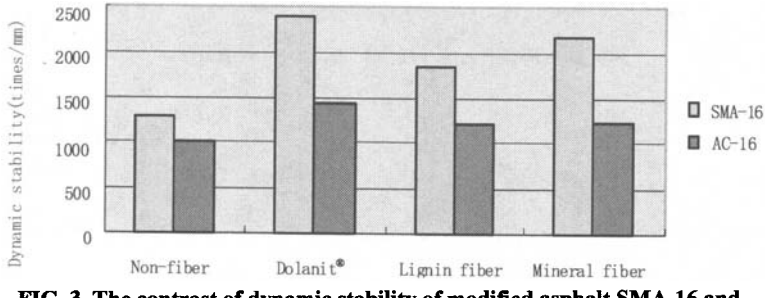

FIG. 3. The contrast of dynamic stability of modified asphalt SMA-16 and AC-16.

In this study, the high temperature performance of asphalt concrete with additional fiber was characterized by dynamic stability and deformation rate. It is known to all that if the dynamic stability is enhanced, the wheel tracking resistance capability will be enhanced too. Asphalt mixture of AC-16, SMA-16, and five kinds of fiber were chosen for dynamic stability test to make a contrast analysis of its results. The results are shown in figure 1 through 3. It can be noticed that when fiber is added, the dynamic stability of SMA mixture is higher than the SMA mixture without adding fiber, and modified SMA is higher compared with ordinary SMA. Especially, the dynamic stability of modified SMA-16 mixture which is added Dolanit® AS is highest compared with others; the dynamic stability of ordinary SMA-16 mixture is higher than that of ordinary AC-16 asphalt mixture with additional fiber; the dynamic stability of modified SMA-16 mixture is higher than Modified AC-16 asphalt mixture with additional fiber. The order of dynamic stability is illustrated as follows: ordinary AC-16 asphalt mixture with additional fiber < ordinary SMA-16 mixture < modified AC-16 asphalt mixture with additional fiber < modified SMA-16 mixture.

When fiber is added in asphalt mixture, because of the absorption effect of fiber on asphalt, especially, after the lighter oil of asphalt is adsorbed by fiber, softening point of asphalt, viscosity and cohesive strength are increased. This increases the asphalt glue stiffness, enhances the dynamic stability of mixture greatly and improves the high temperature stability of mixture.

The results also show that the contributions of SBS modified asphalt is greater than that of modified asphalt with additional fiber. The conclusion is almost the same as the American research achievements but with different approaches (e.g., Brown et al. 1997a and Brown et al. 1997b). The dynamic stability of SMA gradation mixture is higher than intensive gradation asphalt mixture; the increase of dynamic stability of modified asphalt with additional fiber is higher than that of ordinary asphalt concrete with additional fiber. For the asphalt pavement under heavy carry, if the condition permits, it is suggested that the mixture of the modified asphalt with extra fiber should be used and the SMA mixture which with the highest dynamic stability should be adopted to enhance the wheel tracking resistance capability.

CONCLUSIONS

Judging by the Marshall Test index for the asphalt concrete, the fiber content in the mixture has an optimal content as shown from the ratio of residual stability and frozen and thawing splitting strength.

There is no notable difference in the effects of six kinds of fiber on the Marshall Test index of the AC-16 middle value gradation. For the Marshall Test index, the application of the modified asphalt can have the same effects as the ordinary asphalt with additional fiber.

For the SMA-16 mixture under the Marshall Test index, the effect of fiber is quite apparent while the performance of the modified asphalt is insignificant.

It is also found that the contributions of the modified asphalt are bigger than that of fiber. It is shown that the binding power between asphalt and aggregate is a critical

factor.

Through soaking and freezing & thawing splitting tests under the Marshall Test, it has been found that fiber has smaller contributions to the water stability in the AC-16 asphalt concrete, its contributions are even smaller than the contributions of the fiber in the modified asphalt.

In the standard SMA mixture, the modified asphalt contributes more (by 11%) to the residual stability than fiber contributes, the mixture with additional fiber can improve the freezing and thawing splitting strength by 13.6% while the modified asphalt only enhances the strength by 8.2%. The effect of fiber on the water stability in the SMA mixture is more noticeable than that on the AC-16 mixture.

It is known to all that if the dynamic stability is enhanced, the wheel tracking resistance capability will be enhanced too. For the asphalt pavement under heavy carry, the dynamic stability of the pavement of AC-16 modified asphalt mixture with extra fiber or SMA-16 modified asphalt mixture with extra fiber is the strongest, so its wheel tracking resistance capability is the strongest too. However, if the investment is limited, adopting the modified asphalt pavement to increase the wheel tracking resistance capability is an economic measure.

REFERENCES

Brown, E.R., Haddock, J.E., Mallick, R.B. and Lynn, T.A. (1997a). "Development of a Mix Design Procedure for Stone Matrix Asphalt (SMA) Mixtures." *Journal of the Association of Asphalt Paving Technologists*. 66: 1-30.

Brown, E.R., Mallick, R.B., Haddock, J.E., and Bukowski, J. (1997b). "Performance of Stone Matrix Asphalt (SMA) Mixtures in the United States." *Journal of Association of Asphalt Paving Technologists*. 66: 426-457.

Ministry of communications of PRC (2004a). "Specifications for Asphalt Highway Pavement Design (JTJ D50-2006)." *China Communication Press*, Beijing: 81-83.

Ministry of communications of PRC (2004b). "Specifications for Construction and Acceptance of Highway Asphalt Pavements (JTJF40-2004)." *China Communication Press*, Beijing: 79-93.

DEM Models of Idealized Asphalt Mixtures

Zhanping You[1], Sanjeev Adhikari[2] and Qingli Dai[3]

[1]Tomasini Assistant Professor, Department of Civil and Environmental Engineering, Michigan Technological University, 1400 Townsend Drive ,Houghton, MI, 49931-1295; zyou@mtu.edu
[2]Graduate Research Assistant, Department of Civil and Environmental Engineering, Michigan Technological University, 1400 Townsend Drive ,Houghton, MI, 49931-1295; sadhikar@mtu.edu
[3]Research Assistant Professor, Department of Mechanical Engineering-Engineering Mechanics, Michigan Technological University, 1400 Townsend Drive ,Houghton, MI, 49931-1295; qingdai@mtu.edu

ABSTRACT: The stiffness behavior of an idealized asphalt mixture at the different air void levels was investigated in this paper. The asphalt mixture was modeled with the discrete element modeling (DEM) approach by randomly generated air voids in two dimensions (2D) and three dimensions (3D). Air voids were calculated within the DEM model to meet the specific air void level (i.e. 4%, and 10%). Sixteen different 2D idealized models were generated with 4% and 10% air void levels. A 3D idealized model was generated using the 16 2D models. Then the 16 replicates of the 3D models were prepared with 4% and 10% air void levels. Both 2D and 3D models were used to compute the stress-strain response under compressive loads. The moduli of specimens were computed from the stress-strain curve. The result showed modulus decreased with air void increased. The 3D model predicted higher modulus than the 2D models. When air voids increased from 0% to 10%, the modulus decreased 30% on the 3D models and 48% on the 2D models. When comparing modulus prediction of 2D and 3D models, it was found that, at 0% air void level, the prediction was the same for both 3D and 2D. However, at 10% air void levels, 3D models yielded 26% higher modulus than the 2D models. It was found that the modulus deviation on the 3D models was much lower than the 2D models.

BACKGROUND OF MODELING ASPHALT MIXTURE

Asphalt mixture is a heterogeneous material and consists of aggregates, air voids, and asphalt binder. Air voids play an important role in determining the resistance of asphalt mixtures to major pavement distresses including rutting, fatigue cracking, and low temperature cracking. The effects of air voids on the mixture moduli are related to the asphalt mixture design, compaction, pavement structure design, and pavement performance. Therefore, the prediction of the moduli of asphalt mixtures at different air voids levels is an important topic.

The prediction of an asphalt mixture is based on the micromechanical model of mineral particles (coarse and fine aggregates, sand, and fines), binder and air voids. A number of research studies addressed micromechanical models with both non-interacting and interacting particles (Buttlar and You 2001; You and Dai 2007). Most of the existing micromechanical models greatly over- or under-predict the stiffness (or modulus) of asphalt mixtures (Buttlar and Dave 2005). This is due primarily to the inability of the models to properly predict the contribution of the aggregate interlock (i.e., lack of microstructure in the model) to the overall response of the mixture (You and Buttlar 2006). Therefore, microstructure based modeling techniques for asphalt mixture materials are needed to improve the understanding of the fundamental properties of asphalt mixtures and pavements.

In the past decades, the discrete element method has received considerable attention. The application of DEM was extended to many other fields such as the asphalt pavement (Chang and Meegoda 1997), clays (Yao and Anandarajah 2003), granular materials (Zeghal 2004), and tunnels (Melis Maynar and Medina Rodriguez 2005). Buttlar and You (2001) proposed a microfabric approach to model asphalt mixture using the discrete element methods, where various material phases (i.e., air voids, aggregates, and mastic) in the asphalt mixture were modeled with bonded clusters of discrete elements. You and Buttlar (2004) applied the microfabric discrete element modeling approach to predict the asphalt mixture complex modulus across a range of test temperatures and load frequencies. The 2D model had under-predicted the complex modulus. However, it was found that a calibration approach is needed to improve the 2D models or the 3D models are needed to be more representative of the actual 3D behavior. You and Buttlar (2004) applied a clustered DEM to simulate the hollow cylinder tensile (HCT) test, in which various material phases (e.g., aggregates and mastic) are modeled with bonded clusters of discrete elements. It was observed that the mixture complex moduli predicted in the HCT simulations were in good agreement with experimental measurements across a range of test temperatures and loading frequencies for the coarse-grained mixtures.

In this paper, the 2D and 3D micromechanical discrete element models were developed to simulate and characterize the modulus of an idealized asphalt mixture. The asphalt mixture models used in this study are limited to idealized "mixture," which is modeled as a homogenous material (including aggregate and asphalt binder phases) with randomly distributed air voids. Therefore, the aggregate and asphalt phases are not modeled separately in this paper. The discrete element models utilized in this study used the disks, or balls (spheres) to represent the microstructure of the idealized mixture with air voids. The 2D discrete element model is used to characterize the mixture moduli at different air voids. Then, the 3D discrete element model was generated with a number of layered 2D discrete element models. The major challenges included the modeling of the 3D microstructure and air void consideration in the models.

PREPARATION OF THE IDEALIZED DISCRETE ELEMENT MODELS

In order to examine the stiffness behavior of an idealized asphalt mixture, 2D and 3D discrete element models were used to predict mixture moduli of asphalt mixture at different air voids. The 3D model was generated by using a number of 2D discrete element models. Both 2D and 3D were generated by using face-centered packing balls/spheres.

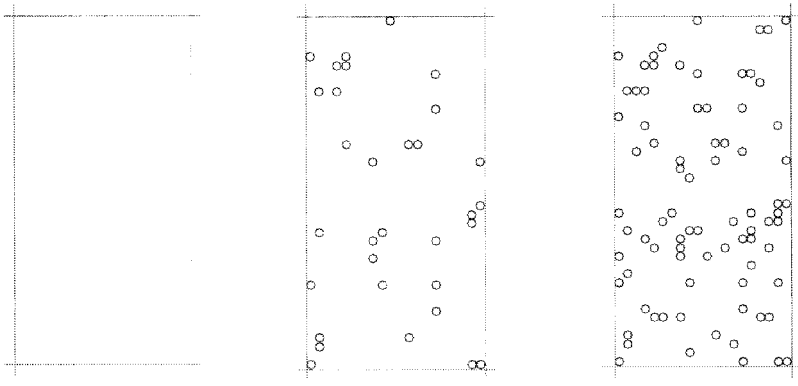

Air Void = 0% **Air Void = 4%** **Air Void = 10%**

FIG. 1. Air void distribution in 2D models.

The 2D idealized discrete element model was generated with a rectangular specimen, which has a height of 80mm (0.08m) and a width of 40mm (0.04m). The radius of each ball (i.e. disk or discrete element) is 1mm. Therefore, there are 800 total balls in the idealized asphalt specimen without air voids. Then, air voids were introduced at 4% and 10% of total volume. When air voids were increased, the total number of balls was decreased. Fig. 1 shows 4% and 10% air void distribution. In order to examine the effect of different air void distribution, 16 replicates of air void distribution were prepared. Fig. 2 shows 16 randomly generated air voids with black color.

The 3D idealized asphalt mixture was generated with a rectangular prism specimen, which has a height of 80mm (0.08m), a length 40mm (0.04m) and a width of 32mm (0.032m). The rectangular prism was generated using sixteen 2D models. The radius of the ball is 1mm. Therefore, there are 12,800 balls in this idealized specimen without air voids. The air voids were introduced at 4% and 10% of total volume. 16 different 3D specimens at a specific air void level were randomly prepared to represent the idealized asphalt mixture. Fig. 2 shows the idealized rectangular prism specimen with 4% air voids. The figure shows the air void distribution (in a different color) in the idealized mixture specimens in 3D space. In order to provide a better

visual effect, the air void distribution within the 3D space is given without the mix elements. It should be noted that the air voids were randomly distributed in the 3D space by randomly layering the 2D models together.

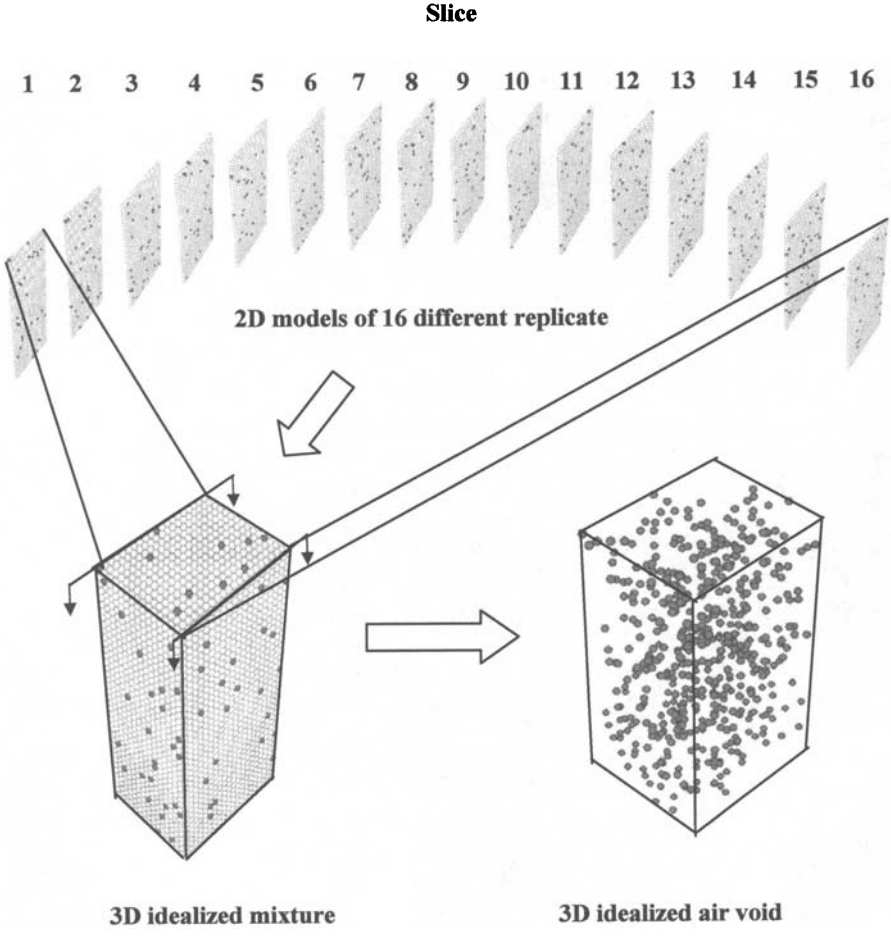

FIG. 2. Illustration of the creation of the 3D model from the 2D models using 4% air voids.

SIMULATION OF THE COMPRESSION TEST

The idealized DEM model was simulated on a compression test by confining the stress environment. Four walls were used for the 2D models and six walls were used the for 3D models. The walls were made longer than necessary to allow for large

amounts of strain to occur during the test. Walls interact with balls, not with one another. The axial compressive force was applied to the top of the specimen with constant speed. 2D specimens are computed by biaxial test and 3D specimens are computed by triaxial compression test. The simple stiffness model was used as a contact model in this study. The stiffness model is an elastic relationship between the contact force and relative displacement between particles. The specimen is loaded by specifying constant velocities on the top and bottom walls and the stress is computed by taking the average wall forces and dividing by appropriate areas. The modulus was computed from the plots of axial deviator stress (i.e., the difference between axial stress and confine stress) versus axial strain (You and Buttlar 2006).

RESULTS OF THE 2D AND 3D DISCRETE ELEMENT MODELS

The modulus of the idealized mixture was predicted under different air void levels. Fig. 3 shows the modulus prediction of the 2D and 3D mixtures of different air void levels. It includes one model without air void, 16 models with 4% air voids, and 16 models with 10% air voids. At each air void level (except 0%), 16 different specimens were prepared with random air voids. From Fig. 3, it is clear that the modulus prediction decreases with increasing air void levels. For a single air void level, each random air void distribution yields a different modulus. When the air void level is higher, then the modulus has more variation. The results of the study have indicated that the coefficient of variance (COV, the percentage of the standard deviation over the mean) increases with the air void level. The results explain that the asphalt mixtures from the field or laboratory usually have a larger deviation in strength and modulus at higher air voids.

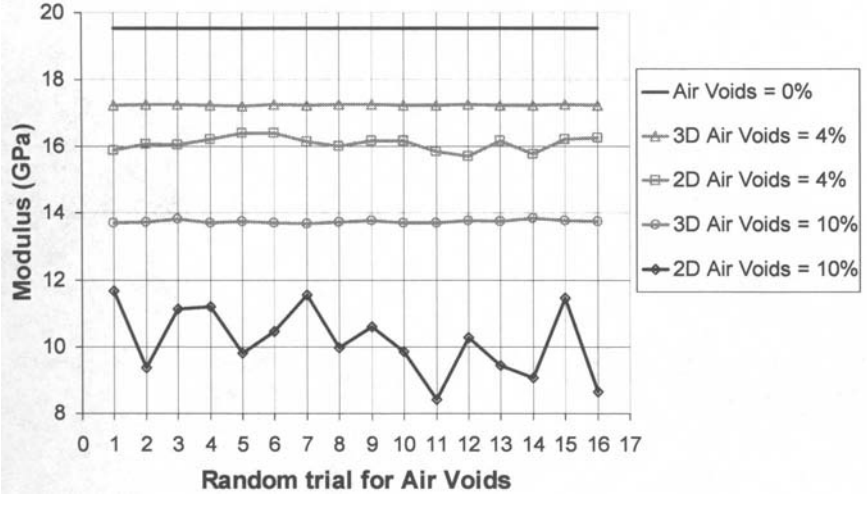

FIG. 3. Idealized mixtures modulus using 16 randomly generated specimens with different air void levels.

When comparing the prediction results of the 2D and 3D, as shown in Fig. 4, it was found that the 3D model predicts a higher modulus than a 2D model. The modulus difference between 2D and 3D increased with the air void level. For example, both 3D and 2D models yield a modulus of 19.55GPa at a 0% air void level. 3D models predicted an average of 17.24GPa while the 2D models predicted 16.09 at a 4% air void level. 3D models yield an average modulus of 13.74GPa compared with the 2D models' 10.19GPa at a 10% air void level. When the air void increased from 0% to 10%, the modulus decreased 30% in the 3D models, compared with 48% in 2D models. Therefore, when the air voids are larger, the 2D mixture modulus prediction is less reliable than that of the 3D models.

In both 2D and 3D predictions, it was found that the larger the air void level, the more the variation of the modulus prediction. However, the variation of 3D models is relatively small in comparison to that of the 2D models. Fig. 5 shows the difference of the COV of the modulus prediction from 2D and 3D models. The 3D models have a COV of 0.08% while 2D models have a COV of 1.27% at a 4% air void level. At a 10% air void level, 3D models have a COV of 0.33% and 2D models have a 10.21% COV. The data indicate that a 2D prediction usually yields inconsistent results compared with those of 3D.

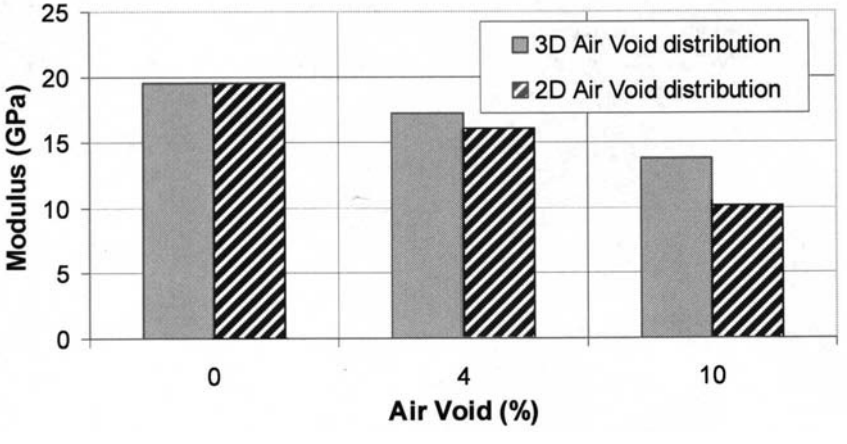

FIG. 4. 3D and 2D mixture modulus Comparison for 0%, 4% and 10% air void levels.

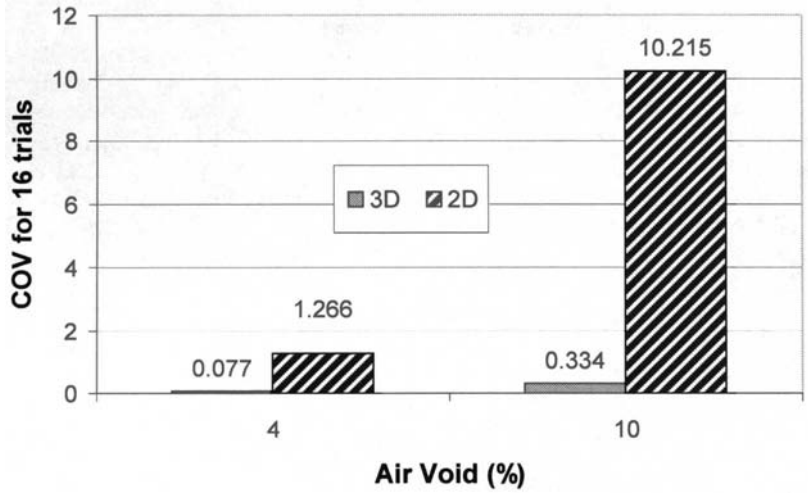

FIG. 5. The coefficient of variation of the modulus prediction from 2D and 3D simulations.

SUMMARY AND CONCLUSIONS

The idealized asphalt mixture was modeled with 2D and 3D discrete element approaches. The effect of air void content and the distribution of air voids for specific air void level were studied. The air voids in the models were randomly generated within the models to reach a specific air void level. The 2D and 3D models were computed by using compressive load to calculate the moduli of the specimen, which were derived from the stress-strain curve. It was found that modulus prediction decreased with increasing air void levels. When comparing the modulus predictions from the 2D and 3D models, it was found that the 3D models yielded higher modulus than the 2D models. The modulus difference between 2D and 3D was increased with air void levels. The average of the predicted modulus difference was 26% at 10% air voids. The COV from different randomly generated 2D models were much larger compared with the 3D models. The results indicate that 3D predictions were more consistent than those of 2D. The 2D models under-predict the mixture modulus, especially when the air void level is high.

ACKNOWLEDGEMENT

This material is based in part upon work supported by the National Science Foundation under Grant CMMI 0701264. The financial support is appreciated.

REFERENCES

Buttlar, W. G., and Dave, E. V. (2005). "A Micromechanics-Based Approach for Determining Presence and Amount of Recycled Asphalt Pavement Material in Asphalt Concrete (With Discussion)." *2005 Journal of the Association of Asphalt Paving Technologists: From the Proceedings of the Technical Sessions*, 74, 829-884.

Buttlar, W. G., and You, Z. (2001). "Discrete element modeling of asphalt concrete: Microfabric approach." *Transportation Research Record*, 1757, 111-118.

Chang, G. K., and Meegoda, J. N. (1997). "Micromechanical Simulation of Hot Mixture Asphalt." *ASCE J. Engng. Mech.*, 123(5), 495-503.

Melis Maynar, M. J., and Medina Rodriguez, L. E. (2005). "Discrete Numerical Model for Analysis of Earth Pressure Balance Tunnel Excavation." 131, 1234-1242.

Yao, M., and Anandarajah, A. (2003). "Three-dimensional discrete element method of analysis of clays." 129, 585-596.

You, Z., and Buttlar, W. G. (2004). "Discrete Element Modeling to Predict the Modulus of Asphalt Concrete Mixtures." *Journal of Materials in Civil Engineering, ASCE*, 16(2), 140-146.

You, Z., and Buttlar, W. G. (2006). "Micromechanical Modeling Approach to Predict Compressive Dynamic Moduli of Asphalt Mixture Using the Distinct Element Method." *Transportation Research Record: Journal of the Transportation Research Board, National Research Council, Washington, D.C.*, 1970, 73-83.

You, Z., and Dai, Q. (2007). "A Review of Advances in Micromechanical Modeling of Aggregate-Aggregate Interaction in Asphalt Mixture." *Canadian Journal of Civil Engineering* 34(2), 239-252.

Zeghal, M. (2004). "Discrete-element method investigation of the resilient behavior of granular materials." 130, 503-509.

Responses of a Transversely Isotropic Layered Half-Space to Multiple Horizontal Loads

Ewan Y.G. Chen[1] and Ernie Pan[2], M. ASCE

[1]Graduate Student, The Department of Civil Engineering, University of Akron, Akron, OH 44325-3905; yc39@uakron.edu
[2]Associate Professor, The Department of Civil Engineering and The Department of Applied Mathematics, University of Akron, Akron, OH 44325-3905; pan2@uakron.edu

ABSTRACT: In this work, the displacements and stresses at any point in a transversely isotropic layered half-space under multiple horizontal loads are studied. The transversely isotropic plane is assumed to be parallel to the surface plane, and uniformly distributed circular loads with different magnitudes, radii and orientations are applied to the pavement surface. Based on the cylindrical system of vector functions in the transformed domain, the governing equations are first decoupled into two sets of equations related to the *LM*-type and *N*-type respectively. Solutions for the multilayered half-space in the transformed domain are then derived by virtue of the propagator matrix method. Solutions in the physical domain are then expressed in terms of the Bessel function integration. The method of superposition is finally utilized for multiple loads. We remark that while the propagator matrix method has been frequently used to solve the vertical loading problem in layered half-spaces, which only involve the *LM*-type equation, the corresponding horizontal loading problem involving multiple circular loads in a transversely isotropic layered half-space has not been addressed in the literature. A computer program has been coded by the authors' research group and numerical results obtained from this program for the isotropic layered half-space have been verified with existing ones. Further presented in this paper are the results for the transversely isotropic layered half-space, with examples elucidating clearly the effect of material anisotropy on the responses, especially on pavement failure. It is also observed that, in terms of computation, the developed program is very accurate, efficient and flexible. For instance, our program can easily handle more than 10,000 field points with more than 1,000 pavement layers.

INTRODUCTION

The Kelvin solution (e.g., Love 1927) for the concentrated load acting in an infinite solid is well known, and many problems of science and engineering importance can be obtained from this fundamental solution. The classical Boussinesq solution (e.g., Love 1927) dealing with a vertical force applied at the surface of a semi-infinite solid has found a number of practical applications in foundation engineering, pavement engineering, et al. While the Cerruti solution (e.g., Love 1927)) is for the problem of a horizontal force applied at the surface of a half-space, the Mindlin solution (Mindlin, 1936) is to solve the problem with the point load in the interior of the half-space. The Mindlin solution can easily be deduced to the other three classical solutions mentioned above. It should be mentioned that all these classical solutions are for the point load and homogenous material.

By integrating solutions of the concentrated load over the loading domain, solution for the case of a uniformly distributed load within a circle can be arrived. However, this solution cannot be extended to the multi-layered structure. Burmister (1943, 1945) pioneered the analytical solutions using layered elastic theory, first for a two-layered pavement and later for a three-layered pavement. It should be noticed that a lot of research for multi-layered structures are focused on the vertical loads, an extension of the Boussinesq problem, whilst the research for the responses of a layered half-space structure to the horizontal load is usually omitted. For example, in the pavement engineering, the vehicle load acting on the pavement surface is usually modeled as a vertical load, omitting the horizontal load in practice, such as the friction force between the tire of the vehicle and pavement surface.

Among the few studies closely related to horizontal loads, Wang (1983) proposed a method, named recursion and back-substitution, and discussed the solution of layered elasticity under vertical and horizontal loads. Pan (1989a) proposed the special vector function to deal with the problem of isotropic layered half-space structure under single load, either vertically or horizontally. Pan (1989b) then introduced two sets of vector functions in both the cylindrical and Cartesian coordinates and derived the general formalism for the transversely isotropic layered half-space under general loads. It should be mentioned that for the layered structure problem, the solutions are extremely complicated as compared to the classical Boussinesq and Cerruti solutions. Thus only single vertical and horizontal load was considered. Later on, Pan (1997) proposed the static Green's functions in the multilayered transversely isotropic half-space, and displacement and stress fields under vertical and horizontal point load were presented and compared. An independent work was presented by Yue and Yin (1998) dealing with similar problems. Matsui et al. (2002) used Hankle transform and biharmonic function to deal with the problem of layered isotropic half-space structure under multiple horizontal loads, and developed a program named Analysis of Multi-layered Elastic Structure (AMES) based on their method.

The goal of this research is, therefore, to discuss in detail the problem of horizontal loading on a multi-layered pavement surface based on the vector functions introduced by Pan (1989b), and to develop a computer program for analyzing the responses of a multilayered pavement system by the horizontal load. By expressing the governing equations in the cylindrical system of vector functions, the original coupling

equations can be decoupled into two types of equations in terms of the vector functions, and solutions can be obtained in the form of integration of Bessel function, including first kind of zero and first orders. In addition, the propagator matrix method is utilized to deal with the layered half-space structure. The principle of superposition thereafter is adopted for multiple loads, and thus the final solutions for transversely isotropic layered half-space structure to multiple loads are established.

A computer program, which is the extension of *MultiSmart3D* coded by the authors' research group (Pan et al. 2007), was generated and numerical results for the isotropic layered half-space were compared with existing ones to demonstrate the accuracy of this method. Also presented are the numerical results for a transversely isotropic layered half-space with examples elucidating clearly the effect of material anisotropy on the pavement response.

GENERAL SOLUTIONS

The transversely isotropic layered half-space is first modeled as in Fig. 1, where the z-axis is positive downward, and the isotropic plane is chosen to be parallel to the horizontal plane. In this model, there are p layers lying on the homogeneous half-space with h_i (i=1, 2... p) being the layer thickness, and H the total thickness above the half-space. The uniform horizontal load acting on the surface z=0. The load configuration is presented in Fig. 2, where X-Y is the global coordinate and P_f is the horizontal projection of the field point z_f. The local coordinate x-y is also chosen with x along the loading direction, and α, β the orientations of the horizontal load and field point to x-axis, respectively.

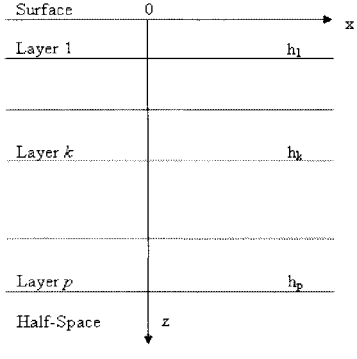

FIG. 1. Geometry of a transversely isotropic multilayered half-space.

By introducing the vector functions in the cylindrical coordinates as in Pan (1989b), the displacement and traction vectors can be expressed as:

$$\boldsymbol{u}(r,\theta,z) = u_r\boldsymbol{r} + u_{\theta\theta}\boldsymbol{\theta} + u_{zz}\boldsymbol{z}$$
$$= \sum_m \int_0^{+\infty} [U_L(z)\boldsymbol{L}(r,\theta) + U_M(z)\boldsymbol{M}(r,\theta) + U_N(z)\boldsymbol{N}(r,\theta)]\lambda d\lambda \quad (1)$$

$$\boldsymbol{t}(r,\theta,z) = \sigma_{rz}\boldsymbol{r} + \sigma_{\theta z}\boldsymbol{\theta} + \sigma_{zz}\boldsymbol{z}$$
$$= \sum_m \int_0^{+\infty} [T_L(z)\boldsymbol{L}(r,\theta) + T_M(z)\boldsymbol{M}(r,\theta) + T_N(z)\boldsymbol{N}(r,\theta)]\lambda d\lambda \quad (2)$$

where $\boldsymbol{r}$,$\boldsymbol{\theta}$, $\boldsymbol{z}$ are unit vectors along the r-,θ-, z- directions, and

$\boldsymbol{L}(r,\theta;\lambda,m) = \boldsymbol{z}S(r,\theta;\lambda,m)$

$\boldsymbol{M}(r,\theta;\lambda,m) = grad(S) = \boldsymbol{r}\partial S/\partial r + \boldsymbol{\theta}\partial S/(r\partial\theta)$

$\boldsymbol{N}(r,\theta;\lambda,m) = curl(\boldsymbol{z}S) = \boldsymbol{r}\partial S/\partial r - \boldsymbol{\theta}\partial S/(r\partial\theta)$

are vector functions with $S(r,\theta;\lambda,m) = J_m(\lambda r)\exp(im\theta)/(2\pi)^{1/2}$. $J_m(\lambda r)$ is the Bessel function of order m.

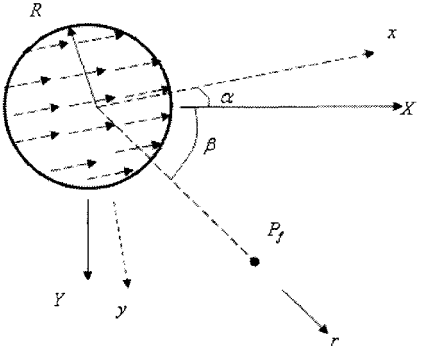

FIG. 2. Geometry of surface loading.

It is noted that for any integrable vector $\boldsymbol{F}$ in the physical domain, its expansion coefficients in the vector function system can be found from the following relations:

$$F_L(\lambda,z) = \frac{2}{\delta_m}\int_0^{2\pi}\int_0^{\infty} \boldsymbol{F}\bullet\boldsymbol{L}^* r dr d\theta$$

$$F_M(\lambda,z) = \frac{2}{\delta_m\lambda^2}\int_0^{2\pi}\int_0^{\infty} \boldsymbol{F}\bullet\boldsymbol{M}^* r dr d\theta \quad (3)$$

$$F_N(\lambda,z) = \frac{2}{\delta_m\lambda^2}\int_0^{2\pi}\int_0^{\infty} \boldsymbol{F}\bullet\boldsymbol{N}^* r dr d\theta$$

where:

$$\delta_m = \begin{cases} 2 & m = 0 \\ 1 & m = 1,2,3,\ldots \end{cases}$$

and the vectors $\boldsymbol{L}^*$,$\boldsymbol{M}^*$,$\boldsymbol{N}^*$ are the complex conjugates of $\boldsymbol{L}$,$\boldsymbol{M}$,$\boldsymbol{N}$.

Thus, using the vector functions a relationship between the physical domain $\boldsymbol{F}(r,\theta,z)$ and transformed domain $\boldsymbol{F}_T(\lambda,z)(T=L,M,N)$ is established. Then the physical domain problem can be first solved in the transformed domain, which is more convenient as will be shown below.

After certain manipulation, the solutions in any layer in terms of the vector functions can be obtained

$$[E^{LM}(z)]_{4\times1} = [Z^{LM}(z)]_{4\times4}[K^{LM}]_{4\times1}$$
$$[E^{N}(z)]_{2\times1} = [Z^{N}(z)]_{2\times1}[K^{N}]_{2\times1} \tag{4}$$

where

$$[E^{LM}(z)] = [U_L \quad \lambda U_M \quad T_L/\lambda \quad T_M]^T$$
$$[E^{N}(z)] = [\lambda U_N \quad T_N]^T$$

and the two column matrices $[K]$ are λ-dependent. The expressions for $[Z]$ are listed in Pan (1989b). As can be seen from (4) that, using the vector functions, the coupled 6×6 equations in the physical domain are decoupled into two sets of equations, called *LM*-type and *N*-type equations. It should be addressed here that these two sets of equations are independent of each other with a dimension of 4×4 and 2×2, respectively, and thus are computational convenient and efficient.

To solve the multilayered pavement, the propagator matrix method is employed. The propagating relations in the k-th layer with the interfaces z_{k-1} and z_k can be expressed as

$$[E^{LM}(z_{k-1})] = [a_k^{LM}][E^{LM}(z_k)]$$
$$[E^{N}(z_{k-1})] = [a_k^{N}][E^{N}(z_k)] \tag{5}$$

where $[a_k]$ is the propagator matrix and its elements are listed in Pan (1989b). Assuming that the displacement and traction vectors across the layer interface are continuous, solutions for an arbitrary field point can then be expressed as

$$[E^{LM}(z)]_{4\times1} = [G^{LM}(z)]_{4\times4}[K_{p+1}^{LM}]_{4\times1}$$
$$[E^{N}(z)]_{2\times1} = [G^{N}(z)]_{2\times4}[K_{p+1}^{N}]_{2\times1} \tag{6}$$

where $[G(z)]=[a_{fk}][a_{k+1}]\ldots[a_{p-1}][a_p][Z_n(H)]$ with $[a_{fk}]$ being the propagator matrix from field point z_f to the layer interface z_k and $[K_{p+1}]$ being the unknown column matrix in the homogeneous half-space.

In the cylindrical coordinate (Fig. 2), the boundary conditions in the physical domain are

$$\boldsymbol{t}(r,\theta,0) = \sigma_{rz}(r,\theta,0)\boldsymbol{r} + \sigma_{\theta z}(r,\theta,0)\boldsymbol{\theta} + \sigma_{zz}(r,\theta,0)\boldsymbol{z} \tag{7}$$

where for $0 \le \theta \le 2\pi$,

$$\sigma_{rz}(r,\theta,0) = q\cos\theta \qquad 0 \le r \le R$$
$$\sigma_{\theta z}(r,\theta,0) = -q\sin\theta \qquad 0 \le r \le R \tag{8}$$
$$\sigma_{zz}(r,\theta,0) = 0 \qquad 0 \le r < \infty$$

By virtue of (3), the corresponding boundary conditions in the transformed domain are

$$T_L(\lambda,0) = 0$$
$$T_M(\lambda,0) = \sqrt{2\pi}\frac{qR}{\lambda^2}J_1(R\lambda) \tag{9}$$
$$T_N(\lambda,0) = -i\sqrt{2\pi}\frac{qR}{\lambda^2}J_1(R\lambda)$$

Using the boundary condition on the surface, the solutions in the transformed

domain can be obtained, and then the solutions in physical domain can be arrived. The final solutions are the real part of the following expressions:

$$u_r(r,\theta,z) = e^{i\theta}[UT(1) - UT(2) + iUTN(1)]$$

$$u_\theta(r,\theta,z) = e^{i\theta}[iUT(2) - UTN(2) + UTN(1)]$$

$$u_z(r,\theta,z) = e^{i\theta}[UT(3)]$$

$$\sigma_{rz}(r,\theta,z) = e^{i\theta}[UT(4) - UT(5) + iUTN(3)]$$

$$\sigma_{\theta z}(r,\theta,z) = e^{i\theta}[iUT(5) - UTN(4) + UTN(3)]$$

$$\sigma_{zz}(r,\theta,z) = e^{i\theta}[UT(6)] \tag{10}$$

$$\sigma_{r\theta}(r,\theta,z) = e^{i\theta}A_{66}\{UTN(5) + 2[UTN(2) - 2UTN(1)]/r + 2i[UT(1) - 2UT(2)]/r\}$$

$$\sigma_{rr}(r,\theta,z) = e^{i\theta}\{A_{13}\sigma_{zz}/A_{33} + i(A_{11} - A_{12})[UTN(2) - 2UTN(1)]/r + (A_{13}^2 - A_{11}A_{33})UT(7)/A_{33} - (A_{11} - A_{12})[UT(1) - 2UT(2)]/r\}$$

$$\sigma_{\theta\theta}(r,\theta,z) = e^{i\theta}\{A_{13}\sigma_{zz}/A_{33} - i(A_{11} - A_{12})[UTN(2) - 2UTN(1)]/r + (A_{13}^2 - A_{12}A_{33})UT(7)/A_{33} + (A_{11} - A_{12})[UT(1) - 2UT(2)]/r\}$$

where, $UT(i)(i=1,2,\ldots 7)$ and $UTN(i)(i=1,2,\ldots 5)$ are listed in Appendix I. It should be stressed that the *UT*s are related to *LM*-type whilst *UTN*s to *N*-type.

Based on the above solutions for single loads, coordinate transform is first applied to convert the solutions from local coordinates to global coordinates, and the superposition principle is then employed to derive the final solutions in the global Cartesian coordinates, which are expressed as

$$\begin{Bmatrix} u_x(P_f) \\ u_x(P_f) \\ u_z(P_f) \end{Bmatrix} = \sum_{i=1}^{N} \left[S^i\right]^T \begin{Bmatrix} u_r(P_f) \\ u_\theta(P_f) \\ u_z(P_f) \end{Bmatrix}^i \tag{11}$$

for displacements and

$$\begin{bmatrix} \sigma_{xx} & \sigma_{xy} & \sigma_{xz} \\ & \sigma_{yy} & \sigma_{yz} \\ & & \sigma_{zz} \end{bmatrix} = \sum_{i=1}^{N} \left[S^i\right]^T \begin{bmatrix} \sigma_{rr} & \sigma_{r\theta} & \sigma_{rz} \\ & \sigma_{\theta\theta} & \sigma_{\theta z} \\ & & \sigma_{zz} \end{bmatrix}^i \left[S^i\right] \tag{12}$$

for stresses with

$$[S] = \begin{bmatrix} \cos(\beta) & \sin(\beta) & 0 \\ -\sin(\beta) & \cos(\beta) & 0 \\ & & 1 \end{bmatrix}$$

In (11) and (12), the superscript i means the contribution of the i-th load.

NUMERICAL SOLUTIONS

The solutions in the physical domain using vector functions are in the form of Bessel function integration which requires numerical computation. The infinite integration can be approximated as the summation of partial integration as

$$\int_0^{+\infty} f(\lambda,z)J_m(\lambda r)d\lambda = \sum_{n=1}^{N} \int_{\lambda_n}^{\lambda_{n+1}} f(\lambda,z)J_m(\lambda r)d\lambda. \tag{13}$$

The accuracy of the partial integration can be controlled by the pre-chosen error tolerance and satisfactory result can usually be achieved by balancing the time cost and accuracy. In this paper, the error tolerance is fixed at 10^{-4} for the relative error and 10^{-5} for the absolute error. To deal with the possible overflow problem caused by multiplication of propagator matrices, the forward and backward propagating approaches proposed by Pan (1997) and later by Yue and Yin (1998) are also adopted here.

Verification of Results

An example dealing with a three-layered half-space pavement presented in Matsui et al. (2002) is given first to verify the present formulation. The pavement parameters are:

$$\begin{aligned} &E_1=2500\text{MPa},\ \nu_1=0.35,\ h_1=0.1\text{m} \\ &E_2=280\text{MPa},\ \nu_2=0.35,\ h_2=0.35\text{m} \\ &E_3=50\text{MPa},\ \nu_3=0.4 \end{aligned} \tag{14}$$

In this example, two horizontal loading cases are considered. The first one is a single circular uniform load with Q=49kN and R=0.15m; the second one is double circular uniform loads with $Q_1=Q_2$=49kN, $R_1=R_2$=0.15m, O_1(0,–0.15,0)m, O_2(0,0.15,0)m, $\alpha_1=-\pi/6$, $\alpha_2=\pi/6$, where Q, R, O, α are load magnitude, load radius, load center and load direction, respectively.

Numerical results of displacements and stresses using present formulations and those using BISAR under both single and double horizontal circular loads are presented in Fig. 3 and Fig. 4, respectively. It is clearly observed that present results agree very well with those by BISAR, which therefore provides an indirect verification to our program.

Effect of Horizontal Load

Figs. 5 and 6 show the strain contour of the pavement under vertical and horizontal loads. The horizontal and vertical strains are computed at depth z=0.0999m (within the first layer) and z=0.4501m (within the half-space substrate, i.e., in the third layer), respectively. The pavement structure is still the one used in previous section as in (14). It is evident that the strains under the two kinds of loads are quite different. Under the vertical load in Fig. 5, the strains are symmetric with respect to both x- and y-axes, and ε_{xx} and ε_{yy} are identical to each other after $\pi/2$ rotation. Under the horizontal load in Fig.6, on the other hand, the strains are anti-symmetric with respect to y-axis and symmetric to x-axis. The locations of the maximum strains and the corresponding magnitudes also change greatly. For example, under the same configuration, for the vertical load case the maximum horizontal tensile strains are $\varepsilon_{xx}=3.3\times10^{-4}$, $\varepsilon_{yy}=3.3\times10^{-4}$, and vertical compressive strain is $\varepsilon_{zz}=-7.42\times10^{-4}$, all located at (x,y)=(0,0), whilst under the horizontal load the corresponding strains are $\varepsilon_{xx}=1.33\times10^{-4}$ at about (0.30m,0), $\varepsilon_{yy}=1.36\times10^{-4}$ at about (–0.18m,0), and $\varepsilon_{zz}=-1.34\times10^{-4}$ at (0.25m,0).

Table 1 predicts the effect of the horizontal load on the maximum strains, where b

is the ratio of the horizontal load to vertical load. To predict the fatigue and rutting performance, the following model (Timm and Newcomb, 2006) is used:

$$N_f = 2.83\times10^{-6}\left(\frac{10^6}{\varepsilon_t}\right)^{3.148} \tag{15}$$

$$N_r = 1\times10^{16}\left(\frac{1}{\varepsilon_v}\right)^{3.87} \tag{16}$$

where

N_f = number of cycles until fatigue failure;

N_r = number of cycles until rutting failure;

ε_t = critical horizontal tensile strain at bottom of asphalt layer;

ε_v = critical vertical compressive strain at top of subgrade layer.

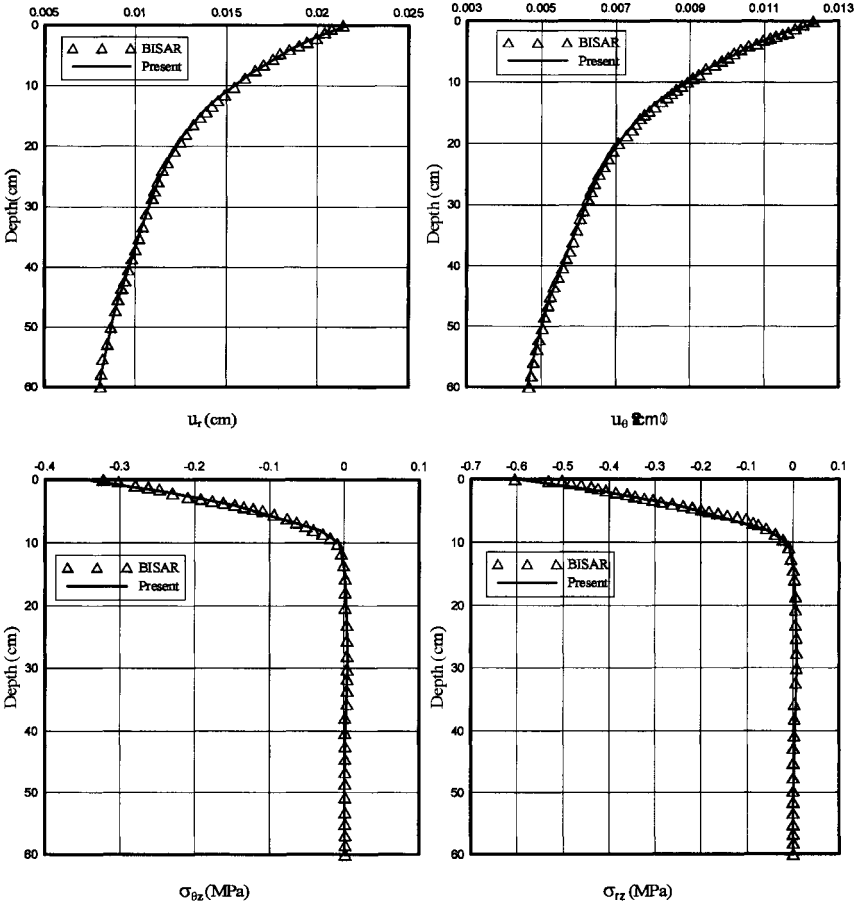

FIG. 3. Comparison of present work and BISAR (single load).

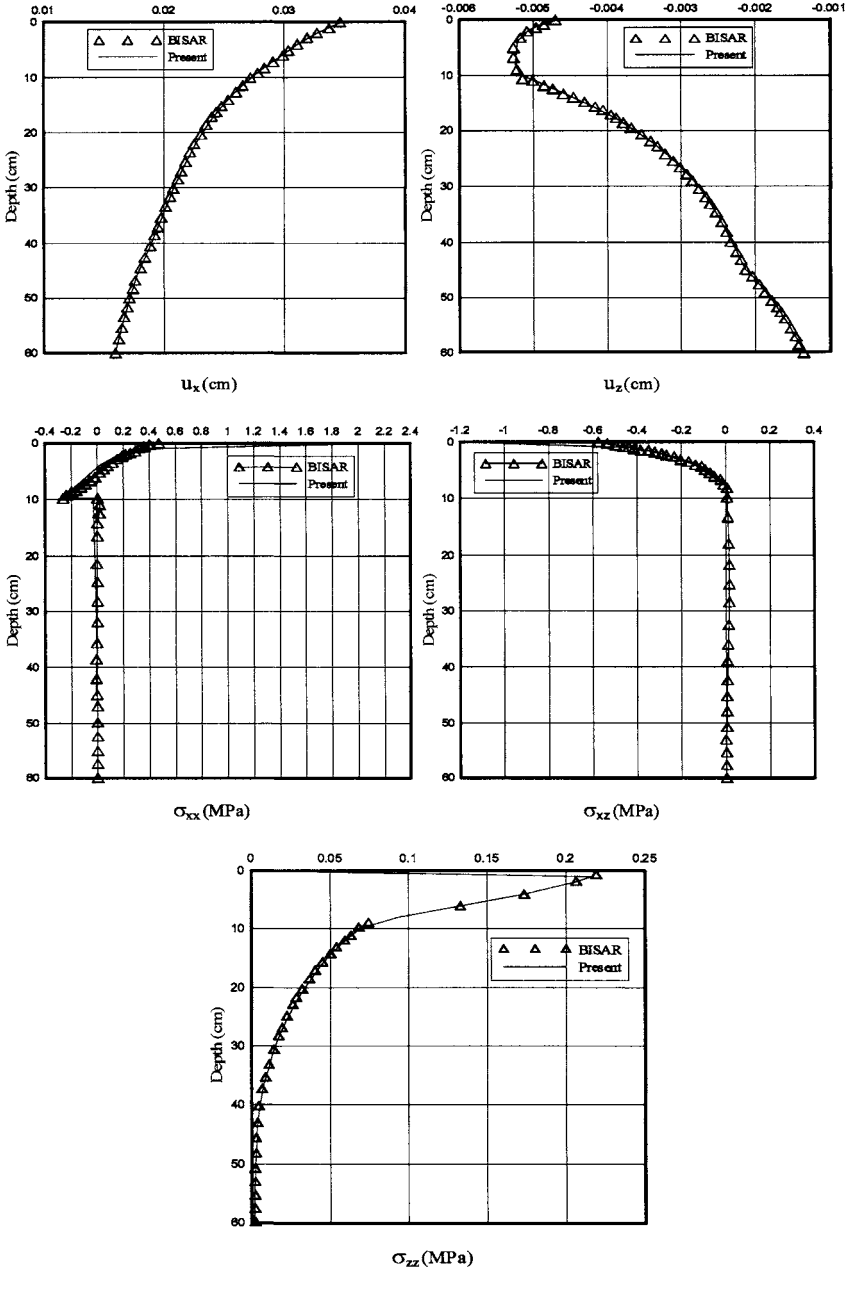

FIG. 4. Comparison of present work and BISAR (double loads).

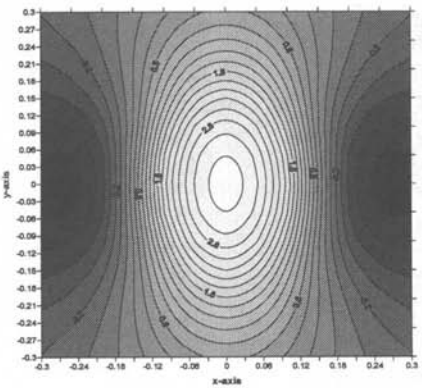

5a. ε_{xx} ($\times 10^{-4}$, at z=0.0999m)

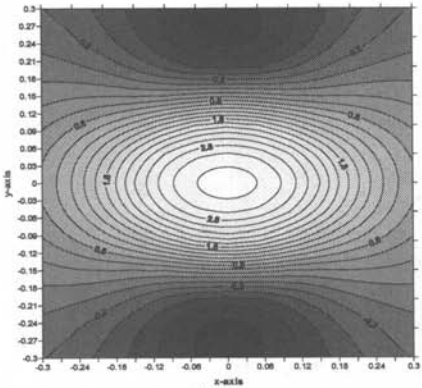

5b. ε_{yy} ($\times 10^{-4}$, at z=0.0999m)

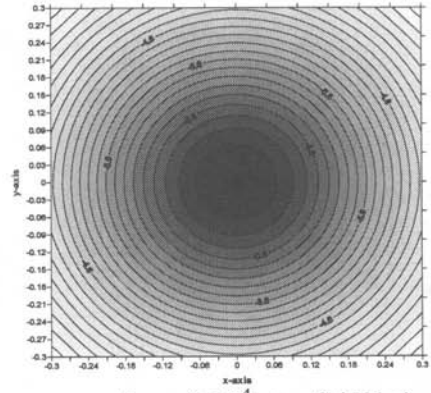

5c. ε_{zz} ($\times 10^{-4}$, at z=0.4501m)

FIG. 5. Vertical loading.

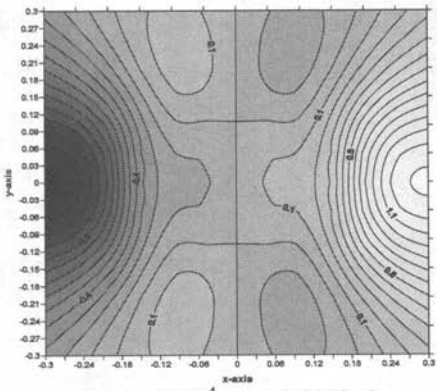

6a. ε_{xx} ($\times 10^{-4}$, at z=0.0999m)

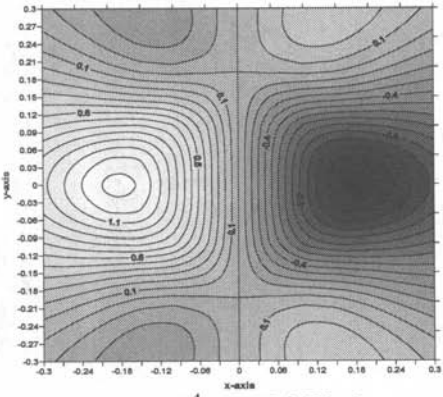

6b. ε_{yy} ($\times 10^{-4}$, at z=0.0999m)

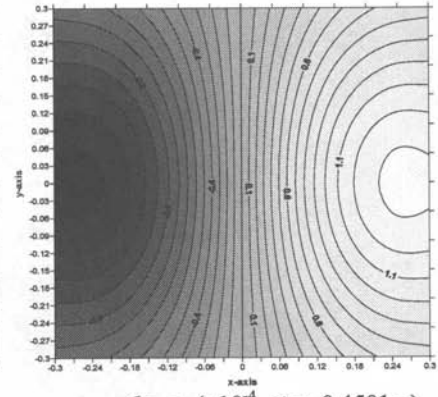

6c. ε_{zz} ($\times 10^{-4}$, at z=0.4501m)

FIG. 6. Horizontal loading.

Table 1. The Effect of Horizontal Load on Fatigue and Rutting Performance

	Fatigue				Rutting	
	ε_{xx} ($\times 10^{-4}$)	ε_{yy} ($\times 10^{-4}$)	ε_t ($\times 10^{-4}$)	N_f($\times 10^{24}$)	ε_v ($\times 10^{-4}$)	N_r($\times 10^{28}$)
b=0	3.3	3.3	3.3	1.9929	-7.4	1.3064
b=0.25	3.4	3.4	3.4	1.8142	-7.6	1.1783
b=1	3.4	4.0	4.0	1.0877	-7.8	1.0660

As can be seen from Table 1, with increasing b, the maximum strains increase, leading to the decrease of N_f and N_r. Thus horizontal load could reduce the fatigue and rutting lifetime. Consequently, ignoring horizontal load would overestimate the failure performance. It also can be observed that the effect of the horizontal load on fatigue is severer than that on rutting. For example, consideration of the horizontal load (e.g. b=1) will reduce a lifetime about 45.42% for fatigue and 18.40% for rutting as compared to the estimation without the horizontal load (e.g. b=0).

Effect of Material Anisotropy

To investigate the effect of pavement anisotropy, Fig. 7 presents the strain contours at depth z=0.0999m for different transversely isotropic pavements (Table 2) under the horizontal load. As mentioned above, the horizontal load would greatly influence fatigue performance which is controlled by the horizontal strain. Thus in Fig. 7 only horizontal strains ε_{xx}, ε_{yy} are presented. It is also noted that for the seven transverse isotropy configurations in Table 2, Case 1 is actually isotropic with the results already being shown in Figs. 6a and 6b. The maximum strains for the seven different cases are also presented in Table 2. The material property definitions in Table 2 are: E and E' are the Young's moduli in the plane of isotropy and in the direction normal to it, respectively; ν and ν' are the Poisson's ratios characterizing the lateral strain responses in the plane of isotropy to a stress acting parallel or normal to it, respectively; G' is the shear modulus in planes normal to the plane of isotropy, and $G=E/2(1+\nu)$. The pavement is again a three-layered structure. However, the material property in each layer is now transversely isotropic. More specifically, the Young's modulus E and Poisson's ratio ν in the first, second and third layers are the same as those listed in (14), and the corresponding $E'$and ν' in each layer are determined using Table 2 for different cases.

Table 2. The Effect of Anisotropy on Fatigue

	E/E'	G/G'	ν/ν'	ε_{xx} ($\times 10^{-4}$)	ε_{yy} ($\times 10^{-4}$)	ε_t ($\times 10^{-4}$)
Case 1	1.0	1.0	1.0	1.4	1.4	1.4
Case 2	1.0	2.0	1.0	1.2	1.3	1.3
Case 3	1.0	3.0	1.0	1.0	1.2	1.2
Case 4	1.5	1.0	1.0	1.3	1.5	1.5
Case 5	3.0	1.0	1.0	1.2	1.8	1.8
Case 6	1.0	1.0	0.75	1.4	1.4	1.4
Case 7	1.0	1.0	1.5	1.4	1.3	1.4

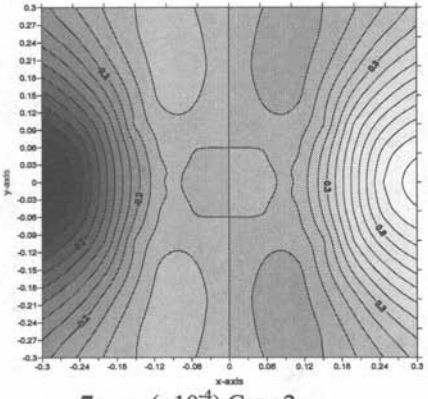

7a. ε_{xx} ($\times 10^{-4}$) Case 2.

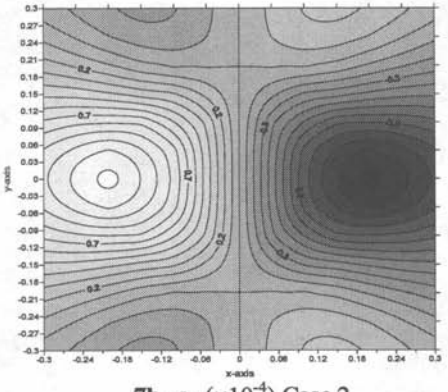

7b. ε_{yy} ($\times 10^{-4}$) Case 2.

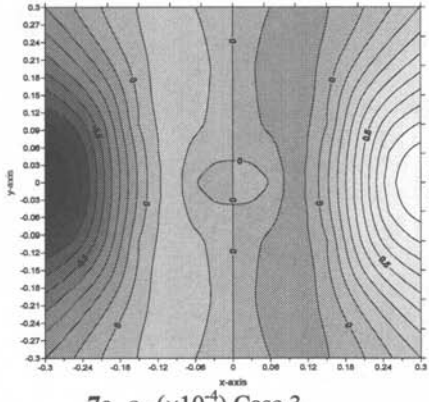

7c. ε_{xx} ($\times 10^{-4}$) Case 3.

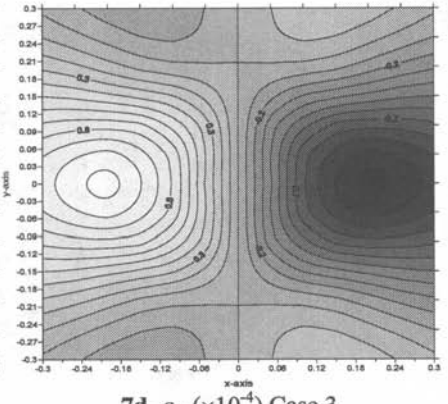

7d. ε_{yy} ($\times 10^{-4}$) Case 3.

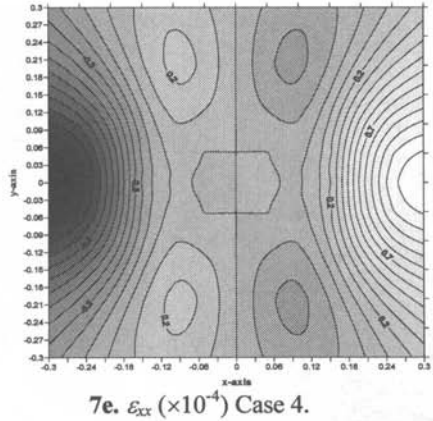

7e. ε_{xx} ($\times 10^{-4}$) Case 4.

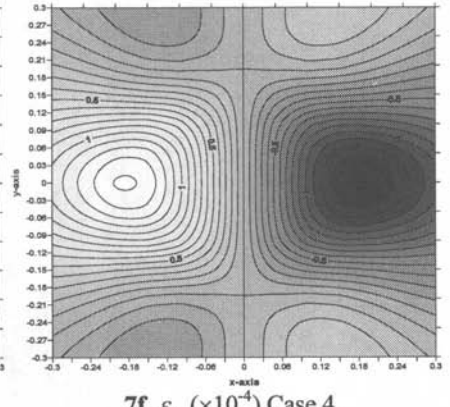

7f. ε_{yy} ($\times 10^{-4}$) Case 4.

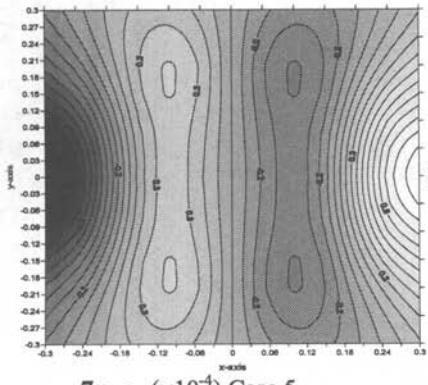

7g. ε_{xx} ($\times 10^{-4}$) Case 5.

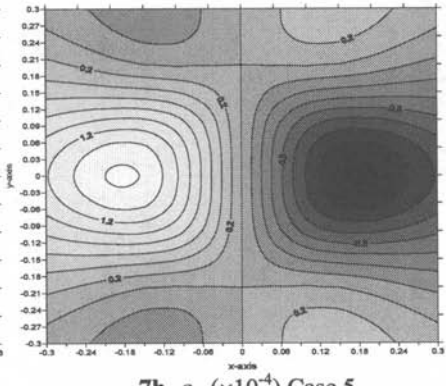

7h. ε_{yy} ($\times 10^{-4}$) Case 5.

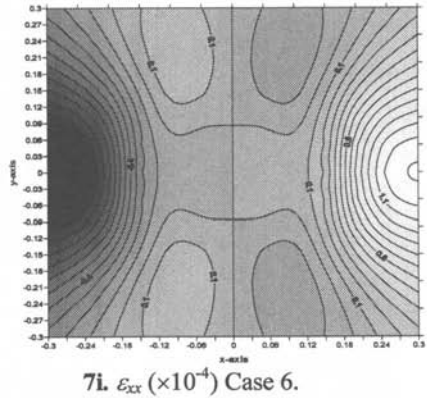

7i. ε_{xx} ($\times 10^{-4}$) Case 6.

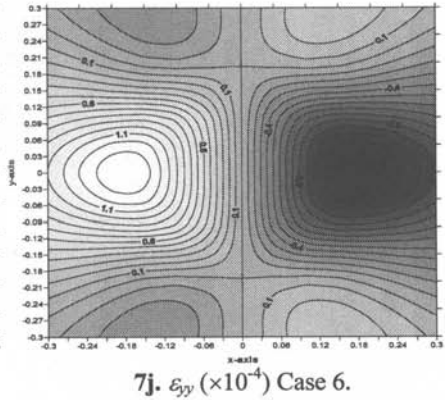

7j. ε_{yy} ($\times 10^{-4}$) Case 6.

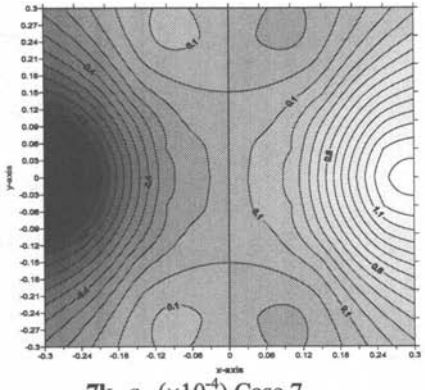

7k. ε_{xx} ($\times 10^{-4}$) Case 7.

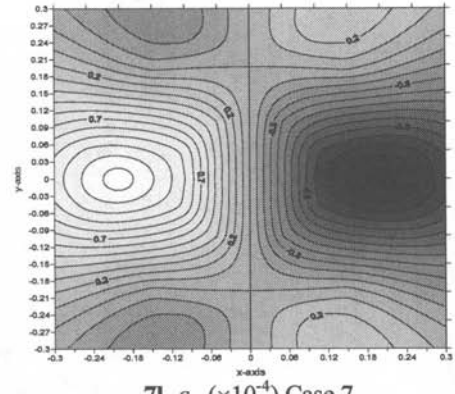

7l. ε_{yy} ($\times 10^{-4}$) Case 7.

FIG. 7. Effect of anisotropy on horizontal strain.

For Cases 1, 2 and 3, it can be seen that with decreasing G', the maximum strain decreases. It is interesting to observe that the maximum strains are all reached by ε_{yy}. Cases 1, 4 and 5 show that maximum strain increases with decreasing E', and the increase is more apparent than the decrease shown in Cases 1, 2 and 3. Thus the strains are more sensitive to E' than to G'. Similarly, the maximum strains are also reached by ε_{yy}. From Cases 1, 6 and 7 it is easy to conclude that the maximum strain slightly decreases with decreasing ν' and are reached by ε_{xx}.

It is also interesting to find that the maxima ε_{xx} for all the seven cases are located within the domain $x\in(0.24\text{m}, 0.36\text{m})$ and $y\in(-0.06\text{m}, 0.06\text{m})$, whilst for the maxima ε_{yy} they are in the domain $x\in(-0.24\text{m}, -0.12\text{m})$ and $y\in(-0.06\text{m}, 0.06\text{m})$, although their magnitudes are different. It can be anticipated that under the same horizontal load configuration the critical strains will always be in the same domains without being affected by the anisotropy configuration.

CONCLUSIONS

In this work, the response of a layered half-space pavement to multiple horizontal loads acting on the surface is established, and a FORTRAN program is developed based on the present solution. The effect of the horizontal load is then discussed showing that the horizontal load has a great influence on the pavement fatigue performance. For example our results show that ignoring the horizontal load would result in an overestimate on the lifetime expectance of the pavement. Further discussed in this paper is the effect of the pavement anisotropy on the strains, showing that the critical strains are mostly sensitive to E, then to G and less to ν. The anisotropy will change greatly the magnitude of the critical strain but slightly its position. Thus to predict the failure performance in pavement engineering, it is anticipated that only certain domains, rather than the whole field, need to be computed, which will greatly reduce the computation time.

APPENDIX

$$UT(1)=\int_0^\infty(\lambda U_M/\lambda)J_0(\lambda r)\lambda^2 d\lambda \qquad UT(4)=\int_0^\infty(T_M)J_0(\lambda r)\lambda^2 d\lambda$$

$$UT(2)=\int_0^\infty(\lambda U_M/\lambda^2 r)J_1(\lambda r)\lambda^2 d\lambda \qquad UT(5)=\int_0^\infty(T_M/r)J_1(\lambda r)\lambda d\lambda=\int_0^\infty(T_M/\lambda r)J_1(\lambda r)\lambda^2 d\lambda$$

$$UT(3)=\int_0^\infty U_L J_1(\lambda r)\lambda d\lambda=\int_0^\infty(U_L/\lambda)J_1(\lambda r)\lambda^2 d\lambda \quad UT(6)=\int_0^\infty T_L J_1(\lambda r)\lambda d\lambda=\int_0^\infty(T_L/\lambda)J_1(\lambda r)\lambda^2 d\lambda$$

$$UT(7)=\int_0^\infty U_M\lambda^2 J_1(\lambda r)\lambda d\lambda=\int_0^\infty(\lambda U_M)J_1(\lambda r)\lambda^2 d\lambda$$

$$UTN(1)=\int_0^\infty(\lambda U_N/\lambda^2 r)J_1(\lambda r)\lambda^2 d\lambda \qquad UTN(2)=\int_0^\infty(\lambda U_N/\lambda)J_0(\lambda r)\lambda^2 d\lambda$$

$$UTN(3)=\int_0^\infty(T_N/r)J_1(\lambda r)\lambda d\lambda=\int_0^\infty(T_N/\lambda r)J_1(\lambda r)\lambda^2 d\lambda$$

$$UTN(4) = \int_0^\infty (T_N) J_0(\lambda r) \lambda^2 d\lambda$$

$$UTN(5) = \int_0^\infty U_N \lambda^2 J_1(\lambda r) \lambda d\lambda = \int_0^\infty (\lambda U_N) J_1(\lambda r) \lambda^2 d\lambda$$

REFERENCES

Burmister, D.M. (1943). "The theory of stresses and displacements in layered systems and applications to the design of airport runways." *Proc. Hwy. Res. Board*, Vol. 23: 126-144.

Burmister, D.M. (1945). "The general theory of stresses and displacements in layered soil systems." *J. Appl. Phys.*, Vol. 16: 89-94, 126-127, 296-302.

Love, A.E.H. (1927). A treatise on the mathematical theory of elasticity, Cambridge University, fourth edition.

Matsui, K., Maina, J. W., Dong, Q., and Inoue, T. (2002). "Development of pavement structural analysis due to horizontal surface force based on elastic theory." *Proc., the 2002 FAA Airport Technology Transfer Conference*, P-37, Atlantic City, New Jersey.

Mindlin, R. D. (1936). "Force at a point in the interior of a semi-infinite solid." *J. Appl. Phys.*, Vol. 7: 195-202.

Pan, E. (1989a). "The static responses of multilayered foundations to general surface loading and body force." *Acta. Mech. Sin.*, 21(3): 344-353 (in Chinese).

Pan, E. (1989b). "Static response of a transversely isotropic and layered half-space to general surface loads". *Phys. Earth Planet. Inter.*, Vol.54: 353-363.

Pan, E. (1997). "Static Ggreen's functions in multilayered half-spaces." *Appl. Math. Modell.*, Vol.21: 509-521.

Pan, E., Alkasawneh, W., and Chen, E. (2007). "An exploratory study on functionally graded materials with application to multilayered pavement design." *Report* FHWA/OH-2007/12, Ohio Department of Transportation, Columbus, Ohio.

Timm, D.H. and Newcomb, D.E. (2006). "Perpetual pavement design for flexible pavements in the U.S." *Int. J. of Pavement Engineering*, 7(2): 111-119.

Wang, K. (1983). "Calculation of stresses, strains and displacements in an *N*-layer elastic continuous system under the action of two complex loads uniformly distributed on circular areas." *Acta. Mech. Sol. Sin.*, Vol.1: 136-153 (in Chinese).

Wardle, L.J. (1981). "Three-dimensional solution for displacement discontinuities in cross- anisotropic elastic media." *CSIRO Aust. Div. Appl. Geomech. Tech. Pap.*, Vol.34: 1-32.

Yue, Z.Q. and Yin, J.H. (1998). "Backward transfer-matrix method for elastic analysis of layered solids with imperfect bonding." *J. Elasticity*, Vol.50: 109-128.

Calculating Thermal Stresses of Asphalt Pavement in Environmental Conditions

Guoping Qian[1], Jianlong Zheng[2], and Qing'e Wang[3]

[1]Instructor, Highway Engineering school of Changsha University of Science and Technology, Changsha P.R.China, 410076; guopingqian@sina.com

[2]Professor, Highway Engineering school of Changsha University of Science and Technology, Changsha P.R.China, 410076; ZJL@csust.edu.cn

[3]Instructor, School of Civil Engineering and Architecture of Central South University, Changsha P.R.China, 410075; wqecsu@126.com

ABSTRACT: Asphalt mixtures are a type of thermorheologically simple materials, so the study work on thermal stresses in asphalt pavements should be carried out beyond the scope of thermalviscoelasticity theory. Taking thermalviscoelasticity theory as a guide, the stress relaxation test of asphalt mixtures is studied in different temperature environment. The test data are analyzed and the interrelated model parameters are fitted by use of the time-temperature equivalence principle of the thermo-rheologically simple materials. Based on the test results, a generalized Maxwell model is established to simulate the viscoelastic property of asphalt mixtures. And the incremental thermalviscoelastic constitutive relation under nonconstant, nonuniform temperature condition is obtained from theoretical derivation. Furthermore, a numerical method for thermalviscoelastic analysis of asphalt pavement is provided by using the incremental constitutive relation. At last, the rationality for the constitutive relation is examined by simulating Thermal Stress Restrained Specimen Test (TSRST), and an application case is given.

INTRODUCTION

Under the conditions of natural environment, the pavement is subjected to varying climate, which leads to a continuing time dependant and space dependant change in pavement's temperature field. And this change in temperature results in the occurrence of stresses in the restrained pavement.

Thermal stresses are a leading cause for asphalt pavement deterioration. In the past several decades, many researchers have carried out numerous studies on this topic (Monismith et al. 1965, Zheng et al. 1992, Shields et al. 1998, Bouldin et al. 2000, Christensen et al. 2000). However, most of them made several assumptions which are disadvantageous to accuracy of calculated results while calculating thermal stresses, as following: 1) Asphalt mixtures are assumed to be elastic; 2) Temperature distribution is uniform space-wise; 3) Temperature variation is linear; 4) Contractions in base are ignored.

Asphalt mixtures are a type of thermorheologically simple materials and sensitive

to temperature. In order to obtain accurate thermal stress results, the study work should be carried out beyond the scope of thermalviscoelasticity theory.

THERMALVISCOELASTICITY OF ASPHALT MIXTURES

Numerous test results have shown that asphalt mixtures are the type of thermorheologically simple materials taken to behave in accordance with the time-temperature superposition principle, and the stress-strain relationship is related not only to time, but also to temperature. In order to determine this relation, the formulation of the isothermal viscoelastic constitutive relation should firstly be considered. Then, the time-temperature superposition principle is used to extend the results for dependence of mechanical properties upon constant temperature states, and to model the material behavior under nonconstant, nonuniform states, in which a temperature shift factor mentioned later is applied.

Stress Relaxing Characteristics of Asphalt Mixtures

Because there exists evident stress relaxing phenomenon in pavement thermal stresses forming and developing process, learning and quantitatively describing stress relaxing characteristics of asphalt mixtures is an essential condition for temperature contracting cracking analysis. So the stress-relaxing test has been done in laboratory in this research. Stress relaxing test is finished by the thermal stress restrained specimen test (TSRST) at different temperatures. Testing material is the asphalt concrete AC-16. Testing results are given in Table 1.

Table 1. Stress Varying with Time in Relaxing Test (MPa)

Time (s)	Test Temperature (℃)						
	-20	-15	-10	-5	0	5	10
10	0.8703	0.5597	0.5128	0.4090	0.2932	0.2765	0.0938
20	0.8684	0.5492	0.4900	0.4029	0.2240	0.2291	0.0704
40	0.8646	0.5413	0.4520	0.3992	0.1475	0.1796	0.0564
70	0.8590	0.5361	0.4330	0.3616	0.0916	0.1376	0.0517
100	0.8533	0.5299	0.4000	0.3021	0.0746	0.1141	0.0447
200	0.8344	0.5157	0.3741	0.2499	0.0685	0.0986	0.0377
400	0.7966	0.4907	0.3207	0.1892	0.0637	0.0824	0.0318
700	0.7398	0.4544	0.2843	0.1989	0.0576	0.0796	0.0262
1000	0.6831	0.4189	0.2503	0.1685	0.0528	0.0699	0.0225
2000	0.5496	0.3367	0.2090	0.1328	0.0418	0.0551	0.0173
4000	0.4286	0.2625	0.1568	0.0901	0.0387	0.0439	0.0135
7000	0.3722	0.2275	0.1110	0.0654	0.0377	0.0378	0.0105
10000	0.3375	0.2059	0.0853	0.0595	0.0375	0.0361	0.0086
20000	0.2860	0.1739	0.0626	0.0478	0.0368	0.0328	0.0056

Relaxation Modulus of Asphalt Mixtures

Because asphalt mixtures are the thermorheologically simple material, the Arrhenius formula is used for calculating the shift factor a_T in test result analysis (Bouldin et al. 2000):

$$a_T = \exp[-A(\frac{1}{T} - \frac{1}{T_0})] \tag{1}$$

where, A is a material factor, as far as the asphalt mixture in this research is concerned, A=20110 (^{0}K); T is temperature (^{0}K); T_0 is reference temperature (^{0}K).

Using the shift factor calculated from expression (1), the test data at else temperature in Table1 are shifted to the results at -5℃ shown in Figure 1.

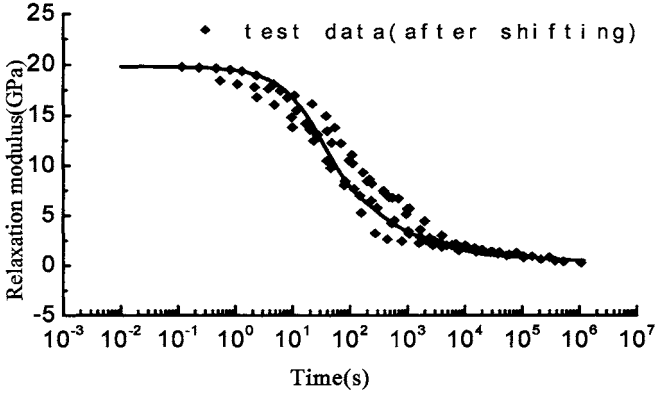

FIG. 1. Results of relaxation test and simulative curve at -5℃.

The Constitutive Model of the Asphalt Mixture

Stress relaxation characteristics of asphalt mixture in temperature varying process can be expressed by generalized Maxwell model, which is made of several parallel Maxwell models. The relaxation modulus can be written as following:

$$E(t) = \sum_{i=1}^{N} E_i \cdot e^{-t/t_i} \tag{2}$$

where, $t_i = \eta_i / E_i$ is the relaxation time of the *ith* Maxwell unit.

Using the constitutive equation (2) for fitting the main curve of relaxation modulus at -5℃ as Figure 1(N=6), the model parameters of the generalized Maxwell model can be calculated as Table 2.

Table 2. Parameters of viscoelastic model

k	1	2	3	4	5	6
E_k(Mpa)	659.95	10406.02	2534.92	431.99	4148.22	1612.87
τ_k(s)	4215497.30	32.12	986.37	145124.72	191.58	7569.68

The relaxation modulus at different reference temperature can be obtained by the shift factors calculated from expression (1). They are shown in Figure 2.

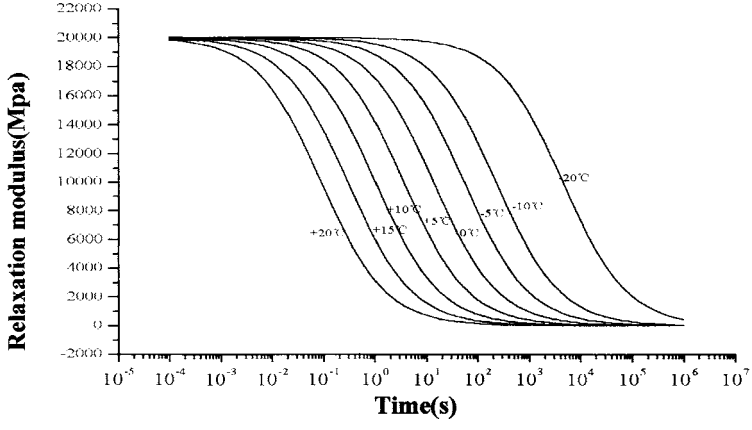

FIG. 2. The Relaxation Modulus vs. Time of AC-16.

METHOD FOR CALCULATING THERMAL STRESSES

The incremental-iterative finite element method taking displacement as the basic unknown quantities are used for calculating thermal stresses in pavement. The incremental thermalviscoelastic constitutive relation under the plane-strain condition is derived by Qian (2006). For viscoelastic asphalt surface, this stress-strain relationship is given by:

$$\begin{bmatrix}\Delta\sigma_x^n\\ \Delta\sigma_z^n\\ \Delta\tau_{xz}^n\end{bmatrix}=\frac{\widetilde{E}_n}{(1+\mu_0)(1-2\mu_0)}\cdot\left(\begin{bmatrix}(1-\mu_0)\Delta\varepsilon_x^n+\mu_0\Delta\varepsilon_z^n\\ \mu_0\Delta\varepsilon_x^n+(1-\mu_0)\Delta\varepsilon_z^n\\ (1-2\mu_0)\Delta\gamma_{xz}^n/2\end{bmatrix}-3\alpha_0\Delta T_n\begin{bmatrix}1\\1\\0\end{bmatrix}\right)-\begin{bmatrix}\sigma_{n,x}^0\\ \sigma_{n,z}^0\\ \tau_{n,xz}^0\end{bmatrix} \quad (3)$$

where,

μ_0 = Poisson ratio of asphalt mixtures,

n = number of the incremental step, [Note : The time interval $(0,t_k)$ is divided into k sub-intervals, as follows $(0, t_1)$, (t_1, t_2), (t_2, t_3), ... , (t_{k-1},t_k), and $\Delta t_n = t_n - t_{n-1}$. Every

variable occurred in the nth step will be marked with "n" as a superscript or a subscript.]

$\widetilde{E}_n(z)$ = Equivalent relaxation modulus, defined by:

$$\widetilde{E}_n = \frac{1}{\Delta t_n}\sum_{i=1}^{N} E_i \int_{t_{n-1}}^{t_n} e^{-\int_{\tau}^{t_n} e^{\frac{\delta H}{R}\left(\frac{1}{T(s,t)}-\frac{1}{T_s}\right)} dt/\tau_i} d\tau \tag{4}$$

$$\begin{bmatrix}\sigma_{n,x}^0\\ \sigma_{n,z}^0\\ \tau_{n,xz}^0\end{bmatrix} = \sum_{i=1}^{N}(1-e^{-\int_{t_{n-1}}^{t_n} e^{\frac{\delta H}{R}\left(\frac{1}{T(s,t)}-\frac{1}{T_s}\right)} dt/\tau_i})\cdot\begin{bmatrix}P_{x,i}^{(n)}\\ P_{z,i}^{(n)}\\ P_{xz,i}^{(n)}\end{bmatrix} \tag{5}$$

where,

$$\begin{bmatrix}P_{x,i}^{(n)}\\ P_{z,i}^{(n)}\\ P_{xz,i}^{(n)}\end{bmatrix} = e^{-\int_{t_{n-2}}^{t_{n-1}} e^{\frac{\delta H}{R}\left(\frac{1}{T(s,t)}-\frac{1}{T_s}\right)} dt/\tau_i}\begin{bmatrix}P_{x,i}^{(n-1)}\\ P_{z,i}^{(n-1)}\\ P_{xz,i}^{(n-1)}\end{bmatrix} + \frac{1}{(1+\mu_0)(1-2\mu_0)}\left(\begin{bmatrix}(1-\mu_0)\Delta\varepsilon_x^{n-1}+\mu_0\Delta\varepsilon_z^{n-1}\\ \mu_0\Delta\varepsilon_x^{n-1}+(1-\mu_0)\Delta\varepsilon_z^{n-1}\\ (1-2\mu_0)\Delta\gamma_{xz}^{n-1}/2\end{bmatrix}\right. \tag{6}$$

$$\left.-3\alpha_0\Delta T_{n-1}\begin{bmatrix}1\\1\\0\end{bmatrix}\right)\frac{E_i}{\Delta t_{n-1}}\int_{t_{n-2}}^{t_{n-1}} e^{-\int_{\tau}^{t_{n-1}} e^{\frac{\delta H}{R}\left(\frac{1}{T(s,t)}-\frac{1}{T_s}\right)} dt/\tau_i} d\tau$$

For an arbitrary element e, the balance equation is obtained from principle of virtual work, as follows:

$$[K_n^e]\cdot\{\Delta d_n^e\} = \{\Delta P_n^T\}^e + \{\Delta P_n^0\}^e \tag{7}$$

where,

$[K_n^e] = \int_e [B]^T \widetilde{E}_n[\widetilde{D}]\cdot[B]dV$ Stiffness matrices of element e,

$\{\Delta P_n^0\} = \int_e [B]^T\{\sigma_n^0\}dV$ Corrective loading column of element e,

$\{\Delta P_n^T\}^e = \int_e [B]^T \widetilde{E}_n[\widetilde{D}]\{\alpha(T)_n\}dV$ Column matrix of nodal displacement of element e.

where,

$[B]$ = Strain matrix,

Ve = element volume,

$[\widetilde{D}]$= Corrective matrix of plane-strain, given by:

$$\left[\widetilde{D}\right]=\frac{1}{(1+\mu_0)(1-2\mu_0)}\begin{bmatrix}1-\mu_0 & \mu_0 & 0\\ \mu_0 & 1-\mu_0 & 0\\ 0 & 0 & (1-2\mu_0)/2\end{bmatrix} \tag{8}$$

In this study, eight-node isoparametric elements are used in the thermal stress analysis. The viscoelastic elements are applied to asphalt surface, element mode of which is given by:

$$\left[K_n^e\right]=\begin{bmatrix}k_{11} & k_{12} & \cdots & k_{18}\\ k_{21} & k_{22} & \cdots & k_{28}\\ \cdots & \cdots & \cdots & \cdots\\ k_{81} & k_{82} & \cdots & k_{88}\end{bmatrix};\ \left\{\Delta P_n^T\right\}^e=\begin{Bmatrix}p_1^T\\ p_2^T\\ \cdots\\ p_8^T\end{Bmatrix};\ \left\{\Delta \mathrm{P_n^0}\right\}^e=\begin{Bmatrix}\mathrm{p_1^0}\\ \mathrm{p_2^0}\\ \cdots\\ \mathrm{p_8^0}\end{Bmatrix} \tag{9}$$

where,

$$\left[k_{ij}\right]=\int_{-1}^{1}\int_{-1}\frac{\widetilde{E}_n}{(1+\mu_0)}\begin{bmatrix}\frac{1-\mu_0}{1-2\mu_0}N_{i,x}N_{j,x}+\frac{1}{2}N_{i,z}N_{j,z} & \frac{\mu_0}{1-2\mu_0}N_{i,x}N_{j,z}+\frac{1}{2}N_{i,z}N_{j,x}\\ \frac{\mu_0}{1-2\mu_0}N_{i,z}N_{j,x}+\frac{1}{2}N_{i,x}N_{j,z} & \frac{1-\mu_0}{1-2\mu_0}N_{i,z}N_{j,z}+\frac{1}{2}N_{i,x}N_{j,x}\end{bmatrix}|J|d\xi d\eta \tag{10}$$

$$\left\{p_i^T\right\}=\begin{Bmatrix}p_{ix}^T\\ p_{iz}^T\end{Bmatrix}=\frac{3\alpha_0}{(1+\mu_0)(1-2\mu_0)}\int_{-1}^{1}\int_{-1}\begin{Bmatrix}N_{i,x}\\ N_{i,z}\end{Bmatrix}\widetilde{E}_n\Delta T_n|J|d\xi d\eta \tag{11}$$

$$\left\{p_i^0\right\}=\begin{Bmatrix}p_{ix}^0\\ p_{iz}^0\end{Bmatrix}=\int_{-1}^{1}\int_{-1}\begin{Bmatrix}N_{i,x}\sigma_{n,x}^0+N_{i,z}\tau_{n,xz}^0\\ N_{i,z}\sigma_{n,z}^0+N_{i,x}\tau_{n,xz}^0\end{Bmatrix}\cdot|J|d\xi d\eta \tag{12}$$

where,

$$\begin{Bmatrix}N_{i,x}\\ N_{i,z}\end{Bmatrix}=\begin{Bmatrix}\frac{\partial N_i}{\partial x}\\ \frac{\partial N_i}{\partial z}\end{Bmatrix}=[J]^{-1}\begin{Bmatrix}\frac{\partial N_i}{\partial \xi}\\ \frac{\partial N_i}{\partial \eta}\end{Bmatrix};[J]^{-1}=\frac{1}{|J|}\begin{bmatrix}\frac{\partial z}{\partial \eta} & -\frac{\partial z}{\partial \xi}\\ -\frac{\partial x}{\partial \eta} & \frac{\partial x}{\partial \xi}\end{bmatrix};\ |J|=\frac{\partial x}{\partial \xi}\frac{\partial z}{\partial \eta}-\frac{\partial z}{\partial \xi}\frac{\partial x}{\partial \eta} \tag{13-15}$$

Linear elastic elements are used for the base, sub-base and sub-grade, calculating mode that can be found in general literature and will not be introduced here.

Then, the equation of FEM can be formed according to a specific method that also can be found in general literature. Finally, results are obtained from solving the balance equation of FEM.

EXPERIMENT VALIDATION AND APPLICATION CASE

In order to validate the rationality for the thermalviscoelastic constitutive relation, the incremental-iterative finite element method is used to simulate one TSRST test process. The initial test temperature is 10℃, temperature change rate is -5℃/h and discrete time is 5s. The test results and theoretical calculation results are shown in Figure 3. (Note: when temperature was -32℃ in the TSRST test, the test sample began to crack).

Figure 3 shows that test results dovetailed fundamentally with theoretical calculation results under working temperature, which revealed that thermoviscoelasticitical constitutive relation established in this paper can truly reflect the stress-relaxation characteristic of bituminous mixture, and the related numerical method is credible. Consequently, the constitutive relation and numerical method both can be used for thermoviscoelasticitical calculation of thermal stress of asphalt pavement.

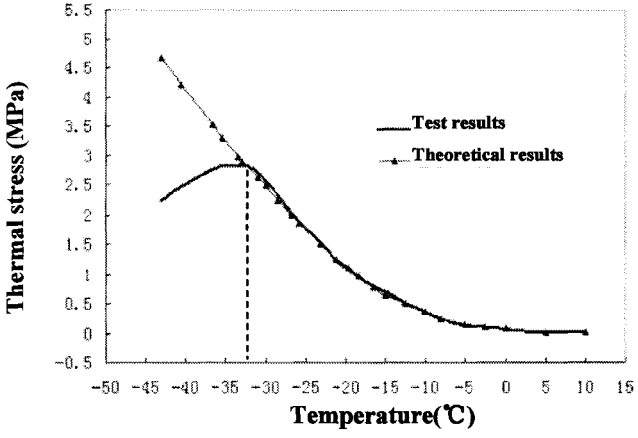

FIG. 3. TSRST test results and simulative curve.

Typical four-layer system is taken as the mechanical model of asphalt pavements and the asphalt concrete is considered as thermal-viscoelastic material and the time increment finite-element method is applied for computing pavement thermal stress corresponding temperature varying process. The temperature field of asphalt pavement can be computed using the method presented by Qian (2001).

In the calculating process, typical climatic conditions are: maximum of daily air temperature 10C,minimum of daily air temperature 0C, maximum of daily solar

radiation 8MJ/m2, wind speed 2m/s, and sunshine time 8 hours. The pavement material and structure parameters are given in Table 3. Figure 4 gives the calculated temperature field at different depths of surface and Figure 5 shows the variation of thermal stress field with time at different depths of surface.

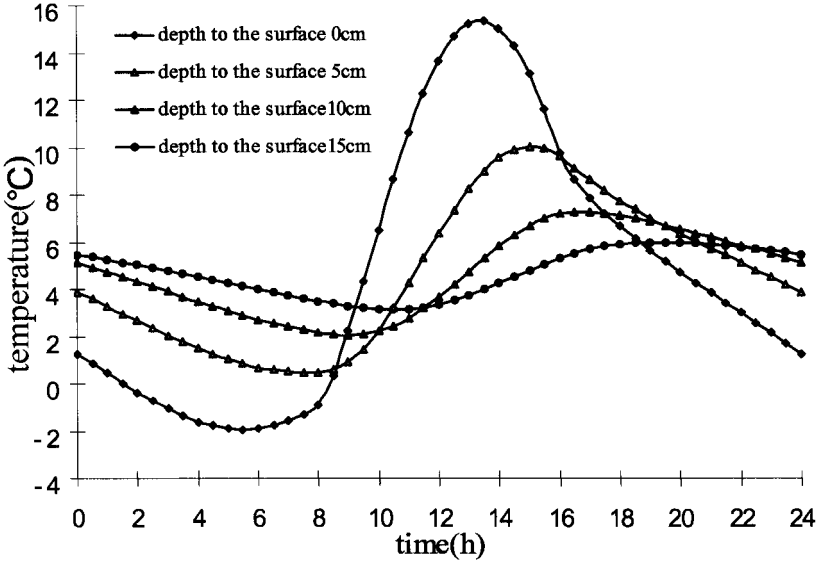

FIG. 4. Temperature field

Table 3. Pavement Material and Structure Parameters

Materials	Modulus E (MPa)	Poisson ratio μ	Expansion coefficient 10^{-5}(1/°C)	λ_i (W/m k)	a_i (m^2/h)	Thickness (cm)
Asphalt Surface	* Note a	0.25	2.0	1.0	0.0022	15
Base	1600	0.15	1.0	1.2	0.0028	36
Subbase	600	0.35	1.5	1.1	0.0026	20
Subgrade	40	0.35	50	1.2	0.0030	N/A

Note: a. Viscoelastic parameters of asphalt surface are obtained from the relaxation test; b. Solar radiating absorption ratio of asphalt surface a_s=0.85.

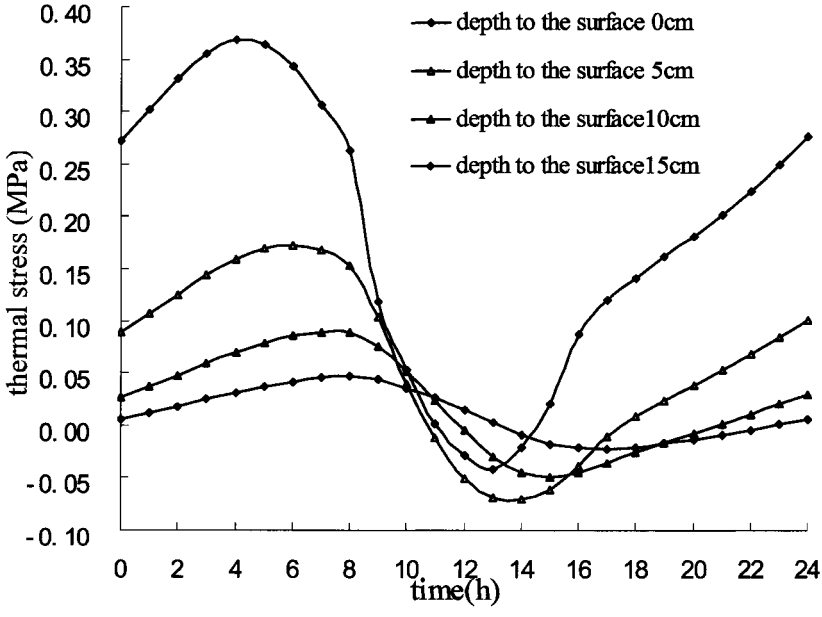

FIG. 5. Thermal stress field.

CONCLUSIONS

By means of the Thermal Stress Restrained Specimen Test (TSRST), the stress relaxing behavior of asphalt mixtures at different temperature are obtained through direct tension test. The viscoelastic fluid feature and thermorheologically simple behavior of the asphalt mixtures are confirmed by laboratory tests. On the basis of the experiments, a general Maxwell model is set up to describe the forming and growing process of thermal stresses in pavement, and a thermo-viscoelastic constitutive model of asphalt mixtures suitable for non-isothermal process is proposed.

The computational model of thermal stress field in asphalt pavement and the corresponding time increment finite-element formulate are derived according to thermo-viscoelastic constitutive equations, in which the calculation of the thermal stresses is combined with the analysis of temperature field in pavement. Analysis results revealed that the derived constitutive equation is suitable for calculating the thermal stresses of asphalt pavement under environmental conditions.

ACKNOWLEDGEMENTS

The research was partially supported by Specialized Research Fund for the Doctoral Program of Higher Education (20050536001), Scientific Research Fund of ministry of communications of P.R.China (2006319825090) and Scientific Research Fund of Hunan Provincial Education Department (06B008). The author would like to acknowledge with thanks the financial support.

REFERENCES

Monismith C.L., Secor G.A. and Secor K.E.(1965). Temperature -induced stresses and deformations in asphalt concrete. Proceeding of the Association of Asphalt Paving Technologists, Vol.34:248-285.

Zheng J.L., Zhang Q.S.(1992). Thermal responses Analysis of surface cracking of semi-rigid base bituminous pavement. Journal of Changsha communications University, Vol.2: 1-11.

Shields D.H., Zeng M.(1998). Nonlinear Viscoelastic Behavior of Asphalt Concrete in Stress Relaxation. Proceedings of the Association of Asphalt Paving Technologists, Vol.67:358-390.

Bouldin M. G., Dongre R., Rowe G. M.M. et al. (2000). Predicting thermal cracking of pavements from binder properties: Theoretical basis and field validation. Proceeding of the Association of Asphalt Paving Technologists, Vol.69:455-488.

Mehta Y.A., Christensen D.W.(2000). Determination of the Linear Viscoelastic Limite of Asphalt Concrete at Low Intermediate Temperature. Proceeding of AAPT, Vol.69: 281-316.

Zheng J.L., Ying R.H., Zhang Q.S.(1996). Experimental research on thermo-viscoelastic fracture parameters of bituminous mixture. China journal of highway and transport, Vol.3:20-28.

Qian G.P., Zheng J.L., Zhou Z.G., Tian X.G.(2006). Incremental Thermalviscoelastic Constitutive Relation of Asphalt Mixtures. Chinese journal of applied mechanics, Vol.23(3):338-343.

Wang.J.L, Bjorn B., Reynaldo R. (2006). Effects of Viscoelastic Stress Redistribution on the Cracking Performance of Asphalt Pavements [J]. Proceeding of AAPT, Vol. 75: 582-619.

Francken L., Part.L.M. (1998). Complex modulus testing of asphaltic concrete: RILEM interlaboratory test program. Transportation Research Record 1545, TBR[C]. Washington D C, National Research Council, 133-142.

Zhou Z.G., Qian G.P., Zheng J.L. Research on the method of testing viscoelastic parameters of bituminous mixtures [J]. Journal of Changsha Communications University,2001(4):23-28.

AASHTO Provisional Standard. (1996). Standard test method for thermal stress restrained specimen tensile strength. AASHTO Designation: TP10-93.

Qian G.P., Zhou Z.G., Zheng J.L. (2001). The Analysis on the Temperature Field of Asphalt Pavement under Environmental Conditions [A]. Transportation research and exploration in China[C]. Nanjing: Chinese civil aviation press: 459-464.0

Numerical Simulation for Interaction between Tyre and Steel Deck Surfacing

Zhendong Qian[1], Tuanjie Chen[2] and Yun Liu[3]

[1]Professor, Transportation College of Southeast University, Nanjing 210096, P.R.China; qianzd@seu.edu.cn
[2]Graduate Student, Transportation College of Southeast University, Nanjing 210096, P.R.China; demo555@126.com
[3]Graduate Student, Transportation College of Southeast University, Nanjing 210096, P.R.China; seuliuyun@126.com

ABSTRACT: The structure of steel deck surfacing is different from that of the common asphalt pavement on highway. The interaction between tyre and surfacing, which took geometric nonlinearity, material nonlinearity and non-linear interaction into consideration, was analyzed in this paper. A strain energy density function called Rivilin model was used to simulate the mechanical performance of tyre. The Lagrange method was adopted to study the geometric nonlinearity induced by the large deformation of tyre. As the friction factor between tyre and surfacing doesn't need to be considered in the static calculation, the restraint function method was used in order to get good convergence efficiency. A contact model was established to study the interaction between tyre and steel box girder surfacing. The research results show that the structural difference between road pavement and steel deck surfacing has some influence on the contact stress. The interaction area, which is used in the design of steel deck surfacing, is suggested to be simplified as a rectangle with a length of 250mm and a width of 140mm.

INTRODUCTION

Most newly built long-span bridges in China are welded steel box girders with orthotropic steel plate decks. Cracking is the main rupture mode of steel deck surfacing which is mostly caused by the traveling vehicle loads. The aim of this paper is to study the interaction between tyre and steel deck surfacing, especially the calculating diagram of the vehicle load for the design of steel deck surfacing.

In the traditional pavement analysis, the uniform distributed load with circle shape is always used to represent the action of vehicle on pavement. In the Specifications for Design of Highway Asphalt Pavement (JTJ014-97) of China, the standard axle load is represented by BZZ-100 (Zeng et al. 2004). The two load patches in Fig. 1 correspond to the rear axle of a standard truck in JTJ014-97. Each of the two load patches corresponds to a single wheel, and each wheel load is 25 kN. The diameter of the equivalent circle is 0.213m. A tire contact pressure is 700kPa. In Fig. 1, P_d is the single wheel load, P is the tire contact pressure, and d is the diameter of the equivalent circle.

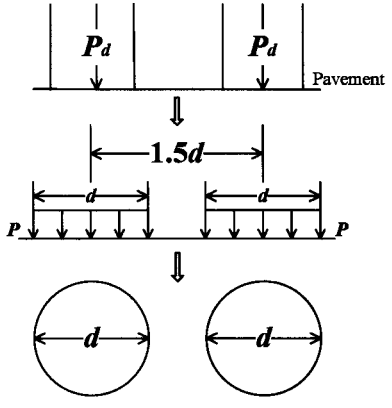

FIG. 1. Calculating diagram of BZZ-100 (Mao 2000).

In the traditional analysis of steel deck surfacing, no unified specification could be referred to in China. The calculation diagram of vehicle load for the design of steel deck surfacing was confirmed according to the specifications for pavement. Mao (2000) assumed that the interface between one single tyre of BZZ-100 and surfacing was in the shape of a square with sides of 189mm. Li and Deng (2002) assumed that the interface between one single tyre of BZZ-100 and surfacing was in the shape of a rectangle with a length of 200mm and a width of 230mm. The contact analysis between tyre and surfacing has not been applied to determine the calculating diagram of vehicle loads.

In this paper, the basic theory of contact between tyre and surfacing was presented firstly. Then, a contact model was established including the tyre model and the local orthotropic steel deck model. Finally, the contact stress of surfacing on steel deck was analyzed by means of FEM, and a more accurate calculating diagram of the standard axle load (JTJ014-97) was put forward for the design of steel deck surfacing.

BASIC THEORY OF CONTACT BETWEEN TYRE AND SURFACING

The material nonlinearity, geometric nonlinearity and contact nonlinearity should be considered in the contact analysis (Li and Wang 2000; Xie and Zhen 2004).

Generally, the latex material in wheel tyre is an isotropic super-elastic material which can be described using several strain energy density functions, such as Rivilin model or Ogden model. The Rivilin model (Wang 1998; Li and Liu 2000) can be expressed as

$$W = \sum_{i=0,j=0}^{\infty} C_{ij} (I_1 - 3)^i (I_2 - 3)^j \tag{1}$$

where W = strain energy density; I_1 , I_2 = the first, second invariable; and C_{ij} = material constant.

Rivilin model can be simplified as follows (Hong and Wu 2006)

$$W = C_{10}(I_1 - 3) + C_{20}(I_1 - 3)^2 + C_{30}(I_1 - 3)^3 \tag{2}$$

Geometric nonlinearity is induced due to the large deformation of wheel tyre. According to virtual principle, the relation of Green strain and Kichhoff stress can be expressed as

$$\int_0^{t+\Delta t} S_{ij}\delta^{t+\Delta t}E_{ij}dv = \delta^{t+\Delta t}w \tag{3}$$

where S_{ij} = Kichhoff stress tensor; E_{ij} = Green strain tensor; w = displacement; and t = time.

The finite element equation of geometric nonlinearity is

$$([K]_0 + [K]_\sigma + [K]_L)\{\delta q\} = \{F\} + \{T\} + \{P\} \tag{4}$$

in which $[K]_0$ = the tangent stiffness matrix indicating the relation of load increment and displacement; $[K]_\sigma$ = the initial stress stiffness matrix indicating the influence of initial stress on structure under great deform; $[K]_L$ = the stiffness matrix of initial displacement indicating the stiffness variation of structure due to great deform; $\{\delta q\}$ = the vector of nodal displacement increment; $\{F\}$ = the vector of body load; $\{T\}$ = the vector of surface load; and $\{P\}$ = the vector of equivalent composition of force in the nodes.

The contact problem belongs to the extreme problem of fonctionelle with constraint conditions. In terms of the contact mode of wheel tire and surfacing, as the friction coefficient is ignored in static calculation, it will achieve better convergence effect if adopting the constraint function method (Cheng et al. 2004).

$$w(g,\lambda) = \frac{g+\lambda}{2} - \sqrt{(\frac{g-\lambda}{2})^2 + \varepsilon_N} \tag{5}$$

where g = the aperture width between the contact areas; λ = the normal contact force; and ε_N = the small variable.

FE CONTACT MODEL

The wheel tyre 265/70R19.5 (11.00R20) (Hong and Wu 2006) was selected as the research object. The glue thickness in basement of crest part of meridian tyre is 5mm. The thickness of belted constraint layer, tyre foundation and inner lining are 6.5mm, 2mm and 2.5mm respectively. The glue thickness in the side of tyre is 3.5mm. The whole thickness of tyre bead is 28mm. The thickness of tyre shoulder is 34mm.

The calculated parameters (Wu and Guan 1996) are referenced in this paper, as shown in Tables 1 and 2. In Table 1, E_{11}, E_{22} and E_{33} are the elastic modulus, G_{13}, G_{23} and G_{31} are the shear modulus. In Table 2, μ_1, μ_2 and μ_3 are the poisson ratios, and ρ is mass density. In Table 3, C_{10}, C_{20} and C_{20} are the mechanical parameters of the vulcanized rubber, μ is the poisson ratio, and ρ is the mass density.

Table 1. Material Properties of Tyre Carcass and Belted Constraint Layer (from Wu and Guan 1996)

Material	E_{11} (Pa)	E_{22} (Pa)	E_{33} (Pa)	G_{13} (Pa)	G_{23} (Pa)	G_{31} (Pa)
Tyre carcass	9.32e8	2.76e6	2.76e6	3.11e8	4.14e6	4.14e6
Belted constraint layer	1.03e10	4.13e6	4.13e6	3.58e8	4.82e6	4.82e6

Table 2. Material Properties of Tyre Carcass and Belted Constraint Layer (from Wu and Guan 1996)

Material	μ_1	μ_2	μ_3	ρ (kg/m^3)
Tyre carcass	0.47	0.47	0.005	1035
Belted constraint layer	0.47	0.47	0.0004	1200

Table 3. Characteristic Parameters of Material of Tyre Crown, Tyre Side and Tyre Bead (from Wu and Guan 1996)

Material	C_{10} (Pa)	C_{20} (Pa)	C_{30} (Pa)	μ	P (kg/m^3)
Tyre crown	7.70e5	-6.71e4	9.55e4	0.5	1025
Tyre side	9.35e5	-1.90e5	1.84e5	0.5	1125
Tyre bead	3.26e5	-1.60e4	1.29e4	0.5	1125

Considering the strong locality exists in the contact problem of wheel tyre and surfacing, the local orthotropic steel deck model was chosen to analyze the contact problem (Qian et al. 2005). Seven trapezoidal stiffeners along the transversal direction and three spans along the longitudinal direction of bridge were chosen including four diaphragms. The spacing of diaphragm plates was 3.75m. The calculation parameters are shown in Table 4. The contact model established by 8-node solid element is shown in Fig.2.

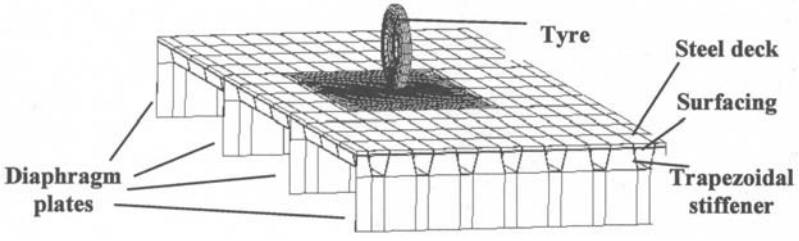

FIG. 2. Contact model.

Table 4. Parameters of the Local Orthotropic Steel Deck Model

Geometric size					
Thickness of steel deck (mm)	Opening width of trapezoidal stiffener (mm)	Height of trapezoidal stiffener (mm)	Thickness of trapezoidal stiffener (mm)	Spacing of trapezoidal stiffeners (mm)	Thickness of pavement (mm)
14	300	280	8	600	50
Material					
Elastic modulus of steel (MPa)	Poisson ratio of steel	Density of steel (kg/m^3)	Elastic modulus of asphalt mixture (MPa)	Poisson ratio of asphalt mixture	Density of surfacing (kg/m^3)
2.1×10^5	0.3	7.85×10^3	680	0.3	2.45×10^3

As the structure was established, some simplifications (Qian et al. 2007) are taken as follows:

1. The material of pavement is continuous, elastic and homogeneously isotropic.
2. The displacement and deformation of the orthotropic plate is tiny.
3. The stress/strain between steel deck and pavement is continuous.
4. The bonding layer is taken in the asphalt concrete pavement layer, because the thickness of bonding layer is much smaller than that of the pavement layer and bridge deck.
5. The transversal and longitudinal translation of the pavement and steel deck are limited, whereas the vertical translation of the pavement and steel deck is free. The bottom of the diaphragm plate is fixed.

LOAD LOCATION OF WHEEL TYRE

The two load locations of wheel tyre are shown in Fig. 3. The center of tire was located at the top of web of longitudinal stiffness rib in case I, and between two webs of longitudinal stiffness rib in case II. These two locations (Qian and Luo 2004) can reflect the structural characteristics of the orthotropic plate.

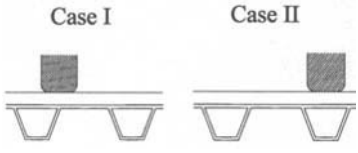

FIG. 3. Location of wheel tyre.

SIMULATION RESULTS

The vertical loads of 5kN, 10kN, 15kN, 20kN, 25kN, 30kN and 35kN were imposed on the center of the tyre profile, respectively. Correspondingly, the inner press of tyre increased from 0.2MPa to 0.4MPa. The grounding contours of contact area between tyre and surfacing in case I and II are shown in Figs. 4 and 5, respectively.

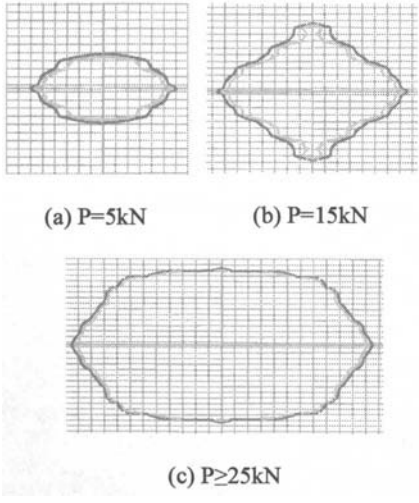

FIG. 4. Grounding configuration under various axle load in case I.

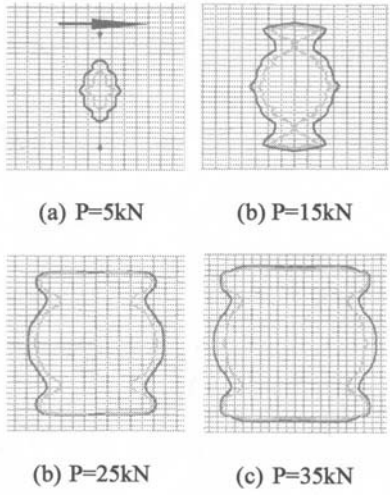

FIG. 5. Grounding contour under various axle load in case II.

The grounding contours are different in case I and case II, especially for small axle load. When the vertical load is 5kN, the grounding contour in case I is in the shape of an ellipse with a long diameter in the longitudinal bridge direction, whiles the grounding contour in case II is rhombic in shape. When the vertical load is 15kN, the grounding contour in case I is in the shape of a lozenge, and it approaches to be a rectangle in case II. When the vertical load is 25kN or more, the grounding contour in case I approaches to be a rectangle, and so does that in case II. The contact problem of tyre and pavement was analyzed (Liu and Li 2001), and the conclusion shows that with the increase of the vehicle load, the contour of contact area between one single tyre and surfacing changes from a circle to a lozenge, and then to a rectangle. The results in this paper indicate that the structural difference between steel deck surfacing and road pavement has some influence in the load graphic formula.

The transversal distributions of grounding stress between tyre and surfacing in case I and case II are shown in Figs. 6 and 7, respectively.

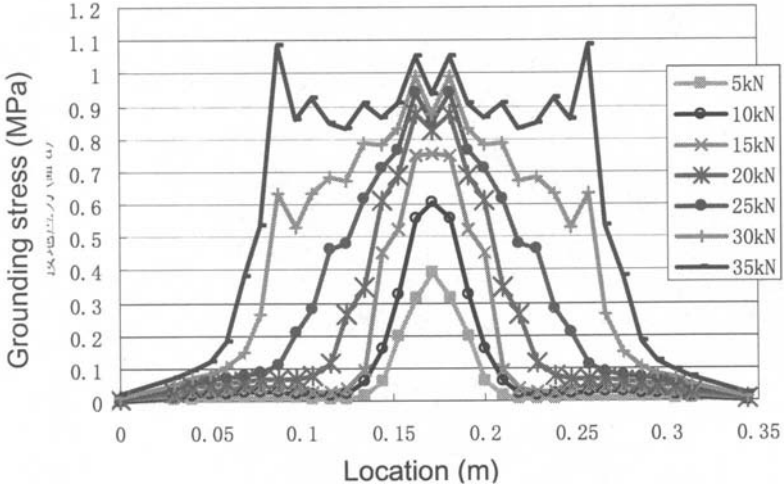

FIG. 6. Transversal distribution of grounding stress in case I.

In Fig. 6, when the axle load is small, the grounding stress distribution contour is triangular in shape. With the increase of axle load, the grounding stress in the sides of contact area increases obviously and the stress distribution contour is rectangular in shape. When the axle load of vehicle is 100kN (the load of one single tyre is 25kN), the grounding stress in the center of contact area approaches to 1MPa and the width of stress distribution contour is about 250mm. When the axle load is 140kN, the grounding stress in the center and sides of contact area both exceed 1MPa, and the width of stress distribution contour exceeds 300mm.

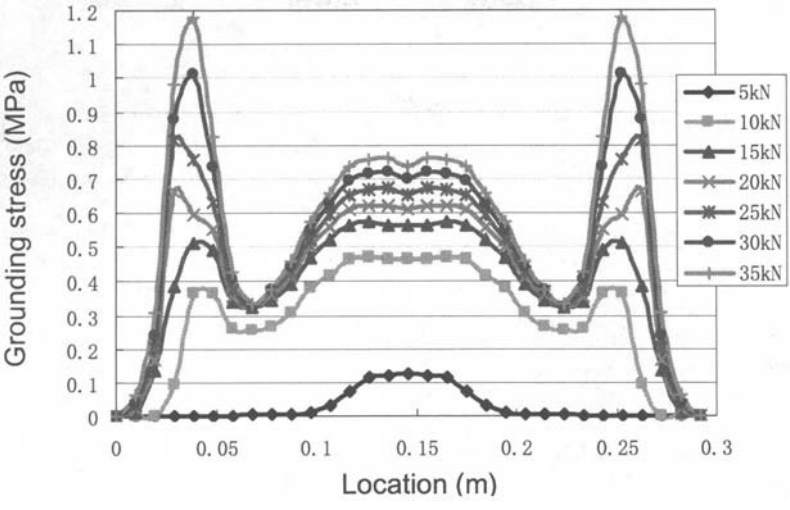

FIG. 7. Transversal distribution of grounding stress in case II.

In Fig. 7, when the axle load is small, the grounding stress distribution contour approaches to be a rectangle. With the increase of axle load, the grounding stress in the sides of contact area increases rapidly, and in turn, the stress distribution contour changes into a saddle. When the axle load is 100kN (the load of one single tyre is 25kN), the grounding stress in the sides of contact area is 0.812MPa, while 0.654MPa in the center.

Case I and Case II have the similarity. With the increase of axle load, the grounding stress in the sides and the center of contact area increase at the same time. The growing rate of the grounding stress in the center of contact area increases in the beginning and then decreases. The growing rate of the grounding stress in the sides of contact area increases all the time, and when the axle load is 20kN, the grounding stress in the sides of contact area exceeds that in the center of contact area.

SIMPLIFICATION OF CALCULATING DIAGRAM OF VEHICLE LOAD

The load chart formula of steel deck surfacing is complicated, and it is impossible to take all of the complicated properties into consideration. In the Specifications for Design of Highway Asphalt Pavement (JTJ014-97) of China, the grounding area of one single tire was simulated by a circle with a diameter of 213mm. In this paper, the research results show the grounding area of one single tire of BZZ-100 is approximate to a rectangle with a width of 250mm. Therefore, it is more suitable to suppose the contact area to be a rectangle. In fact, when the vehicle travels on the steel deck surfacing, the tyres can move in a big range, and the tyres can not be located at the positions exactly in case I or case II. In order to provide a more accurate calculating diagram for the design and optimization of steel deck surfacing, the standard vertical load of one single tyre on steel deck surfacing

can be simplified as a rectangle with a length of 250mm and a width of 140mm.

CONCLUSIONS

The contact model between tyre and steel deck surfacing is established, and the interaction between tyre and steel deck surfacing is researched. Based on the discussion, it can be concluded as follows:

1. The external contour and stress distribution of contact area between tyre and steel deck surfacing are different from that in the highway pavement. With the increase of axle load, the load area of tyre changes from a strip or a lozenge to a rectangle.
2. When the axle load is small, the grounding stress in the center of contact area is larger than that in the sides of contact area. When the axle load is large, the result is opposite.
3. The calculating diagram of BZZ-100, which is used in the design of steel deck surfacing, can be supposed to be a rectangle with a length of 250mm and a width of 140mm.

ACKNOWLEDGEMENTS

The authors are grateful to the Chinese National Science Foundation grant no. 50578038.

REFERENCES

Cheng, G., Zhao G.Q., and Guan Y.M. (2004). "FEA and test research on static contact of meridian tire." *J. Automotive Engineering*. 26(5): 588-592.

Hong, Z.Y., and Wu, G.Z. (2006). "Finite element analysis for of radial tire." *J. Tire Industry*. 26(1): 55-61.

Li, C., and Deng, X.J. (2002). "Analysis of the deck pavement on steel box bridge." *J. Highway and Transportation Research and Development*. 19(2): 60-62.

Li, C., and Wang, Y.S. (2000). "Analysis of reaction of tire grounding." *J. Tire Industry*. 20(5): 276-277.

Li, L.J., and Liu, F. (2000). "Non-linearity of FE of contact deform of meridian tire." *J. Synthetic Rubber Industry*. 23(6): 313-316.

Liu, F., and Li, L.J. (2001). "Non-linearity FEA of contact problem of tire and pavement." *J. Applied Mechanics*. 18(4): 141-146.

Mao, Q. (2000). Research on mechanical behavior of pavement on long-span steel deck bridge deck. *Thesis of Engineering Master*, School of Transportation of Southeast University, China.

Qian, Z.D., and Luo, J. (2004). "Pavement stress analysis of orthotropic steel deck." *J. Traffic and Transportation Engineering*. 4(2): 10-13.

Qian, Z.D., Liu Y., and Huang, W. (2007). "Analysis of the dynamic response of steel-deck pavement with roughness." *China Civil Engineering Journal*. 40(4): 49-53.

Qian, Z.D., Luo, J., and Jing, M.M. (2005). "Mechanical analysis of asphalt concrete paving projects on steel bridge deck." *China J. Highway and Transport*. 18(2): 61-64.

Wang, D.X. (1998). "Evolution and application of FEA of tire." *J. Tire Industry*. 18(6): 395-403.

Wu, W.D., and Guan, D.H. (1996). "Research on the contact of tire and pavement by test model parameters." *J. Tsinghua University*. 36(10): 46-49.

Xie, S.Y., and Zhen, C.C. (2004). "The influence of tire contact press on pavement structure." *J. Chang'an University*. 24(1): 12-16.

Zeng, M.L., Liu, T., and Mwanza, A.D. (2004). "Comparison between JTJ014 and AASHTO methods for asphalt pavement design." *J. Central South Highway Engrg*. 29(4): 14-19.

Fatigue Characteristic of Asphalt

Yiqiu Tan[1], Liyan Shan[2] and Xiaomin Li[3]

[1]Professor, School of Transportation Science and Engineering, Harbin Institute of Technology, No. 202, Haihe Road Nangang District Harbin, China, 150090; yiqiutan@163.com

[2]Ph.D. Candidate, School of Transportation Science and Engineering, Harbin Institute of Technology, No. 202, Haihe Road Nangang District Harbin, China, 150090; myshanliyan@126.com

[3]Ph.D. Instructor, School of Transportation Science and Engineering, Harbin Institute of Technology, No. 202, Haihe Road Nangang District Harbin, China, 150090; hitlxm@126.com

ABSTRACT: The objective of this paper is to research the fatigue characteristic of asphalt. The fatigue characteristic of four kinds of asphalt in continuous loading and loading with rest interval were both researched. DSR was used to measure the rheology characteristic of asphalt. The experiments adopted 15℃ and stress-controlled condition. Four indexes were used to evaluate the fatigue characteristic of asphalt in different kinds of loadings, they are DER (Dissipated Energy Ratio), DR (Damage Rate), δ and 50% reduction in initial complex modulus (50% G^*). The results show that the indexes used in continuous loading test can't reflect the fatigue characteristic of asphalt accurately. Rest periods can lengthen the fatigue life of asphalt, and the modulus of asphalt can recover during rest periods. It is not available to evaluate the fatigue characteristic of asphalt only in continuous loading test. Both the fatigue life in continuous loading and the healing ability should be used to evaluate the fatigue characteristic of asphalt.

INTRODUCTION

At present, fatigue is one of the main distress modes of asphalt pavements in China. So it is essential to understand the fatigue behavior of asphalt and asphalt mixture in order to improve asphalt mixture design and pavement performance. Asphalt is an important composition of asphalt mixture, and its fatigue characteristic has significant effects on mixture, so researching the fatigue characteristic of asphalt is a chief work.

Now the fatigue characteristic of asphalt is usually determined by continuous loading test, and the corresponding fatigue evaluation indexes are also proposed in continuous loading test, such as DER (Dissipated Energy Ratio), DR (Damage Rate), δ and 50% reduction in initial complex modulus (50% G^*) and so on. All the indexes are also used to evaluate the fatigue characteristic of asphalt mixture. Many researchers have used 50%G^* to evaluate the fatigue performance such as Hicks et al. (1993), Smith and Hesp

(2000). Now, more and more researchers would like to use dissipated energy to evaluate the fatigue characteristic, including DER and DR. Jo Sias Daniel and William M. Bisirri (2005) used DER to characterize the fatigue in pavement materials. Yan Yuan (2005) evaluated the merits and drawbacks of DR in evaluating the fatigue performance. Reese (1997) proposed evaluation of changes in the phase angle during fatigue testing.

All the indexes can reflect the fatigue characteristic of asphalt in some extent. But they can't explain the fatigue mechanism of asphalt in essence. Otherwise, asphalt pavements are actually loaded discontinuously due to rest periods between load pulses. Hence, it becomes pertinent to study the fatigue characteristic of asphalt in loading with rest interval.

Now there are some researches about the fatigue characteristic of asphalt mixture in loading with rest interval, such as Goodrich (1988, 1991); Christensen and Anderson (1992); Smith and Hesp (2000); and Yong-Rak Kim et al. (2003). They used dynamic mechanical analysis (DMA) to characterize fatigue characteristic of asphalt mixture in loading with rest interval. And differences among these studies include the sample geometry used, the sample composition, and the loading sequence (including rest periods). María Costro and José A. Sánchez (2006) used rectangle specimen different from DMA to do fatigue test. All the researches showed that rest periods can increase the fatigue life. For asphalt, there are few researches about its characteristic in loading with rest interval. The study of Bahia et al. (1999) showed significant effects of rest periods on fatigue damage recovery of asphalt in dynamic shear rheometer (DSR) tests.

All the researches showed that the fatigue life was longer in loading with rest interval than the fatigue life in continuous loading, and asphalt can heal during rest periods. It also indicated that only using the fatigue indexes in continuous loading test is not reasonable. The characteristic after rest periods can also reflect the fatigue characteristic of asphalt. The fatigue characteristic of asphalt should be studied in both tests, and it is reasonable to combining the characteristic in continuous loading and loading with rest interval to evaluate the fatigue characteristic of asphalt.

TEST METHOD

Four kinds of asphalt were adopted, that was A-90#, A-70#, B-90# and B-70#. They are all neat asphalt. A and B are used to distinguish their sources, and 70# and 90# deputy their marks. Their penetration (25℃), ductility (5℃) and soft point are shown in Table 1. The penetration results show that among all the asphalt B-90# is the most soft one. The penetration value of A-70# and B-70# are close. Ductility of A-90# and B-90# at 5℃ is almost the same. A-70# and B-70# presented break fracture at 5℃. The sequence of soft point is B-70#>B-90#>A-70#>A-90#.

Table 1. The basic performance of asphalt

Asphalt	A-90#	A-70#	B-90#	B-70#
Penetration(25℃), (0.1mm)	89.2	71.5	93.5	69.4
Ductility(5℃), (cm)	10.6	-	10.5	-
Soft Point, (℃)	47	49	50	51

DSR (Figure 1) was used to measure the rheology characteristic of asphalt. Because fatigue failure mainly appears at medium temperature, 15℃ was chosen in the tests. Based on the Yu Jia (2005), the plate with the diameter of 8mm should be used and the distance between the two plates should be 2mm, when the temperature is between 4℃ to 40℃. So the plate with the diameter of 8mm was used in this research. All the asphalt specimens were in stress-controlled condition. The test frequency was 10rad/s. Stress level has important influence on fatigue. If the stress level is too great, the fatigue life will be too short; and if the stress level is too small, the test period will be too long. Stress sweep test was used to confirm the stress level. Figure 2 is the stress sweep results of A asphalt. In order to cut the test time and not make the fatigue life too short, 3.0E+05Pa was chosen for A asphalt. In order to compare the performance of all kinds of asphalt, B asphalt also adopted 3.0E+05Pa. Two kinds of loading modes were used, with and without rest periods respectively. In continuous loading mode, the specimen was sheared continuously until it damaged. In loading mode with rest interval, the specimen was sheared until its modulus reached nearly 50 percent of its initial modulus. Then give it half an hour for rest. After rest, the specimen was sheared until it gets failure. In both tests, no distortion was observed in the asphalt at the periphery of the plates. And combining another observation, fatigue failure appeared to be the result of internal micro-damage.

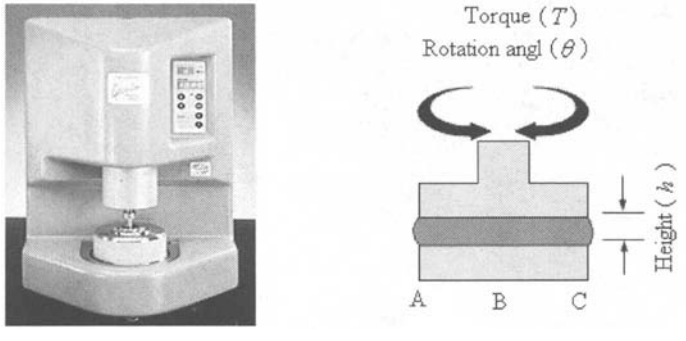

FIG. 1. Dynamic shear rheometer.

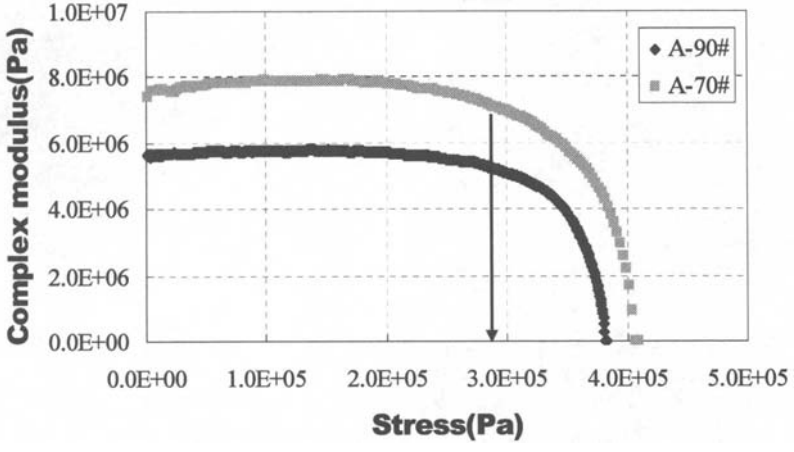

FIG. 2. Stress sweep result.

EVALUATION METHOD

Four indexes were mainly used to evaluate the fatigue characteristic of asphalt in continuous loading test, they are 50% G^*, DER, DR and δ. For 50% G^*, failure is defined at the point when the modulus of the specimen reaches 50 percent of its initial value. DER is an index based on dissipated energy. The formula of DER is shown in Eq. 1. There are two indexes based on DER. One (N_p) is the number of cycles at the turning point in the curve of the number of cycles versus DER, the other (N_{p20}) is the number of cycles at the point when the difference between DER curve and K=1 reaches 20%. DR is another index based on dissipated energy. Its equation is shown in Eq. 2. The turning point in the curve of the number of cycles versus DR is defined as fatigue failure. Carpenter and Shen (2006) used the ratio of dissipated energy change to evaluate the fatigue performance, and they name it RDEC. In fact, DR and RDEC is the same in essence. For phase angle, fatigue is also the turning point of the curve.

$$DER = \frac{\sum_{i=1}^{n} w_i}{w_n} \tag{1}$$

where,

ω_i = Dissipated energy in load cycle i; and
ω_n = Dissipated energy in load cycle n .

$$DR = \frac{w_i - w_{i-1}}{w_{i-1}} \tag{2}$$

where,

ω_i = Dissipated energy in load cycle i; and

ω_{i-1} = Dissipated energy in load cycle $i-1$.

Otherwise, in the loading test with rest interval, complex modulus, dissipated energy and phase angle before and after rest periods were used to evaluate the healing characteristic of asphalt.

TEST RESULTS AND ANALYSIS

Figures 3 through 6 show the results of asphalt in continuous loading test. Complex modulus increases incessantly with the number of cycles increasing, as shown in Figure 3. Phase angle can also reflect the change of fatigue performance of asphalt. In Figure 4, phase angle increases with time. At first, it increases slowly. When the number of cycles gets to some level, phase angle increases quickly.

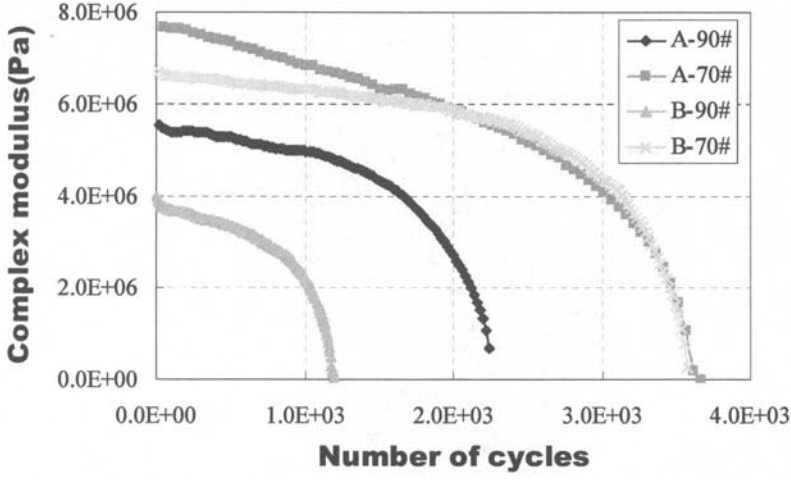

FIG. 3. Relationship between the number of cycles and modulus.

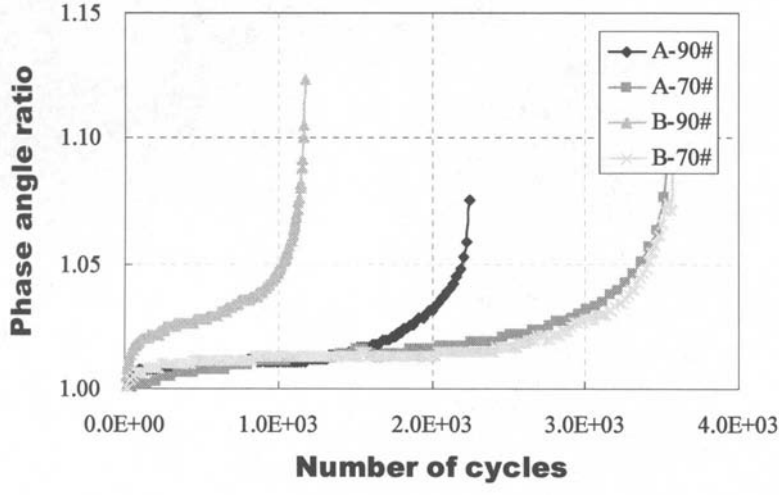

FIG. 4. Relationship between the number of cycles and phase angle ratio.

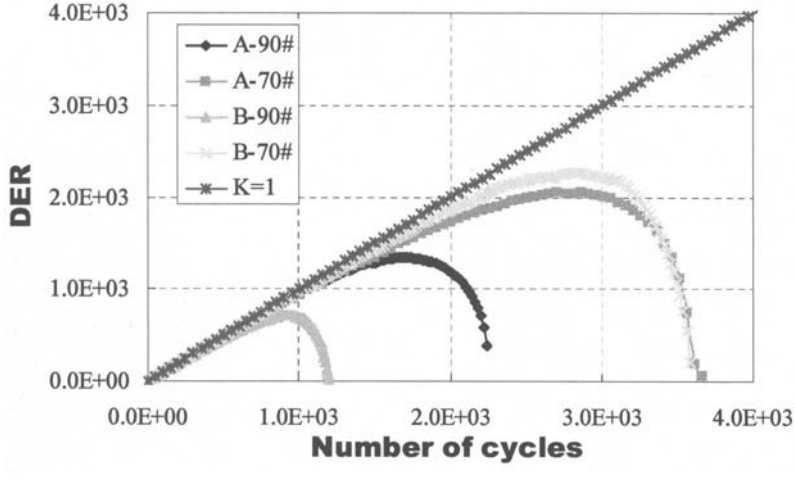

FIG. 5. Relationship between the number of cycles and DER.

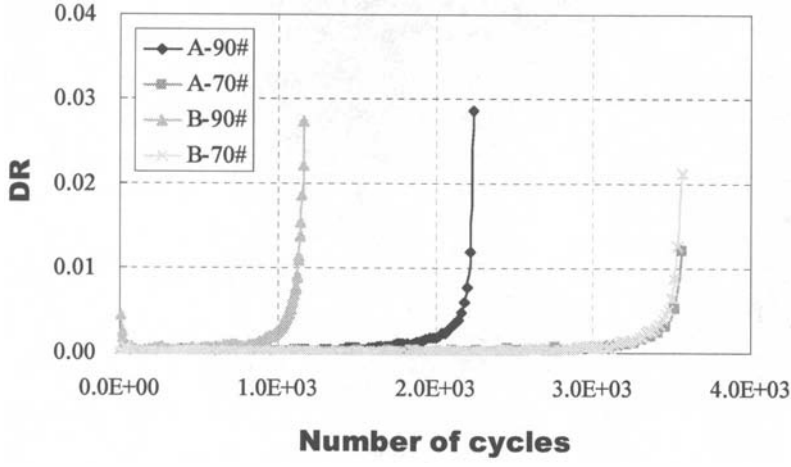

FIG. 6. Relationship between the number of cycles and DR.

Figure 5 shows the relationship between DER and the number of cycles. There is an obvious turning point in the curve. When the specimen starts to bear the load, the curve of DER versus the number of cycles is almost a beeline. With the number of cycles increasing, the curve starts to departure the curve of K=1. Energy can be used to explain this phenomenon. In the front part of the curve, the energy loses as the form of viscouselasticity, and the failure can be ignored. So the DER curve is almost a beeline. More energy loses for the production of cracks, and DER increases gradually. For more energy losing, the DER curve starts to departure the curve of K=1. With cracks expanding, the dissipated energy in a cycle increases rapidly, so the ratio of accumulative dissipated energy to dissipated energy of one cycle decreases, that is DER decreases.

The curve of DR (Figure 6) can also be explained by dissipated energy. At the beginning of loading, the dissipated energy changes very little, and the dissipated energy ratio approaches zero. With the specimen being sheared continually, cracks start to expand, so the dissipated energy of one cycle increases and DR increases. This change principle is similar to DER.

The above figures can also show the relationship among the fatigue performance of different asphalt. The specific fatigue lives of all the asphalt are shown in Table 2. No matter using any index, the fatigue life of asphalt A-90# is longer than that of asphalt B-90#, and the fatigue performance of 70# asphalt are better than that of 90# asphalt. But the fatigue performance between asphalt A-70# and B-70# are not clear. Using N_p, the fatigue life of A-70# is longer than that of B-70#. Using 50% G^*, N_{p20}, DR or δ, the fatigue life of B-70# is longer than that of A-70#. The results using the four indexes can only distinguish the fatigue performance between A-90# and B-90#, but can't determine which one is better between A-70# and B-70#. That explains that the indexes can reflect

the fatigue performance in some extent, but they have some deficiency. For one kind of asphalt, the fatigue life may be different using different indexes. The fatigue life sequence among different kinds of asphalt may be different using different indexes.

Table 2. Fatigue life in 3.0E+05 Pa using different indexes

Index	50% G^*	DER(N_p)	DER(N_{p20})	DR	δ
A-90#	1907	1612	1610	1943	2029
B-90#	1047	924	890	1127	987
A-70#	3112	2861	2460	3180	3313
B-70#	3277	2812	2831	3345	3379

Note: N_p is the turning point in the curve of the number of cycles versus DER, N_{p20} is the point when the difference between DER curve and K=1 reaches 20%

The above are the characteristics of asphalt in continuous loading. As the introduction stated, rest periods have important effects on fatigue life, and the characteristic of asphalt in loading with rest interval will be analyzed in the following paragraphs.

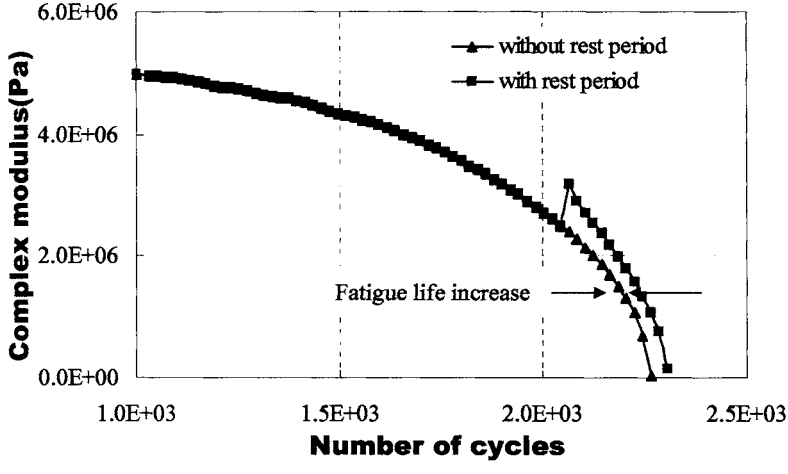

FIG. 7. Response of A-90# in loading with rest interval.

Figure 7 is the response of A-90#. As the figure shown, complex modulus increases after the rest period, and the introduction of rest periods can lengthen the fatigue life of asphalt. After the rest period, dissipated energy and phase angle decrease, the increasing or decreasing rate of different indexes are shown in Table 3. The healing performance of A-90# is better than that of B-90#, and the healing performance of B-70# is better that of

A-70#. And the higher the grade is, the better the healing performance is.

Table 3 shows that the healing ability of 90# is better than that of 70# asphalt. Comparing the fatigue life in continuous loading and the healing characteristic after rest periods, for 90# asphalt, the healing ability is accordance with the fatigue life, that is the fatigue life of A-90# is longer than that of B-90#, and the healing ability of A-90# is better than that of B-90#. For 70# asphalt, the fatigue performance between the two kinds of asphalt can't be distinguished as Table 2 shows. But the healing performance can be distinguished using the indexes in Table 3. That means besides the fatigue characteristic in continuous loading, the healing characteristic of asphalt in loading with rest interval should also be used to distinguish the fatigue characteristic. But which index is more suitable both in continuous loading and loading with rest interval needs to be studied further.

Table 3. Changing rate of each index for different asphalt

Asphalt	Index		
	Increasing rate of G^* (%)	Decreasing rate of Dissipated Energy (%)	Decreasing rate of δ (%)
A-90#	15.09	25.32	3.3
B-90#	14.50	24.88	2.8
A-70#	10.09	18.91	2.3
B-70#	11.44	20.87	2.7

CONCLUSIONS

The aim of this research is to study the fatigue characteristic of asphalt in continuous loading test and loading test with rest interval. Based on the experimental findings and comparison of these results, the conclusions derived from this investigation are as follows:

1. 50% G^*, DER, DR and δ can reflect the fatigue characteristic of asphalt in some aspects, but they have some deficiency. They can't distinguish the fatigue performance of different asphalt in some conditions. The fatigue life of the same asphalt may be different by using different indexes.
2. After rest periods, complex modulus will increase, and dissipated energy and phase angle will decrease. Rest periods can lengthen the fatigue life of asphalt. Asphalt has healing ability.
3. Healing ability of asphalt has important influence on fatigue performance. Both the fatigue life in continuous loading and the healing ability should be used to evaluate the fatigue characteristic of asphalt. But which index is more suitable both in continuous loading and loading with rest interval needs to be studied further.

ACKNOWLEDGMENTS

The writers would like to acknowledge "National Natural and Science Fund

(50778057)" for their financial support.

REFERENCES

Bahia, H., Zhai, H., Bonnetti, K., and Kose, S. (1999). "Non-linear viscoelastic and fatigue properties of asphalt binders." *J. Assn. Asphalt Paving Technologists*, 68, 1-34

Christensen, D. W., and Anderson, D. A. (1992). "Interpretation of dynamic mechanical test data for paving grade asphalt cements." *J. Assn. of Asphalt Paving Technologists*, 61, 67-116

Carpenter, S. H., and Shen, S. (2006). "A dissipated energy approach to study Hot-Mix Asphalt healing in fatigue." *Transportation Research Record (TRR): Journal of the Transportation Research Board* (No. 1970), 78-185

Goodrich, J. L. (1988). "Asphalt and polymer modified asphalt properties related to the performance of asphalt concrete mixes." *J. Assn. Asphalt Paving Technologists*, 57, 116-175

Goodrich, J. L. (1991). "Asphaltic binder rheology, asphalt concrete rheology, and asphalt concrete mix properties." *J. Assn. Asphalt Paving Technologist*, 60, 80-120

Hicks, R.G, Finn, F. N., Monismith, C. L., and Leahy, R. B. (1993). "Validation of SHRP binder specification through mix testing." *J. Assn. Asphalt Paving Technologists*, 62, 565-614

Jo Sias Daniel, William M.Bisirri. (2005) "Characterizing fatigue in pavement materials using a dissipated energy." *GSP 130 Advance in Pavement Engineering*, 1-10

J.-P. Planche, D. A. Anderson, G. Gauthier, Y. M. Le Hir and D. Martin.(2004) "Evaluation of fatigue properties of bituminous binders." *Materials and Structures*, 37, 356-359

María Costro, and José A. Sánchez. (2006). "Fatigue and healing of asphalt mixtures: discriminate analysis of fatigue curves." *Journal of Transportation Engineering*, 132 (2), 168-174

Reese, R. (1997). "Properties of aged asphalt binder related to asphalt concrete fatigue life." *J. Assn. Asphalt Paving Technologists*, 66, 604-632

Smith, B. J., and Hesp, S. (2000). "Crack pinning in asphalt mastic and concrete: regular fatigue studies." *Transportation Research Record 1728*, Transportation Research Board, Washington, D. C., 72-81

Yong-Rak Kim, D. N. Little, P. E., F. ASCE, and R. L. Lytton, P. E., F. ASCE. (2003). "Fatigue and healing characterization of asphalt mixures." *Journal of Materials in Civiling Engineering*, 15 (1), 75-83

Yan Yuan (2005). "Fatigue performance evaluation of modified asphalt binder." *Dissertation of South China University of Technology*, 14-16

Yu Jia, Rong-ji Cao, and Ben-jin Li Translation (2005). "Superpave fundamentals reference manual" China Communications Press

Coefficient of Thermal Expansion of Concrete for Rigid Pavement Design

Nam Tran[1], A.M. ASCE, Micah Hale[2], M. ASCE, and Kevin Hall[3], M. ASCE

[1]Lead Research Engineer, National Center for Asphalt Technology at Auburn University, 277 Technology Parkway, Auburn, AL 36830; nht0002@auburn.edu

[2]Associate Professor, Department of Civil Engineering, University of Arkansas, 4190 Bell Engineering Center, Fayetteville, AR 72701; micah@uark.edu

[3]Professor and Head, Department of Civil Engineering, University of Arkansas, 4190 Bell Engineering Center, Fayetteville, AR 72701; kdhall@uark.edu

ABSTRACT: The new Mechanistic-Empirical Pavement Design Guide (MEPDG) requires the coefficient of thermal expansion (CTE) of concrete materials as a direct input to determine critical pavement distresses. Since equipment for measuring CTE was not available for commercial procurement at the time of this study, an automated device was developed in this study in accordance with AASHTO TP 60. The device is easy to use and provide sufficient data for design applications. Preliminary precision statements of the AASHTO TP 60 protocol using the developed measuring device were established for use at this moment, and they would be refined when additional CTE data become available. Further analyses of CTE data found that the type of coarse aggregates used for a mixture significantly influenced both the CTE values and pavement performance predictions. While the effect of nominal maximum aggregate size on the CTE and predicted pavement performance was not significant in this study, further evaluation of this effect should be done because of limited nominal maximum aggregate sizes used in this study.

INTRODUCTION

The coefficient of thermal expansion (CTE) has long been recognized as an important property of portland cement concrete (PCC). CTE is measured as the change in length per change in temperature. In the 1993 Edition of the American Association of State Highway and Transportation Officials (AASHTO) Guide for the Design of Pavement Structures (AASHTO 1993), CTE is used only for transverse joint sealant design in jointed plain concrete pavements (JPCP) and longitudinal reinforcement design in continuously reinforced concrete pavements (CRCP). It is not a direct input for structural pavement design. In the new Mechanistic-Empirical Pavement Design Guide (MEPDG) developed under National Cooperative Highway Research Program (NCHRP) Project 1-37A (ARA 2004), the CTE is required as a direct input for structural pavement design procedures. It is used directly or indirectly

to determine joint and crack openings as well as critical PCC slab distresses.

Many state agencies currently do not routinely determine the CTE of PCC materials. During the design process, a typical CTE is used rather than a mixture specific value. This, however, may lead to improper predictions of the pavement thermal responses and potential distress developments using the MEPDG design procedures in the future. Studies (Hall 2005, Nantung 2005) have identified the CTE of PCC materials as a very sensitive parameter affecting rigid pavement distress predictions by the MEPDG software. Thus, conducting CTE tests will help better predict the effect of mixture specific thermal response on pavement performance and utilize the benefit of MEPDG.

This paper is prepared based on the results of a research project sponsored by the Arkansas State Highway and Transportation Department (AHTD), which includes (1) development of testing equipment for measuring the CTE; (2) establishment of preliminary precision statements for the CTE test method using the developed measuring device; (3) evaluation of factors that significantly affect the CTE; and (4) analyses of the sensitivity of predicted pavement performance to the measured CTE.

DEVELOPMENT OF TESTING EQUIPMENT

The CTE of PCC materials can be determined using the testing procedure described in AASHTO TP 60, *Standard Test Method for the Coefficient of Thermal Expansion of Hydraulic Cement Concrete*. However, the procedure and equipment for this test method are currently undergoing evaluation, and the equipment is currently not available for commercial procurement. Therefore, a concrete thermal expansion measuring device in compliance with AASHTO TP 60 was designed and built by Challenge Technology for this project. Figure 1 shows the device.

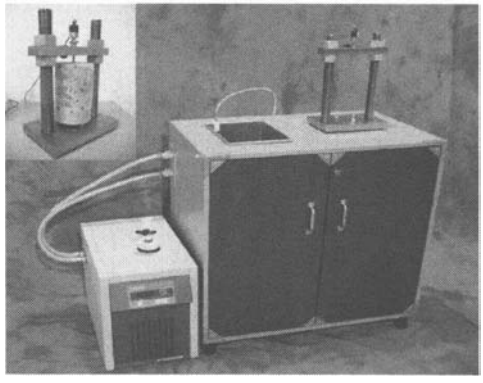

FIG. 1. Coefficient of thermal expansion measuring device.

The device contained a water bath suitable for submerging a measuring frame and test sample, mounted in a cabinet separate from a heating/cooling recirculation unit. Isolating the recirculation unit from the cabinet minimized the effect of vibration and

electronic noise on the measuring system. The measuring frame was made of A304 stainless steel to prevent corrosion problems and to minimize frame expansion during heating. A high-precision linear variable differential transducer (LVDT) was mounted on the stainless frame and centered above a saturated cylindrical concrete specimen, which was supported by three hemispherical points. The LVDT was used with a 16-bit data acquisition system to precisely record the change in sample length with corresponding temperature changes.

The device was equipped with a fully automated temperature control and specimen length measurement to minimize user interactions during testing, and to subsequently improve reliability and accuracy of the test. The thermistor was used to monitor and also control water bath temperature. In addition, it was found that water level changes due to evaporation had a significant impact on length change measurement due to changes in the submerged part of the measuring frame, which expands and contracts during heating and cooling. A water level controller was used to insure a constant water level to eliminate the effect of evaporation.

The device also includes user friendly software developed in compliance with the AASHTO TP 60 protocol. It monitors all test startup and run parameters. The software automatically controls a uniform increase and decrease in temperature between 10°C and 50°C. The software has graphical and text displays of temperature and length change information while test is running. The software automatically repeats the test until two successive CTE measurements are within 0.3 μstrain/°C. Data is saved at 10 minute intervals, allowing for further data analysis. The system also includes an automated calibration procedure, using an A304 stainless steel standard sample and calibration software to insure accuracy in various ambient temperature environments.

PRELIMINARY PRECISION OF AASHTO TEST METHOD USING DEVELOPED DEVICE

The AASHTO TP 60 test procedure and equipment are currently under evaluation; no precision or bias has been established for this test. In order for this test method and the developed device to be used in the future, the precision and bias of the AASHTO TP 60 protocol using the developed CTE measuring device must be established. Since development of precision and bias statements for a test method requires a significant effort, this study only attempted to establish preliminary precision and bias statements for the AASHTO TP 60 test protocol using the developed CTE measuring device. These statements will be further refined when more CTE data are available.

The study undertaken to establish the preliminary precision of the AASHTO TP 60 test protocol using the developed CTE device was designed and executed in accordance with ASTM C802, *Standard Practice for Conducting an Interlaboratory Test Program to Determine the Precision of Test Methods for Construction Materials*. The interlaboratory study was performed in two laboratories at the University of Arkansas and Challenge Technology. The two laboratories determined the coefficients of thermal expansion of three cylindrical specimens for each of four mixtures, including a standard concrete mixture using 3/4" sandstone aggregates, standard mixture using 3/4" limestone aggregates, self-consolidating concrete mixture

using 3/8" limestone aggregates, and cement paste. The cement paste was wet-sieved from the standard mixture using 3/4" limestone aggregates. The specimens were prepared in accordance with ASTM C31/C192. Thus, the data constitute an analysis with $p = 2$ laboratories; q = four materials; and n = three replicates.

The CTE data measured in the two laboratories are summarized in Table 1. The analysis of the interlaboratory test results was performed in accordance with ASTM C802. The analysis included the following steps:

- Processing for outliers – The Dixon test described in ASTM E178, *Standard Practice for Dealing with Outlying Observations*, was used to examine the data. No outliers were eliminated through this process.
- Performing within and between analysis for all materials – The analysis determined the estimates of precision, including variances, standard deviation, and coefficients of variation. These precision components were developed in accordance with ASTM C802 and ASTM C670, *Practice for Preparing Precision and Bias Statements for Test Methods for Construction Materials*.
- Investigating for interactions – The analysis shows that the variability of the CTE results of cement paste is much higher than the variability of the test results for other materials. Two levels of standard deviation may exist, one for concrete mixtures with coarse aggregates, and another for cement paste. Thus, the precision statements may be required for the two materials.

Table 1. Summary of Interlaboratory Test Results

Mixture	Sample	CTE (μstrain/°C)		Typical CTE (μstrain/°C)	
		U of A	Challenge	Average*	Std Dev*
Standard with 3/4" Sandstone	1	12.13	11.97		
	2	11.84	12.02		
	3	12.04	11.99		
	Average	12.01	11.99	11.7	1.4
Standard with 3/4" Limestone	1	10.37	10.19		
	2	10.22	10.21		
	3	10.33	10.17		
	Average	10.31	10.19	9.7	1.3
Self-Consolidating with 3/8" Limestone	1	10.44	10.69		
	2	10.60	10.40		
	3	10.73	10.64		
	Average	10.59	10.58	9.7	1.3
Cement Paste	1	12.42	12.74		
	2	12.76	12.53		
	3	12.44	11.93		
	Average	12.54	12.40		

* After Mallela et al. 2005

Based on the analyses, the following preliminary precision statements are proposed for use with the AASHTO TP 60 protocol using the developed CTE measuring device. It is acknowledged that further research efforts will be needed to refine these statements. The statements are developed in accordance with ASTM C670.

- *Single-Operator Precision* – The single-operator coefficient of variation of a single test result has been found to be 0.9 percent for concrete mixtures with coarse aggregates and 2.6 percent for cement paste. Therefore, results of two properly conducted CTE tests by the same operator should not differ by more than 2.5 percent or 7.3 percent of the average of the two results when the cylindrical specimens are made of concrete mixtures with coarse aggregates or cement paste only, respectively.
- *Multilaboratory Precision* – The multilaboratory coefficient of variation of a single test result has been found to be 1.3 percent for concrete mixtures with coarse aggregates and 3.7 percent for cement paste. Therefore, results of two properly conducted CTE tests in different laboratories on the same material should not differ by more than 3.6 percent or 10.4 percent of the average of the two results when the cylindrical specimens are made of concrete mixtures with coarse aggregates or cement paste only, respectively.

EFFECT OF MIX CONSTITUENT PROPERTIES ON VARIABILITY OF CTE

Further analyses of the CTE results show that the CTE of PCC materials is influenced by mixture constituent properties, including the content and type of coarse aggregates used in the concrete mixture. As shown in Table 1, cement paste seems to have a higher coefficient of thermal expansion than coarse aggregates. This agrees with earlier findings (Won 2005, Mallela et al. 2005). The observation implies that the CTE of a concrete mixture will vary if the percentage of coarse aggregates changes during construction. Thus, the effect of the variability of concrete CTE during construction on pavement performance should be quantified.

A concrete mixture using sandstone aggregates has a slightly lower thermal coefficient than cement paste. The difference between the two average CTE values was less than 0.5 μstrain/°C. Won (2005) reported that some coarse aggregate, such as gravels, even had a higher thermal coefficient than cement paste. Among four concrete mixtures used in this study, a standard concrete mixture using 3/4" limestone aggregates had the lowest CTE. Other studies (Mallela et al. 2005, Hossain 2006) also reported that limestone aggregates seem to have a lower CTE compared to other coarse aggregates. The effect of the coarse aggregate content on the CTE is only significant if the CTE values of the coarse aggregates and cement paste are significantly different, as for the limestone aggregates and cement paste in this study.

Two nominal maximum aggregate sizes (NMAS) of 3/4"and 3/8" were used in this study. The two concrete mixtures using these limestone aggregates had very close CTE results. The difference between the two average values was less than 0.4 μstrain/°C. The effect of NMAS on CTE should be further studied.

Based on these observations, it is recommended that a future testing plan for developing typical CTE inputs for implementation of the MEPDG in a state should

include all aggregate and cement types used for PCC materials in rigid pavement construction.

EFFECT OF CTE VARIABILITY ON PAVEMENT PERFORMANCE

The variability of concrete CTE observed in this study is influenced by two sources: (1) the variability of the test method; and (2) mixture constituent properties, including the content and type of coarse aggregates. A sensitivity analysis was performed to evaluate the effect of the CTE variability on rigid pavement performance predictions provided by the MEPDG software (version 0.900). A summary of the inputs used in the sensitivity analysis is presented in Table 2.

CTE values shown in Table 2 included the default CTE of 10 μstrain/°C recommended in the MEPDG software and the four CTE results determined in this study – 10.3, 10.6, 12.1 and 12.4 μstrain/°C for a standard mixture with 3/4" limestone aggregates, self-consolidating concrete with 3/8" limestone aggregates, standard mixture with 3/4" sandstone aggregates, and cement paste, respectively. Other inputs which were used in the analysis but not shown in Table 2 are default values recommended in the MEPDG software. The analyses were performed by varying the CTE input. Other inputs were kept constant. Three pavement distresses, including International Roughness Index (IRI), fatigue cracking, and faulting, were predicted by the MEPDG software for a 20-year design period.

Table 2. Inputs for Sensitivity Analysis of Concrete CTE

Description	Input
General Information	
Type of Design	Jointed Plain Concrete Pavement
Reliability	50%
Design Life	20 years
Traffic Volume	
Two-way AADTT	10,000
Lanes in Design Direction	2
Climate	Fayetteville, AR
Concrete Layer	
Thickness	30 (cm)
Coefficient of Thermal Expansion	10.0, 10.3, 10.6, 12.1, 12.4 (10^{-6}/°C)
Granular Base	
Thickness	20 (cm)
Modulus	275 (MPa)
Subgrade	
Classification	A-7-6
Modulus	35 (MPa)

It is acknowledged that changing the amount of coarse aggregates in the mixture also varies the strength of concrete, resulting in different pavement performance predictions. A thorough investigation regarding the effect of these interactions on

pavement performance predictions would require a considerable research effort and is beyond the scope of this study. The main purpose of this analysis is not to quantify the effects of constituent properties on CTE results and pavement performance predictions, but to investigate the trends of these effects.

Figure 2 presents predicted pavement distresses, including IRI, cracking, and faulting. The pavement performance predictions are similar for the two limestone concrete mixtures having different nominal maximum aggregate sizes. Since the evaluation of the effect of aggregate size is limited to only two nominal maximum aggregate sizes of 3/4" and 3/8", this effect should be further investigated.

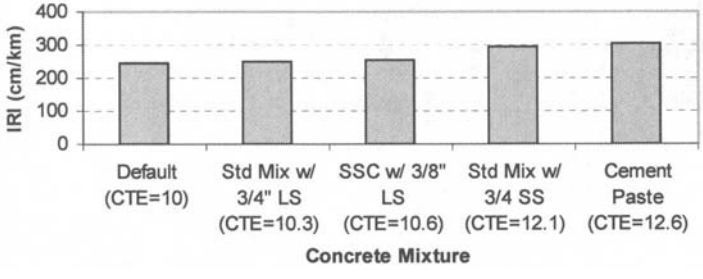

(a) International Roughness Index versus coefficient of thermal expansion.

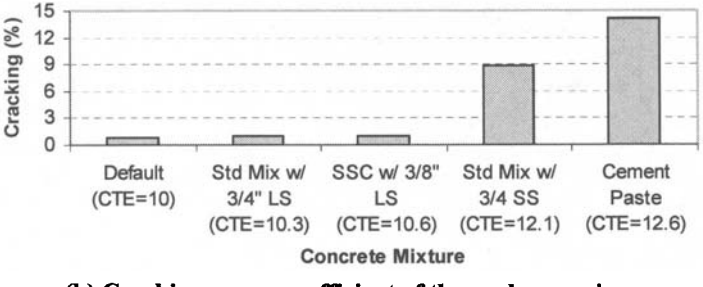

(b) Cracking versus coefficient of thermal expansion

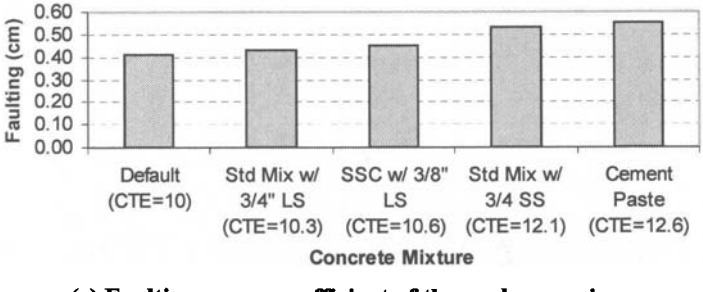

(c) Faulting versus coefficient of thermal expansion

FIG. 2. Effect of constituent properties on pavement performance predictions.

As seen in Figure 2, the predicted pavement distresses for the two standard mixtures containing limestone and sandstone aggregates are different. The differences are about 15 percent for IRI and 20 percent for faulting. Thus, the type of aggregates used for a concrete mixture significantly affects the mixture CTE and predicted pavement distresses.

Compared to the standard mixture with limestone aggregates, cement paste has a higher CTE value, resulting in higher predicted pavement distresses. Thus for limestone aggregates, the content of coarse aggregates significantly affects the CTE and predicted pavement distresses. However, compared to the standard mixture with sandstone aggregates, cement paste has a similar CTE value, resulting in similar predicted pavement distresses. Thus in this case, the CTE is not sensitive to the content of coarse aggregates. The sensitivity of the CTE and pavement performance prediction to the content of coarse aggregates is therefore dependent on the type of coarse aggregates used in the mixture.

CONCLUSIONS

The following observations and conclusions are made based on the results of this study:

- The CTE measuring equipment developed in accordance with the AASHTO TP 60 for this study is easy to use and provides accurate data for future design applications.
- The preliminary precision statements proposed in this study can be used at this moment and should be refined when additional CTE data become available.
- The CTE values and pavement performance predictions are similar for the two limestone concrete mixtures having nominal maximum aggregate sizes of 3/4" and 3/8". Since the evaluation of the effect of aggregate size is limited to only two nominal maximum aggregate sizes, this effect should be further evaluated.
- The type of coarse aggregates used for a mixture significantly influences the CTE and pavement performance predictions.
- Coarse aggregates and cement paste have different CTE. Thus, the content of coarse aggregates used for a mixture may significantly affect the CTE and pavement performance predictions, and the effect is dependent on the type of coarse aggregates used for the mixture. For this study, the effect is significant for limestone aggregates but not significant for sandstone aggregates.

RECOMMENDATIONS

The following recommendations are made based on the findings in this study:

- The AASHTO TP 60 protocol and the developed CTE measuring device with the preliminary precision statements can be used for determining the CTE for future design applications.
- It is recommended that a future testing plan for developing typical CTE inputs for implementation of the MEPDG in a state or region should include all aggregate and cement types used for PCC materials in rigid pavement construction. The

interaction effect of aggregate and cement types on the CTE and pavement performance predictions should be evaluated.

ACKNOWLEDGEMENTS

This paper was prepared under research project TRC-0708, "PCC Materials Input Values for Mechanistic Empirical Pavement Design Guide", sponsored by the Arkansas State Highway and Transportation Department and the Federal Highway Administration. The views expressed in this paper and the accuracy of the data and facts contained herein are the sole responsibility of the authors, and do not necessarily represent the official views of the listed sponsoring agencies. This paper does not constitute a standard, specification, or regulation. Comments contained in this paper related to specific testing equipment should not be considered an endorsement of any commercial product or service; no such endorsement is intended or implied.

REFERENCES

AASHTO (1993). *Guide for Design of Pavement Structures*. American Association of State Highway and Transportation Officials, Washington, D.C.

ARA, Inc., ERES Consultants Division (2004). *Guide for Mechanistic-Empirical Design of New and Rehabilitated Pavement Structures*. NCHRP Project 1-37A, Final Report, Applied Research Associates, Inc., ERES Consultants Division.

Hall, K. D. and Beam S. (2005). "Estimating the Sensitivity of Design Input Variables for Rigid Pavement Analysis with a Mechanistic-Empirical Design Guide." *Transportation Research Record* (No. 1919), TRB, National Research Council, Washington, D.C.

Hossain, M., Khanum, T., Tanesi, J., Schieber, G. and Montney, R. (2006). "The PCC Coefficient of Thermal Expansion Input for the Mechanistic-Empirical Pavement Design Guide." *Proc., the 85th Annual Meeting of Transportation Research Board* (CD-ROM), TRB, National Research Council, Washington, D.C.

Mallela, J., Abbas, A., Harman, T., Rao, C. , Liu, R. and Darter, M. (2005). "Measurement and Significance of Coefficient of Thermal Expansion of Concrete in Rigid Pavement Design." *Transportation Research Record* (No. 1919), TRB, National Research Council, Washington, D.C.

Nantung, T., Chehab, G., Newbolds, S., Galal, K., Li, K. and Kim, D. (2005). "Implementation initiatives of the Mechanistic-Empirical Pavement Design Guide in Indiana." *Transportation Research Record* (No. 1919), TRB, National Research Council, Washington, D.C.

Won, M. (2005). "Improvements of Testing Procedures for Concrete Coefficient of Thermal Expansion." *Transportation Research Record* (No. 1919), TRB, National Research Council, Washington, D.C.

Two Dimensional and Three Dimensional Discrete Element Models for HMA

Zhanping You[1], Sanjeev Adhikari[2] and Qingli Dai[3]

[1]Tomasini Assistant Professor, Department of Civil and Environmental Engineering, Michigan Technological University, 1400 Townsend Drive ,Houghton, MI, 49931-1295; zyou@mtu.edu
[2]Graduate Research Assistant, Department of Civil and Environmental Engineering, Michigan Technological University, 1400 Townsend Drive ,Houghton, MI, 49931-1295; sadhikar@mtu.edu
[3]Research Assistant Professor, Department of Mechanical Engineering-Engineering Mechanics, Michigan Technological University, 1400 Townsend Drive ,Houghton, MI, 49931-1295; qingdai@mtu.edu

ABSTRACT: Hot Mix Asphalt (HMA) is a composite material that consists of mineral aggregates, asphalt binders and air voids. A Discrete Element Model (DEM) of the HMA microstructure was developed to study the stiffness behavior in both two dimensions (2D) and three dimensions (3D). Image analysis techniques were used to capture the HMA microstructure. The HMA microstructure was divided into two phases: aggregates phase (i.e., aggregates larger than 1.18mm sieve) and mastic phase (i.e., with binder and aggregates smaller than 1.18 mm). Air voids were modeled within the DEM to meet a specific air void level (i.e. 0%, 4%, and 7%) by using a random algorithm. The 3D microstructure of the asphalt mixture was obtained by using a number of parallel 2D images. The input data on the models included not only the aggregate and mastic properties, but also the microstructure of the aggregate skeleton and mastic distribution. Both 2D and 3D models were used to compute the stress-strain response under compressive loads. The moduli of the specimens were computed from the stress-strain curve in the DEM simulation. The moduli of the 2D and 3D models were then compared with the experimental measurements. It was found that the 3D discrete element models were able to predict the mixture dynamic modulus across a range of temperatures and loading frequencies. The 3D model predictions were much better than that of the 2D model. In addition, the effect of different air void percentages was discussed in this paper. As air void increased, the predicted modulus decreased.

INTRODUCTION

Hot mix asphalt (HMA) is a complex composite material made of aggregates, asphalt binder and air voids. The micromechanical behavior of this composite material is determined by the interaction between its constituents. This multiphase material has different properties from the original components—aggregate and mastic. The mastic includes fine aggregate, sand and fines embedded in a matrix of

asphalt binder. A cubic inch of asphalt mixture may include millions of mineral particles (coarse and fine aggregates, sand, and fines) (Buttlar and You 2001; You and Buttlar 2005; You and Dai 2007).

In this paper, the 2D and 3D micromechanical discrete element models were developed to simulate and characterize the modulus of a HMA asphalt mixture specimen. The discrete element models utilized in this study used disks for 2D and balls for 3D to represent the microstructure of the HMA mixture with air voids. The 2D discrete element model will be used to characterize the mixture moduli at different air voids. Then, the 3D discrete element model is generated with a number of layered 2D discrete element models. One of the unique features of the models is that the air void phase was modeled in both 2D and 3D.

DISCRETE ELEMENT MODELING

The discrete element method was developed to be used in rock mechanics (Cundall 1971). A micromechanical model for asphalt concrete was developed to investigate pavement rutting (Rothenburg et al. 1992). An innovative feature of the model was the inter-granular interactions. Using this model, if the aggregate properties (such as Young's modulus, Poisson's ratio, aggregate normal stiffness, shear stiffness, and friction angle) and the binder/mastic properties (such as bitumen viscosity, elastic bulk modulus, and asphalt content) are known, it is possible to predict mixture properties. Rothenburg's model is useful for modeling asphalt concrete because it considers not only the aggregate-binder interaction but also intergranular interactions in the presence of the binder. Another discrete element model was developed based on the TRUBAL program to simulate HMA (Chang and Meegoda 1997). An idealized model was prepared to investigate the mechanical behavior of idealized asphalt materials (Collop et al. 2004). It was stated that the DEM can be possibly used to predict initial elastic, visco-elastic and visco-plastic behavior of asphalt mixtures.

Buttlar and You (2001) showed that the traditional micromechanical models, such as the composite spheres model and the arbitrary phase geometry model, do not adequately describe the complex microstructure of asphalt mixtures. These models over- or under-predict the stiffness (or modulus) of asphalt mixtures due to a primary inability of the models to properly predict the contribution of the aggregate interlock (i.e., lack of microstructure in the model) to the overall response of the mixture (You and Buttlar 2006). The 3D models were expected to have a better capability to predict the mixture's aggregate interlock and improve the predictions.

The discrete element models can simulate the complex behavior of a material by combining simple contact constitutive models with complex geometrical features. There are a number of contact models available. The constitutive model acting at a particular contact consists of three parts: a stiffness model, a slip model, and a bonding model (Itasca Consulting Group 2004b). The stiffness model provides an elastic relationship between the contact force and relative displacement. The slip model enforces a relation between shear and normal contact forces, such that the two contacting balls may slip relative to one another. The bonding model serves to limit the total normal force and shear force that the contact can carry by enforcing bond-

strength limits. The stiffness model is the most important parameter used in this study, which focuses on stiffness estimation. The stiffness model also provides an elastic relationship between the contact force and relative displacement between particles. The discrete (distinct) element codes, Particle Flow Code (PFC) 2D and 3D were used in this study.

PREPARATION OF THE 2D AND 3D DISCRETE ELEMENT MODELS

The asphalt mixture's microstructure was captured using a high-resolution flat scanner, manipulated using image processing techniques and reconstructed into an assembly of 2D discrete elements. A three-dimensional image was constructed by using a combination of different layers of 2D images. The microstructure for this study was obtained by scanning images of many slices of the mixture, as shown in Fig. 1. Image processing techniques were used to identify the aggregate skeleton from the image. For example, in this study an aggregate size larger than 1.18 mm was selected as the minimum aggregate size in the aggregate skeleton. The particles finer than 1.18 mm were used as the mastic.

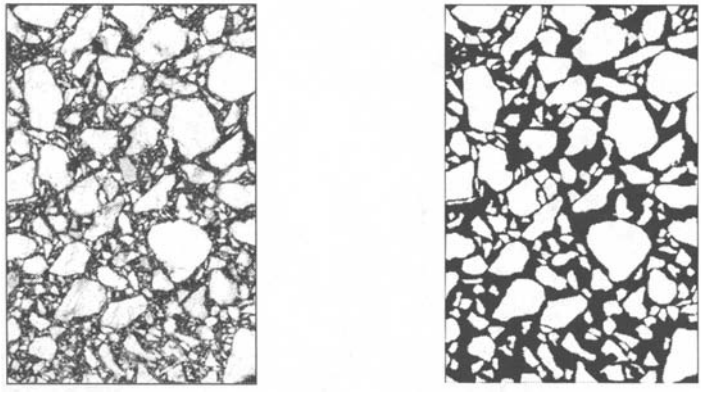

a. Raw image of HMA surface **b. Image of aggregate >1.18 mm**

FIG. 1. Examples of the images: before and after image processing.

The 2D rectangular shaped specimen was generated with the height of 242 units (81mm) and width of 160 units (53mm) from the images. The radius of each ball (discrete element) was 1 unit (0.33mm). There were total of 9,680 balls in the digital specimen. The aggregate volume was calculated by the number of aggregate elements by the number of total elements, which was 53% (5,124 balls). Randomly generated air voids were used throughout the model. The air void was generated in the mastic element, keeping the aggregate constant. When the air voids were introduced at 4% and 7%, respectively, the total number of discrete elements was reduced accordingly. Fig. 2 shows the different images of 2D discrete element models at different air void levels (i.e., 4%, and 7%), aggregate domain and mastic domains. It should be noted

that the air voids were not directly modeled with a number of disks in this paper. Air void balls were deleted in the DEM model.

a) Air void distribution indicated by disks

b) Discrete elements of the aggregate and mastic phase with 0% air void content

FIG. 2. Discrete element models: Air void distribution illustration, the discrete elements for the aggregate and mastic phase.

The 3D rectangular prism shaped specimen was generated with a height of 242 units (81mm), width of 160 units (53mm) and depth of 96 units (32 mm), using 4 different prepared 2D models. The radius of each sphere was 1 unit (0.33mm). There were a total of 464,640 spheres in this 3D asphalt mixture specimen without air voids. The volume of the aggregate was estimated at 53% (245,952 balls). Fig. 3 shows the generation of the 3D model using the four 2D models at 4% air void level. The 2D and 3D discrete element models were constructed using regular packing spheres.

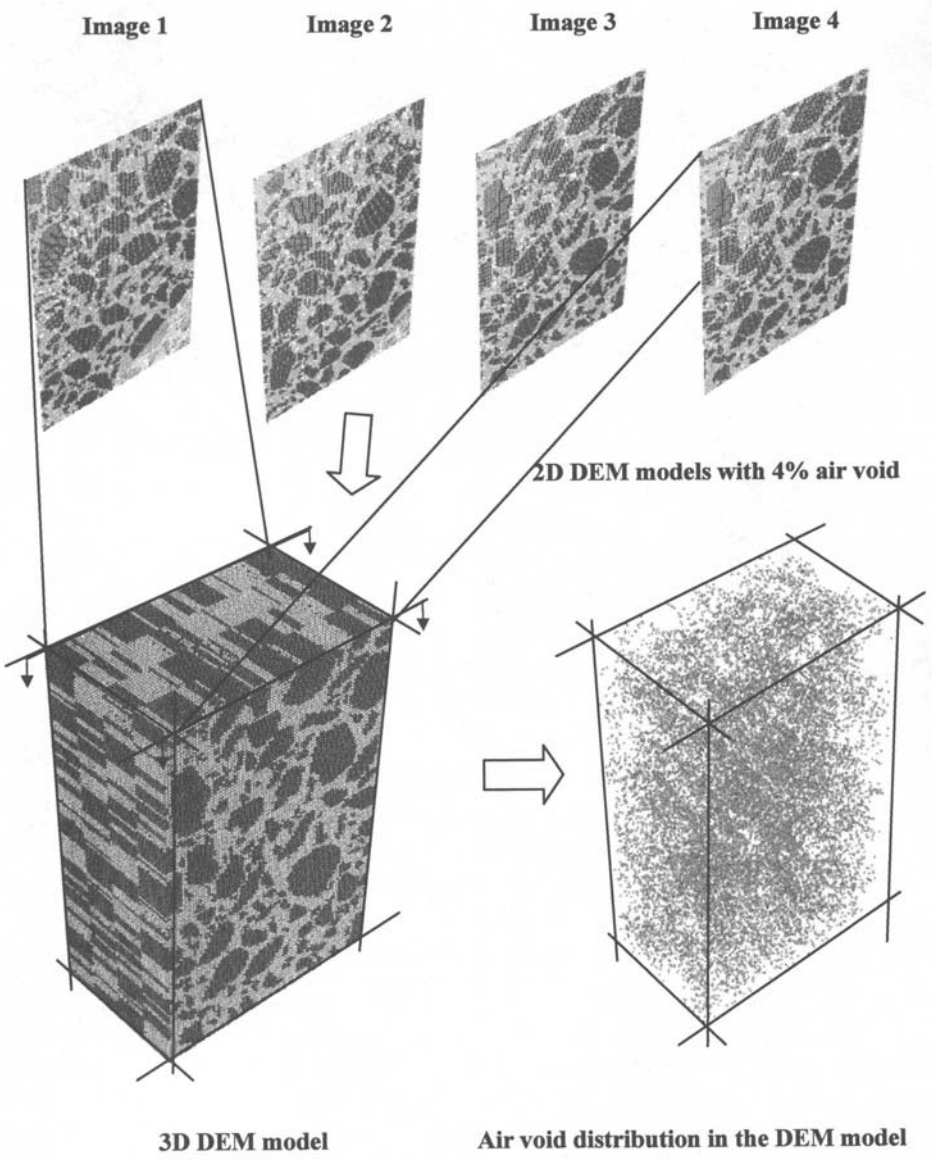

FIG. 3. 3D model generation from the 2D models using 4% air voids.

COMPUTATION OF DEM MODEL

The DEM model of the asphalt mixture was simulated in a compression test by confining the stress environment. 2D specimens were computed by a biaxial test and 3D specimens are computed by a triaxial compression test. The walls were made longer than necessary to allow for large amounts of strain to occur during the test. Walls interact with balls, not with one another. The axial compressive force was applied to the top of the specimen with constant loading speed. The force, length and time used were in Newtons, meters, and seconds respectively. A detailed discussion of the biaxial and the triaxial compression tests can be found in other literature (Itasca Consulting Group 2004b). The stiffness model used was a contact model and provides an elastic relationship between the contact force and relative displacement between particles. Thornton (Thornton 1979) provides expressions for the strength of closed-packing cubic arrays of spheres.

For a cubic array of spheres (with six neighbors), when a radius R is considered, the relationship of the increment in axial force ΔF_a and increment of axial stress $\Delta\sigma_a$ can be written as equation:

$$\Delta\sigma_a = \frac{\Delta F_a}{(2R)^2} \tag{1}$$

where, R is the radius of the particles.

The increment in strain $\Delta\varepsilon_a$ and the relative normal displacement between two adjacent particles Δu can be expressed as

$$\Delta\varepsilon_a = \frac{\Delta u}{2R} \tag{2}$$

This displacement gives rise to a normal force. The apparent normal stiffness is the series combination of K_n for both particles:

$$\Delta F_a = (\frac{1}{2}K_n)\Delta u = (\frac{1}{2}K_n)(2R\Delta\varepsilon_a) = K_n R\Delta\varepsilon_a \tag{3}$$

Therefore, from these equations, the expression for the apparent Young's modulus E of the assembly in terms of the input normal stiffness, K_n, can be written as:

$$E = \frac{\Delta\sigma_a}{\Delta\varepsilon_a} = \frac{K_n}{4R} \tag{4}$$

The specimen was loaded by specifying the velocities of the top and bottom walls. The stress was computed by taking the average wall forces and dividing by appropriate areas. The strains in the radial and axial directions were computed using the current radius or specimen length, and the original radius or specimen length. Throughout the loading process, the confining stress was kept constant by adjusting the radial wall velocity using a numerical servo-mechanism. After the confining stress state had been reached, the specimen was tested by releasing the top and bottom platens from servo control and specifying the velocities of the top and bottom platens. During each test, the servo control kept the confining stress constant at the requested value. Then the velocities of the top and bottom platens initiated the compression test in that direction (z, in this case). It was easy to control the simulation, for example, the simulation was completed when a specific axial strain level was reached. The

modulus was computed from the plots of axial deviator stress (i.e., the difference between axial stress and confine stress) versus axial strain (Itasca Consulting Group 2004a). Contact deviator stress and strain histories were traced to capture the macro and micromechanical responses in the specimens. The modulus was computed from the plots of axial deviator stress versus axial strain.

SPECIMEN PREPARATION AND LABORATORY TESTS

Asphalt mixtures, sand mastic and stone cylinders were prepared for the compression tests. Asphalt mixtures were prepared using 4.8% asphalt content and 4% air voids. The aggregate used in this study was a 19 mm nominal maximum aggregate size (NMAS) mixture. The sand mastic comprised of the portion of the aggregate gradation finer than 1.18 mm combined with the volume of binder normally used in the entire HMA. The asphalt content in sand mastic was around 14.4% by weight of the sand mixture, and therefore the sand mastic was flowable at high temperatures. Stone cylinders were cored from the rock. Dynamic (complex) modulus was measured for all three different specimens using the uniaxial compressive tests. The dynamic modulus of both the sand mastic and HMA were tested across a range of loading frequencies (0.1, 1, 5, and 10 Hz) and test temperatures (0, -10, and -20°C). The laboratory measurements of the HMA mixture were compared with the dynamic modulus prediction to evaluate the DEM modeling. The measurements of the sand mastic were used as input parameters of the HMA mixture models. The aggregate used in this study was a mix of two or more types of geological rocks. Two different rock cores were tested and the averaged found. For this study, an aggregate modulus of 55.5GPa was used in the models.

RESULTS OF THE DISCRETE ELEMENT MODELS

The modulus of the HMA mixture was predicted using the 2D and 3D DEM models. Compressive test simulations were conducted using the 2D and 3D discrete element models. The comparison of the predictions and laboratory measurements of the mixture moduli under a range of mastic moduli is shown in Fig. 4. The asphalt mixture was compacted to a 4% air void level, and the modeling results were from the 4% models. The dynamic modulus of the asphalt mastic across a range of loading frequencies (0.1, 1, 5, and 10 Hz) and test temperatures (0, -10, and -20°C) were measured and used as input parameters in the DEM models. The moduli of the sand mastic were used as input parameters in the 2D and 3D HMA models. Therefore, at each loading frequency and test temperature, the predicted HMA modulus was in fact corresponding to the specific loading frequency and temperature. It was found that for each temperature, the 3D DEM prediction was very close to the mixture modulus measurements. Fig. 4 shows that the 3D model prediction is much better than that of the 2D model.

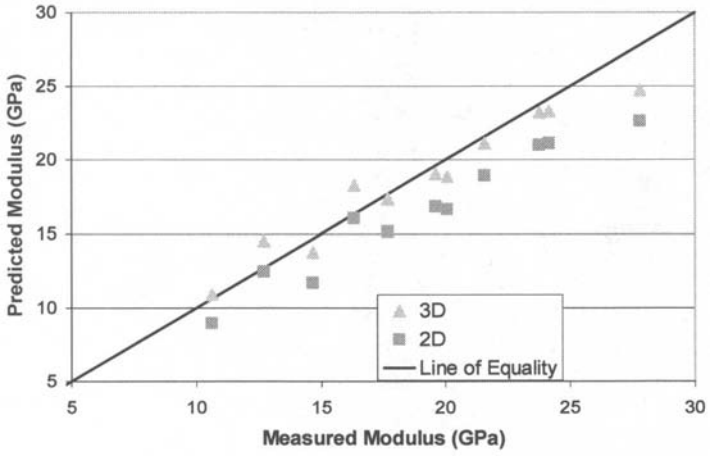

FIG. 4. Comparing dynamic modulus (E*) prediction using 3D and 2D DEM and laboratory measurements of the asphalt mixture at 4% air void.

Fig. 5 shows the 3D model prediction from three air void levels (i.e., 0%, 4%, and 7%). The prediction in the figure at 0% air void level over-predicts the modulus of the mixture. Therefore, in order to closely simulate the mixture modulus, 4% air void was introduced into the 3D model by removing some mastic elements, as discussed in previous sections. With the introduction of 4% air voids, the mixture prediction decreased. It was also observed that the 4% model prediction closely matched the laboratory mixture measurements. At 4% air void level, the difference between the 3D model predictions and the laboratory measurements was within 5% on average. When the 7% air void was introduced into the models, it was found that the predictions were lower than those of the 4% model. When comparing the 2D and 3D models, it was found that 3D models yielded a better prediction for this mixture. When the air void content increased, the mixture modulus prediction decreased. But when the air void was fixed at a 4% level, the mixture modulus decreased 20% for 2D and 13% for 3D models on average. From 4% to 7% air voids level, the mixture modulus prediction decreased 22% and 12% for the 2D and 3D models, respectively. It was found that the 3D models have higher prediction than the 2D models for the three air void levels.

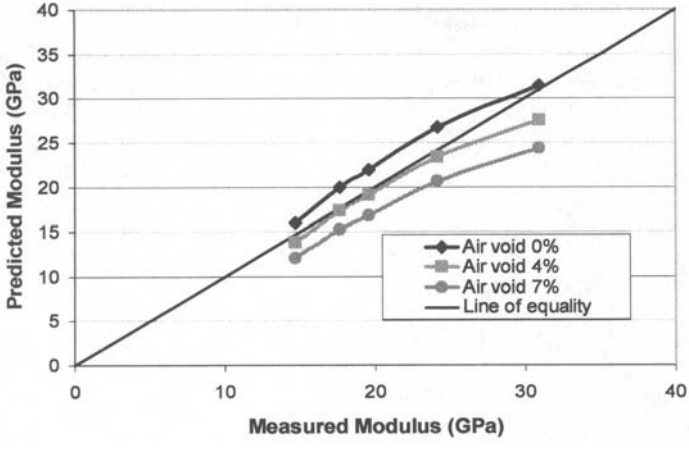

FIG. 5. Comparing 3D prediction and measurement modulus of the asphalt mixture using 0%, 4%, and 7% air voids.

CONCLUSIONS

The HMA was simulated with both 2D and 3D discrete element models. The DEM prediction was compared with experimental measurements. The effects of air void content and the distribution of air voids were studied. The air voids in the models were randomly generated within the models to reach a specific air void level. The 3D model of the HMA mixture was obtained by a number of 2D models. The 2D and 3D models were computed by using compressive loads to calculate the moduli of the specimen, which were derived from the stress-strain curve. The input data to the 3D models included not only the aggregate and mastic properties but also the microstructure of the aggregate skeleton and mastic distribution as well as the air void microstructure. The moduli of the 3D models were then compared with the experimental data. It was found that the 3D discrete element models were able to predict the mixture modulus across a range of temperatures and loading frequencies. It was found that modulus prediction decreased with increasing air void levels. When comparing the modulus predictions from the 2D and 3D models, it was found that the 3D models yielded higher modulus than the 2D models. It is expected that the 3D models of the exact heterogonous asphalt mixture will better assist the understanding of the mechanism of design and construction of asphalt mixtures.

ACKNOWLEDGEMENT

This material is based in part upon work supported by the National Science Foundation under Grant CMMI 0701264. The financial support is appreciated.

REFERENCES

Buttlar, W. G., and You, Z. (2001). "Discrete element modeling of asphalt concrete: Microfabric approach." *Transportation Research Record*, 1757, 111-118.

Chang, G. K., and Meegoda, J. N. (1997). "Micromechanical Simulation of Hot Mixture Asphalt." *ASCE J. Engng. Mech.*, 123(5), 495-503.

Collop, A. C., McDowell, G. R., and Lee, Y. (2004). "Use of the distinct element method to model the deformation behavior of an idealized asphalt mixture." *International Journal Pavement Engineering*, 5 1-7.

Cundall, P. A. (1971). "A Computer Model for Simulating Progressive Large Scale Movements in Blocky Rock Systems." *Proceedings of the Symposium of the International Society of Rock Mechanics*, II-8, 129-136.

Itasca Consulting Group. (2004a). *PFC 2D Version 3.1*, Minneapolis, Minnesota 55415

Itasca Consulting Group. (2004b). *PFC 3D Version 3.1*, Minneapolis, Minnesota 55415

Rothenburg, L., Bogobowicz, A., and Hass, R. "Micromechanical Modelling of Asphalt Concrete in Connection with Pavement Rutting Problems." *7th International Conference on Asphalt Pavements*, 230-245.

Thornton, C. (1979). "Conditions for failure of a face-centered cubic array of uniform rigid spheres." *Geotechnique*, 29(4), 441-459.

You, Z., and Buttlar, W. G. (2005). "Application of Discrete Element Modeling Techniques to Predict the Complex Modulus of Asphalt–Aggregate Hollow Cylinders Subjected to Internal Pressure." *Journal of the Transportation Research Board, National Research Council*, 1929, 218-226.

You, Z., and Buttlar, W. G. (2006). "Micromechanical Modeling Approach to Predict Compressive Dynamic Moduli of Asphalt Mixture Using the Distinct Element Method." *Transportation Research Record: Journal of the Transportation Research Board, National Research Council, Washington, D.C.*, 1970, 73-83.

You, Z., and Dai, Q. (2007). "A Review of Advances in Micromechanical Modeling of Aggregate-Aggregate Interaction in Asphalt Mixture." *Canadian Journal of Civil Engineering* 34(2), 239-252.

Analysis on Property Changes of Neat and Modified Asphalt under Ultraviolet Aging

Jiani Wang [1], Yiqiu Tan [2], Zhongjun Xue [3], Zhongliang Feng [4] and Huining Xu [5]

[1] Ph.D. School of Traffic Science and Engineering, Harbin Inst. of Tech., Harbin, Heilongjiang, China/wangjiani3328@126.com

[2] Professor, School of Traffic Science and Engineering, Harbin Inst. of Tech., Harbin, Heilongjiang, China/yiqiutan@163.com

[3] Ph.D. School of Traffic Science and Engineering, Harbin Inst. of Tech., Harbin, Heilongjiang, China/xuezhongjun@yahoo.com.cn

[4] Engineer Jiangsu Transportation Research Institute, Nanjing, Jiangsu, China

[5] Ph.D. School of Traffic Science and Engineering, Harbin Inst. of Tech., Harbin, Heilongjiang, China

ABSTRACT: This paper discusses the changing of aged asphalt's properties with several neat and modified asphalt binders, and their mixtures performance. Results of Penetration, softening points, ductility test indicated that thermal-oxidation and ultraviolet radiation aging are two different aging behaviors to binders, regardless modified or not. Changes of physical and rheologcial properties after ultraviolet aging not consist with those after thermal aging, Dynamic Shearing Rheometer (DSR) and Bending Beam Rheomter (BBR) test indices showed that visco-elastic properties of both unmodified and modified binder evidently changed after ultraviolet aging, low temperature performance fallen thusly. Low-temperature bending and indirect tensile tests results revealed that asphalt mixture moisture stability and thermal cracking resistances turn to poor due to ultraviolet aging, and validated the different influences between thermal and ultraviolet aging on performances of binder and asphalt mixture.

INTRODUCTION

Bituminous binder is easy to age in field, especially under thermal and/or UV radiation conditions. UV aging and thermal aging are two quite different types of aging (Ye et al. 2006), but the current asphalt performance evaluation system gives little consideration on UV aging. Because of the difference in air composition and length of solar radiation path between plateaus and low latitude plains, plateaus have a unique climate and environmental feature due to its more intensive radiation

strength, longer daylight time, and especially the much higher percentage of UV radiation content, which ranging from 20% to 25% of the total solar light energy, is five times as that in plains (Xiao et al. 2003). Such intensive UV radiation aging causes serious degradation on asphalt performance and attenuates the pavement durability.

EXPERIMENTAL METHODOLOGY

Artificial Aging Procedures

The UV radiation equipment was presented in another paper of the authors, which was published in 2003(Tan et al.2003). The UV aging test was at 73°C for 9 hours, so that the radiation energy is equivalent to the total energy received outdoor in 5 months at Lasa, ultraviolet radiation intensity is about 35KJ/cm^2·a, a western city of China. The asphalt mixture UV aging test used similar equipments and procedure: the mixture was tested in a 'semi-compacted state' at 73°C with air-blowing for 48 hours.

Basic Physical Properties of Binders

The binders used in this study included three neat binders (denoted as KL, LH, and XT) from different sources with the same penetration grade and two polymer-modified asphalt binders (K-SBS and K-SBR). Each binder listed in the following text was assigned an identification code which provides information of the source and physical state of the material. For example, KL-O means an original asphalt sample from KL; K-SBS-T means a thermal aged K-SBS sample. Binders' basic physical properties are summarized in Table 1 and Figure 1.

Table 1. Physical Indices of Original & Aged Binders

Binder variety		KL	LH	XT	K-SBS	K-SBR
Penetration (25°C; 0.1mm)	Original bitumen (Po)	79	82	81	96	99
	Thermal aged (Pt)	60	74	54	78	82
	UV aged (Pu)	46	51	49	69	68
Ductility (10°C;cm)	Original bitumen (Do)	52.7	74.6	45.3	167.5	165
	Thermal aged (Dt)	36	36.2	29.8	153.5	123.5
	UV aged (Du)	11.8	30	23.1	139	113.5
Softening point (°C)	Original bitumen (So)	46.3	42.6	45.9	61.9	71.7
	Thermal aged (St)	48.1	47.3	50	60.7	66
	UV aged (Su)	56.7	48.0	54.2	64.9	67.3

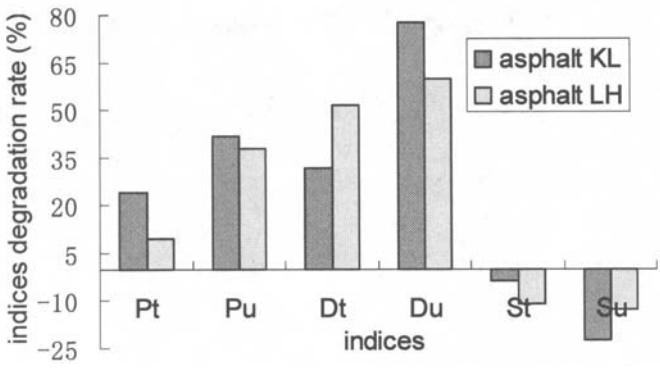

FIG. 1. Physical indices degradation rates of two aged binders.

Bituminous Binder Experiments

The DSR test was conduced with a Gemini-150 rheometer in a parallel-plate configuration with a gap of 2000μm at 0°C to see their performance at critical range of low- and medium temperature clearly, 0°C is chosen as the test temperature; the stress was 1.5×10^4Pa at a frequency of 0.1rad/s. AASHTO MP5 method was adopted in the BBR test, the temperature was -12°C. ASTM D-4124 method of Corbett was used to separate the original and aged bitumen samples for chemical component study. The rheological indices and chemical components before and after aging are shown in Tables 2 through 4.

Table 2. Loss Modulus (MPa) & Phase Angle (°)

Binder variety	KL		LH		XT		K-SBS		K-SBR	
	δ	*G″*	*δ*	*G″*	*δ*	*G″*	*δ*	*G″*	*δ*	*G″*
Original binder	20.3	1.19	13.1	0.97	13.2	0.96	30.8	1.30	32.1	1.32
Thermal aging	18.9	1.03	12.7	0.99	11.2	0.85	30.3	1.30	31.7	1.37
UV aging	13.8	0.8	12.0	0.92	10.0	0.74	28.4	1.21	18.9	1.18

Table 3. Stiffness (S) & m Values (m)

Binder variety	KL		LH		XT		K-SBS		K-SBR	
	S	*m*	*S*	*m*	*S*	*m*	*S*	*m*	*S*	*m*
Original binder	45.8	0.54	120	0.5	76.6	0.39	90.3*	0.42*	119*	0.44*
Thermal aging	62.5	0.9	146	0.45	112	0.43	99*	0.41*	96.1*	0.48*
UV aging	70.3	0.47	152	0.45	141	0.39	30.8	0.49	52.3	0.39

Remark: * test temperature is -18°C

Table 4 Chemical Components of Original and Aged Binders

Chemical components	KL-O	KL-T	KL-U	LH-O	LH-T	LH-U	XT-O	XT-T	XT-U
Saturates (symbol : S)	31.5	30.0	29.9	35.9	34.7	34.6	23	19	18.7
Aromatic (symbol : Ar)	33.6	24.5	23.2	35.1	30.9	30.7	45.3	43.5	44.6
Resin (symbol : R)	33.5	43.6	44.9	24.3	27.4	28.1	20.5	25.8	23.7
Asphaltene (symbol: At)	1.5	1.8	2.1	4.7	6.9	6.6	10.3	11.7	13

Asphalt Mixture Experiment

To exclude disturbing from unrelated factors, the crucial mixture indices such as gradation and air void were maintained in all tests. An AC-13 II gradation was adopted for these mixtures. The asphalt mixtures' low-temperature flow deforming ability was evaluated by indirect creep test. By means of measuring the deformation rate of a three-point bending beam during putting fixed stress on it, the losing of creep rate of can be calculated. The prism specimen size was 250mm×30mm×35mm, the fixed stress in this test was about 10% of the failure load, lasted for 20~30mins at 0° C. AASHTO T-283 test was used to investigate the moisture stability of mixtures. Moisture stability of asphalt mixtures was evaluated on the tensile strength ratio. The experimental results were listed in Table 5 and Table 6, respectively.

Table 5. Losing of Creep Rate of UV Aged Asphalt Mixtures

Asphalt variety		KL	LH	XT	K-SBS	K-SBR
Creep Rate	Thermal aging	2.00E-06	1.29E-06	2.86E-06	7.79E-06	3.50E-06
(1 /s /MPa)	UV aging	2.89E-06	7.82E-07	1.81E-06	6.53E-06	2.04E-06
Losing of creep rate (%)		-44.5	39.5	36.8	16.2	41.9

Table 6 Tensile Strength Ratio (TSR) of UV Aged Asphalt Mixtures

Asphalt variety	KL	LH	XT	K-SBS	K-SBR
TSR of un-UV aging (%)	83.8	81.5	87.3	93.1	76.7
TSR of UV aging (%)	76.8	90.7	79.6	86.1	82.7

RESULTS AND DISCUSSION

Influences on Binder Properties

Changes of physical properties

Table 2 presents the physical indices of the original, thermal and UV aged binders. After UV aging, the values of penetration and ductility decreased while softening points increased. It shows the changes of the physical indexes of bitumen KL and LH. KL is more UV radiation sensitive because larger physical indices changes can be seen, showing a poor ability of anti-ultraviolet (Figure1.). On contrary, LH is not very sensitive to UV, as only small changes by UV aging.

Changes of rheological properties

This study applied the DSR and BBR tests to investigate the influence on rheological properties by UV radiation. Rheological properties can be well reflected by the loss modulus G'' and phase angle δ. The energy dissipated as flowing deformation to resist loading is expressed as the loss modulus G'', and δ is an index for the ratio of viscosity and elasticity. As degradation of rheological properties, lower values of G'' and δ are undesired when the working temperature is lower than normal. Reductions of these two indices reveal that UV aging changes the viscoelastic character of asphalt, improves elasticity and decreases viscosity (in Table 3). As a result, the low-temperature flow property drops.

Two BBR indices, the stiffness, S, and the slope m-value, m, at 60 sec, were used to evaluate the low temperature performance. The results are shown in Table 3, where the effects of UV aging are clearly exhibited by the variations of S and m. It can be observed that S increased, and m decreased during UV aging. The variation tendencies of S and m imply rheological properties fall after UV aging.

The above experiment results displayed that UV aging gave noticeable influences on the binders' physical and rheological properties. Because of the decrease in rheological properties, low-temperature flow deforming ability falls significantly.

Influences comparison of UV and thermal aging

To compare the influences of thermal and UV aging on the properties of bitumen, the penetration and loss modulus of binders were listed in order as shown in Figure 2, where it can be seen that the changes of the physical and rheological properties after UV aging are not consistent with those after thermal. It clearly indicates some noticeable differences in their aging properties.

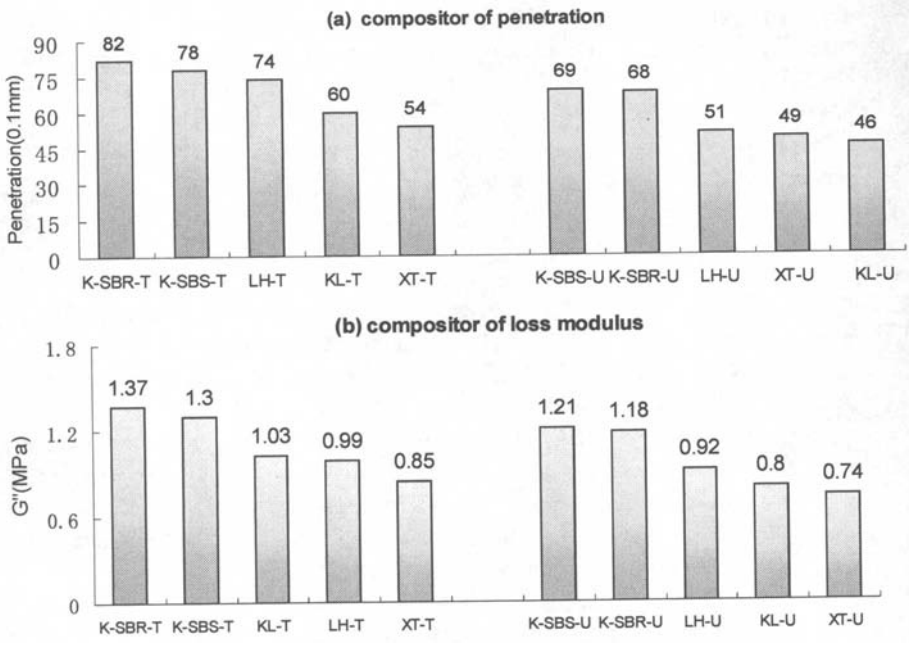

FIG. 2. Physical and rheological Indices Compositor of Thermal and UV Aged Bitumen

Relationship between UV aging behaviors and chemical components

The aging mechanisms of UV radiation and thermal are differ in the initiation process. Thermal oxidation is caused by polymer chemical bond thermal decomposition, while the initiation process of UV aging is that some chromophores absorb UV radiation then transfer from ground state to excited state, thus conduce the breaking of chemical bonds (Wu 2003). Some studies have shown that carbonyl plays a key role in UV aging. Carbonyl content and its transformation are the decisive conditions to the reaction degree of photo-oxidation. Carbonyl is converted from oxidation reaction of cyclophanes, which is mostly contained in aromatics and resin. Therefore, aromatics and resin are two crucial components.

The transformation trend between components can be briefly expressed as: aromatic transforms to resin, and resin transforms to asphaltene at the same time. As the product of the aging reaction, the proportion of asphaltene in gross stably increases at a consistent speed. Therefore, it is feasible to evaluate aging degree by observing the variation of the proportion of asphaltene (Petersen 1993 and Jin et al.2001).From Table 4, it can be find that asphaltene content of KL and XT after UV aging was

higher than those after thermal aging, with an increase of 40% and 26.2%, but LH shows an opposite results comparing to thermal aged. The results of asphaltene amount increasing induced related properties, such as low temperature performance, temperature susceptibility and fatigue life span changed thusly. The variation trend of the asphaltene amount reflects asphalts' sensitivities to UV radiation, consistent with the changes of physical and rheological properties.

Influences on Asphalt Mixture Performance

Influences on low-temperature performance and moisture stability

As the low-temperature performance is mainly binder dependent (Julie et al.1996), this paper studies influences of UV aging on low-temperature performance of asphalt mixture with creep test. From the test results shown in Table 6, a falling trend of creep rate can be seen on most of the asphalt mixtures, displays a degradation of the anti-cracking ability.

Moisture stability is another aspect of asphalt performance influenced greatly by UV aging due to the changes on consistency and viscosity. The results of AASHTO T-283 test show a decrease in TSR (and thus the moisture stability) in four asphalt mixtures (in Table 5) and the decrease also reveals a strong binder dependency. The moisture stability is consistent with the binder aging properties.

Relationship Between Aged Asphalt Mixture and Binder To investigate the relationship of the aging behaviors of asphalt binder and mixture, a regression curve was established in Figure 3. The curve shows a noticeable linear correlation between S and the losing of creep rate indicating a clear relationship of the low-temperature rheological performances of mixture and binder after UV aging; and the curve of modified binder is very similar to that of neat binder.
The correlation analysis of the binder's physical-chemical properties and TSR was conducted. As a conditional index for temperature susceptibility, penetration can reflect binder's consistency as well. Since moisture stability is adhesion determined to some extent, changing of penetration affects the TSR directly, this is shown clearly in the regression curve in Figure 4.

It must be mentioned that above curve only can be looked as a raw trend line rather than regression curve, shown the possible relationships between neat and modified asphalt, binder and mixture. precise regression correlation depends on further research sustained with abundant validations in field and test data.

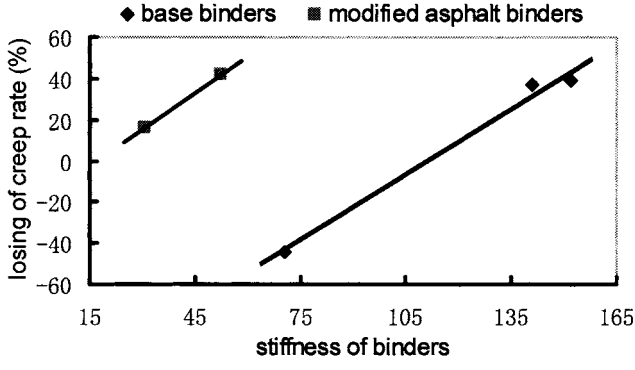

FIG. 3. Losing of Creep Rate of Mixtures vs. Stiffness of Binders .

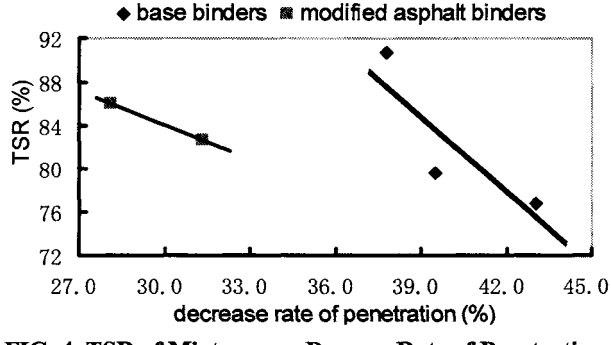

FIG. 4. TSR of Mixtures vs. Decease Rate of Penetration .

CONCLUSIONS

This paper presents the study of the influence of UV aging on binder and asphalt mixture performance by experiments, comparing sensitivities to UV radiation and thermal and observing changing of asphalt mixture performance during UV aging. Based on these investigations, some conclusions can be drawn:

- UV radiation aging has obvious effects on the performance of both bitumen and asphalt mixture, especially bitumen's low-temperature flow deforming ability and thus the mixtures' anti-cracking ability.

- For the same asphalt, binder's physical aging behavior is highly consistent with its rheological properties. The transformations taking place in chemical

components during UV aging ties up to the changes of the properties. In addition, there are close correlations between the mixture's low-temperature deforming ability and binder's stiffness; and the moisture stability evaluation index, TSR, and the penetration, respectively.

- Most bitumen has different sensitivities to thermal and UV radiation. Evaluation method based on thermal aged asphalt does not truly reflect influences of UV aging, and there will be some limitations on the substitution of UV by thermal aging.

ACKNOWLEDGMENTS

This project is supported by program for New Century Excellent Talents in University and Specialized Research Fund for the Doctoral Program of Higher Education of China (Grant No.20060213002).

REFERENCES

Jin Minglin, Yang Junhe, Feng Anzhu, etal. (2001). "Analysis of ageing behaviour of south korea 70 asphalt part (I) Changes of component and property." *Coal Conversion.* 24(4): 92-95.

Julie E. Kliewer, Huayang Zeng, Ted S. Vinson. (1996). "Aging and low-temperature cracking of asphalt concrete mixture." *Journal of Cold Regions Engineering.* 9: 134-148.

Petersen J C. (1993). "Asphalt oxidation–an overview including a new model for oxidation proposing that physicochemical factors dominate the oxidation ki-netics." *Fuel Science and Technology International.* 11(1): 57-58 .

Tan Yiqiu, Feng Zhongliang, Zhou Xingye. (2003). "The evaluation method study of anti-ultraviolet aging ability of asphalt." *Chinese Science paper Online,* www.paper.edu.cn.

Wu Shikang. (2003). "Polymer Photochemistry: Fundamentals and Applications." Science Press, Beijing.

Xiao Yide, Wang Guangyong, Li Xiaogang. (2003). "Corrosion behavior of atmospheric environment and corrosion feature of materials in our western area. " *Journal of Chinese Society for Corrosion and Protection.* 23(4): 248-255.

Ye Fen, Yang Jin, Huang Peng. (2006). "Performance of modified asphalt aging under ultraviolet radiation." *Pavement Mechanics and Performance* GSP(154), ASCE: 102-109.

A Viscoplastic Foam Model for Prediction of Asphalt Pavement Compaction

Kaiming Xia[1] and Liqun Chi[2]

[1]Machine Research, TC-E 852, P.O. Box 1875, Caterpillar Inc, Peoria, IL 61656-1875 USA; Xia_Kaiming@cat.com
[2]Machine Research, TC-E 852, P.O. Box 1875, Caterpillar Inc, Peoria, IL 61656-1875 USA; Chi_Liqun@cat.com

ABSTRACT: Compaction is one of the most important factors affecting the future performance of asphalt pavement. Hot mixture asphalt materials exhibit significant time-dependent response under mechanical and thermal loadings, which can involve elastic, creep and plastic permanent deformation. The irreversible permanent deformation part will generate compaction. Foam-type model has been considered an efficient material model to predict compaction effect. In this paper, we extended the rate-independent crushable foam plasticity model to a viscoplastic model. A user material subroutine was developed and integrated in commercial finite element software ABAQUS, which can be used to predict compactor performance. Based on the large deformation theory and mass conservation, the change of compacted density can be predicted due to compaction. Some representative simulations are presented to show the effectiveness of the proposed material model.

INTRODUCTION

Compaction in the pavement engineering is usually taken to mean the increasing density of a material by applying compactive effort and removing the entrained air, i.e. decreasing air voids. In pavement engineering, compacted density has been considered as an important index to evaluate the degree of asphalt compaction, which has direct impact on the strength and resilient modulus of pavement materials. Many research efforts have been exerted on understanding the mechanical behavior of asphalt mixtures, but very few researchers have applied large deformation theory to predict pavement compaction. Much effort was focused on developing empirical method and tests. Asphalt material exhibits significant time-dependent response under mechanical and thermal loading, which can involve elastic, creep and plastic deformations (Lu and Wright 1998). The response of the asphalt mixtures may be categorized into three groups: elastic, viscoelastic and viscoplastic (Saleeb et al. 2005). In this paper, we extended the rate-independent foam type plasticity model to allow for time-dependent viscoplasticity and applied it to predict the asphalt compaction. Many kinds of viscoplastic theories have been proposed, among them

are Perzyna-type (Perzyna 1966), the Duvaut-Lions model and Consistency-type viscoplasticity (Wang et al. 1997). Perzyna's model has been the most popular in model of computational solid mechanics because it uses commonly available rate-independent models. This approach represents a modification of the classical plasticity theory by introduction of a time-rate rule in which the yield function of classical plasticity is incorporated. An Euler backward algorithm can be used for the return mapping of the stress to the viscoplastic yield surface. The viscoplastic model of material behavior is of much practical interest, which allows the treatment of non-associated plasticity and strain softening situations, which present difficulties in conventional plasticity approaches. More important is the fact that the viscoplastic model can be used to model plastic behavior in a simple manner when stationary conditions are reached and, at the other extreme, can reproduce standard creep phenomena.

The Foam-type material model has been considered an efficient material model to predict compaction effect in our previous simulation of landfill compaction. However, the available crushable foam model in ABAQUS does not contain the viscous effect, which typifies the asphalt material mechanical behavior. In this paper, we presented a viscoplasticity model based on the plastic crushable-foam type constitutive model by introducing a time-dependent effect, which can be classified as a consistency approach and different from the classical Perzyna and the Duvaut-Lions model. The application of this viscoplastic foam type model will be focused on the prediction of compacted density due to the compactor load, which can be extended to predict rutting for flexible pavement.

CRUSHABLE FOAM MODEL

Crushable foams have been used for the analysis of energy absorption structures (Abaqus 2007). The elastoplastic constitutive model is able to capture the volumetric hardening, which is suitable for modeling the compaction process of lower-density waste materials. The crushable foam model with volumetric hardening is shown in FIG. 1.

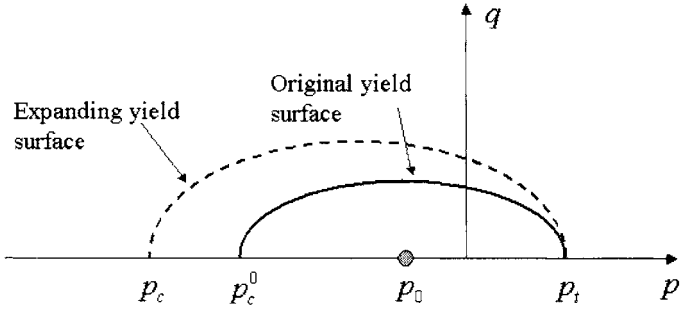

FIG. 1. Volumetric hardening crushable foam model.

The yield surface and plastic flow potential for the crushable foam models are defined as follows:

$$F = \sqrt{q^2 + \alpha^2 (p - p_0)^2} + B = 0 \tag{1}$$

$$g = \sqrt{q^2 + \beta^2 p^2} \tag{2}$$

where p and q are defined as the pressure and Mises stress

$$p = \frac{1}{3}\mathrm{Tr}\boldsymbol{\sigma} = K\mathrm{Tr}\boldsymbol{\varepsilon} \quad \text{and} \quad q = \sqrt{3/2}\|\mathbf{s}\| \tag{3}$$

In this case, we can have the yield function and plastic flow potential as follows:

$$F(\boldsymbol{\sigma}) = \sqrt{\frac{3}{2}\|\mathbf{s}\|^2 + \alpha^2 (p - p_0)^2} + B = 0 \text{ and } g(\sigma) = \sqrt{\frac{3}{2}\|\mathbf{s}\|^2 + \beta^2 p^2} \tag{4}$$

Both yield function and flow potential are represented as an ellipse in the $I_1 - \|\mathbf{s}\|$ stress plane with α and β representing the shape of the yield ellipse ad the ellipse for the flow potential, respectively; p_0 is the center of the yield surface and defined as $p_0 = (p_c + p_t)/2$, and B is the length of the vertical q-axis of the yield ellipse and calculated by $B = \alpha(p_c - p_t)/2$. The flow potential is an ellipse centered in the origin. The yield surface and flow potential are depicted in Figure 1. The hardening is controlled by P_c, which can be assumed to be density dependent or similar formulation to the general CAP model.

For simplicity and clarity, the viscoplastic constitutive equation of the crushable foams model is cast here in a small deformation framework first, which can be directly extended to a finite deformation framework as necessary. For viscoplasticity, the strain rate can be decomposed into an elastic part $\dot{\boldsymbol{\varepsilon}}^e$ and viscoplastic part $\dot{\boldsymbol{\varepsilon}}^{vp}$:

$$\dot{\boldsymbol{\varepsilon}} = \dot{\boldsymbol{\varepsilon}}^e + \dot{\boldsymbol{\varepsilon}}^{vp} \tag{5}$$

The elastic response of the material is assumed to be characterized by a constant isotropic tensor $\mathbf{D} = K\mathbf{1} \otimes \mathbf{1} + 2G\mathbf{I}_{dev}$ such that the stress response of the material is given by:

$$\dot{\boldsymbol{\sigma}} = \mathbf{D} : \dot{\boldsymbol{\varepsilon}}^e = \mathbf{D} : \left(\dot{\boldsymbol{\varepsilon}} - \dot{\boldsymbol{\varepsilon}}^{vp}\right) \tag{6}$$

where K is bulk modulus and G is shear modulus.

The viscoplastic component of the strain rate is related to the gradient of a loading

function with respect to stress (Perzyna, 1966):

$$\dot{\varepsilon}^{vp} = \eta \left\langle \Phi\left(\frac{F}{\sigma_y}\right) \right\rangle \frac{\partial F}{\partial \sigma} \tag{7}$$

In his classical work, η is referred to as the fluidity parameter with units of inverse time and denotes the relative rate of viscoplastic strain. The quantity of $\partial F/\partial \sigma$ in Eq. 7 denotes the current direction of the viscoplastic rate, $\dot{\varepsilon}^{vp}$. The scalar function Φ is expressed with the argument of yield function, F, which is the yield function with associative plasticity and also is called the flow function, increases monotonically with F and defines the current magnitude of the viscoplastic strain rate. The notation $\langle\ \rangle$ implies that

$$\left\langle \Phi\left(F/\sigma_y\right) \right\rangle = 0 \quad \text{for} \quad F \le 0 \quad \text{and} \quad \left\langle \Phi\left(F/\sigma_y\right) \right\rangle = \Phi\left(F/\sigma_y\right) \quad \text{for} \quad F > 0 \tag{8}$$

The most commonly used forms of the flow function $\Phi(F)$ are given by $\Phi(F) = \left(F/\sigma_y\right)^N$, where N is a material parameter and σ_y is the normalizing constant with the same units as those of F and has been always employed as the uniaxial yield stress. In the Perzyna and Duvaut-Lions viscoplastic theories, an important distinction from the inviscid plasticity theory stems from the fact that the current stress states can be outside the yield surface and that the yield function may have a value larger than zero. Therefore, the Kuhn-Tucker conditions are not applicable. If the external loading remains constant the stresses return to the yield surface as a function of time. Because of this feature viscoplastic theories are commonly called overstress laws. Here we consider another approach in which the strain-rate contribution (viscosity) is important through a similar approach as that of rate-dependent yield surface. By doing so the Kuhn-Tucker conditions remain valid and therefore this approach is very close to the consistency method (see Wang et al. 1997). The yield function and the consistency condition for a rate-dependent material can be written as

$$\dot{\lambda} \ge 0, \quad F(\sigma, H) \le 0, \quad \dot{\lambda} F(\sigma, H) = 0 \quad \text{and} \quad \dot{\lambda} \dot{F}(\sigma, H) = 0 \tag{9}$$

where $\mathbf{n}$ is the gradient to yield surface; $\dot{\lambda}$ is a scalar rate term called the viscoplastic consistency parameter which can be determined via the enforcement of the Kuhn-Tucker (loading-unloading) conditions. In the consistency approach the yield surface can expand and shrink not only by hardening or softening, but also by hardening or softening rate effects.

$$F_{VP} = \Phi(F) - \eta \dot{\lambda} \le 0 \tag{10}$$

The basic need of integrating the viscoplastic constitutive equations at integration point for finite element can be stated as follows. We employ the operator splitting methodology that leads to elastic-predictor plastic-corrector algorithm, and we

integrate the constitutive equations via the backward Euler integration algorithm (Simo and Hughes 1998). We assume that we know the solution state variables $\left(\boldsymbol{\varepsilon}_n, \boldsymbol{\varepsilon}_n^{vp}, \boldsymbol{\sigma}_n, \mathbf{s}_n, \boldsymbol{\lambda}_n\right)$ at time t_n. The incremental strain $\Delta\boldsymbol{\varepsilon}_{n+1} = \boldsymbol{\varepsilon}_{n+1} - \boldsymbol{\varepsilon}_n$ over a given time step $[t_n, t_{n+1}]$ and need to update the state variables $\left(\boldsymbol{\varepsilon}_{n+1}, \boldsymbol{\varepsilon}_{n+1}^{vp}, \boldsymbol{\sigma}_{n+1}, \mathbf{s}_{n+1}, \boldsymbol{\lambda}_{n+1}\right)$ at time t_{n+1} by integrating the rate constitutive equations. So in the first step, a purely elastic state is computed. If the trial state violates the constitutive equation, a correction is needed based on the trial state variables. This correction ensures that an admissible state variable can be obtained with respect to the viscoplastic yield surface. The updated stress can be written as follows:

$$\boldsymbol{\sigma}_{n+1} = \boldsymbol{\sigma}_n + \mathbf{D} : \Delta\boldsymbol{\varepsilon}_{n+1}^{e} = \boldsymbol{\sigma}_n + \mathbf{D} : \left(\Delta\boldsymbol{\varepsilon}_{n+1} - \Delta\boldsymbol{\varepsilon}_{n+1}^{vp}\right) \tag{11}$$

Elastic Predictor:

In accordance with the operator-split, a given strain increment $\Delta\boldsymbol{\varepsilon}_{n+1}$ is first assumed to result in an incremental elastic response which leads to the so-called incrementally elastic trial stress predictor computed as

$$\boldsymbol{\sigma}_{n+1}^{tr} = \boldsymbol{\sigma}_n + \mathbf{D} : \Delta\boldsymbol{\varepsilon}_{n+1} = \boldsymbol{\sigma}_n + K\mathrm{Tr}\left(\Delta\boldsymbol{\varepsilon}_{n+1}\right)\mathbf{1} + 2G\Delta\mathbf{e}_{n+1} \tag{12}$$

where $\Delta\mathbf{e}_{n+1}$ is the incremental deviatoric strain. By taking the trace and deviatoric parts of the elastic trial stress leads to:

$$p_{n+1}^{tr} = p_n + K\mathrm{tr}\left(\Delta\boldsymbol{\varepsilon}_{n+1}\right) \tag{13}$$

$$\mathbf{s}_{n+1}^{tr} = \mathbf{s}_n + 2G\mathbf{I}_{dev} : \Delta\boldsymbol{\varepsilon}_{n+1} \tag{14}$$

The trial yield function $F\left(\boldsymbol{\sigma}_{n+1}^{tr}\right)$ is then calculated based on the trial stress and hardening parameters. If $F\left(\boldsymbol{\sigma}_{n+1}^{tr}\right) > \mathrm{Tol}$, then the predicted elastic trial state lies outside of the elastic domain, a plastic correction must be taken.

Inelastic Corrector:

When the elastic trial stress state leads to $F\left(\boldsymbol{\sigma}_{n+1}^{tr}\right) > 0$, the behavior is inelastic and the return map solution for the viscoplastic model given by that trial stress state should be returned to the yield surface $g\left(\boldsymbol{\sigma}_{n+1}^{ad}\right) = 0$ through the second step inelastic correction. To complete the stress update, the viscoplasticity consistency parameter λ_{n+1} is computed such that the stress state lies on the viscoplastic yield surface $g(\boldsymbol{\sigma}) = 0$. The formulation is completed by integration of the constitutive equation (14) for the time interval t_n to t_{n+1} using a backward Euler evaluation of the integrals to obtain

$$\Delta t\Phi(F) - \eta\lambda_{n+1} = 0 \tag{15}$$

where $\lambda_{n+1} = \dot{\lambda}\Delta t$, the discrete consistency parameter may be obtained by combining the scalar coefficient to obtain a single nonlinear equation in λ_{n+1}. Accordingly, we

have the discrete constitutive equation. In general, the above equation is nonlinear and must be solved numerically by using modified Newton or Newton-Raphson method. For large loading rates, the stress state may lie outside the yield surface. The function Φ together with the fluidity parameter η reflects the rate dependency of the model. For nonzero fluidity η, the presence of Δt in Eq. 15 implies a rate dependency, with results depending on time duration for applying and changing loads on the continua. When η equal zero, the behavior will correspond to elasticity. When η goes to infinity, the behavior corresponds to plasticity. Once the inelastic consistency parameter λ_{n+1}^{*} is obtained, the stress can be updated in the exactly same way as pure plasticity. Since ABAQUS/Explicit was used to simulate the compaction process and proved to be very efficient. Consistent tangent modulus for this material model was not needed and not provided in this paper. For large deformation, the rate of deformation (based on ABAQUS manual) is used to calculate the incremental strain with respect to the current configuration, the return mapping algorithm for viscoplasticity is same as that for the small strain formulation. Based on the ABAQUS manual, the stress rotation will be automatically taken care in ABAQUS internally, no need to calculate it in the user subroutine.

PREDICTION OF COMPACTED DENSITY

The proposed viscoplastic foam model was integrated in ABAQUS and combined with the large deformation updated Lagrangian formulation, which can be used to predict the density change or compaction. In updated Largrangian formulation, an incremental displacement is defined with respect to the configuration at time t_n, which is considered as the reference configuration for the current load step. The updated Lagrangian formulation can therefore be visualized as a series of intermediate total Lagrangian formulations. Based on the mass conservation, the volume relationship between reference and current configurations can be established as

$$d\Omega_{t_n} = Jd\Omega_0 \tag{16}$$

And the relative compaction density can be updated at time t_{n+1} by

$$\rho_{n+1} = \frac{\rho_0}{\mathrm{Det}F_{n+1}} \quad \text{or} \quad \rho_{n+1} = \frac{\rho_n}{\mathrm{Det}f_{n+1}} \tag{17}$$

Here ρ_0 is the initial relative density and ρ_{n+1} is the relative density at time step t_{n+1}. Therefore, large deformation analysis has a lot of advantage in the predicting soil compaction in civil engineering. The deformation gradient or intermediate deformation gradient are defined as follows:

$$\mathbf{F} = \frac{\partial \varphi}{\partial \mathbf{X}} = \mathbf{1} + \frac{\partial \mathbf{u}}{\partial \mathbf{X}} \quad \text{or} \quad f = \frac{\partial x_{n+1}}{\partial x_n} \tag{18}$$

REPRESENTATIVE SIMULATIONS

To demonstrate the applicability of the viscoplastic model, two finite element simulations have been conducted and provided here.

Example 1.

Our first example is a simple problem (see FIG. 2). A column is fixed at the bottom end and subjected to compression load at the top. In order to qualitatively validate the model, both plasticity and viscoplasticity cases were investigated. The model parameters used for the numerical simulation were: Young's Modulus, $E = 10.0\text{MPa}$, Poisson's ratio 0.35, $\alpha = 0.7$, $\beta = 1.1$, $P_t = 0.2\text{MPa}$, $P_c = -0.6\text{MPa}$. FIG. 3 shows the comparison between plastic model and viscoplasticity model with different fluidity parameters. For plasticity, the permanent deformation develops almost instaneously, while the viscoplastic deformation is time dependent. The deformation rate is controlled by model parameter fluidity η. The results also shows that when fluidity parameter η becomes bigger, the material will behave closely to elastic behavior, when fluidity converges to zero, the behavior will behave closely to plasticity. Therefore viscoplastic behavior can be considered an intermediate behavior between the two extremes: plasticity and elasticity.

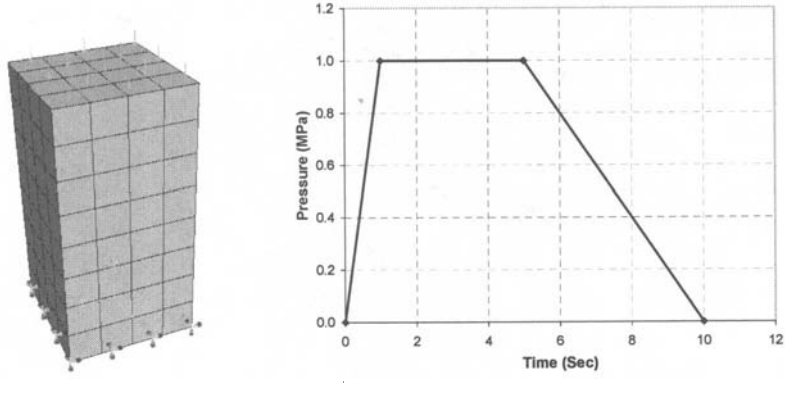

FIG. 2. A compression column, viscoplastic material, boundary condition.

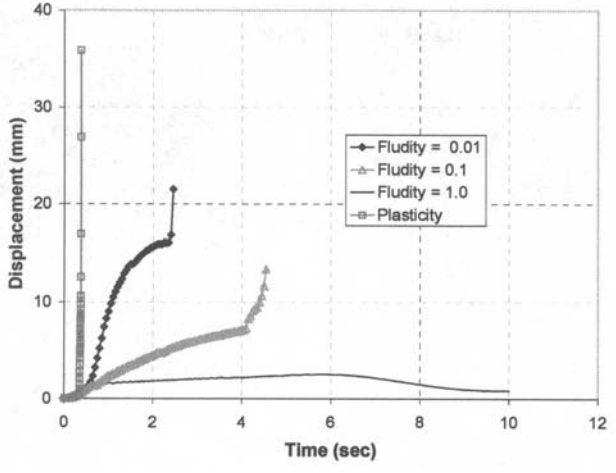

FIG. 3. Displacement versus time.

Example 2. Asphalt Compaction

This example is designed to simulate the asphalt compaction induced by the wheel-pavement interaction. FIG. 4 is the three-dimensional finite element model representing the symmetric part of the wheel-pavement interaction. The top layer is asphalt mixture and modeled with the proposed foam-type viscoplasticity. The second layer gravel and third layer subgrade soil are relatively stiffer and assumed to deform elastically.

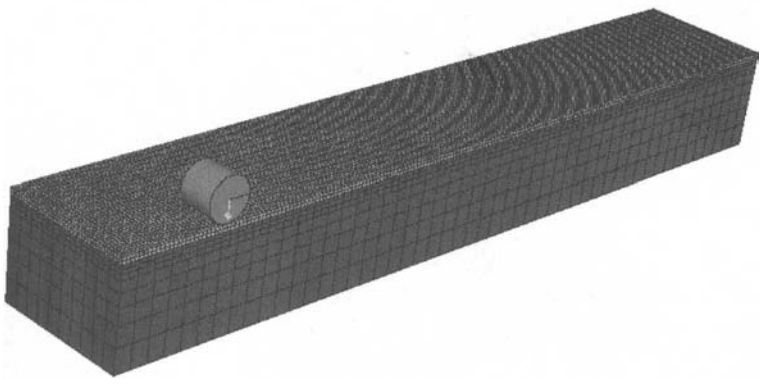

FIG. 4. Finite element model for wheel-pavement interaction.

The initial densities for these three layers are 1900kg/m^3, 2700kg/m^3, 1700kg/m^3. The model parameters used for the top layer are: Young's Modulus, $E = 20.0\text{MPa}$, Poisson's ratio 0.32, $\alpha = 0.6$, $\beta = 1.1$, $P_t = 0.05\text{MPa}$, $P_c = -0.3\text{MPa}$. The vertical load was applied at the wheel center. The rigid wheel is driven back and forth by applying angular velocity at the wheel center. FIG. 5 shows the spatial density distribution projected onto the deformed configuration during machine rolling compaction. This demonstrates that large deformation has advantage on prediction of compaction.

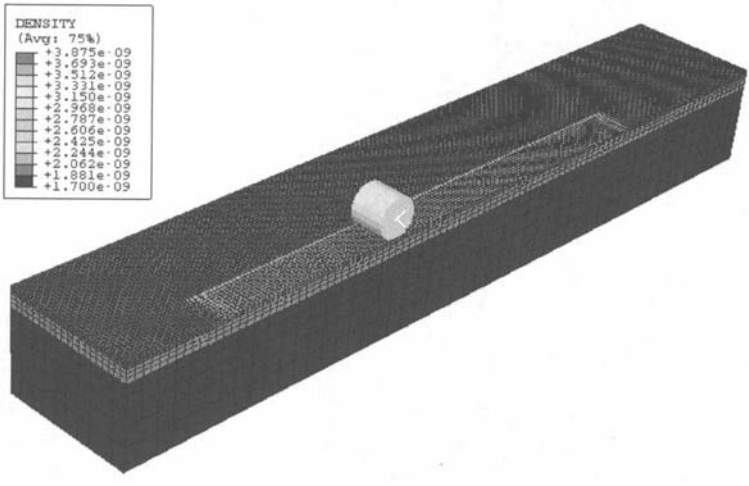

FIG. 5. Density contour due to rolling wheel compaction.

CONCLUSIONS

A viscoplastic foam-type material model with volumetric hardening was proposed and integrated in the commercial finite element analysis package ABAQUS. We combined the material model with large deformation theory to simulate wheel-asphalt interaction, which can effectively predict the density change after each machine pass. The development of deformations with time can also be included if necessary. The representative numerical examples showed that the approach employed in this paper can be used to describe the viscoplastic behavior of asphalt mixtures and simultaneously simulate the compacted density as well as rutting for flexible pavement. As mentioned earlier in this paper, asphalt compaction achieved at the time of construction is very critical to the future pavement performance. In the past

compaction research has always been focused on empirical and test approaches, very little effort was exerted on numerical modeling. In fact large deformation formulation can be directly applied to predict the spatial density distribution induced by compactor. Clearly this is an important application for geometric nonlinearity. We believe this should be the future research direction on asphalt compaction modeling. Certainly some robust HMA and SMA constitutive models should be developed and integrated in finite element codes.

ACKNOWLEDGEMENTS

The authors wish to thank Steve Hornbrook, Paul Corcoran, Warren Hartmann and Bill Evans for their support and helpful discussions.

REFERENCES

ABAQUS Theory Manual Version 6.6.3, 2007.

Lu, Y. and Wright P.J. (1998), "Numerical approach of visco-elastoplastic analysis for asphalt mixtures," Computers and Structures, Vol.69: 139-147.

Perzyna, P. (1966), "Fundamental problems in viscoplasticity," Advanced Appl. Mech., Vol.9: 243-377.

Saleeb, A., Liang R.Y., Qablan, H. and Powers, A. (2005), "Numerical simulation techniques for HMA rutting under loaded wheel tester," Int. J. Pavement Engrg., Vol.6(1): 57-66.

Simo, J. and Hughes, T.J.R. (1998), "Computational Inelasticity," Springer.

Wang, W.M., Sluys, L.J. and De Borst, R. (1997), "Viscoplasticity for instabilities due to strain softening and strain-rate softening," Int. J. Numer. Methods in Engrg, Vol.40: 3839-3864.

White, G and Gnanendran, C. (2005), "The influence of compaction method and density on the strength and modulus of cementitiously stabilized pavement materials," The Int. J. Pavement Engrg, Vol.6(2): 97-110.

Thermal Stress Calculation and Analysis in Steel Bridge Deck Pavement

Jun Yang[1], Guotao Yang[2], Haizhu Lu[3] and Chaoen Yin[4]

[1]Professor, Deputy Director of Institute of Road and Railway Engineering, Southeast University, Sipailou 2#, Nanjing, 210096, P.R.China; yangjun@seu.edu.cn
[2]Graduate Student, Institute of Road and Railway Engineering, Southeast University, Sipailou 2#, Nanjing, 210096, P.R.China; luckyygt@163.com
[3]Gradute Student, Institute of Road and Railway Engineering, Southeast University, Sipailou 2#, Nanjing, 210096, P.R.China; lhz-seu@163.com
[4]Gradutate Student, Institute of Road and Railway Engineering, Southeast University, Sipailou 2#, Nanjing, 210096, P.R.China; yinchao_1984@163.com

ABSTRACT: Low temperature property of asphalt mixture has been one of the worldwide focuses in pavement research. This paper focuses on property of stone matrix asphalt (SMA), mastic asphalt (MA) with that of epoxy asphalt mixture, which are currently widely used in steel bridge deck pavement. During calculation, a three-parameter solid model is employed with its corresponding parameters obtained by nonlinearly regressing the data from bending creep test. Additionally, based on the principle of time-temperature equivalence and linear superposition, thermal stress equation is achieved, through which thermal stress of the three kinds of mixture are calculated with an assumption of constant cooling rate. By comparing the calculation results with that of thermal stress restrained specimen tensile test (TSRST), this equation is found to be adequate to compute the thermal stress at low temperature. Also in this study, the thermal stress is calculated concerning full bonding conditions between steel deck and the mixture. It shows that when the thermal expansion coefficient of the steel deck is ignored, thermal stress will be exaggerated to a great degree. Also, it is found that epoxy asphalt mixture performs the best in terms of low temperature performance.

INTROCUCTION

Low temperature property of asphalt mixture has been one of the worldwide focuses in pavement research. Exposed to the fluctuating temperature, both surface and underlying part of the pavement will experience the action of expansion or contraction due to the heat transfer in the pavement. However, because of the constraint imposed from both the exterior and interior of the pavement system, thermal stress is caused .Once thermal stress exceeds the tensile strength, pavement will crack. Moreover, as a kind of temperature sensitive structure, there is good chance for the strength, stiffness and thermal properties of asphalt pavement to vary with temperatures. Besides, the elusive nonlinear relationship between the

mechanical properties of asphalt mixtures also adds to the complexity of thermal stress analysis in asphalt pavement (Xia and Wang 2003).

VISCOELASTIC MODELING

As is known, asphalt concrete exhibits noticeable viscoelasticity at low temperatures, which always requires a reasonable viscoelastic model to conduct the mechanics analysis. Thanks to the years' research in this respect, till now more than ten types of viscoelastic models have been developed, which can primarily be divided into two categories:

Empirical model, that is established based on the regressed data from the test to address both the initial and stable stage of the creep developing.

Composite model, that is based on the different combination of springs and dashpot, which occupies a majority of all these kinds of models, such as Maxwell Model, Kelvin Model, Jeffreys Model, Burgers Model and etc.

Asphalt concrete becomes brittle when temperature drops, that is, viscosity reduces and elasticity increases. Herein, the three-parameter solid model is adopted, where an elastic solid model is in series with Kelvin model, as shown in Figure 1.

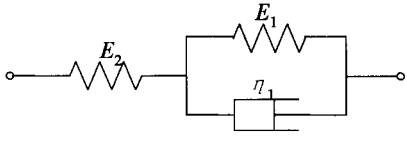

FIG. 1. The three-parameter solid model (after Zhang 1993).

Therefore, the constitutive equation of the three-parameter solid model is

$$\sigma + \frac{\eta_1}{E_1 + E_2}\sigma' = \frac{E_1 E_2}{E_1 + E_2}\varepsilon + \frac{\eta_1 E_2}{E_1 + E_2}\varepsilon' \tag{1}$$

where σ, ε = stress and strain of the model, respectively;
η_1 = the compliance of the dashpot;
E_1, E_2 = the elastic modulus of the spring in the Kelvin model and the other one;
σ', ε' = the developing rate of the stress and strain over time;

The creep compliance $J(t)$ and stress relaxation equation $Y(t)$ can be obtained by mathematic transformation of the constitutive equation.

$$J(t) = \frac{1}{E_2} + \frac{1}{E_1}(1 - e^{-\frac{\eta_2 t}{E_2}}) \tag{2}$$

$$Y(t)=\frac{\sigma}{\varepsilon_0}=E_2\left[1-\frac{E_2}{E_1+E_2}(1-e^{-\frac{t}{p_1}})\right] \tag{3}$$

where

$$p_1=\frac{\eta_1}{E_1+E_2} \tag{4}$$

PARAMETER IDENTIFICATION OF THE VISCOELASTIC MODEL

The key point is to obtain the three parameters for further analysis and computation. As shown in Eq. 2, the nonlinearity of the parameters makes the parameter identification a difficult job. Therefore in this study, Levenberg-Marquardt (L-M) method, which is based on the improvement of Newton's method, is used for parameter identification of viscoelastic model (Zhou et al. 2001). In Newton's method, a demanding initial value is required for the parameter, which is usually difficult to acquire, while L-M method is not so strict in this respect. Therefore, in this study L-M method is employed.

Bending beam creep test was conducted on the material test system *MTS*-810 with the test temperature at 10 °C below freezing. The stress level is ten percent of the critical failure stress with loading duration of one hour. The size of the specimen is 250mm long, 30mm wide and 35mm high.

The bending strain in the creeping test was recorded with time. Creep compliance simply equals to bending creep strain divided by the constant stress, so the equation of time-dependent bending strain is of the same type with Eq. 2, which is the simple equation of exponential function with time. The relationship between bending strain and time was, therefore, fitted according to Eq. 2 with the L-M method. The results of the fitting parameters are shown in Table 1. Test creeping curves of time-dependent bending strain of the three kinds of mixtures are illustrated in Figure 2, together with the fitting curves.

Table 1. Viscoelastic parameters of the three-parameter solid model (-10 °C)

Material type	Viscoelastic parameters		
	E_1 (*MPa*)	η_1 (*MPa·s*)	E_2 (*MPa*)
MA	5.054e+03	9.270e+06	2.057e+05
Epoxy asphalt	8.782e+03	1.008e+07	3.139e+05
SMA	5.064e+03	3.950e+06	1.938e+05

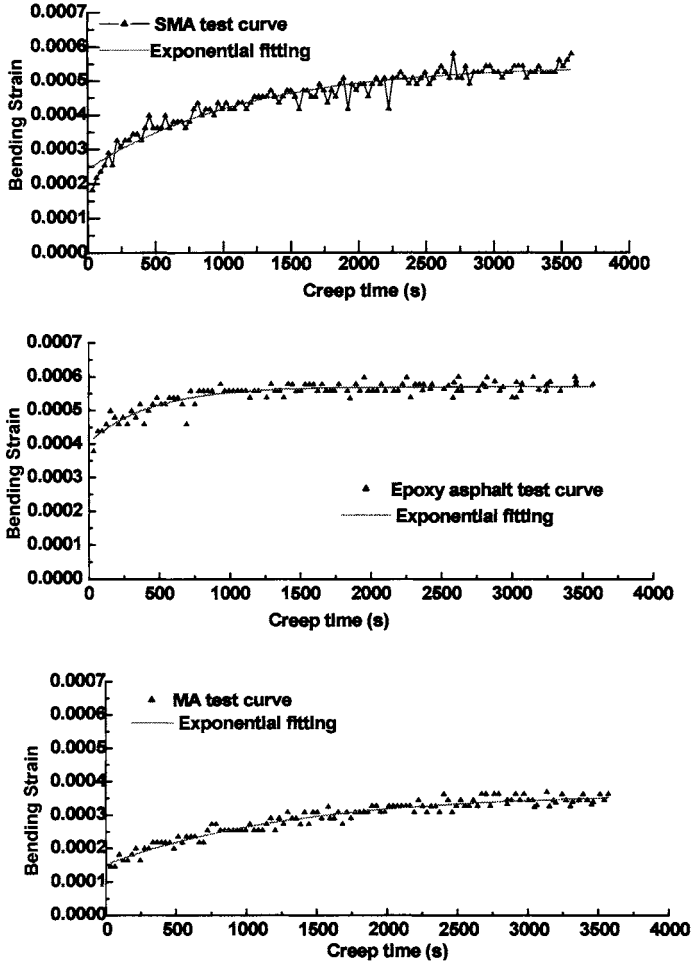

FIG 2. Creeping curves of SMA, MA and Epoxy Asphalt Mixtures.

THERMAL STRESS COMPUTATION

Deduction of thermal stress equation

With time-temperature equivalence conversion, material properties in a three-dimension space are reflected onto the two-dimension space. Moreover, the test results in a limited time and temperature range are also extended to a much wider time and temperature range. Consequently, both test work and technical requirement for the instruments are significantly reduced. Time-temperature equivalence is

usually formulated as Arrhenius equation in studying low temperature properties of asphalt mixture (Franken 1993), shown as (5).

$$B(T) = \exp\left[\frac{H}{R}\left(\frac{1}{T} - \frac{1}{T_0}\right)\right] \tag{5}$$

where $B(T)$ = shift factor, used to deduce the relaxation modulus in a temperature drop process from a reference temperature;

T_0, T = reference temperature and test temperature, K;

H = surface activation energy, which is to be determined in tests, and is approximately 2.1×10^5 J/mol for asphalt mixture;

R = the universal gas constant, 8.31 J/(mol·K).

The relaxation modulus at the reference temperature can be converted to that at other temperatures through time-temperature equivalence conversion, shown as (6).

$$Y(t,T) = Y(\frac{t}{\alpha_T}, T_0) = E_2\left[1 - \frac{E_2}{E_1 + E_2}\left(1 - e^{-\frac{t}{p_i B(T)}}\right)\right] \tag{6}$$

Linear superposition principle is one of the most fundamental and important principles in viscoelastic mechanics, which was initially developed by Boltzmann only as an empirical relation, also known as Boltzmann superposition principle. This paper combined the discretization method and Boltzmann superposition principle in calculating thermal stress concerning continuous and larger drop of the temperature (Zhang 2006).

As a matter of fact, the actual thermal stress is achieved through the continuous superposition of the new emerging thermal stress and relaxation stress in the process of temperature drop. This thermal stress superposition is illustrated in Figure 3.

The time is discretized into Δt_i by t_i, and the temperature is assumed approximatively to drop instantly at the beginning of the time section Δt and keeps constant in this time section. So the whole process for temperature dropping is in a stepwise way (Figure 3-a). The contraction strain will be proportional to the temperature decrement at the rate of linear expansion coefficients $\alpha(T)$, which is also a constant in the limited temperature scope (Figure 3-b). Therefore, due to the viscoelastic behavior of the material, the stress development will be a typical relaxation curve in the whole process. The relation between the relaxation stress and strain is as follow,

$$\Delta\sigma_i = \Delta\varepsilon_i Y(t,T) \tag{7}$$

where $\Delta\varepsilon_i$ = the strain in each discretized time section;

$Y(t, T)$ = the relaxation modulus varying over time and temperature obtained by

creep test of the material at different temperatures, here $t = t_i - t_0$, $T = (T_{i-1} + \Delta T_i / 2)$.

In the next discretized time section, new stress curve happens. And thermal stress is attained by superposing the relaxation stress in each ΔT_i by Boltzmann superposition principle (Figure 3-c). For example, thermal stress at t_f is calculated as $\sigma_f = \sigma_{f1} + \sigma_{f2} + \sigma_{f3}$.

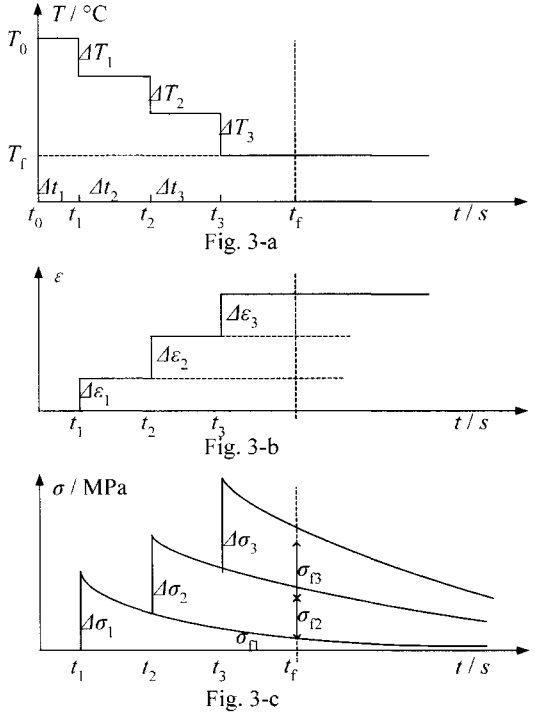

FIG 3. Superposition of contraction and relaxation stresses (after Zhang 1993).

Neglecting steel deck contraction due to temperature drop, the thermal stress of asphalt concrete pavement can be calculated with Eq. 8. However, in actual situation, as temperature drops, steel deck will shrink. Because of the different thermal expansion coefficients between steel deck and asphalt concrete, deformation discrepancy exists between them. Under these conditions, thermal stress will be calculated with Eq. 9. Herein in both situations, assumption is made that there exists full bonding condition between the steel deck and the pavement thereon and the overlaying pavement is enclosed by all sides. Also temperature field and thermal expansion coefficients in each material is deemed uniform throughout the dropping in temperature, so no differential contraction or bending moment is considered.

$$\sigma_x(T)=\sum_{T_0}^{T_f}Y\left(t_f-t_i,T_i\right)\Delta T_i\alpha(T) \tag{8}$$

$$\sigma_x(T)=\sum_{T_0}^{T_f}Y\left(t_f-t_i,T_i\right)\Delta T_i\left[\alpha(T)-\beta\right] \tag{9}$$

Here, $Y\ (t_f - t_i,\ T_i)$ represents the relaxation modulus of asphalt concrete from time t_j to t_f; T_0, T_f represent the initial temperature and ending temperature; ΔT_j is the temperature decrement from t_j to t_f; $\alpha(T)$ is the linear thermal expansion coefficient of asphalt at the temperature T; β is the thermal expansion coefficient of steel deck.

Through Eqs. 6, 8 and 9, thermal stress in the pavement when temperature drops will be computed.

Conditions for thermal stress computation in pavement

Pavement structure is largely influenced by variation of climate, like abrupt drops of temperature, in which the temperature field and thermal stress in pavement structure are both quite different from those with a periodical varying temperature. Herein, thermal stress calculation is focused on the condition of continuous temperature drop.

Some assumptions are made for calculating the thermal stress as follows:

1. Asphalt concrete pavement is homogenous and isotropic and temperature variations between pavement and steel box beam are consistent, neglecting the influence of temperature gradients;
2. There exists a full bond between the pavement and the steel deck, neglecting the stress caused by the movement discrepancy between the steel deck and the pavement; thermal stress is uniformly distributed along the thickness;
3. Steel deck is an elastic system with a constant thermal expansion coefficient in the calculation area;
4. The linear thermal expansion coefficient $\alpha(T)$ of asphalt mixture remains constant during the assumed cooling process. The thermal expansion coefficients of the materials focused in this paper are given in Table 2.

Table 2. Linear expansion coefficients of materials focused in this paper

Material Type	SMA	MA	Epoxy Asphalt	Steel Deck
Linear expansion coefficients (10^{-5} / °C)	2.4	3.0	1.6	1.0

Comparison of calculated results and tests results

After extensive analysis of different test methods on thermal cracking, it is found that the thermal stress restricted specimen test (abbreviated as TSRST below) fulfills the goal best to simulate most of the in-situ conditions of pavement (Hao 2002). In this study, TSRST is performed and a systematic data acquisition and analysis method is applied.

Table 3. Thermal stress in asphalt pavements

Time (s)	Temp. (°C)	SMA (MPa)		MA (MPa)		Epoxy Asphalt (MPa)	
		theory	test	theory	test	theory	test
0	2	0	0	0	0	0	0
720	0	0.82	0.775	1.42	1.43	0.91	0.57
2520	-5	3.06	2.57	4.24	4.65	2.37	2.69
4300	-10	5.37	4.99	7.32	7.86	5.86	5.03
5146	-12.35			8.76	9.08		
6100	-15	7.7	7.88			8.07	7.57
7900	-20					9.88	10.48
8476	-21.6					11.72	14.89

Thermal stress was tested on the three materials through TSRST. Size of the specimens of the materials is 30mm×30mm×200mm. The initial temperature is 2 °C and the cooling rate of is 10 °C/h. In Table 3 the test results and computation show good agreement, which means that the method used in this paper works well in computing thermal stress of asphalt mixture. Comparing the results in Table 3 with those in Table 4, the thermal expansion coefficient of steel deck considered, the thermal stress in the asphalt pavement will be much smaller. Of the three types of materials, epoxy asphalt concrete is the best in low temperature property considering steel deck effect. This can be explained by the similarity of epoxy asphalt concrete with steel deck in thermal property at low temperatures. Therefore, despite an extremely high relaxation modulus (in Table 1), thermal stress in epoxy asphalt is the lowest, as also explains the rarity of thermal cracking in epoxy asphalt on steel deck.

Table 4. Thermal stress in pavement considering the effect of steel deck

Temperature (°C)	Time (s)	SMA (MPa)	MA (MPa)	Epoxy Asphalt (MPa)
2	0	0	0	0
0	720	0.47	0.78	0.34
-5	2520	1.78	2.81	0.89
-10	4300	3.13	4.87	1.82
-15	6100	4.48	6.92	2.19
-20	7900	5.84		3.7
-21.6	8476			4.39

CONCLUSIONS

1. Based on the three-parameter solid model and the principle of time-temperature equivalence and linear superposition, the stress calculation equation is achieved, whose validity is also verified by the test results.
2. When taking thermal expansion coefficient of the steel deck into account, the thermal stress is much smaller compared with that neglected.
3. When the steel deck contraction considered, the low temperature property of the epoxy asphalt concrete is the best among the three kinds of pavement materials.
4. A good bond condition between the steel deck and pavement is recommended, which will reduce thermal stress to some extent.

REFERENCES

Xia, Y.X. and B.G. Wang (2003), *Computational Structural Mechanics for Pavement*, China Communications Press, Beijing.

Zheng, D.L. (1993), *Bitumen and Bituminous Mixture*, China Communications Press, Beijing.

Zhou Z.G., G.P. Qian and J.L. Zheng (2001), "Research on the Method of Testing Viscoelastic Parameters of Bituminous Mixtures," *Journal of Changsha Communications University*, 17(4), 1–6.

Franken L (1993), "Laboratory Simulation and Modeling of Overlay Systems," *Proceedings of 2nd International RILEM Conference*, 1996, Cambridge University Press, Cambridge.

Zhang X.N. (2006), *Viscoelastic Mechanics of Bitumen and Bituminous Mixtures: Principle and Application*, China Communications Press, Beijing.

Hao P.W. and Z.L. Liu (2002), "Study on Thermal Stress Restrained Specimen Test of Asphalt Mixture," *Petroleum Asphalt*, 16(1), 9–11.

Equivalency of Using the Binder or the Mastic Modulus to Estimate the Mixture Modulus

Cristian Druta[1], Linbing Wang[2], George Z. Voyiadjis[3] and Chris Abadie[4]

[1]Postdoctoral Research Associate, Virginia Tech Transportation Institute, Blacksburg VA 24061, cdruta1@vt.edu
[2]Associate Professor, Virginia Tech, Department of Civil and Environmental Engr., Blacksburg VA 24061, Tel. (540)231-5262; wangl@vt.edu
[3]Boyd Professor, Louisiana State University, Department of Civil and Environmental Engineering, Baton Rouge LA 70803, Tel. (225)578-8668; voyiadjis@eng.lsu.edu
[4]Materials Administrator, Louisiana Transportation Research Center, 4101 Gourrier Avenue Baton Rouge, LA 70808, Tel. (225)767-9109; chrisabadie@dotd.la.gov

ABSTRACT: This paper presents an investigation in applying the Hirsch model to predict the mixture modulus through using the binder modulus and the mastic modulus and their corresponding volume compositions. By comparing the model predictions using the two different methods with the experimental results, it is found that the two methods are equivalent.

INTRODUCTION

Permanent deformation or rutting in asphalt concrete develops gradually as the number of loading applications increases (Anderson et al. 1991; Ishai and Craus 1996; Anderson et al. 2001). Rutting is a combination of the continuing compaction and shearing due to traffic loading (Bonnaure et al. 1977; Bahia 1995; Roberts et al. 1996; Li and Metcalf 2005). Asphalt concrete being a composite material (Buttlar and Roque 1996; Buttlar et al. 1999) essentially is comprised of three constituents: asphalt binder, mineral aggregate, and air voids. Each constituent, as well as the asphalt-aggregate interface, contributes to the HMA's resistance to permanent deformation (Mallick 1999; Bahia et al. 2003).

Complex shear modulus G* was introduced in 1993 for asphalt binder specification as part of the SHRP Program (Jo et al. 1998; Shashidhar and Romero 1998; Stuart et al. 2000; Roberts et al. 2002). It was intended for a better evaluation of the rheological behavior of asphalt binders at different temperatures. It was also utilized for asphalt mixtures through testing using the Superpave Shear Tester (SST). Also, the elastic dynamic modulus, E*, can be calculated from G* and ν, Poisson's ratio (Hirsch 1962; Shenoy and Romero 2001; Kaloush and Witczak 2002). When designing asphalt pavement structures, the elastic modulus is a basic design parameter. Therefore, it is preferable that the modulus of AC be predicted during the

design process in order to improve the design and the pavement performance prediction.

Micromechanical approaches for predicting the shear modulus of mastics and mixtures were employed by Buttlar and Roque (1996). The micromechanical model developed by Christensen et al. (2003) and used in this research estimates the shear modulus of asphalt concrete using binder modulus and volumetric composition VMA and VFA (Christensen and Bonaquist 2005). The model is based upon a previous version of the law of mixtures, called the Hirsch model, which combines series and parallel elements of phases (aggregate and asphalt binder). The purpose of this research is to assess the equivalency of estimating the mixture modulus using the binder modulus and the mastics modulus.

OBJECTIVE

The main objective of this study was to predict the shear moduli of asphalt mixtures with different asphalt contents by using the binder and mastic complex moduli and their volumetric compositions (VMA and VFA). One type of binder (PG64-22), in five percentages by mass, and one type of aggregate (granite) were mixed and tested at two temperatures (55° and 64 °C) and at a constant air void content of 6%. Binder and mastic specimens were tested with a dynamic shear rheometer, while the asphalt concrete specimens were tested with the Superpave shear tester. The major motivation is to investigate whether it is equivalent to use binder modulus or mastic modulus for predicting the mixture modulus.

MATERIALS

Filler and Aggregate

The filler used for making the mastic specimens was granite and the aggregate selected for the HMA specimens was crushed granite. Both materials were provided by the Louisiana Transportation Research Center. The selected coarse and fine aggregates were supplied in two sizes, #78 and #9, according to ASTM D 448, "Standard Classification for Sizes of Aggregate for Road and Bridge Construction". Properties of the granite aggregate are provided in Table 1 (Waltham 2003). This aggregate has a rough-textured structure providing good interlock in asphalt concrete mixes (HMAs). A coarse-graded Superpave mixture was selected for this study. The gradation of the aggregate is shown in Figure 1.

Table 1. Properties of granite

Aggregate type	Dry density (kg/m^3)	Dry UCS (MPa)	Elasticity modulus (GPa)	Tensile strength (MPa)	Shear strength (MPa)	Friction angle ϕ°
Granite	2.720	200	75	2.67	35	55

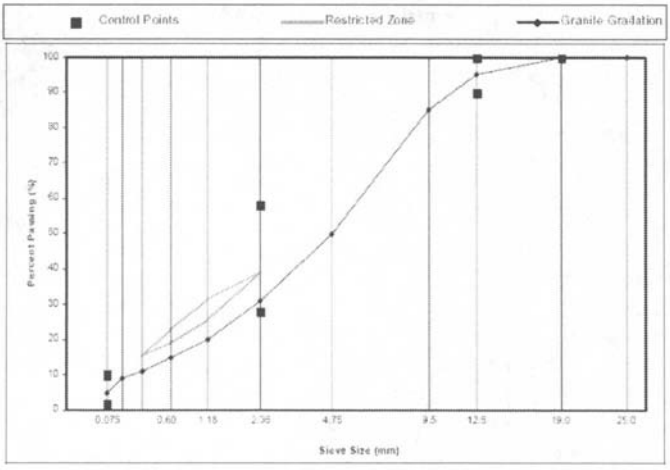

FIG. 1. Granite gradation.

Asphalt binder

The asphalt binder used in this study was a PG64-22 unmodified base asphalt binder, which is commonly used in Louisiana.

EXPERIMENTAL STUDY

Mastic samples preparation

The granite mineral filler was dried for one hour in an oven at 160°C before being mixed with the asphalt, in order to remove all the moisture. Then, measured quantities of 25 (g) of binder were heated at 150 °C for 10 minutes and then mixed with 20% of filler volume fraction of bulk material. After being heated, the binder was removed from the oven and the heated filler was added and was mixed until a homogeneous mixture was obtained; then the mixture was poured into silicon molds to make samples for the DSR (Dynamic Shear Rheometer) measurements.

HMA samples preparation

Once the aggregate blends were selected and the initial trial asphalt binder content was calculated, the HMA mixtures were prepared. Aggregates were heated for one hour in order to eliminate all the moisture. The aggregates and asphalt binder were heated to 159° ± 3 °C then mixed and short-term aged for 2 hours at 135 °C. After aging, all the mixtures were compacted in a gyratory compactor at a temperature of 145° ± 3 °C and to a target air void content of 7%.

All asphalt mixes in this study were prepared at the Louisiana Transportation Research Center (LTRC) using the gradation from Figure 1 and five asphalt binder contents, from 3% through 7% (by mass) in 1% increments. Filler content was kept constant at 20% by mass of total asphalt content. Ten disk-shaped samples, 150 mm in diameter and 50 mm in height, were produced after cutting from larger specimens, two for each asphalt content. The portions cut from the large disk for the shear testing had air void contents around 6% (Druta 2006).

DSR testing

The rheological properties of the binder and mastic were measured using an Automated Dynamic Shear Rheometer (ADSR) using the single shear oscillation mode. All the samples were tested in the strain mode, at a constant strain rate of 12% and a frequency of 10 (rad/s) or 1.592 (Hz), in accordance with SHRP specifications. The plates selected for testing were 25 (mm) in diameter with a gap between the plates of 1 (mm). The shear complex modulus G* and the phase angle δ were calculated automatically during the rheometer testing. Samples were tested at temperatures of 55° and 64 °C.

SST testing of HMA specimens

The Superpave Shear Tester (SST) was developed under SHRP as a way to measure the shear characteristics of HMA. Six SST tests can be performed with the SST for measuring the mix performance characteristics. The Simple Shear, Frequency Sweep, Uniaxial Strain, Volumetric Shear, Repeated Shear at Constant Stress Ratio, and Repeated Shear at Constant Height tests measure properties that may be useful in calculating the resistance to permanent deformation and fatigue cracking. The shear frequency sweep test performed for this study, which is usually used to evaluate permanent deformation, is presented below.

Testing Procedures, Results and Discussion

Shear Frequency Sweep at Constant Height (FSCH) for asphalt mixtures

The shear frequency sweep or shear dynamic modulus G* test conducted with the Superpave Shear Tester (SST) was developed under the SHRP research program to measure mixture properties that can be used to predict mixture performance (Shenoy and Romero 2001). During the loading cycles, the specimen height is maintained constant by applying sufficient axial stress and this is accomplished by controlling the vertical actuator through an axial LVDT. The data (deformation and load) obtained from the FSCH test is used to automatically calculate two material properties: dynamic shear modulus G* and phase angle δ. During testing, the load is applied to the asphalt concrete specimen until a shear strain of 0.01% is obtained. This ensures that the sample is solely tested in the linear elastic range. Figure 2 shows the dependencies of shear complex modulus on frequency loading and testing temperatures. Similarly to the asphalt mastics, the curves for the mixtures exhibited

the same trend, with larger G* values at higher frequencies and smaller values at lower frequencies, compared to the curve at 25 °C. Also, larger values were obtained for the lower temperature (55 °C) compared to the higher temperature (64 °C). Compared to the mastic's shear moduli (at 1.59 Hz), the shear moduli for asphalt concrete mixtures, at the same frequency, increased by three orders of magnitude, from around 130 kPa to 162 MPa at 55 °C and from 45 kPa to 55 MPa at 64 °C.

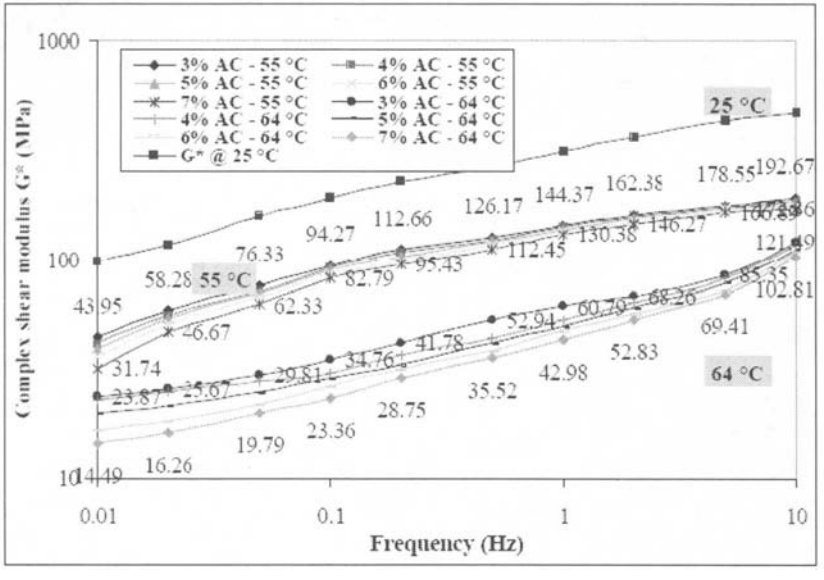

FIG. 2. Shear complex modulus dependency on temperature and loading frequency of asphalt mixtures.

Also, Figure 2 shows that the shear complex modulus depends not only on temperature, but also on the asphalt binder content. As observed from the figure, the shear modulus decreases with the increase in asphalt content for both temperatures of 55° and 64 °C. The decrease was around 20 MPa at the 10 Hz frequency and 10 MPa at 0.01 Hz. This shows that the shear modulus is more affected by the aggregate interaction while sheared, more asphalt content resulting in less friction between the aggregate particles due to the increased asphalt film thickness between the particles.

Also, by using the Williams-Landel-Ferry equation and the data from the frequency sweep and combining it, at the two temperatures (55° and 64°C), and translating the individual curves along the time axis (using the shift factor a_T), single master curves are obtained as shown in Figure 3 below.

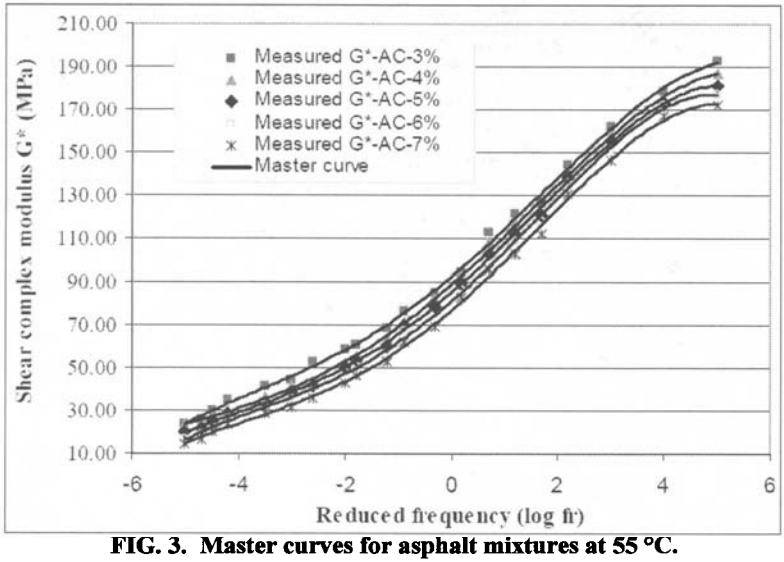

FIG. 3. Master curves for asphalt mixtures at 55 °C.

Hirsch Model

The Hirsch model developed by Christensen et al (2003) was used to estimate the complex shear modulus G* of asphalt concrete specimens by using the binder and mastic shear complex moduli.

The following equation was employed for estimation, in terms of the complex shear modulus, *G**, VFA, and VMA:

$$G^*_{mix} = P_c\{[E_a(1 - VMA/100) + G^*_{binder}[(VFA \cdot VMA)/10{,}000]\} + (1 - P_c)[(1 - VMA/100)/E_a + VMA/VFA \cdot G^*_{binder}]^{-1} \quad (1)$$

where: P_c is the contact factor
E_a is the aggregate elastic modulus (MPa)
G^*_{mix} is the complex shear modulus for the mixture (mastic) (Pa)
G^*_{binder} is the complex shear modulus for the binder (Pa)
VFA is voids filled with asphalt (%)
VMA is voids in mineral aggregate (%)
Expression for P_c is given by:

$$P_c = [3 + (VFA \cdot G^*_{binder})/VMA]^{0.678}/[396 + (VFA \cdot G^*_{binder})/VMA]^{0.678} \quad (2)$$

Values for G^*_b (binder) and G^*_m (mastic) were determined experimentally using the DSR oscillation at constant strain. The predictions of G^*_{mix} can be estimated by two different methods, one using the binder and aggregates, the other using the mastics and aggregates. Figure 4 shows that there is a good correlation between the predicted

values and the measured values using both methods (all R^2 being higher than 0.8). The small difference in the predictions using the two different methods indicates that these two methods are equivalent.

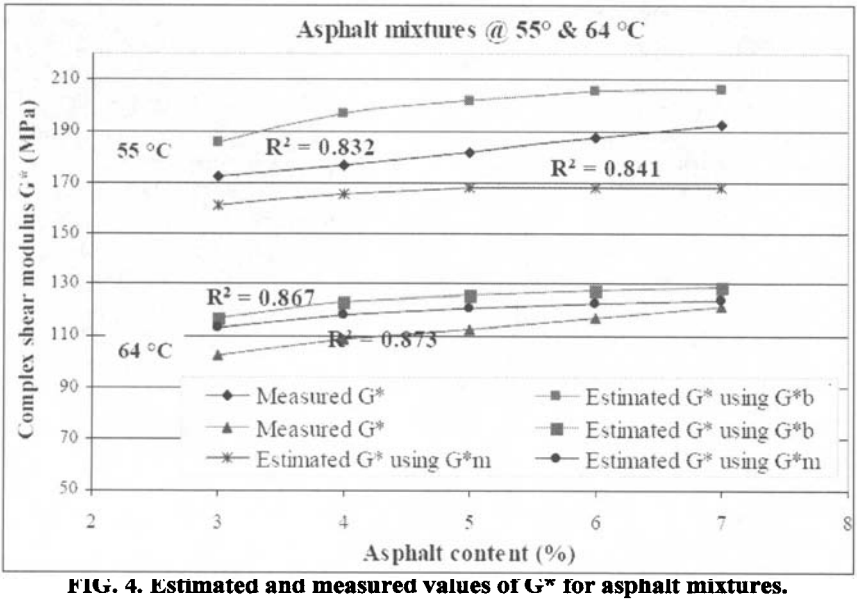

FIG. 4. Estimated and measured values of G* for asphalt mixtures.

SUMMARY AND CONCLUSIONS

The main goal of this study was to estimate the shear modulus of asphalt mixtures at different asphalt contents using the binder and mastic shear complex modulus through testing by Dynamic Shear Rheometer (DSR) and Superpave Shear Tester (SST) and the Hirsch model. This approach shows that the shear complex modulus of the asphalt mixtures could be estimated using either the binder or the mastic shear modulus in the Hirsch micromechanical model. The results obtained from the model using the shear modulus and volumetric composition provided a good correlation. It indicates that it is equivalent to use either binder or mastic modulus for predicting the mixture modulus in the Hirsch model.

REFERENCES

AASHTO TP4 (1999). "Standard Method for Preparing and Determining the Density of Hot Mix Asphalt (HMA) Specimens by Means of the SHRP Gyratory Compactor." AASHTO TP4 Provisional Standards.

AASHTO Standard T315-02 (2002). "Standard Test Method for Determining the Rheological Properties of Asphalt Binder Using a Dynamic Shear Rheometer (DSR)."

AASHTO 320-03 (2003). "Determining the Permanent Shear Strain and Stiffness of Asphalt Mixtures using the Superpave Shear Tester (SST)."

ASTM D 4013 (1989). "Standard Practice for Preparation of Test Specimens of Bituminous Mixtures by Means of Gyratory Shear Compactor", ASTM Standards.

ASTM D 2041 (2000). "Standard Test Method for Theoretical Maximum Specific Gravity and Density of Bituminous Paving Mixtures" ASTM Standards.

Anderson, D.A., Christensen, D.W., and Bahia, H. (1991). "Physical properties of asphalt cement and the development of performance related specifications." AAPT Proceedings, 60, 437-475.

Anderson, R.M., Steger, R.K., Huber, G.A., and Romero, P (2003). "Precision of shear tests used for evaluating asphalt mixtures." TRB 82nd Annual Meeting CD, Washington, D.C.

Bahia, H.U. (1995). "Critical evaluation of asphalt modification using the SHRP concepts" TRR 1488, 82-88.

Bahia, H.U. et al. (2003). "Simplistic mixture design using the SGC and the DSR." J. Assoc. of the Asphalt Paving Technologists, 72, 196-225.

Bonnaure, F. et al. (1977). "A new method of predicting the stiffness of asphalt paving mixtures, J. Assoc. of Asphalt Paving Technologists, 46, 64-100.

Buttlar, W.G. and Roque, R. (1996). "Evaluation of empirical and theoretical models to determine asphalt mixtures stiffnesses at low temperatures." J. Assoc. of Asphalt Paving Technologists, 65, 99-141.

Buttlar, W.G. et al. (1999). "Understanding asphalt mastic behavior through micromechanics" TRR, 1681, 157-169.

Christensen, D.W., Pellinen, T., and Bonaquist, R.F. (2003). "Hirsch model for estimating the modulus of asphalt concrete." AAPT, 72, 184-204.

Christensen, D.W. and Bonaquist, R.F. (2005). "VMA: One key to mixture performance." Paper submitted to the South Central Superpave Center for Publication in the National Superpave Newsletter.

Druta, C. (2006). "A micromechanical approach for predicting the complex shear modulus and accumulated shear strain of asphalt mixtures from binder and mastics." Dissertation, Louisiana State University, Baton Rouge, Louisiana.

Hirsch, T.J. (1962). "Modulus of elasticity of concrete affected by elastic moduli of cement paste matrix and aggregate."ACI J., 59(3), 427452.

Ishai, I. and Craus, J. (1996). "Effects of some aggregate and filler characteristics on behavior and durability of asphalt paving mixtures." TRR 1530, National Research Council, Washington, D.C., 75-85.

Jo, D., Kim, R., and Lee, H. (1998). "Effects of aging on viscoelastic properties of asphalt-aggregate mixtures." TRR, 1630(0334), 21-27.

Kaloush, K.E. and Witczak, M.W. (2002). "Tertiary flow characteristics of asphalt mixtures." J. Assoc. of Asphalt Paving Technologists, 71, 248-280.

Li, Y. and Metcalf, J.B. (2005). "Two-Step approach to prediction of asphalt concrete modulus from two-phase micromechanical models." J. of Materials in Civil Engineering, 17(4), 407-415.

Mallick, R.B. (1999). "Use of Superpave gyratory compactor to characterize hot-mix asphalt." TRR 1681 , Transportation Research Board, Washington, D.C., 86-96.

Roberts, F.L. et al. (1996). "Hot-mix asphalt materials, mixture design, and construction." NAPA Research and Education Foundation, Second Ed., 76-84.

Roberts, F.L., Mohammad, L.N., and Wang, L.B. (2002). "History of hot mix asphalt mixture design in the United States." J. of Materials in Civil Engineering, 14(4), 279-293.

Shashidhar, N. and Romero, P. (1998). "Factors affecting the stiffening potential of mineral fillers." TRR, 1638(0989), 94-100.

Shenoy, A. and Romero, P. (2001). "Superpave shear tester as a simple standardized measure to evaluate aggregate-asphalt mixture performance." J. of testing and Evaluation, JTEVA, 29(5), 472-484.

Stuart, K.D., Mogawer, W. S., and Romero, P. (2000). "Evaluation of the Superpave asphalt binder specification for high-temperature pavement performance." AAPT, 69, 148-176.

Waltham, T. (2003). "Foundations of engineering geology." First Ed.,E & FN Spon, 44-50.

This page intentionally left blank

Author Index

Page number refers to first page of paper

This page intentionally left blank

Subject Index

Page number refers to first page of paper